

# **3-D EQUILIBRIUM RECONSTRUCTION IN THE HSX STELLARATOR**

by

John C. Schmitt

A dissertation submitted in partial fulfillment of  
the requirements for the degree of

Doctor of Philosophy

(Electrical and Computer Engineering)

at the

UNIVERSITY OF WISCONSIN–MADISON

2011

© Copyright by J. C. Schmitt 2011

All Rights Reserved

## Abstract

Plasmas in the quasi-helically symmetric (QHS) configuration of the HSX stellarator are predicted to have a Pfirsch-Schlüter current that is helical due to the lack of toroidal curvature and a neo-classical bootstrap current that is in the opposite direction to that in a tokamak. Each current is predicted to be reduced in magnitude by the high effective transform ( $\approx 3$ ) of QHS systems. The equilibrium currents in the HSX stellarator are measured with a set of magnetic diagnostics which includes Rogowski coils, diamagnetic loops, two poloidal belts separated by  $1/3$  of a field period, and internal coils. Each belt, mounted on the external side of the vacuum vessel, consists of 16 3-axis magnetic pick-up coils to measure the local magnetic field, and the 15 internal coils measure the poloidal field. Measurements confirm the helical rotation of the Pfirsch-Schlüter current and the reversal of the bootstrap current. Electron temperature and density profiles are measured with a Thomson scattering system and ion temperature profiles are measured with a ChERS system. The measured profiles are used to calculate the neoclassical fluxes and flows with the PENTA code which includes the effects of momentum conservation between plasma species. The inductive response of the plasma is calculated, including the effects of the 3-D shaping of the column. The 3-D equilibrium reconstruction code, V3FIT, uses the measured magnetic diagnostic signals as constraints to reconstruct the pressure and current profiles. The reconstructed pressure profile and stored energy agree well with the Thomson scattering and flux loop measurements. Later in the plasma discharge, the measurements are dominated by the bootstrap current which rises on a timescale comparable to the length of the discharge. The reconstructed current profile is consistent with the calculated bootstrap current when the effects of momentum conservation between plasma species and the 3-D inductive response of the plasma column are considered. The reduction of the Pfirsch-Schlüter and bootstrap currents by the high effective transform is confirmed. Uncertainty in the reconstructed profiles is largest near the magnetic axis.

For Mom and Dad.



## **ACKNOWLEDGMENTS**

To Electron and Proton: Meow!

# TABLE OF CONTENTS

	Page
<b>ABSTRACT</b> . . . . .	i
<b>LIST OF TABLES</b> . . . . .	vii
<b>LIST OF FIGURES</b> . . . . .	ix
<b>1 Introduction</b> . . . . .	1
1.1 Neoclassical Bootstrap Current . . . . .	8
1.2 Timescales and Temporal Evolution . . . . .	11
1.3 Equilibrium Reconstruction with Magnetic Diagnostics . . . . .	13
1.4 Thesis Outline . . . . .	17
References . . . . .	20
<b>2 Magnetohydrodynamic Equilibrium and Neoclassical Bootstrap Currents</b> . . . . .	24
2.1 Basic MHD . . . . .	25
2.2 Pfirsch-Schlüter Current . . . . .	26
2.3 Neoclassical Parallel Bootstrap Current . . . . .	29
2.3.1 Large Aspect Ratio Tokamak . . . . .	31
2.3.2 Nonaxisymmetric Transport Analysis: Radial Electric Field, Flows, Viscosity and Momentum Conservation Between Plasma Species . . . . .	35
2.4 Parallel currents with and without momentum conservation . . . . .	41
2.5 Summary . . . . .	47
References . . . . .	49
<b>3 Temporal Modeling of Parallel Current</b> . . . . .	51
3.1 Plasma Current Evolution in a Cylindrical Geometry . . . . .	51
3.2 Plasma Current Evolution in a General Nonaxisymmetric Toroidal Configuration . . . . .	54
3.2.1 Current and Magnetic Flux Relations via Ampere’s Law . . . . .	54
3.2.2 Rotational Transform . . . . .	59
3.2.3 VMEC Coordinates and Susceptance Matrix Components . . . . .	59

	Page
3.2.4 Parallel Electric Field: Faraday's Law and Ohm's Law . . . . .	62
3.2.5 Boundary Conditions . . . . .	67
References . . . . .	68
<b>4 Magnetic Diagnostics and Equilibrium Reconstruction . . . . .</b>	<b>69</b>
4.1 Flapper Probe . . . . .	69
4.2 Magnetic Diagnostics . . . . .	70
4.2.1 External Magnetic Vector Diagnostic Array . . . . .	71
4.2.2 Internal Magnetic Diagnostics . . . . .	74
4.2.3 Rogowski Coil . . . . .	75
4.3 Magnetic Diagnostic Signal Processing . . . . .	77
4.4 Effects of the Vacuum Vessel . . . . .	84
4.5 Response Functions to Rapidly Calculate Magnetic Signals . . . . .	86
4.6 Modeling and Reconstruction of Plasma Pressure and Current Profiles . . . . .	90
References . . . . .	96
<b>5 3-D Equilibrium Reconstruction . . . . .</b>	<b>98</b>
5.1 QHS 50 kW with Balanced Fueling . . . . .	101
5.2 Helical rotation of Pfirsch-Schlüter current . . . . .	109
5.3 Reconstruction of Plasma Pressure and Current Profiles . . . . .	113
5.3.1 Reconstruction with the Internal Poloidal Array and Rogowski Coil . . . . .	114
5.3.2 Reconstruction with the External Magnetic Diagnostic Array, Internal Poloidal Array and Rogowski Coil . . . . .	119
5.4 100 kW QHS with Balanced Fueling . . . . .	124
5.5 50 kW QHS, $\rho_{ECRH} \sim 0.3$ . . . . .	132
5.6 Summary . . . . .	138
References . . . . .	142
<b>6 Conclusions and Future Work . . . . .</b>	<b>143</b>
6.1 Benchmarking PENTA . . . . .	144
6.2 Improving the Reconstruction . . . . .	145
6.2.1 Improve S/N ratio . . . . .	145
6.2.2 Optimize the Diagnostic Set . . . . .	146
6.2.3 Other Methods of Measuring Magnetic Fields . . . . .	147
6.2.4 Other Reconstruction Constraints . . . . .	147
6.3 Vessel Eddy Currents . . . . .	148
6.4 Magnetic Islands . . . . .	149

	Page
6.5 Mirror Flip Field . . . . .	151
6.6 Near-ECH Fueling . . . . .	152
References . . . . .	153

## APPENDICES

Appendix A: <u>V</u> ariational <u>M</u> oments <u>E</u> quilibrium <u>C</u> ode . . . . .	155
Appendix B: Limiter Specification for V3FIT . . . . .	169
Appendix C: MHD Relationships . . . . .	175
Appendix D: Boundary Conditions for Current Diffusion Equation . . . . .	181
Appendix E: Numerical Implementation of the Diffusion Equation . . . . .	185
Appendix F: Alignment of the Magnetic Diagnostics . . . . .	188
Appendix G: Singular Value Decomposition . . . . .	198
Appendix H: Mirror Flip Field . . . . .	204
Appendix I: QHS Near-ECH Fueling . . . . .	221

## LIST OF TABLES

Table	Page
5.1 Configuration space explored with balanced fueling in the QHS configuration. . . . .	100
5.2 QHS, $50kW$ , $\rho_{ECRH} \lesssim 0.1$ . V3FIT reconstruction results using the internal poloidal array, Rogowski coil, and limiter signal. . . . .	118
5.3 QHS, $50kW$ , $\rho_{ECRH} \lesssim 0.1$ . V3FIT reconstruction results using the signals from the external magnetic diagnostic array, internal poloidal array, Rogowski coil, and limiter signal. . . . .	120
5.4 QHS, $100kW$ , $\rho_{ECRH} \lesssim 0.1$ . V3FIT reconstruction results using internal poloidal array, Rogowski coil, and limiter signal. . . . .	132
5.5 QHS, $100kW$ , $\rho_{ECRH} \lesssim 0.1$ . V3FIT reconstruction results using the signals from the external magnetic diagnostic array, internal poloidal array, Rogowski coil, and limiter signal. . . . .	134
5.6 QHS, $50kW$ , $\rho_{ECRH} \sim 0.3$ . V3FIT reconstruction results using the signals from the external magnetic diagnostic array, Rogowski coil, and limiter signal. . . . .	139
5.7 Configuration space explored with balanced fueling in the QHS configuration. Resonance location, heating power and operating $\bar{N}_e$ , extrapolated steady state current, and net current with MC in i-root and e-root dominant solution, and without MC in the i-root dominant solution. . . . .	141
A.1 Comparison between the $(R, Z)$ -coordinates of the magnetic axis calculated by DES-CUR for two set of flux surfaces with different launch points. . . . .	164
H.1 Configuration space explored with balanced fueling in the Mirror configuration. . . . .	205

Table	Page
H.2 Mirror CCW, $100kW$ , $\rho_{ECRH} \lesssim 0.1$ . V3FIT reconstruction results using internal poloidal array, Rogowski coil, and limiter signal. . . . .	211
H.3 Mirror CW, $100kW$ , $\rho_{ECRH} \lesssim 0.1$ . V3FIT reconstruction results using internal poloidal array, Rogowski coil, and limiter signal. . . . .	214
H.4 Mirror CW, $100kW$ , $\rho_{ECRH} \lesssim 0.1$ . V3FIT reconstruction results using internal poloidal array, Rogowski coil, and limiter signal. . . . .	219

## LIST OF FIGURES

Figure	Page
1.1 $ B $ on a flux surface for an axisymmetric tokamak. . . . .	4
1.2 $ B $ along field line for an axisymmetric tokamak. . . . .	4
1.3 The Helically Symmetric eXperiment. . . . .	5
1.4 $ B $ on a flux surface for QHS. . . . .	5
1.5 $ B $ along field line for QHS. . . . .	5
1.6 Boozer spectrum of $ B $ for QHS. . . . .	6
1.7 Boozer spectrum of $ B $ in Mirror. . . . .	7
1.8 Reconstructed and calculated rotational transform profiles for LHD. . . . .	13
2.1 $\mathbf{J}_{P,S} \cdot \mathbf{B}$ in QHS at three toroidal angles along 1/2 of a field period, calculated by a line-following technique. . . . .	27
2.2 $\mathbf{J}_{P,S} \cdot \mathbf{B}$ in QHS at three toroidal angles along 1/2 of a field period, calculated by VMEC. . . . .	27
2.3 The centrally-peaked radial pressure profile for the Pfirsch-Schlüter current density contours in Figure 2.2. . . . .	28
2.4 $ B $ , $\nabla B$ , and a field line, $\vec{B}$ , on a flux surface for a large aspect-ratio axisymmetric tokamak and the QHS configuration. . . . .	29
2.5 $\langle J_{\parallel PS}^2 / J_{\perp}^2 \rangle$ as calculated with VMEC for QHS and an equivalent tokamak. . . . .	30
2.6 QHS, 50 kW, $\rho_{ECRH} \lesssim 0.1$ : Measured net toroidal current for an ensemble average of shots with the magnetic field in the CCW and CW directions. . . . .	30
2.7 Orbits of passing particles. . . . .	31

Figure	Page
2.8 Orbits of trapped particles. . . . .	31
2.9 Trapped particle fraction for the QHS magnetic configuration. . . . .	33
2.10 Effective collisionality, $\nu^*$ for the electron population in QHS, $50\text{ kW ECRH}$ , $\rho_{ECRH} \lesssim 0.1$ . . . . .	33
2.11 Measured parallel (to $\mathbf{B}$ ) ion flow and calculated values that included and neglect momentum conservation. . . . .	37
2.12 Normalized monoenergetic coefficient, $D_{31}^*$ in the QHS configuration for $\rho \simeq 0.5$ . . . .	41
2.13 Normalized monoenergetic coefficient, $D_{31}^*$ in the Mirror configuration for $\rho \simeq 0.5$ . . . .	41
2.14 Example density profile. . . . .	42
2.15 Example temperature profile. . . . .	42
2.16 The radial electric field in QHS with and without momentum conservation. . . . .	44
2.17 The parallel current density in QHS with and without momentum conservation. . . . .	44
2.18 The parallel ion flow in QHS with and without momentum conservation. . . . .	44
2.19 The parallel electron flow in QHS with and without momentum conservation. . . . .	44
2.20 Ion and electron fluxes vs. $E_r$ for QHS at $\rho = 0.2$ . . . . .	45
2.21 Ion and electron parallel flows and total parallel current vs. $E_r$ in QHS at $\rho = 0.2$ , both with and without MC . . . . .	45
2.22 The radial electric field in Mirror with and without momentum conservation. . . . .	46
2.23 The parallel current density in Mirror with and without momentum conservation. . . .	46
2.24 The parallel ion flow in Mirror with and without momentum conservation. . . . .	46
2.25 The parallel electron flow in Mirror with and without momentum conservation. . . . .	46
2.26 The enclosed parallel current profile for QHS. . . . .	47
2.27 The enclosed parallel current profile for Mirror. . . . .	47



Figure	Page
3.1 Cylindrical coordinate system. . . . .	53
3.2 Toroidal coordinate system. . . . .	53
3.3 Radial profiles of susceptance matrix coefficients for the QHS magnetic configuration and an equivalent tokamak. . . . .	63
3.4 Radial profiles of susceptance matrix coefficients for several magnetic configurations possible in HSX when energizing the auxiliary field coils in different ways: QHS, 10% Mirror Flip14, 11% Well, and 11% Hill.. . . .	63
4.1 The toroidal current measurement with and without the presence of hard x-rays caused by dB/dt electrons. . . . .	70
4.2 Sketch of the internal flapper probe in its extended position and Poincaré plots of vacuum magnetic surfaces in the QHS magnetic configuration. . . . .	70
4.3 External magnetic diagnostic ‘triplet’. . . . .	72
4.4 Triplets, covered with a protective copper shield, mounted on a nylon belt and wrapped around the vacuum vessel. . . . .	72
4.5 Outboard view of the external diagnostic array. . . . .	73
4.6 Inboard view of the external diagnostic array. . . . .	74
4.7 The calculated positions of the internal poloidal array. . . . .	75
4.8 Photograph of the steel hose of the internal poloidal array. . . . .	75
4.9 Illustration of a Rogowski coil. . . . .	76
4.10 Main field current measured by the shunt resistor and Rogowski coil. . . . .	80
4.11 The x-, y-, and z- components of the calculated magnetic vector, $\tilde{B}_i$ along with 1- $\sigma$ uncertainties for an external magnetic diagnostic triplet. . . . .	81
4.12 The measured field due to the plasma before offset removal and after. . . . .	82
4.13 The measured field due to the plasma before offset removal and after. . . . .	82

Figure	Page
4.14 Calculated poloidal magnetic field for an internal poloidal diagnostic and 1- $\sigma$ uncertainties. . . . .	83
4.15 The compensated net current during a set of plasma discharges in QHS as measured by the internal Rogowski and external Rogowski. . . . .	85
5.1 Flowchart showing the process from measured data to reconstructed plasma profiles. .	99
5.2 The HSX stellarator, viewed from above. . . . .	101
5.3 QHS, 50 kW, $\rho_{ECRH} \lesssim 0.1$ : Measured net toroidal current for an ensemble average of 6 shots with the magnetic field in the CCW and CW directions. . . . .	102
5.4 QHS, 50 kW, $\rho_{ECRH} \lesssim 0.1$ : Measured loop voltage (ens. avg.). . . . .	102
5.5 The net toroidal current at ECH turn-off, the estimated decay time, and the extrapolated steady state value. . . . .	103
5.6 QHS, 50 kW, $\rho_{ECRH} \lesssim 0.1$ : $T_e$ for CCW and CW. $T_i$ from ChERS. . . . .	104
5.7 QHS, 50 kW, $\rho_{ECRH} \lesssim 0.1$ : $N_e$ for CCW and CW. . . . .	104
5.8 QHS, 50 kW, $\rho_{ECRH} \lesssim 0.1$ Line-averaged central chord density measurement for two shots of the subset used in Figure 5.3. . . . .	104
5.9 QHS, 50 kW, $\rho_{ECRH} \lesssim 0.1$ . Diamagnetic flux loop measurement. . . . .	104
5.10 QHS, 50 kW, $\rho_{ECRH} \lesssim 0.1$ $B_\theta$ component of the magnetic field due to the plasma for CCW and CW. . . . .	105
5.11 QHS, 50 kW, $\rho_{ECRH} \lesssim 0.1$ $B_r$ component of the magnetic field due to the plasma for CCW and CW. . . . .	105
5.12 QHS, 50 kW, $\rho_{ECRH} \lesssim 0.1$ : Stable ambipolar $E_r$ solutions with and without MC. . .	106
5.13 QHS, 50 kW, $\rho_{ECRH} \lesssim 0.1$ , With MC: Ion, electron and total parallel current. . . .	106
5.14 QHS, 50 kW, $\rho_{ECRH} \lesssim 0.1$ , Without MC: Ion, electron and total parallel current. . .	107
5.15 QHS 50 kW, $\rho_{ECRH} \lesssim 0.1$ : Enclosed current profile for different possible scenarios of current density. . . . .	108

Figure	Page
5.16 QHS 50 kW, $\rho_{ECRH} \lesssim 0.1$ : Parallel conductivity of the plasma. . . . .	108
5.17 QHS 50 kW, $\rho_{ECRH} \lesssim 0.1$ : Simulated evolving current density profile. . . . .	109
5.18 QHS 50 kW, $\rho_{ECRH} \lesssim 0.1$ : Simulated induced current density profile. . . . .	110
5.19 QHS 50 kW, $\rho_{ECRH} \lesssim 0.1$ : Simulated and measured loop voltage. . . . .	110
5.20 QHS 50 kW, $\rho_{ECRH} \lesssim 0.1$ : Plasma pressure profile and <i>TWO_LORENTZ</i> fitline. .	111
5.21 QHS 50 kW, $\rho_{ECRH} \lesssim 0.1$ : Enclosed current calculated by IEG, and arctan fitlines. .	111
5.22 QHS 50 kW, $\rho_{ECRH} \lesssim 0.1$ . $B_r$ and $B_\theta$ components of the external magnetic diagnostic signals. . . . .	112
5.23 Sketch of the Pfirsch-Schlüter current density at the location of the two external magnetic vector diagnostic belts. . . . .	113
5.24 QHS 50 kW, $\rho_{ECRH} \lesssim 0.1$ : Measured plasma pressure profile, the Lorentz-fit initial guess, and reconstructions. . . . .	115
5.25 QHS 50 kW, $\rho_{ECRH} \lesssim 0.1$ : Measured plasma pressure profile, reconstruction, and the profile with the minimum $\chi^2$ found during parameter scan. . . . .	115
5.26 QHS 50 kW, $\rho_{ECRH} \lesssim 0.1$ : The calculated enclosed current profile, the arctan-fit initial guess, and reconstructions. . . . .	116
5.27 QHS 50 kW, $\rho_{ECRH} \lesssim 0.1$ : The calculated enclosed current profile, reconstruction, and the profile with the minimum $\chi^2$ found during parameter scan. . . . .	117
5.28 QHS 50 kW, $\rho_{ECRH} \lesssim 0.1$ : Signals for the internal poloidal diagnostic array at $t_{exp} = t_{sim} = 50$ ms. . . . .	117
5.29 QHS, 50kW, $\rho_{ECRH} \lesssim 0.1$ : $\chi^2_\nu$ for pressure profile parameter scan. . . . .	119
5.30 QHS 50 kW, $\rho_{ECRH} \lesssim 0.1$ : Measured plasma pressure profile, the Lorentz-fit initial guess, and reconstructions. . . . .	121
5.31 QHS 50 kW, $\rho_{ECRH} \lesssim 0.1$ : The modeled enclosed current profile, reconstruction, and the profile with the minimum $\chi^2$ found during parameter scan. . . . .	121

Figure	Page
5.32 QHS 50 kW, $\rho_{ECRH} \lesssim 0.1$ : The calculated enclosed current profile, the arctan-fit initial guess, and reconstructions. . . . .	121
5.33 QHS 50 kW, $\rho_{ECRH} \lesssim 0.1$ : The calculated enclosed current profile, reconstruction, and the profile with the minimum $\chi^2$ found during parameter scan. . . . .	121
5.34 QHS 50 kW, $\rho_{ECRH} \lesssim 0.1$ : $B_r$ , $B_\theta$ , and $B_t$ signal components of all 32 triplets of the external diagnostic array. . . . .	122
5.35 Magnetic diagnostic signals due to the current profile and pressure profile, calculated separately. . . . .	124
5.36 The total magnetic signal for the initial guess and reconstruction, from Figure 5.34. . .	124
5.37 QHS 50 kW, $\rho_{ECRH} \lesssim 0.1$ : Signal components for the internal poloidal array. . . .	125
5.38 QHS 100 kW, $\rho_{ECRH} \lesssim 0.1$ : $T_e$ for CCW and CW. $T_i$ from ChERS. . . . .	126
5.39 QHS 100 kW, $\rho_{ECRH} \lesssim 0.1$ : $N_e$ for CCW and CW. . . . .	126
5.40 QHS, 100 kW, $\rho_{ECRH} \lesssim 0.1$ : Measured net toroidal current for an ensemble average of 6 shots with the magnetic field in the CCW and CW directions. . . . .	126
5.41 QHS, 100 kW, $\rho_{ECRH} \lesssim 0.1$ : Measured loop voltage (ens. avg.). . . . .	126
5.42 QHS 100 kW, $\rho_{ECRH} \lesssim 0.1$ : Stable ambipolar $E_r$ solutions with MC and without MC. . .	127
5.43 QHS 100 kW, $\rho_{ECRH} \lesssim 0.1$ , with MC: Ion, electron and total parallel current. . . .	128
5.44 QHS 100 kW, $\rho_{ECRH} \lesssim 0.1$ , without MC: Ion, electron and total parallel current. . .	129
5.45 QHS 100 kW, $\rho_{ECRH} \lesssim 0.1$ : Enclosed current profile for different possible scenarios of current density. . . . .	130
5.46 QHS 100 kW, $\rho_{ECRH} \lesssim 0.1$ : Parallel conductivity of the plasma, including the effects of trapped particles. . . . .	130
5.47 QHS 100 kW, $\rho_{ECRH} \lesssim 0.1$ : Measured and simulated loop voltage for the i-root dom. and i-root only profiles of the bootstrap current. . . . .	130
5.48 QHS 100 kW, $\rho_{ECRH} \lesssim 0.1$ : Measured plasma pressure profile, the Lorentz-fit initial guess, and reconstruction. . . . .	131

Figure	Page
5.49 QHS 100 kW, $\rho_{ECRH} \lesssim 0.1$ : Measured plasma pressure profile, reconstruction, and the profile with the minimum $\chi^2$ found during parameter scan. . . . .	131
5.50 QHS 100 kW, $\rho_{ECRH} \lesssim 0.1$ : The calculated enclosed current profile, the arctan-fit initial guess, and reconstruction. . . . .	131
5.51 QHS 100 kW, $\rho_{ECRH} \lesssim 0.1$ : The calculated enclosed current profile, reconstruction, and the profile with the minimum $\chi^2$ found during parameter scan. . . . .	131
5.52 QHS 100 kW, $\rho_{ECRH} \lesssim 0.1$ : Measured plasma pressure profile, the Lorentz-fit initial guess, and reconstruction. . . . .	133
5.53 QHS 100 kW, $\rho_{ECRH} \lesssim 0.1$ : Measured plasma pressure profile, reconstruction, and the profile with the minimum $\chi^2$ found during parameter scan. . . . .	133
5.54 QHS 100 kW, $\rho_{ECRH} \lesssim 0.1$ : The calculated enclosed current profile, the arctan initial guess, and reconstruction. . . . .	133
5.55 QHS 100 kW, $\rho_{ECRH} \lesssim 0.1$ : The calculated enclosed current profile, reconstruction, and the profile with the minimum $\chi^2$ found during parameter scan. . . . .	133
5.56 QHS, 50kW, $\rho_{ECRH} \sim 0.3$ : $T_e$ for CCW and CW. $T_i$ from ChERS. . . . .	135
5.57 QHS, 50kW, $\rho_{ECRH} \sim 0.3$ : $N_e$ for CCW and CW. . . . .	135
5.58 QHS, 50kW, $\rho_{ECRH} \sim 0.3$ : Measured net toroidal current for an ensemble average of 7 shots with the magnetic field in the CCW and CW directions. . . . .	135
5.59 QHS, 50kW, $\rho_{ECRH} \sim 0.3$ : Measured loop voltage (ens. avg.). . . . .	135
5.60 QHS, 50kW, $\rho_{ECRH} \sim 0.3$ : Stable ambipolar $E_r$ with MC and without MC. . . . .	136
5.61 QHS, 50kW, $\rho_{ECRH} \sim 0.3$ , with MC: Ion, electron and total parallel current. . . . .	136
5.62 QHS, 50kW, $\rho_{ECRH} \sim 0.3$ , without MC: Ion, electron and total parallel current. . . . .	137
5.63 QHS, 50kW, $\rho_{ECRH} \sim 0.3$ : Enclosed current profile for different possible scenarios of current density. . . . .	137
5.64 QHS, 50kW, $\rho_{ECRH} \sim 0.3$ : Parallel conductivity of the plasma. . . . .	137
5.65 QHS, 50kW, $\rho_{ECRH} \sim 0.3$ : Measured and simulated loop voltage. . . . .	138

Figure	Page
5.66 QHS 50 kW, $\rho_{ECRH} \sim 0.3$ : Measured plasma pressure profile, the Lorentz-fit initial guess, and reconstruction. . . . .	140
5.67 QHS 50 kW, $\rho_{ECRH} \lesssim 0.1$ : Measured plasma pressure profile, reconstruction, and the profile with the minimum $\chi^2$ found during parameter scan. . . . .	140
5.68 QHS 50 kW, $\rho_{ECRH} \sim 0.3$ : The calculated enclosed current profile, the arctan initial guess, and reconstruction. . . . .	140
5.69 QHS 50 kW, $\rho_{ECRH} \lesssim 0.1$ : The calculated enclosed current profile, reconstruction, and the profile with the minimum $\chi^2$ found during parameter scan. . . . .	140
6.1 The relationship between parallel flow velocity and the radial electric field at $r/a=0.2$ as calculated by PENTA. . . . .	145
6.2 $J \cdot B$ at three toroidal locations during the plasma evolution. . . . .	149
6.3 $ B $ and $\vec{B}$ on the vacuum vessel during the plasma evolution. . . . .	150
6.4 Poicaré plot of surfaces in the Hill 6% configuration with 4/4 island structure. . . . .	152
A.1 $P(s)$ for $AM(0) = AM(1) = AM(3) = AM(4) = AC(5) = AC(6) = AC(7) = 1$ and $AM(2) = (0.25, 1, 4)$ . . . . .	160
A.2 $P(s)$ for $AM(0) = AM(1) = AM(2) = AM(4) = AC(5) = AC(6) = AC(7) = 1$ and $AM(3) = (0.25, 1, 4)$ . . . . .	160
A.3 $P(s)$ for $AM(0) = AM(1) = AM(2) = AM(3) = AC(5) = AC(6) = AC(7) = 1$ and $AM(4) = (0.25, 1, 4)$ . . . . .	160
A.4 $I(s)$ and $I'(s)$ for $AC(0) = 0, AC(1, 4) = 1, AC(2) = (0.25, 1, 4), AC(3) = (1, 1.5, 2)$ . . . . .	161
A.5 $I(s)$ and $I'(s)$ for $AC(0) = 0, AC(1) = AC(2) = AC(4) = 1, AC(3) = (0.25, 1, 4)$ . . . . .	161
A.6 $I(s)$ and $I'(s)$ for $AC(0) = 0, AC(1) = AC(2) = AC(3) = 1, AC(4) = (0.25, 1, 4)$ . . . . .	161
A.7 Poincaré plot of flux surfaces and Fourier series expansions for surfaces near the LCFS of the QHS magnetic configuration. . . . .	162
A.8 The same surfaces as in Figure A.7, zoomed in to the region near the top of the D-shape. . . . .	162
A.9 The magnetic signals due to plasma currents for an external magnetic diagnostic triplet. . . . .	165

Figure	Page
B.1	The limiter at the boxport location. . . . . 171
B.2	Outline of graphite limiter in a retracted position and with its inner edge at the LCFS of the QHS configuration. . . . . 172
B.3	Contour plot of $f(R, Z)$ on a vertical slice at the boxport location and Poincaré plot of the LCFS. . . . . 173
C.1	A torus. . . . . 176
F.1	A subset of the auxiliary coil set, the vacuum vessel and diagnostic ports. . . . . 188
F.2	Typical current waveform applied to the auxiliary coils. . . . . 189
F.3	Signal response on triplet #17 due to the applied current in Figure F.2 on auxiliary coil A3. . . . . 189
F.4	Comparison between calculated and measured signals of the external magnetic diagnostic array. . . . . 190
F.5	The main field current, as measured by the main shunt resistor, a 3rd-order fit polynomial, and its derivative as a function of time. . . . . 191
F.6	Comparison between calculated and measured signals of the external magnetic diagnostic array. . . . . 192
F.7	Projections of misaligned vector . . . . . 194
F.8	Rotation vector components and misalignment angle. . . . . 195
F.9	Comparison of expected signals for internal poloidal array. . . . . 196
G.1	Sample pressure profiles. . . . . 199
G.2	Sample current density profiles. . . . . 199
G.3	The vacuum vessel and virtual triplets. . . . . 200
G.4	Normalized eigenvalues for the SVD with the complete virtual diagnostic set. . . . . 201

Figure	Page
G.5 Normalized eigenvalues for the SVD that includes the external magnetic diagnostic triplets and internal poloidal array. . . . .	202
G.6 Normalized eigenvalues for the SVD that includes only the internal poloidal array. . .	202
H.1 Mirror, 100 kW, $\rho_{ECRH} \lesssim 0.1$ : $T_e$ for CCW, and CW $\bar{N}_e \sim 4.2$ and CW $\bar{N}_e \sim 5.5$ . $T_i$ from ChERS. . . . .	204
H.2 Mirror, 100 kW, $\rho_{ECRH} \lesssim 0.1$ : $N_e$ for CCW and CW. . . . .	204
H.3 Mirror, 100 kW, $\rho_{ECRH} \lesssim 0.1$ : Net toroidal current for ensemble average of shots in CCW and CW. . . . .	205
H.4 Mirror, 100 kW, $\rho_{ECRH} \lesssim 0.1$ : Stable ambipolar $E_r$ solutions with MC and without MC. . . . .	206
H.5 Mirror, 100 kW, $\rho_{ECRH} \lesssim 0.1$ , With MC: Ion, electron and total parallel current. . . .	206
H.6 Mirror, 100 kW, $\rho_{ECRH} \lesssim 0.1$ , Without MC: Ion, electron and total parallel current. .	207
H.7 Mirror, 100 kW, $\rho_{ECRH} \lesssim 0.1$ , Without MC: Enclosed current profile for different scenarios of current density. . . . .	207
H.8 Mirror, 100 kW, $\rho_{ECRH} \lesssim 0.1$ : Parallel conductivity of the plasma. . . . .	208
H.9 Mirror CCW, 100 kW, $\rho_{ECRH} \lesssim 0.1$ : Measured and simulated loop voltage. . . . .	209
H.10 Mirror CCW, 100 kW, $\rho_{ECRH} \lesssim 0.1$ : Measured plasma pressure profile, the Lorentz-fit initial guess, and reconstruction. . . . .	210
H.11 Mirror CCW, 100 kW, $\rho_{ECRH} \lesssim 0.1$ : Measured plasma pressure, reconstruction, and the minimum found during parameter scan. . . . .	210
H.12 Mirror CCW, 100 kW, $\rho_{ECRH} \lesssim 0.1$ : The calculated enclosed current profile, the arctan initial guess, and reconstruction. . . . .	210
H.13 Mirror CCW, 100 kW, $\rho_{ECRH} \lesssim 0.1$ : The calculated enclosed current profile, reconstruction, and the minimum found during parameter scan. . . . .	210
H.14 Mirror CW, 100 kW, $\rho_{ECRH} \lesssim 0.1$ : Measured and simulated loop voltage. . . . .	211



Figure	Page
H.15 Mirror CW, 100 kW, $\rho_{ECRH} \lesssim 0.1$ : Measured plasma pressure profile, the Lorentz-fit initial guess, and reconstruction. . . . .	212
H.16 Mirror CW, 100 kW, $\rho_{ECRH} \lesssim 0.1$ : Measured plasma pressure profile, reconstruction, and the minimum found during parameter scan. . . . .	212
H.17 Mirror CW, 100 kW, $\rho_{ECRH} \lesssim 0.1$ : The calculated enclosed current profile, the arctan initial guess, and reconstruction . . . . .	213
H.18 Mirror CW, 100 kW, $\rho_{ECRH} \lesssim 0.1$ : The calculated enclosed current profile, reconstruction, and the minimum found during parameter scan. . . . .	213
H.19 Mirror CW, 100 kW, $\rho_{ECRH} \lesssim 0.1$ : Stable ambipolar $E_r$ solutions with MC and without MC. . . . .	213
H.20 Mirror CW, 100 kW, $\rho_{ECRH} \lesssim 0.1$ , With MC: Ion, electron and total parallel current. . . . .	215
H.21 Mirror, 100 kW, $\rho_{ECRH} \lesssim 0.1$ , Without MC: Ion, electron and total parallel current. . . . .	215
H.22 Mirror, 100 kW, $\rho_{ECRH} \lesssim 0.1$ : Enclosed current profile for different scenarios of current density. . . . .	216
H.23 Mirror, 100 kW, $\rho_{ECRH} \lesssim 0.1$ , higher line-averaged density case: Parallel conductivity of the plasma, including trapped particle effect. . . . .	216
H.24 Mirror CW, 100 kW, $\rho_{ECRH} \lesssim 0.1$ : Measured and simulated loop voltage. . . . .	217
H.25 Mirror CW, 100 kW, $\rho_{ECRH} \lesssim 0.1$ : Measured plasma pressure profile, the Lorentz-fit initial guess, and reconstruction. . . . .	218
H.26 Mirror CW, 100 kW, $\rho_{ECRH} \lesssim 0.1$ : Measured plasma pressure profile, reconstruction, and the minimum found during parameter scan. . . . .	218
H.27 Mirror CW, 100 kW, $\rho_{ECRH} \lesssim 0.1$ : The calculated enclosed current profile, the arctan initial guess, and reconstruction. . . . .	218
H.28 Mirror CW, 100 kW, $\rho_{ECRH} \lesssim 0.1$ : The calculated enclosed current profile, reconstruction, and the minimum found during parameter scan. . . . .	218
I.1 QHS, $\bar{N}_e = 2 \times 10^{18}/m^3$ , 50 kW, $\rho_{ECRH} \lesssim 0.1$ : $T_e$ for CCW and CW. $T_i$ from ChERS. . . . .	221
I.2 QHS, $\bar{N}_e = 2 \times 10^{18}/m^3$ , 50 kW, $\rho_{ECRH} \lesssim 0.1$ : $N_e$ for CCW and CW. . . . .	221

Figure	Page
I.3 QHS, $\bar{N}_e = 3 \times 10^{18}/m^3$ , $50 \text{ kW}$ , $\rho_{ECRH} \lesssim 0.1$ : $T_e$ for CCW and CW. $T_i$ from ChERS.	222
I.4 QHS, $\bar{N}_e = 3 \times 10^{18}/m^3$ , $50 \text{ kW}$ , $\rho_{ECRH} \lesssim 0.1$ : $N_e$ for CCW and CW. . . . .	222
I.5 QHS, $\bar{N}_e = 4 \times 10^{18}/m^3$ , $50 \text{ kW}$ , $\rho_{ECRH} \lesssim 0.1$ : $T_e$ for CCW and CW. $T_i$ from ChERS.	222
I.6 QHS, $\bar{N}_e = 4 \times 10^{18}/m^3$ , $50 \text{ kW}$ , $\rho_{ECRH} \lesssim 0.1$ : $N_e$ for CCW and CW. . . . .	222
I.7 QHS, $\bar{N}_e = 5 \times 10^{18}/m^3$ , $50 \text{ kW}$ , $\rho_{ECRH} \lesssim 0.1$ : $T_e$ for CCW and CW. $T_i$ from ChERS.	223
I.8 QHS, $\bar{N}_e = 5 \times 10^{18}/m^3$ , $50 \text{ kW}$ , $\rho_{ECRH} \lesssim 0.1$ : $N_e$ for CCW and CW. . . . .	223
I.9 Measured toroidal current for the 4 densities with the magnetic field in the CCW and CW directions. . . . .	224
I.10 Extrapolated steady state current and the net toroidal current predicted by PENTA for an ion-root dominated solution. . . . .	225

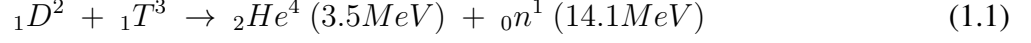
# Chapter 1

## Introduction

The world demand for energy is increasing. Over the last 30 years, the consumption of energy has increased every year, except in 2009, when the financial and economic crisis caused a 0.6% decrease in GDP [1]. According to the U.S. Energy Information Administration, the vast majority of the world's energy,  $\sim 85\%$ , currently comes from fossil fuels, such as oil, coal, and natural gas [2]. An abundance of scientific data indicates that the burning of fossil fuels for energy is increasing the  $\text{CO}_2$  concentration in the atmosphere. The data indicates that this is causing global temperatures to rise and is increasing the risk of extreme weather patterns, such as increased summer dryness (risk of drought) and winter wetness in most parts of the northern middle and high latitudes [3]. Because of the large environmental impact, alternative energy sources are sought after to decrease reliance on oil and coal based sources of energy to reduce  $\text{CO}_2$  emissions. Meanwhile, the safety of conventional nuclear fission facilities has been called into question due to the recent crisis at the Fukushima nuclear power plant [4].

A fusion reaction between light nuclei releases an enormous amounts of energy. In the fusion reaction, a small amount of the original mass from the particles is converted into kinetic energy which is carried by the products of the fusion reaction [5]. For example, a promising fusion reaction involves the nuclei of two hydrogen isotopes, deuterium and tritium. The fusion product of a D-T fusion reaction is an alpha particle with 3.5 MeV of kinetic energy and a neutron with 14.1 MeV

of kinetic energy:



The reaction rate for this fusion process depends on the collisional cross-section of the reaction, which is a function of the temperature of the atoms. For D-T fusion, the maximal cross-section occurs around 10-100 keV, or  $10^8$ - $10^9$  °C, while the maximum cross section occurs at still higher temperatures for other possible fusion reactions involving light nuclei (such as D-D and D-He<sup>3</sup>). At these temperatures, the fuel is completely ionized and is in the plasma state.

Strong magnetic fields are used to confine the high temperature plasma inside of some type of vessel. The magnetic field is responsible for containing the plasma and preventing it from interacting with the relatively cold vessel wall. The alpha particles released by the D-T fusion reaction are charged particles and are confined by the magnetic field, while the neutrons are not confined by the magnetic field and escape the confinement volume. The energetic neutrons will collide with a blanket material surrounding the plasma, absorb the kinetic energy of the neutron and convert it to thermal energy which can be used to heat steam and generate electricity. To reach self sustaining operation, the plasma must reach a self-heated state where the heating power of the alpha particles exceeds the power losses in the plasma. This condition, called ‘ignition’, is achieved when the triple product of the plasma density, temperature, and energy confinement time satisfies

$$nT\tau_E > 5 \times 10^{21} KeV \ s \ m^{-3} \quad (1.2)$$

In magnetically confined fusion, the magnetic field lines form closed flux surfaces to ensure good confinement. The equilibrium field has both toroidal and poloidal components,  $\mathbf{B} = \mathbf{B}_T + \mathbf{B}_P$  [5] [6]. Axisymmetric tokamaks generate the toroidal magnetic field with a set of external field coils that wind around the plasma column in a poloidal direction. The poloidal field is generated by a toroidal current in the plasma which can be driven inductively by an external transformer coil that uses the plasma column as the secondary winding. However, the transformer has a finite limit of volt-seconds that it can supply, which precludes this method as the only source of current drive in a

tokamak. Therefore, supplemental sources of toroidal current are required for steady-state tokamak operation. Alternative methods of driving currents in the plasma include electron cyclotron current drive (ECCD) such as by the Okhawa [7] or Fisch-Boozer [8] effect, ion cyclotron current drive (ICCD) or neutral beam injection (NBI).

In a large-aspect ratio axisymmetric tokamak with minor radius  $r$ , major radius  $R_0$ , and inverse aspect ratio  $\epsilon_t = r/R_0$ , the magnetic field strength on a flux surface is

$$\frac{B}{B_0} = \frac{1}{1 + \epsilon_t \cos \theta} \approx 1 - \epsilon_t \cos \theta \quad (1.3)$$

The magnetic field strength varies with the poloidal angle,  $\theta$ . The rotational transform describes the angular pitch of the field lines on a flux surface,  $t = d\theta/d\zeta$ , where  $\zeta$  is the toroidal angle. With  $t$ , Eqn 1.3 can be used to express the field strength along the field line as a function of toroidal angle, with an arbitrary starting angle,  $\zeta_0$ .

$$\frac{B}{B_0} \approx 1 - \epsilon_t \cos(t(\zeta - \zeta_0)) \quad (1.4)$$

The magnitude of  $B$  on a flux surface in an large-aspect ratio axisymmetric tokamak is shown in Figure 1.1, along with the path of a field line on that surface for  $t \sim 1.05$ . The toroidal symmetry in  $|B|$  is clearly seen. The  $|B|$  along that field line is shown in Figure 1.2. Because the magnetic field is toroidally symmetric in a tokamak, the particle motion is described by an Euler-Lagrange equation and the toroidal canonical momentum is conserved [9]. The particles follow closed trajectories on the flux surface and are well confined. In a stellarator, the toroidal and poloidal components are generated predominantly by the external field coils. No other source of current is required to generate vacuum flux-surfaces and this is the reason that the stellarator is often called a ‘current-less’ configuration. Conventional stellarators are constructed with continuous helical windings and the magnetic field strength is not symmetric on a flux surface. In addition to the toroidal ripple,  $\epsilon_t$ , additional helical modulations of the field strength are present:

$$\frac{B}{B_0} \approx 1 - \epsilon_t \cos \theta - \sum \epsilon_{h,nm} \cos(n\zeta - m\theta) \quad (1.5)$$

The additional modulation of  $|B|$  from the helical component has a detrimental result: There is no longer a direction of symmetry in  $|B|$  and there is no equivalent to the conservation of canonical momentum and, therefore, no guarantee of good particle confinement as in a tokamak.

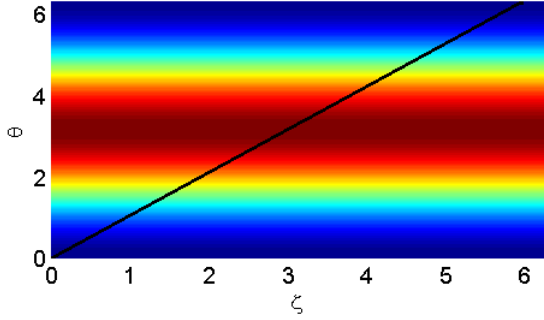


Figure 1.1  $|B|$  on a flux surface for an axisymmetric tokamak is symmetric in the toroidal angle,  $\zeta$ , and varies with the poloidal angle,  $\theta$ .

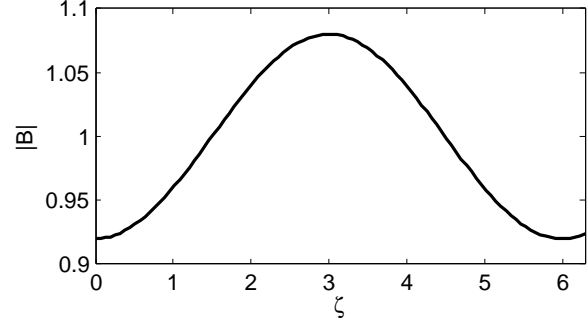


Figure 1.2  $|B|$  along field line for an axisymmetric tokamak.

A class of equilibria [10] were found to exist for which the drift orbits and associated transport are predicted to be identical to a tokamak. These ‘isomorphic’ equilibria are described by a magnetic field strength that depends on a single helicity (a single  $(n, m)$  combination). It has been shown that quasi-helically symmetric stellarators strictly confine guiding center orbits [11], restoring the good confinement properties of an axisymmetric tokamak.

The Helically Symmetric Experiment (HSX) [12], Figure 1.3, is a four-field period quasi-helically symmetric stellarator designed to have a direction of symmetry of  $|B|$  in a helical direction. A set of 48 modular field coils generate the magnetic field required. In Figure 1.4,  $|B|$  on the flux surface and a field line on the surface is shown for the QHS magnetic configuration. In Figure 1.5,  $|B|$  along the field line is shown. The Fourier decomposition of  $|B|$  along the field lines provides the full magnetic spectrum [13]:

$$\frac{B}{B_0} = \sum_{n,m} b_{n,m} \cos(n\zeta - n\theta) \quad (1.6)$$

The magnetic spectrum of the QHS configuration, as a function of normalized radius,  $\rho = \sqrt{\Phi/\Phi_{LCFS}}$  (square-root normalized toroidal flux), is shown in Figure 1.6. In the figure, the  $b_{0,0}$  component has been suppressed. The dominant spectral term is clearly the  $b_{4,1}$  term for most of the plasma column, exceeding the contribution from the rest of the terms by an order of magnitude. Near the

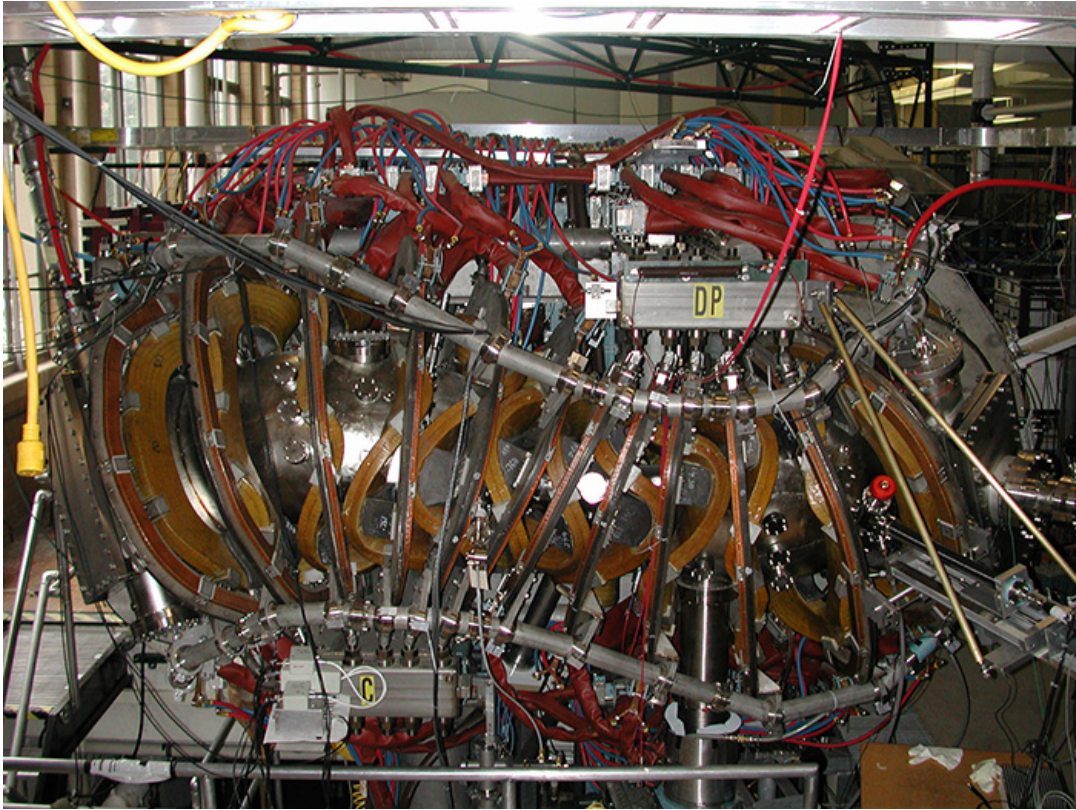


Figure 1.3 The Helically Symmetric eXperiment.

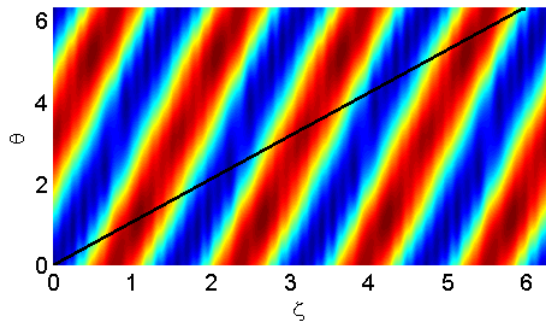


Figure 1.4  $|B|$  on a flux surface for the quasi-helically symmetric (QHS) magnetic configuration.

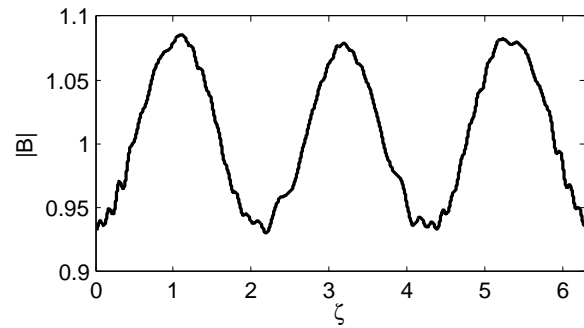


Figure 1.5  $|B|$  along field line for QHS.

axis, the other terms are more significant because of the relative decrease of the magnitude of the  $b_{4,1}$  helical spectral term.

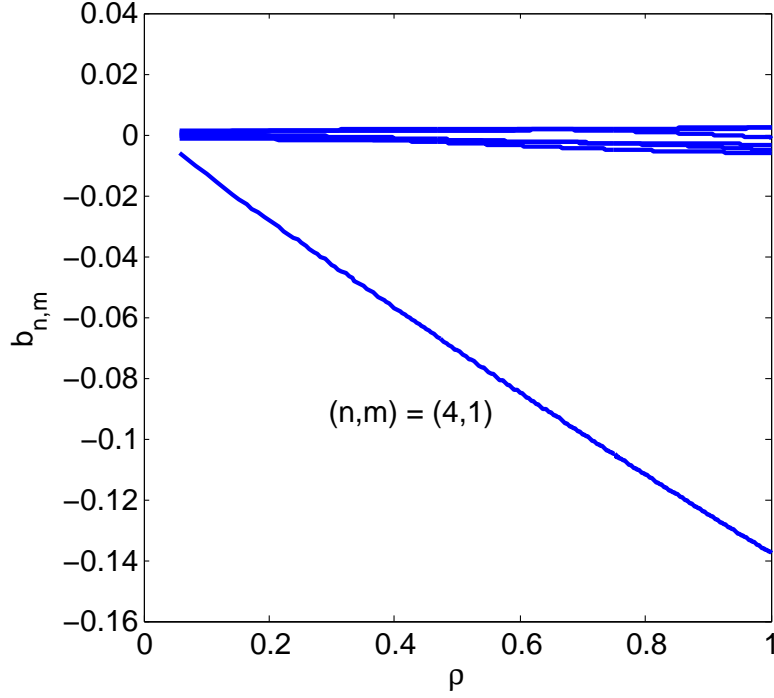


Figure 1.6 Boozer spectrum of  $|B|$  as a function of radius for the QHS configuration. The largest 7 terms are shown, excluding  $b_{0,0}$ .

In HSX, the equation for  $|B|$  on a flux surface is dominated by the  $b_{4,1}$ -helicity component and is given approximately by

$$\frac{B}{B_0} = 1 - b_{4,1} \cos(4\zeta - 1\theta) \quad (1.7)$$

$$= 1 - b_{4,1} \cos((4 - 1t)\zeta) \quad (1.8)$$

Eqn 1.8 is analogous to the Eqn 1.3 with the substitutions of  $t_{eff} = (n - mt) \approx 3$  and  $\epsilon_t = b_{n,m} = b_{4,1}$ . The 3 ripples are seen in Figures 1.4 and 1.5. By restoring a direction of symmetry in  $|B|$ , good confinement of particles is guaranteed, similar to that in an axisymmetric tokamak. The high effective transform,  $t_{eff} \approx 3$ , and negligible toroidal curvature has been verified experimentally for HSX [14].

HSX is equipped with a set of planar auxiliary field coils, as seen in Figure 1.3, to allow for some flexibility in the magnetic spectrum and rotational transform. In the Mirror magnetic configuration, for example, the auxiliary field coils are energized so that the magnetic spectrum



has  $b_{4,0}$  &  $b_{8,0}$  terms, breaking the symmetry of the single-helicity  $(n, m) = (4, 1)$  field, as seen in Figure 1.7. By breaking the symmetry, the neoclassical transport is raised back towards the level of a conventional stellarator [15]. The auxiliary coils can also be used to alter (increase/decrease)

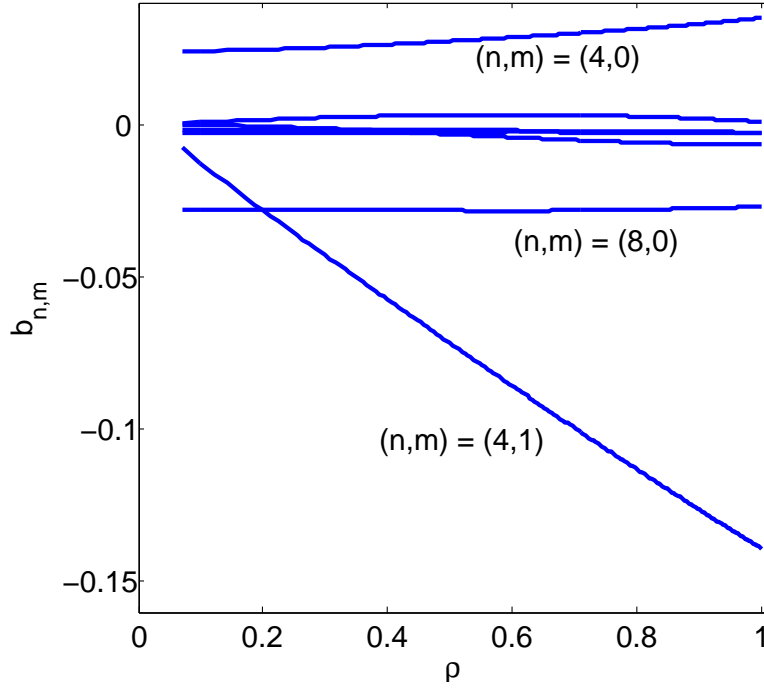


Figure 1.7 Boozer spectrum of  $|B|$  as a function of radius for the Mirror configuration. The largest 7 terms are shown, excluding  $b_{0,0}$ s.

the rotational transform without drastically changing the magnetic spectrum by either adding or subtracting net toroidal flux. Discussed in Chapter 6, this can control which vacuum magnetic resonances are inside of the confinement volume. The  $(n, m) = (4, 4)$  &  $(8, 7)$  rational surfaces can be in the confinement volume by adjusting the rotational transform from just under 1 to just over 1.14.

In a toroidal fusion experiment, the pressure on the flux surface equilibrates very quickly along the field lines, so that the pressure is nearly constant on the entire surface. The radial pressure gradient generates a diamagnetic current perpendicular to the field lines. As will be shown in Section 2.2, the condition of  $\nabla \cdot \mathbf{J} = 0$  requires that another current, parallel to  $\mathbf{B}$  must exist in the plasma. This current is called the Pfirsch-Schlüter current [16]. In a tokamak, this current is a

dipole current that generates a net vertical magnetic field which causes a radial outward shift of the plasma flux surfaces, called the Shafranov shift [17]. In the QHS configuration, this dipole current is reduced by  $\sim 3$ , rotates with the toroidal angle and is in the opposite direction compared to a tokamak. The decrease in current reduces the Shafranov shift. For the surfaces to shift 1/2 of the minor radius in QHS, the value of the plasma beta, the ratio between plasma pressure ( $p = nk_B T$ ) and magnetic pressure ( $B^2/2\mu_0$ ) must reach  $\beta = \frac{2\mu_0 p}{B^2} \sim 35\%$  [12]. As part of this dissertation, the dipole magnetic field generated by the Pfirsch-Schlüter current and its helical rotation is measured and verified by magnetic diagnostics, and the measured signals are used to reconstruct information about the plasma pressure profile with a 3-D reconstruction code. This is presented in Chapter 5.

## 1.1 Neoclassical Bootstrap Current

Both tokamaks and stellarators share the characteristic of an inhomogeneous  $|B|$  on the flux surfaces. This results in a population of particles that are trapped in magnetic ‘wells’ along the field lines. These trapped particles do not contribute to the parallel electrical conductivity,  $\sigma_{\parallel} = 1/\eta_{\parallel}$ . Also, the momentum exchange from collisions between the trapped and passing particles on a flux surface leads to a net fluid flow. Since the particles have an electrical charge, this flow is a non-inductive source of current called the bootstrap current [16]. This current is parallel to the field lines. It is desired to operate a tokamak with a high fraction of the net toroidal current coming from the bootstrap current. Maximizing the bootstrap current minimizes the amount of current required from other sources. A review of the theory for the bootstrap current in tokamaks and the evidence for these trapped particle effects in most recent tokamaks, including JT-60, TFTR, and JET is in Reference [18].

Over the years, the modeling of the bootstrap current in stellarators has improved and experiments have demonstrated that the stellarator magnetic field can be adjusted to change both the magnitude and direction of the bootstrap current. One of the first experiments to demonstrate the existence of the bootstrap current in a stellarator configuration was the Advanced Toroidal Facility (ATF) torsatron. Measurements of the net current agreed with calculations of the neo-classical bootstrap current to within about (25%) . In this case, the bootstrap current density was

calculated in two parts: a toroidal, tokamak-like component and a helical component. For each component, the current was calculated with an analytic interpolation function between different collisional regimes. For the helical component, the calculation was benchmarked with a monoenergetic code [19].

Using an analytic expression of the bootstrap current [20], it was shown that the bootstrap current could be tailored or eliminated by balancing the contributions from the two type of trapped particles; those that are trapped in toroidal ripples and those in helical ripples. If a toroidal system has a main toroidal component,  $b_{1,0}$ , and one helical component with  $n \gg m$ , then if  $b_{n,m} = \frac{nb_{1,0}}{m\epsilon}$ , the net bootstrap current should be close to zero [21].

Another method, valid for the low-collisionality ( $1/\nu$ ) regime, using a flux-surface averaged geometric factor to relate the radial temperature and density gradients to parallel flows [22], correctly models the effects that the ‘bumpiness’ of the flux surface has on the bootstrap current. In Heliotron J, the relative magnitude of three field components, the toroidal,  $b_{01}$ , the helical,  $b_{41}$ , and the bumpiness term,  $b_{4,0}$  interact in a complicated way. With  $b_{0,1} = 0.01$  and  $b_{4,1} = 0.02$ , scanning the magnitude of  $b_{4,0}$  from -0.04 to 0.04 reverses the direction of the bootstrap current. For  $b_{0,1} > b_{4,1}$ , the bumpiness term does not change the geometric factor much, while for  $0 < b_{0,1} < b_{4,1}$ , the bumpiness term can reverse the current at values around small negative  $b_{4,0} \sim 0.01 - 0.03$  [23]. The  $(\theta, \zeta)$  position of the maximum value of the magnetic field strength, which depends on the magnitudes of  $b_{0,1}$ ,  $b_{4,1}$ , and  $b_{4,0}$ , plays an important role in determining the direction of the bootstrap current.

There are many reasons to be concerned with the bootstrap current and its control. The bootstrap current will alter the radial profile of  $\epsilon$  and affect the location of low-order rational surfaces, which can affect confinement. On the W7-AS stellarator, it was found that higher temperature and density gradients increase the total current and the net increase of  $\epsilon$ . This occurs without any degradation of confinement until  $\epsilon = 1/2$  surfaces were at the last closed flux surface (LCFS) of the column. Then,  $T_e$  decreased by about 70% and tearing modes would develop. No disruption occurred because of the improved positional stability from the external poloidal field [24]. When low-order rational surfaces were located just outside of the LCFS, improved confinement regimes

were found [25]. The mechanism of improved confinement is not understood, but it may be linked to a region of decreased viscous damping near (but not at) islands outside of the LCFS [26]. The bootstrap current and its effect on the rotational transform are important to understand, particularly when evaluating the performance of island divertors, like the one planned for W7-X [27]. In addition to the role that rational surfaces play at the edge of the plasma column, they may also play an important role for internal transport barriers (ITBs). In TJ-II, an ITB was correlated with the location of rational surfaces at or near the ECH location [28].

Recently, the presence of a bootstrap current driven by the radial electric field,  $E_r$ , has been predicted, an effect unique to non-axisymmetric devices [29]. In a stellarator, the direction of the viscous flow damping is a function of collisionality. Particles in the Pfirsch-Schlüter regime are damped in a different direction than those in the  $1/\nu$ -regime. This is not the case for tokamaks, in which the direction of damping is the same regardless of collisionality [9]. For electrons in the  $1/\nu$ -regime and ions in the Pfirsch-Schlüter regime (similar to HSX plasmas), the flows driven by  $E_r$  in a stellarator are damped in different directions, and the net  $E_r$ -driven current flows opposite to that driven by the pressure gradient, reducing and possibly reversing the total bootstrap current density.

Until recently, the calculation of the transport coefficients in a general toroidal geometry for arbitrary collisionality and  $E_r$  has not included the effects of flows and momentum conservation (MC) between plasma species self-consistently. Often, the drift kinetic equation (DKE) is solved in an asymptotic limit regarding collisionality regime and radial electric field. A method of calculating the neoclassical viscosity, diffusion and current coefficients for general toroidal plasmas, including the effects of MC among plasma species and the radial electric field, has been described analytically [30] [31]. A numerical code that evaluates the expressions therein, called PENTA, is written in FORTRAN [32] and in MATLAB [33]. It should be noted that the numerical evaluation makes use of monoenergetic transport coefficients calculated by DKES [34]. The MC-inclusion technique reproduces ambipolar transport in the axisymmetric limit, and is valid for any arbitrary toroidal geometry. In terms of the effective ripple,  $\epsilon_{eff}$ , a quantity that describes the transport in

the  $1/\nu$  regime in toroidal devices [35], PENTA is valid for several orders of magnitude spanning from  $\sim 10^{-5}$  for ITER [36] to  $\sim 1$  for conventional stellarators.

## 1.2 Timescales and Temporal Evolution

The relevant timescales for the varying effects is important to consider. In toroidal devices, the MHD currents reach steady-state on an Alfvénic timescale, defined as the circumference of the device,  $2\pi R$ , divided by the Alfvén velocity,

$$\tau_A = \frac{2\pi R}{v_A} = \frac{2\pi R \sqrt{\mu_0 \rho_m}}{B} \quad (1.9)$$

Here,  $\rho_m$  is the mass density. For typical HSX plasma parameters,  $\tau_A \leq 1 \mu s$ . The net toroidal current, which has both a bootstrap and an inductive component, evolves on a much longer magneto-diffusion timescale, which is defined as the square of the minor radius,  $a$ , divided by the magnetic diffusivity,

$$\tau_{\eta_{\parallel}/\mu_0} = \frac{a^2}{\eta_{\parallel}/\mu_0} = \frac{a^2 \mu_0 n_e q_e^2}{m_e \nu_e} \quad (1.10)$$

The electron density, mass and collision frequency are given by  $n_e$ ,  $m_e$ , and  $\nu_e$ . In HSX,  $\tau_{\eta_{\parallel}/\mu_0} \geq 40 \text{ ms}$  is characteristic of plasmas with near-axis electron cyclotron heating (ECH) due to the high electron temperature,  $T_e$ . Because the time scales of the toroidal current diffusion are comparable to the experimental time,  $\tau_{exp} = 50 \text{ ms} \sim \tau_{\eta_{\parallel}/\mu_0}$ , modeling of the temporal behavior is required to describe the current enclosed within the plasmas. In principle, the change in current leads to a modification of the magnetic confinement field and rotational transform. These effects are small in the plasmas presented in this dissertation. Low-order rational surfaces are not expected to be present in the confinement volume while the ECH is applied. So while a self-consistent calculation of the bootstrap current is necessary for cases where the magnetic configuration is altered enough to change the underlying transport properties (specific to each configuration), this self-consistent calculation are not needed for HSX plasmas.

Several events can lead to a change in the current profile: a toroidal loop voltage applied with a transformer-coupled solenoid (inductive, or ohmic-drive), a change in the gradients and

transport-related fluxes and related flows (i.e. bootstrap current), or a change in either RF- or NBI-current drive. The relaxation of the current profile from its initial state to its steady-state in a large aspect-ratio circular tokamak can be expressed as a sum of Bessel-like basis functions [37]. In non-axisymmetric devices, the relaxation of the current profile is more complicated because of the 3-D helical shape of the plasma column which leads to a coupling of the toroidal and poloidal currents to each of the toroidal and poloidal magnetic fields [38]. As explained in Chapter 3, a  $2 \times 2$  susceptance matrix,  $S$ , relates the toroidal and poloidal currents,  $I$  and  $F$ , to the radial derivatives of the poloidal and toroidal magnetic fluxes,  $\Psi'$  and  $\Phi'$ .

$$\mu_0 \begin{bmatrix} I \\ F \end{bmatrix} = \begin{bmatrix} S_{11} & S_{12} \\ S_{21} & S_{22} \end{bmatrix} \begin{bmatrix} \Psi' \\ \Phi' \end{bmatrix} \quad (1.11)$$

Numerical simulations of LHD plasmas that include these 3-D effects [39], [40], [41] were in reasonable agreement with measurements of the rotational transform, Figure 1.8 [42]. While the rotational transform was in reasonable agreement, the current density profile,  $I'$ , which is proportional to the radial derivative of  $t$ , can not be resolved with much precision. The model for the bootstrap current in this case was based on an analytic solution for particles in the  $1/\nu$  and Pfirsch-Schlüter regime, with a connection formula between the two regimes. The effects of  $E_r$  are not modeled in these expressions (it is a small  $E_r$  estimate) [43] [44].

For the W7-X stellarator, now in the final construction phase in Greifswald, Germany, the performance of the island divertor will depend on how well the rotational transform at the edge of the plasma column is controlled. If the rotational transform is too high or too low, then the island region outside of the LCFS will not be located in the correct position to be on the edge limiter and the plasma will interact with the vessel wall and increase the impurity content of the plasma or damage internal components that are not shielded by the limiter. To account for this, a predictive 1-D transport model will be used for feed forward control of the  $t$  profile in W7-X, where the current profiles are expected to evolve to steady-state on timescales of 10's of seconds [45]. With the measured plasma temperature and density profiles, the steady-state bootstrap current and rotational transform will be rapidly calculated. To maintain the  $t_{LCFS}$  within an acceptable range, the total current will be compensated with ECCD [46]. It is critical that the calculation of the

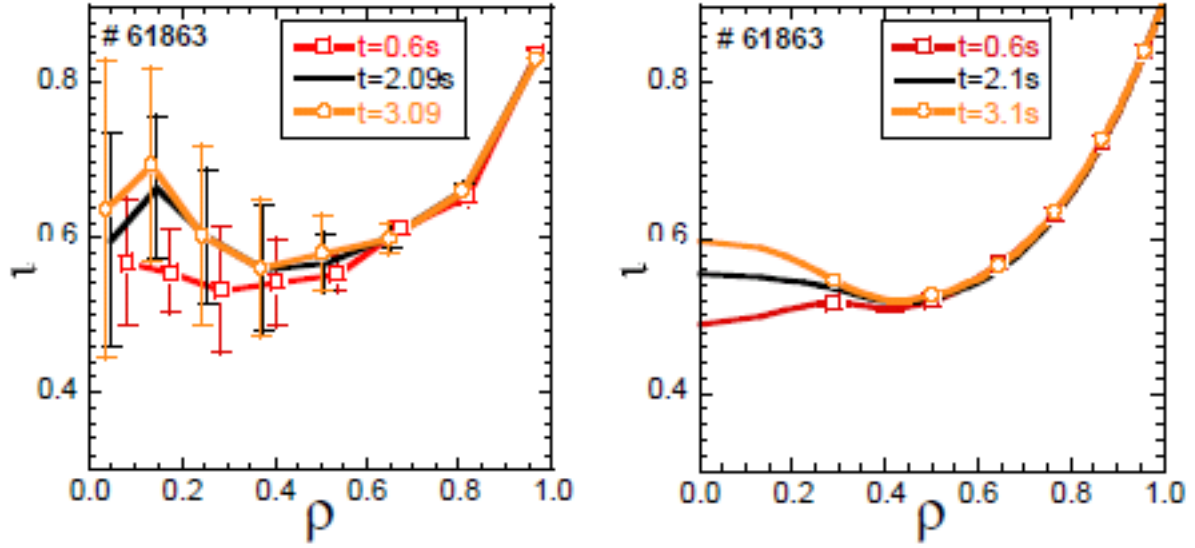


Figure 1.8 Measured (left) and calculated (right) rotational transform profiles for LHD. Figure from [42].

bootstrap current is accurate and fast. It is also important that the deposition efficiency (current drive) of the ECCD is correctly predicted. The various methods of achieving ECCD in stellarators are discussed elsewhere [47] [48] [49].

### 1.3 Equilibrium Reconstruction with Magnetic Diagnostics

In tokamaks, magnetic diagnostics provide essential information regarding the main electromagnetic parameters of the plasma, including the plasma current,  $I_p$ , the internal inductance,  $l_i$ , shape of the plasma boundary and the amplitude and mode numbers of fluctuations. The information is used in real-time control loops to maintain the desired plasma parameters and by almost all other diagnostics [50].

In the Doublet III experiment, it was found that 3 pieces of information could be resolved from magnetic diagnostic information. The reconstruction involves repeatedly solving the Grad-Shafranov equation to search for a current density profile that produces diagnostic signals that best-fit the measured signals. With this strategy, the total plasma current ( $I_p$ ), the poloidal beta ( $\beta_p$ ), and the peakedness of the current profile (related to the internal inductance,  $l_i$ ) could be

determined. For non-circular discharges, the values of  $\beta_p$  and  $l_i$  can be separately determined; for circular discharges, only  $\beta_p + l_i/2$  could be determined [51]. With more shaping to the plasma column, more information could be extracted from the magnetic measurements. Variations of the reconstruction code, EFIT [52] are in use around the world on various tokamaks. The non-inductive current profile has been reconstructed in DIID [53] and MSTFIT is in use at the Madison Symmetric Torus RFP [54].

Equilibrium reconstruction is not a routine process for stellarators. Complicated by the 3-D nature of the magnetic fields, no simple Grad-Shafranov (G-S) equation exists from which the equilibrium can be quickly calculated. A fully 3-D equilibrium solver (VMEC, Appendix A) is required, which needs much more computational time to solve than the G-S equation. Because modern stellarators are designed for, and are achieving, higher level of plasma beta and bootstrap current, the deviation of the equilibrium surfaces from the vacuum configuration increases and a 3-D reconstruction is required. Even tokamaks with small asymmetries need a 3-D reconstruction, such as the planned ITER experiment. ITER will have ferromagnetic blanket materials that break the axisymmetry and the eddy currents induced in the blanket will affect the diagnostic signals, so they must be modeled and accounted for in the data for the reconstruction to be accurate.

For stellarators in general, the amount of information in the magnetic field generated by the plasma is increased, compared to a tokamak. This is because of the non-circular cross-section of the plasma column and the variation of the shape of the cross-section with toroidal angle in a stellarator. For stellarators, expressions of the radial and poloidal components of the magnetic field outside of the plasma volume have additional integral relations of the pressure and current profile than for a tokamak (see Eqns 41 and 42 in Reference [55]). Accuracy of the information of the plasma parameter profiles is largely increased in stellarators compared with the possible precision of the magnetic diagnostics in tokamaks [55]. The information of the size of the plasma column, rotational transform on the boundary, main harmonic amplitude of stellarator field, boundary surface shift and poloidal magnetic flux can all be extracted from the measured magnetic field. It is, in principal, possible to extract more info about plasma pressure profile by measuring the magnetic field generated by the dipole current carefully, although this requires more diagnostics than used in



a tokamak [56]. Early studies regarding magnetic diagnostics and equilibrium information for stellarators focused on cases with no net toroidal current. For the TJ-II stellarator in Madrid, Spain, with model pressure profiles specified by two parameters, it was shown that only two magnetic diagnostics were required to adequately reconstruct the pressure profile [57]. This is not a strong result, however, since only very simple (linear) plasma pressure profiles were considered.

The challenges for 3-D equilibrium reconstruction are similar to those encountered in tokamaks: It is difficult to discern pressure and current profiles with small differences [58] and because the magnetic field outside the plasma is the integrated effects of current density in the plasma, there are few independent quantities that can be extracted from the data [59]. So, while there is more information about the plasma profiles contained in the magnetic field of a stellarator, there are open questions as to which information can be extracted (measured) and to what degree of accuracy.

One of the limits of the early 3-D reconstruction work was that a large amount of computational time was required to calculate the 3-D MHD equilibrium. With computational power increasing thanks to Moore's law, the speed, accuracy and fidelity of the MHD calculation has improved dramatically. This has enabled the reconstruction of stellarator plasmas with magnetic diagnostics to be studied more carefully.

Function parameterization (FP) is one such computational study that provides insight into the prospects of the reconstruction based on magnetic diagnostics [60]. FP is a method to invert computational models that map input parameters to the measurements. Here, the input parameters describe the plasma pressure profile, current profile, and other relevant pieces of information, such as the main field current and magnetic configuration. A large database of input parameters is generated, which span the operational space of the particular configuration. Next, the MHD equilibrium solution for each set of inputs is calculated, and the magnetic signals for each diagnostic is calculated. These are the simulated measurements. The next step is to remove redundant or insignificant information from the measurements. By applying principal component analysis (PCA) to the matrix of (input parameters) $\times$ (measurements), [61], the number of dimensions in the measurements can be reduced [62], and the inverse mapping from the measurements back to the input parameters can be found.

The recovery of pressure profiles for the W7-AS plasma profiles with no net current using the FP technique was studied [63]. The results of the study were that only two moments of the pressure profile were readily recoverable: an average pressure profile and a peaking factor. There was little or no chance to resolve the higher-order structure of the pressure profile with more than 15% – 25% certainty [64]. A similar study was performed for the future successor to W7-AS, the W7-X stellarator, but both pressure and current profiles were variable [65]. Two profile parameters for each the pressure and current could be resolved. While disappointing in terms of equilibrium reconstruction, this result is, in part, due to the optimization of the W7-X stellarator. It is optimized to minimize the plasma currents.

In contrast to W7-X, a singular value decomposition (SVD) study of magnetic diagnostics on the quasi-axisymmetric stellarator, NCSX, which involved the calculation of 1800 likely equilibrium and corresponding magnetic signals, predicted that up to 19 unspecified plasma profile parameters could be extracted from a dense set ( $60 \times 20 = 1200$ ) of diagnostic signals [66]. The final set of diagnostics included only 225 magnetic diagnostics, but because the machine was canceled before it became operational, further analysis of the diagnostic set and reconstruction capabilities have not been performed.

The FP technique provides insight into how well a reconstruction performs in a global sense (over the span of the input database), but it does not provide information on how well the reconstructed profiles represent the experimental ones in a local sense (local in parameter space). An alternative method of reconstructing the plasma profiles for 3-D configurations, which is more like the method involved in EFIT, involves using SVD to approximate a quasi-newton algorithm for choosing new parameters in a nonlinear least-squares minimization routine [67]. This code is called V3FIT. The search for the reconstructed pressure and current profiles is an iterative one. The MHD equilibrium for an ‘initial guess’ of profiles is solved, and the magnetic signals are calculated [68]. For each variable input parameter, that parameter is adjusted and the equilibrium solution and diagnostic signals are calculated. That parameter is then set back to its original value and the next input parameter is adjusted until each parameter has been varied. The path to minimizing the mismatch between the measured and modeled signals is optimized by the SVD step

because it selects the search direction based on the signals that are found to be statistically most significant in the local parameter space.

External magnetic diagnostics are not the only way to measure the effects of plasma current. Other methods are available, but not practical for HSX, at least at present. Polarimetric measurements of the Faraday rotation angle of probe beams provide a line-integrated density-weighted parallel B measurement,  $\sim \int dl N_e B_{\parallel}$  [69] [70]. In HSX the rotation angle is estimated to be too small to be reliably measured [71]. Another method is based on motional Stark effect polarimetry (MSE) [72] [73]. A diagnostic neutral beam is launched into the plasma. The Stark splitting of the emission line results in a polarization angle that depends on the magnetic field pitch. HSX does have a diagnostic neutral beam, but the splitting of the emission line is likely to be too small to observe in HSX.

## 1.4 Thesis Outline

This dissertation describes the modeling and reconstruction of the equilibrium currents that are present in the HSX stellarator during plasma operations. In Chapter 2, the MHD equilibrium currents (diamagnetic and Pfirsch-Schlüter) and their properties in HSX are presented. The neo-classical bootstrap current, driven by viscous damping between trapped and circulating particles is also discussed in Chapter 2. A qualitative description of the bootstrap current in tokamaks is outlined. The important effect of  $E_r$  and momentum conservation are included for the stellarator picture, and the PENTA code is described. PENTA is used extensively to calculate the steady state parallel current and parallel conductivity. The DKES coefficients used by PENTA have been benchmarked [74], but the results of PENTA have not been checked against other MC-codes.

In typical plasma discharges in the HSX stellarator, the net toroidal current continues to evolve (rise) on the timescale of the experiment and don't reach steady-state by the end of the shot. The temporal evolution of the net toroidal current is described in Chapter 3. The evolution is first discussed in a cylindrical geometry. The modeling for a general non-axisymmetric toroidal configuration is then presented. A 1-D diffusion equation is derived which describes how the current or rotational transform evolves during the plasma discharge. The diffusion equation uses a  $2 \times 2$

susceptance matrix,  $S$ , relating the toroidal and poloidal current to radial derivatives of the toroidal and poloidal magnetic flux. The  $S$ -matrix is calculated from geometric information describing the shape of the flux surface. The outlined technique is appropriate for any toroidal configuration, can be calculated rapidly, and can incorporate several different boundary conditions (prescribed net current, loop voltage, or free-resistive relaxation). The diffusion equation is solved numerically by a time evolution code called `iota_evolution_generate` (IEG) which simulates the evolving rotational transform and current profile as a function of time. The bootstrap current density and the parallel conductivity from PENTA are used as inputs for IEG.

In Chapter 4, a set of magnetic pick-up coils or sensors is described. These diagnostics are used to measure the magnetic field generated by the plasma current outside of the plasma column. Post-shot signal processing is performed to remove the effects of the background magnetic vacuum field from each diagnostic, and these signals are used as constraints in a 3-D equilibrium reconstruction. To facilitate this, two software codes, V3RFUN and V3FIT are described. V3RFUN calculates a Green's function response of each magnetic diagnostic due to the magnetic fields generated by both the field coils and the plasma current [68]. This response is calculated once and stored in a database. The V3FIT code reads the information of the current distribution from the output of an equilibrium solver (VMEC, in this case) and uses the response functions to calculate the total signal for each magnetic diagnostic. V3FIT then uses a singular value decomposition (SVD) to approximate a quasi-newton algorithm in a least-squares minimization routine, where the profiles of the plasma pressure and current are adjusted to find a best-fit between the measured and modeled signals.

In Chapter 5, the results of experiments in the QHS magnetic configuration with near-axis ECH (50 kW and 100 kW) and off-axis ECH heating are presented. The measured  $T_e$ ,  $N_e$ , and  $T_i$  profiles and the calculated bootstrap current and  $\sigma_{\parallel}$  profiles are shown. The evolved current profile, based on the PENTA calculation, is used as an initial guess for the 3-D reconstruction, and the reconstructed profiles are compared to the measured profiles.

Chapter 6 will discuss the conclusions of the experimental results and unresolved questions regarding the bootstrap current in the HSX stellarator and provide suggestions for possible future research topics, including benchmarking PENTA, improving the reconstruction of the plasma profiles, and studying effects of rational surfaces (magnetic islands) in HSX plasmas.

## References

- [1] [www.enerdata.net/enerdatauk/press-and-publication/publications/decrease-world-energy-demand-first-time-30-years.php](http://www.enerdata.net/enerdatauk/press-and-publication/publications/decrease-world-energy-demand-first-time-30-years.php) (2010).
- [2] [www.eia.gov/totalenergy/data/annual/txt/ptb1101.html](http://www.eia.gov/totalenergy/data/annual/txt/ptb1101.html) (2007).
- [3] [www.ipcc.ch](http://www.ipcc.ch)
- [4] E. Strickland, IEEE Spectrum, 4 April 2011.
- [5] J. Wesson, “Tokamaks”, Clarendon Press, Oxford (2004).
- [6] M. Wakatani, “Stellarator and Heliotron Devices”, Oxford University Press, Oxford (1998).
- [7] Tihiro Ohkawa, “Steady-State Operation of Tokamaks by r-f heating”, GA-A13847, 1976.
- [8] N. J. Fisch and A. H. Boozer, PRL **45**, 720 (1980).
- [9] Per Helander and D. J. Sigmar, “Collisional Transport in Magnetized Plasmas”, Cambridge University Press, New York (2002).
- [10] A. H. Boozer, Physics of Fluids **26**, 496 (1983).
- [11] J. Nührenberg and R. Zille, Physics Letters A **129**, 112 (1988).
- [12] D. T. Anderson, et al., “HSX: A Helically Symmetric Toroidal Experiment”, Dept. of Energy Proposal (1992).
- [13] A. H. Boozer, Phys. Fluids **24**, 1999 (1981).
- [14] J. N. Talmadge, et al., Phys. Plasmas **8**, 5165 (2001).
- [15] J. M. Canik, et al., Phys. Plasmas **14**, 056107 (2007).
- [16] Jeffrey Freidberg, “Plasma Physics and Fusion Energy”, Cambridge University Press, New York (2007).
- [17] V. D. Shafranov, Atomic Energy **13**, 1149 (1963).

- [18] M. Kikuchi and M. Azumi, Plasma Physics and Controlled Fusion **37**, 1215 (1995).
- [19] M. Murakami, et al., PRL **66**, 707 (1991).
- [20] A. H. Boozer and H. J. Gardner, Phys. Fluids B **2**, 2408 (1990).
- [21] A. G. Peeters, Plasma Physics and Controlled Fusion **42**, B231 (2000).
- [22] K. C. Shaing, et al., Physics of Fluids B **1**, 1663 (1989).
- [23] Y. Nakamura, et al., Fusion Science and Technology **50**, 281 (2006).
- [24] F. Wagner, et al., “Operational Experience in W7-AS Discharges with Rotational Transform from Bootstrap Current”, 25th EPS Conference Controlled Fusion and Plasma Physics, Praha, B049PR, p.0395 (1998).
- [25] F. Wagner, et al, Phys. Plasmas **12**, 072509 (2005).
- [26] H. Wobig and J. Kisslinger, Plasma Physics and Controlled Fusion **42**, 823 (2000).
- [27] Y. A. Turken, et al., Proc. 31st EPS Conf. on Plasma Physics, London, 28G, P-1.198 (2004).
- [28] F. Castejón, et al., Nuclear Fusion **44**, 593 (2004).
- [29] Nakajima, et al., “Physical Mechanism of  $E_\Psi$ -Driven Current in Asymmetric Toroidal Systems”, National Institute for Fusion Science, NIFS-172 (1992).
- [30] H. Sugama and S. Nishimura, Phys. Plasmas **9**, 4637 (2002).
- [31] H. Maaßberg, C. D. Beidler, and Y. Turkin, Phys. Plasmas **16**, 072504 (2009).
- [32] D. A. Spong, Phys. Plasmas **12**, 056114 (2005).
- [33] J. Lore, Ph. D. dissertation, University of Wisconsin-Madison, Madison (2010).
- [34] W. I. van Rij and S. P. Hirshman, Phys. Fluids B **1**, 563 (1989).
- [35] V. V. Nemov and S. V. Kasilov, Phys. Plasmas **6**, 4622 (1999).
- [36] M. Morimoto, et al., Fusion Engineering and Design **84**, 2118 (2009).
- [37] D. R. Mikkelsen, Phys. Fluids B **1**, 333 (1989).
- [38] P. I. Strand and W. A. Houlberg, Phys. Plasmas **9**, 2782 (2001).
- [39] Nakamura, et al., 33rd EPS Conference on Plasma Physics, Rome, P-4.122 (2006).
- [40] Nakamura, et al., 16th International Stellarator/Heliotron Workshop, Ceratopia Toki, Japan, P2-015 (2007).

- [41] Nakamura, et al., Plasma and Fusion Research **3**, S1058 (2008).
- [42] Nakamura, et al., “Time Evolution of the Bootstrap Current Profile in LHD Plasmas”, 22nd IAEA Fusion Energy Conference, Geneva, EX/P6-20 (2008).
- [43] K. C. Shaing, et al., Physics of Fluids **29**, 521 (1986).
- [44] K. C. Shaing, et al., Physics of Fluids B **1**, 1663 (1989).
- [45] Yu. A. Turkin, et al., “Predictive transport modeling for the W7-X”, 31st EPS Conference on Plasma Physics, London, ECA Vol. 28G, P-1.198 (2004).
- [46] Yu. A. Turkin, et al., Fusion Science and Technology **50**, 387 (2006).
- [47] V. Erckmann, U. Gasparino, H. Maaßberg, Plasma Physics and Controlled Fusion **34**, 1917 (1992).
- [48] F. Castejón, et al., Phys. Fluids B **4**, 3689 (1992).
- [49] H. Maaßberg, et al., Plasma Physics and Controlled Fusion **47**, 1137 (2005).
- [50] G. Vayais, et al., Review of Scientific Instruments **74**, 2409 (2003).
- [51] J. L. Luxon and B. B. Brown, Nuclear Fusion **22**, 813 (1982).
- [52] L. L. Lao et al., Nuclear Fusion **20**, 1025 (1990).
- [53] C. B. Forest, et al., PRL **73**, 2444 (1994).
- [54] J. K. Anderson, Ph. D. dissertation, University of Wisconsin-Madison (2001).
- [55] V. K. Pashnev and V. V. Nemov, Nuclear Fusion **33**, 435 (1993).
- [56] A. B. Kuznetsov and S. V. Shchepetov, Nuclear Fusion **37**, 371 (1997).
- [57] J. A. Jiménez, et al., 10th International Stellarator Workshop, Madrid, Spain, 208 (1995).
- [58] S. V. Shchepetov, et al., Plasma Physics and Controlled Fusion **43**, 417 (2001).
- [59] V. D. Pustovitov, Nuclear Fusion **41**, 721 (2001).
- [60] B. Ph. van Milligen and N.J. Lopes Cardozo, Computer Physics Communications **66**, 243 (1991).
- [61] I. T. Jolliffe, Applied Statistics **21**, 160 (1972).
- [62] J. A. Cumming and D. A. Wooff, Computational Statistics & Data Analysis **52**, 550 (2007).
- [63] H. P. Callaghan, et al., Nuclear Fusion **39**, 509 (1999).



- [64] H. P. Callaghan, et al., Plasma Physics and Controlled Fusion **42**, 1013 (2000).
- [65] J. Geiger, et al., Contrib. Plasma Phys. **50**, 736 (2010).
- [66] N. Pomphrey, et al., Phys. Plasmas **14**, 056103 (2007).
- [67] J. D. Hanson, et al., Nuclear Fusion **49**, 075031 (2009).
- [68] S. P. Hirshman, E. A. Lazarus, J. D. Hanson, S. F. Knowlton, and L. L. Lao, Phys. Plasmas **11**, 595 (2004).
- [69] D. L. Brower, et al., PRL **88**, 185005 (2002).
- [70] A. J. H. Donné, et al., Rev. Sci. Instrum. **75**, 4694 (2004).
- [71] C. B. Deng, private communication.
- [72] C. C. Petty, et al., Plasma Physics and Controlled Fusion **43**, 1077 (2005).
- [73] K. Ida, et al., Review of Scientific Instruments **76**, 053505 (2005).
- [74] C. D. Beidler, et al., “Results From the International Collaboration on Neoclassical Transport in Stellarators (ICNTS)”, 22nd IAEA Fusion Energy Conference, TH/P8-10 (2008).

## Chapter 2

### Magnetohydrodynamic Equilibrium and Neoclassical Bootstrap Currents

This chapter presents the models describing the equilibrium currents in the HSX stellarator. The solution to the magnetohydrodynamic (MHD) equilibrium relates the plasma pressure gradient to the diamagnetic and Pfirsch-Schlüter current, which are part of the total equilibrium current. The Pfirsch-Schlüter current is a dipole current that rotates helically with  $|B|$  contours in HSX, rotating  $360^\circ$  in the poloidal direction along a single field period. The neoclassical viscosity between trapped and circulating populations of particles on a flux surface drives the bootstrap current. In a tokamak, the bootstrap current has a relatively simple expression and there is no radial electric field dependence, but it will be shown that in a stellarator, when momentum conservation is included between the plasma species, the bootstrap current has a strong dependence on the radial electric field. The main current-carrying components of the plasma are the passing particles. The value of the bootstrap current that is calculated is a steady-state estimate. It is not a self-consistent estimate in the sense that the modifications to the magnetic spectrum due to the presence of the bootstrap and MHD current are not considered. These effects on the magnetic spectrum are small: major resonances in the rotational transform profile are avoided, and the  $|B|$ -spectrum shows little change because of the high effective transform that results in small currents. The time for the bootstrap current to reach steady-state is on the scale of the slowing down time between like particle collisions, which is on the order of  $ms$  in HSX plasmas. In Chapter 3, the reaction of the plasma to the onset of the bootstrap current is considered and leads to an evolving current profile in the plasma column.

## 2.1 Basic MHD

In magnetohydrodynamics, the force-balance equation and the divergence-free condition of plasma current are

$$\mathbf{J} \times \mathbf{B} = \nabla p \quad (2.1)$$

$$\nabla \cdot \mathbf{J} = 0 \quad (2.2)$$

The Lorentz ( $\mathbf{J} \times \mathbf{B}$ ) force generated by the plasma current balances the force of the plasma pressure gradient, and the equilibrium current on each flux surface is divergence-free. The component of the current that is perpendicular to the field lines and lies within the flux surface is found by taking  $\mathbf{B} \times$  Eqn 2.1. With  $\Phi$  as the toroidal flux enclosed by a flux surface and expanding  $\nabla p = \frac{dp}{d\Phi} \nabla \Phi$ ,

$$\mathbf{J}_\perp = \frac{\mathbf{B} \times \nabla \Phi}{B^2} \frac{dp}{d\Phi} \quad (2.3)$$

This is the magnetization or diamagnetic current, which is driven by the pressure gradient and is proportional to the geodesic curvature, [1]. Since both  $\mathbf{B}$  and  $\nabla \Phi$  vary on a flux surface,  $J_\perp$  is not constant on the flux surface. To maintain a divergence-free current, Eqn 2.2 implies that a parallel (to  $\mathbf{B}$ ) current is required:

$$\nabla \cdot \mathbf{J} = \nabla \cdot \mathbf{J}_\perp + \nabla \cdot \mathbf{J}_\parallel \quad (2.4)$$

$$\nabla \cdot \mathbf{J}_\perp = -\nabla \cdot \mathbf{J}_\parallel \quad (2.5)$$

By writing

$$J_\parallel = hB \frac{dp}{d\Phi} \quad (2.6)$$

where  $h$  is a single valued function of space, and using Eqn 2.3, Eqn 2.5 becomes a magnetic differential equation [2]:

$$\mathbf{B} \cdot \nabla h = \nabla \cdot \left( \frac{\mathbf{B} \times \nabla \Phi}{B^2} \right) \quad (2.7)$$

$$= -2 \frac{(\mathbf{B} \times \nabla B) \cdot \nabla \Phi}{B^3} \quad (2.8)$$

The parallel current,  $\mathbf{J}_{\parallel}$ , consists of two parts. The first part, the Pfirsch-Schlüter current, exactly balances the diamagnetic current and has no net parallel component on the flux surface.

$$\langle \mathbf{J}_{\parallel PS} \cdot \mathbf{B} \rangle = 0 \quad (2.9)$$

The angled set of brackets,  $\langle \rangle$ , is a flux-surface average operator. The Pfirsch-Schlüter current will be discussed in more detail in section 2.2. The second part of the solution allows for a net parallel component,

$$\langle \mathbf{J}_{\parallel} \cdot \mathbf{B} \rangle = J_{\parallel, net} \neq 0 \quad (2.10)$$

Section 2.3 will discuss the contributions to this term.

## 2.2 Pfirsch-Schlüter Current

Consider the quantity  $1/B^2$  in Eqn 2.7. By employing Boozer flux coordinates [3] where  $\zeta_B$  and  $\theta_B$  are the toroidal and poloidal angular coordinates, respectively,  $1/B^2$  can be expressed as a Fourier series:

$$\frac{1}{B^2} = \frac{1}{B_0^2} \sum_{n,m} \delta_{n,m} \cos(n\zeta_B - m\theta_B) \quad (2.11)$$

The amplitude of the spectral component is  $\delta_{n,m}$ , and  $(n, m)$  are the toroidal ( $n$ ) and poloidal ( $m$ ) mode number pairs. The Pfirsch-Schlüter current is expressed as [4]

$$\mathbf{J}_{PS} = \frac{\mathbf{B}}{B_0^2} \frac{dp}{d\Phi} \sum_{(n,m) \neq (0,0)} \frac{nI + mF}{n - mt} \delta_{n,m} \cos(n\zeta_B - m\theta_B) \quad (2.12)$$

The quantity  $I$  is the total toroidal current enclosed within a flux surface and  $F$  is the total poloidal current *external* to a flux surface. In the quasi-helically symmetric (QHS) magnetic configuration of HSX [5], the largest contribution is from the dominant spectral component,  $\delta_{4,1}$ :

$$\mathbf{J}_{PS,QHS} = \frac{\mathbf{B}}{B_0^2} \frac{dp}{d\Phi} \underbrace{\frac{4I + F}{4 - t}}_{\text{reversal, reduction}} \delta_{4,1} \underbrace{\cos(4\zeta_B - \theta_B)}_{\text{toroidal rotation}} \quad (2.13)$$

The helical axis of symmetry and the effective elimination of the  $(n, m) = (0, 1)$  toroidal curvature term in the QHS configuration has three consequences. First, the dipole Pfirsch-Schlüter

current rotates with the helical  $|B|$  contours due to the  $\cos(4\zeta_B - \theta_B)$  dependency. Numerical methods to calculate the normalized quantity,  $h\mathbf{B}$  in Eqn 2.6, and the Pfirsch-Schlüter current,  $\mathbf{J}_{P,S}$ , by field-line following are derived elsewhere [6], [7]. Figure 2.1 shows the quantity  $\mathbf{J}_{P,S} \cdot \mathbf{B}$  on vertical slices at three toroidal angles in the QHS configuration. The results from the VMEC code (see Appendix A), are shown in Figure 2.2. The pressure profile for these two cases is shown in Figure 2.3, which is peaked on-axis and is typical of centrally-heated plasmas in HSX. In the VMEC input file for this case, the net toroidal current was set to 0,  $\langle \mathbf{J}_{\parallel} \cdot \mathbf{B} \rangle = 0$ . The region of  $(\mathbf{J}_{P,S} \cdot \mathbf{B} > 0)$  rotates from the outboard side of the plasma column at  $\zeta = 0^\circ$  to the top of the column at  $\zeta = 22^\circ$  and to the inboard side at  $\zeta = 45^\circ$ , which is 1/2 of a field period from the first slice. There is good agreement between the line-following method and VMEC. The shape of the edge of the plasma column in the VMEC case does not reflect the level of detail as in the line-following results because of the finite Fourier series used to represent the MHD quantities and inverse coordinates.

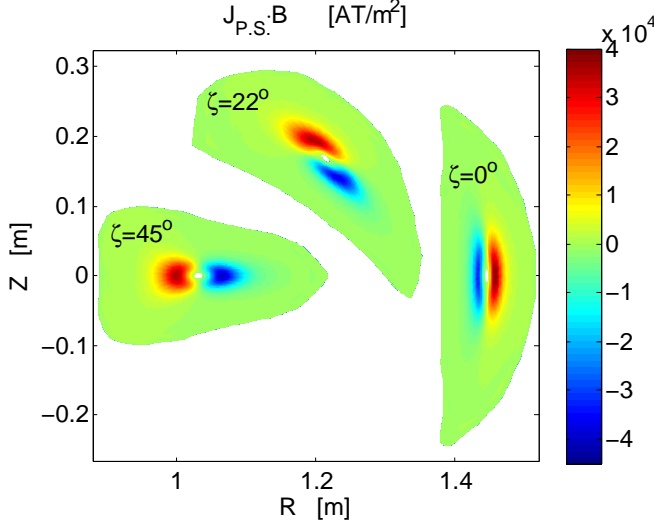


Figure 2.1  $\mathbf{J}_{P,S} \cdot \mathbf{B}$  in QHS at three toroidal angles along 1/2 of a field period, calculated by a line-following technique.

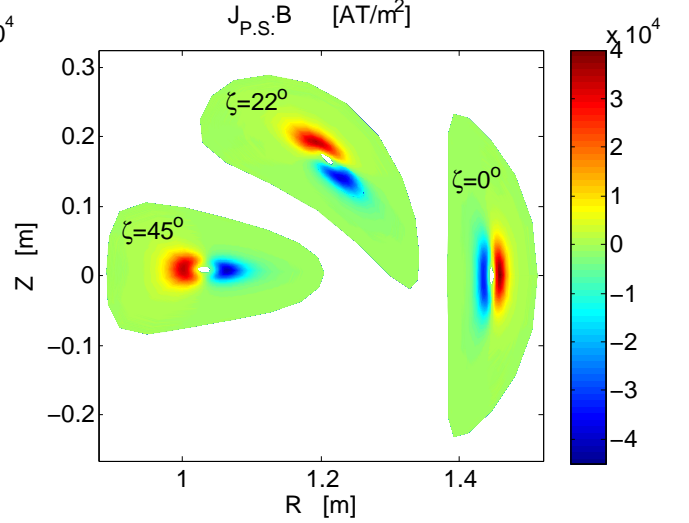


Figure 2.2  $\mathbf{J}_{P,S} \cdot \mathbf{B}$  in QHS at three toroidal angles along 1/2 of a field period, calculated by VMEC.

The second consequence of Eqn 2.13 is that the Pfirsch-Schlüter current is directed opposite to that in a tokamak. This arises because the  $\mathbf{B} \times \nabla B$ -direction in HSX is opposite to that in a

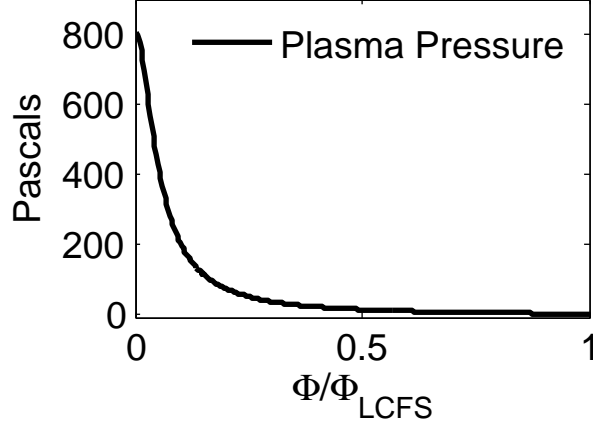


Figure 2.3 The centrally-peaked radial pressure profile for the Pfirsch-Schlüter current density contours in Figure 2.2.

tokamak, Eqn 2.8 and Figure 2.4. More specifically, this holds true for the region where the QHS field is most ‘tokamak-like’, where the low-field side is on the outboard side,  $\zeta = 0, \theta = 0$ . This can also be seen with Eqn 2.12 with  $(n, m) = (0, 1)$  as the dominant term and comparing it to Eqn 2.13:

$$\mathbf{J}_{PS,tok} = \frac{\mathbf{B}}{B_0^2} \frac{dp}{d\Phi} \frac{F}{-t} \delta_{0,1} \cos(-\theta_B) = -\frac{\mathbf{B}}{B_0^2} \frac{dp}{d\Phi} \frac{F}{t} \delta_{0,1} \cos(\theta_B) \quad (2.14)$$

The third consequence of Eqn 2.13 is that the magnitude of the current is reduced by a factor of  $n - mt \approx 3$ . A useful measure of the reduction of the Pfirsch-Schlüter current is made by comparing the quantity  $\langle J_{\parallel PS}^2 / J_{\perp}^2 \rangle$  in QHS with an equivalent tokamak. An ‘equivalent tokamak’ is defined as a tokamak with the same effective (average) major and minor radii and the same rotational transform as the QHS configuration,  $t \sim 1$ , described in Appendix A. The results of the VMEC calculation for this quantity in QHS and for an equivalent tokamak is in Figure 2.5. The pressure profiles for each case is  $2000 \left(1 - \frac{\Phi}{\Phi_{LCFS}}\right)^2$ . The Pfirsch-Schlüter current density is reduced in QHS by a factor  $\approx 3$ -3.5, favorably increasing the equilibrium beta limit. The achievable equilibrium beta limit due to a Shafranov shift of 1/2 of the minor radius is approximately 35% [5].

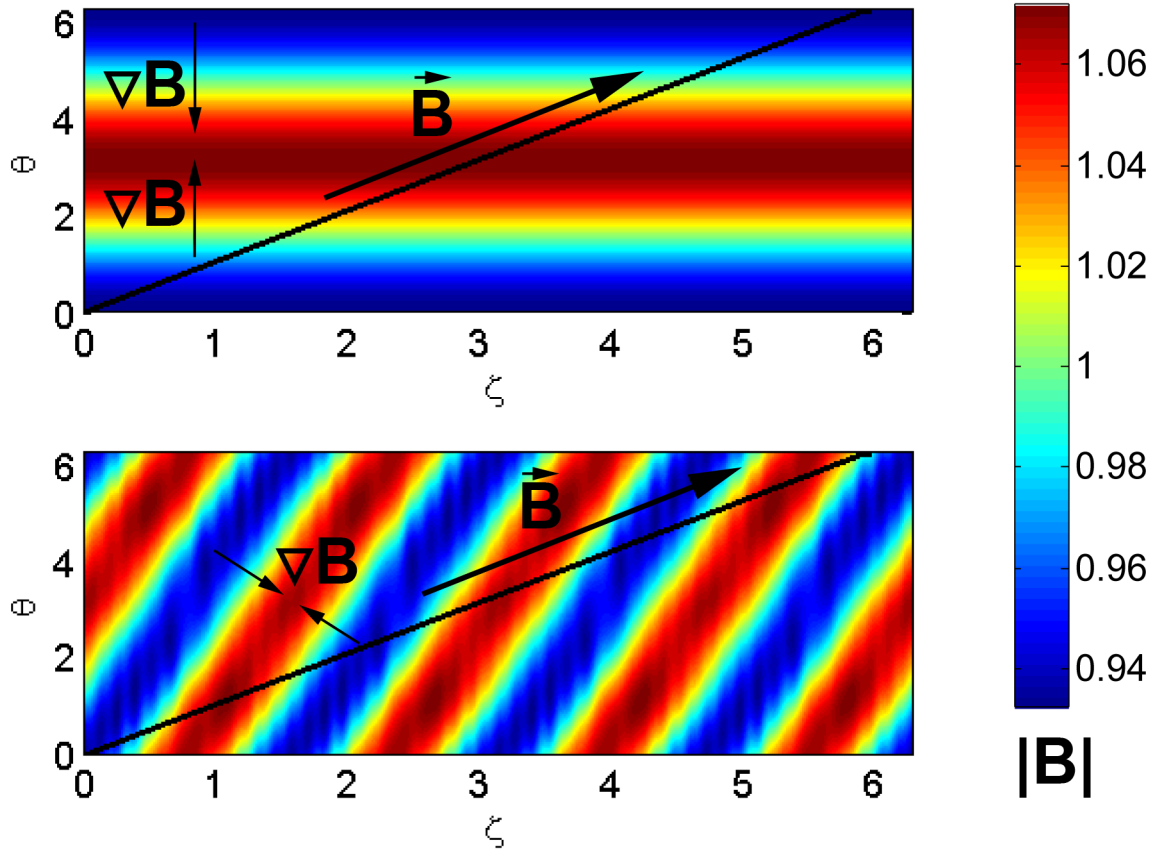


Figure 2.4  $|B|$ ,  $\nabla B$ , and a field line,  $\vec{B}$ , on a flux surface for a large aspect-ratio axisymmetric tokamak (top) and the QHS configuration (bottom).

### 2.3 Neoclassical Parallel Bootstrap Current

Recall the second part of the parallel current on the flux surface, Eqn 2.10. This term is the sum of inductive and non-inductive sources. In HSX, there is no direct inductive drive during the shot (no ohmic heating transformer), and the electron cyclotron heating source is launched perpendicular to the plasma column and should drive little to no parallel current. Plasma discharges in the QHS magnetic configuration with similar density and temperature profiles but with the main magnetic field reversed show similar levels of toroidal current, but in opposite directions, as seen in Figure 2.6. This is the expected behavior of a plasma with bootstrap current but little to no

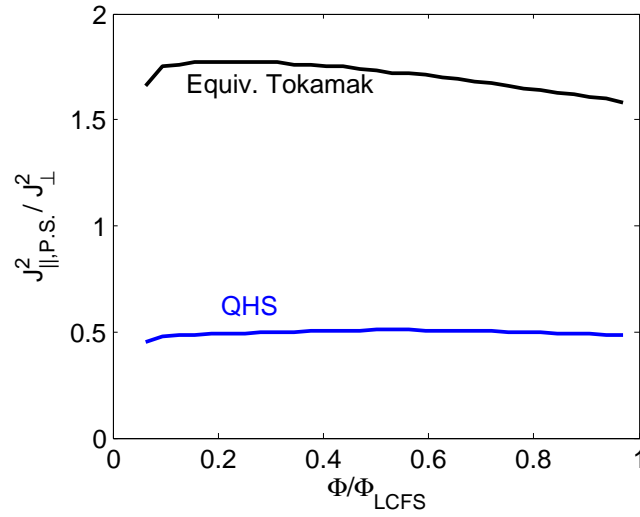


Figure 2.5  $\langle J_{||PS}^2 / J_{\perp}^2 \rangle$  as calculated with VMEC for QHS and an equivalent tokamak.

ECCD. The net toroidal current was also independent of small changes in the time-varying main field current ( $\sim 0.3\%$ ).

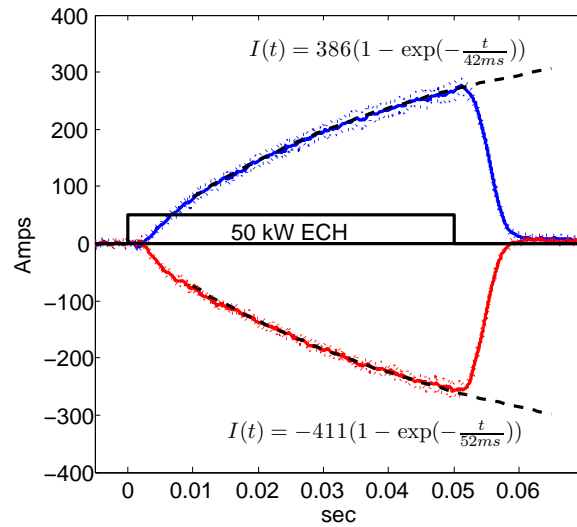


Figure 2.6 QHS, 50 kW,  $\rho_{ECRH} \lesssim 0.1$ : Measured net toroidal current for an ensemble average of shots with the magnetic field in the CCW (blue) and CW (red) directions.



### 2.3.1 Large Aspect Ratio Tokamak

The toroidal (or helical) curvature in toroidal plasmas results in two classes of particles for each species on a flux surface: trapped and passing [8]. The trapped particles are confined inside the magnetic potential well, or ripple-trapped, along the field line, whereas the passing particles have enough kinetic energy to pass beyond the magnetic potential and circulate around the surface. The trapped particles have a collective drift velocity, and the collisions between the passing particles and the trapped particles leads to a net current, called the bootstrap current.

In a large-aspect ratio axisymmetric tokamak, with minor radius  $r$  and major radius  $R_0$ ,  $\epsilon = r/R_0$ , and the magnetic field strength along a field line is given by

$$\frac{B}{B_0} = \frac{1}{1 + \epsilon \cos \theta} \approx 1 - \epsilon \cos \theta \quad (2.15)$$

The magnetic field strength varies with the poloidal angle,  $\theta$ . The guiding center drift of particles confined within such a field exhibit two different types of behavior depending on the ratio of their parallel velocity,  $v_{\parallel}$ , and total velocity,  $v$ . For particles with  $|\frac{v_{\parallel}}{v}| \gtrsim \sqrt{2\epsilon}$ , the particles make complete toroidal orbits, but experience a small excursion in their orbit due to  $\nabla B$  and curvature drifts. Those that have  $v_{\parallel} > 0$  (parallel to the direction of  $\mathbf{B}$ ) trace out orbits with a radius that is slightly larger than the flux surface, while those with  $v_{\parallel} < 0$  trace out orbits with a radius slightly smaller. The projection of these two trajectories for ‘passing’ particles onto a single poloidal slice (a vertical slice through the plasma column at a single toroidal angle) is shown in Figure 2.7.

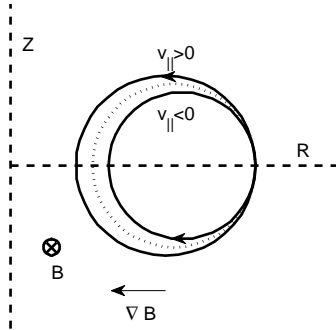


Figure 2.7 Orbits of passing particles. The flux surface is shown as a dotted line.

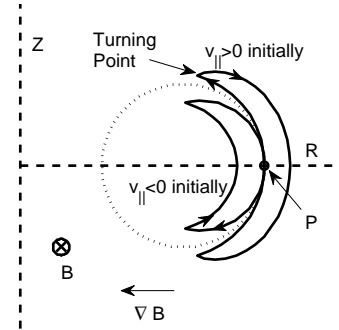


Figure 2.8 Orbits of trapped particles. The flux surface is shown as a dotted line.

Particles with  $\left| \frac{v_{\parallel}}{v} \right| \lesssim \sqrt{2\epsilon}$  become ‘trapped’ in the magnetic wells. They do not have sufficient parallel velocity to pass beyond the maximum value of the magnetic field. Instead, they have turning points where their parallel velocity becomes zero and then reverses direction. The poloidal projection of these orbits represent bananas; hence the name, ‘banana orbits’, Figure 2.8. Consider the particles that start at the tangent point of the two banana orbits, ‘P’. Those that start with  $v_{\parallel} > 0$  drift off the flux surface to a slightly larger radius until they reach the turning point where  $v_{\parallel} = 0$  and reverse direction. It continues to drift further off of the surface until it passes through  $Z = 0$  and then experiences a drift inwards until it returns to the starting surface. The particles that start with  $v_{\parallel} < 0$  drift inwards during the 1st 1/2 period of a bounce orbit, and then drift outward on the 2nd 1/2 period.

The distance a moderately trapped particle travels between the turning points in a tokamak is  $\pi R_0/t$ . The total particle velocity is related to the thermal velocity by  $v^2 \sim \frac{3}{2}v_T^2$ , so the average parallel velocity for a typical trapped particle is  $v_{\parallel,t} \sim \sqrt{2\epsilon}v/2 \sim \sqrt{\epsilon}v_T$ . The time for a trapped particle to travel between turning points is  $\tau_b \sim \pi R_0/(tv_{\parallel}) \sim \pi R_0/(t\sqrt{\epsilon}v_T)$ . The bounce frequency is  $\omega_b = 2\pi/2\tau_b = t\sqrt{\epsilon}v_T/R_0$ . The time for a trapped particle to collisionally scatter in pitch angle to become untrapped is  $\tau_{eff} \sim \epsilon\tau_{90^\circ}$ , where  $\tau_{90^\circ} = 1/\nu$  is the time for the particle to scatter  $90^\circ$  in pitch angle. The effective collision rate to untrap is then  $\nu_{eff} \sim \nu/\epsilon$ . The only particles that complete banana orbits are those that do not untrap faster than they traverse the banana orbit. For a significant number of particles on the flux surface to be in the ‘banana’ regime, the normalized collision rate must be small,  $\nu^* = \frac{\nu_{eff}}{\omega_b} \sim \frac{R_0\nu}{tv_T\epsilon^{3/2}} \ll 1$ . The trapped particle fraction,  $f_{t,QHS} = 1 - \frac{3}{4} \langle B^2 \rangle \int_0^{B_{max}^{-1}} d\lambda \frac{\lambda}{\langle (1-\lambda B)^{1/2} \rangle}$  [9], where  $\lambda$  is the pitch angle, and effective electron collisionality,  $\nu^*$ , for a 50 kW ECRH QHS plasma are shown in Figures 2.9 and 2.10. (The plasma profiles are in Figures 5.6 and 5.7) The QHS magnetic configuration has a trapped particle fraction around 30 – 50% , and the effective collisionality for this case is  $\nu^* \sim 0.1 \ll 1$  across most of the plasma column, so the electrons are well in to the banana, or  $1/\nu$  regime.

If there is a negative density gradient in the plasma, then there will be more particles that follow the shifted-in orbits than the shifted-out orbits. If there is a negative temperature gradient, the particles on the shifted-in orbits will be faster than those on the shifted-out orbits. In either

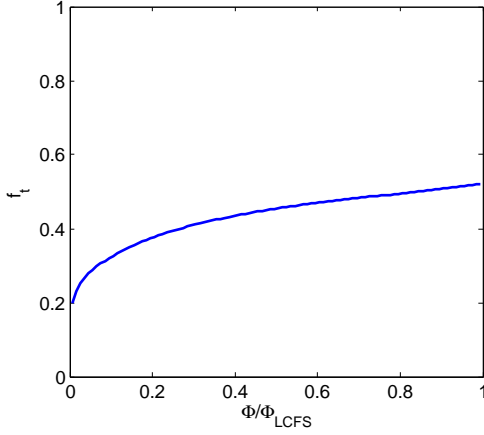


Figure 2.9 Trapped particle fraction for the QHS magnetic configuration.

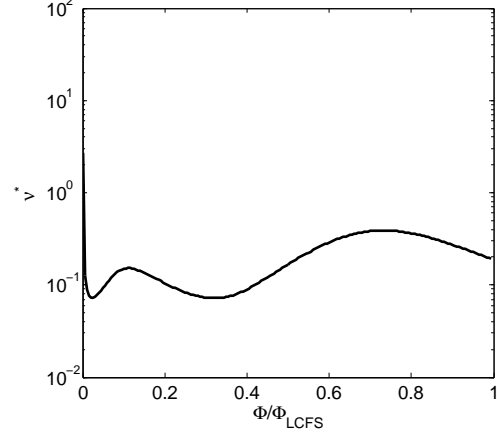


Figure 2.10 Effective collisionality,  $\nu^*$  for the electron population in QHS,  $50 \text{ kW ECRH}$ ,  $\rho_{ECRH} \lesssim 0.1$ .

case, there will be an imbalance in the effective number of charged particles passing the point P in the direction parallel to B, and a net current will be generated. The current generated by the trapped particles in a plasma with temperature  $T = \text{constant}$  and a density gradient is [8]

$$J_t = -\frac{\sqrt{\epsilon}}{t} \frac{T}{B_0} \frac{dn}{dr} \quad (2.16)$$

The difference in the orbits of the passing particles also results in a parallel current. In this case,

$$J_p = -\frac{1}{t} \frac{T}{B_0} \frac{dn}{dr} \quad (2.17)$$

This current is larger than that from the trapped particles by  $1/\sqrt{\epsilon}$ .

Consider the rate of momentum transfer from the passing particles to the trapped particles and from the trapped particles to the passing particles. In each case, the quantity is (density)  $\times$  (mass)  $\times$  (velocity)  $\times$  (collision rate).  $\langle v_{\parallel,p} \rangle = u_p = J_p/(qn_p)$  and  $\langle v_{\parallel,t} \rangle = u_t = J_t/(qn_t)$  are the fluid flow velocities for the passing and trapped particles, respectively, in terms of the current, electronic charge,  $q$ , and density associated with the different populations. In the large-aspect tokamak limit, the trapped particle fraction,  $f_t \sim \sqrt{2\epsilon}$  is small, because  $\epsilon \ll 1$ . The density of the passing particles is  $n_p \approx n$  and the density of the trapped particles is  $n_t \approx \sqrt{2\epsilon}n$ . The collision rate is  $\nu$  for the passing particles and  $\nu/\epsilon$  and for the trapped particles. The momentum transfer

rates from the passing to trapped particles,  $\delta P_{p \rightarrow t}$  and for trapped to passing particles,  $\delta P_{t \rightarrow p}$  are

$$\delta P_{p \rightarrow t} \sim m u_p n_p \nu = m \frac{J_p}{q} \nu = -\frac{mT}{qtB_0} \nu \frac{dn}{dr} \quad (2.18)$$

$$\delta P_{t \rightarrow p} \sim m \frac{J_t \nu}{q \epsilon} = -\frac{mT}{qtB_0} \frac{\nu}{\sqrt{\epsilon}} \frac{dn}{dr} \quad (2.19)$$

The momentum transfer from the trapped particles to the passing particles is larger by a factor of  $\sim 1/\sqrt{\epsilon}$ . In steady state, this momentum transfer manifests itself as a steady fluid flow in the passing particles,  $u_B$ . The momentum transfer rate from the passing particles to the trapped particles is

$$\delta P_{p \rightarrow t} \sim m(u_p + u_b)n\nu = m \left( \frac{J_p}{q} + u_b n \right) \nu \quad (2.20)$$

In steady state, the total rate of momentum transfer between the trapped and passing particles is zero,  $\delta P_{p \rightarrow t} = \delta P_{t \rightarrow p}$ , so

$$-\frac{mT}{qtB_0} \nu \frac{dn}{dr} + m u_B n \nu = -\frac{mT}{qtB_0} \frac{\nu}{\sqrt{\epsilon}} \frac{dn}{dr} \quad (2.21)$$

$$J_B \equiv q u_B n = \frac{T}{tB_0} \frac{dn}{dr} \left( 1 - \frac{1}{\sqrt{\epsilon}} \right) \approx -\frac{1}{\sqrt{\epsilon}} \frac{T}{tB_0} \frac{dn}{dr} \quad (2.22)$$

The bootstrap current,  $J_B$ , is caused by momentum transfer from the trapped particles to the passing particles, and results in a fluid flow in the passing particles. The bootstrap current is larger than that from orbit drifts by orders of magnitude:  $J_B \sim J_p/\sqrt{\epsilon} \sim J_t/\epsilon$ . The trapped particles are necessary to drive the bootstrap current, but the largest effect comes from the momentum balance between the trapped and circulating particles.

The preceding explanation for the source of the bootstrap current is appropriate for the large-aspect ratio tokamak, but the coefficients were only crude estimates. More exact expressions for the bootstrap current in a tokamak were derived for: the large-aspect tokamak limit, including the effects of the temperature and density gradients separately [8], finite toroidal field ripple, low collisionality regime [10], finite aspect-ratio limit, low collisionality regime [11], and temperature and density scalings of the bootstrap current for tokamaks were derived from computational studies [12].

### 2.3.2 Nonaxisymmetric Transport Analysis: Radial Electric Field, Flows, Viscosity and Momentum Conservation Between Plasma Species

For stellarators and heliotrons, estimates of the bootstrap current typically involve solving the drift kinetic equation (DKE) in some asymptotic limit. The moment method approach has been used to describe the neoclassical transport fluxes and parallel plasma flows for both axisymmetric [9] and non-axisymmetric toroidal plasmas. For example, the bootstrap current density for each of the following non-axisymmetric plasmas is available, in the limit of small fluid flow: the Pfirsch-Schlüter collisional regime [13], plateau [14], and banana regime [6] [13] [15] [16]. Connection formulas are sometimes used to smoothly connect the estimates of the several regimes [17]. Monte-Carlo calculations [18] of the bootstrap current for arbitrary collisional frequency and  $E_r$ , a variational numerical method [19], and very recently, one based on a method that conserves momentum between the species of which the plasma consists [20], are all used as benchmarks for the other estimates. Two extrema are of particular relevance in the HSX stellarator: the bootstrap current density while neglecting the effects of momentum conservation and  $E_r$  [21], and the case where  $E_r$  is self-consistently included in the transport calculations and the effect of momentum conservation between the plasma species is included [22].

If the effects of the radial electric field are ignored, and particles are assumed to be in the  $1/\nu$  regime, then for a toroidal device dominated by a single magnetic harmonic, such as a quasi-helical stellarator or axisymmetric tokamak, the bootstrap current for a magnetic configuration dominated by a single harmonic is [21]:

$$J_B = 1.46 \frac{g}{B_0} \frac{m \sqrt{b_{n,m}}}{n - mt} \left[ 1.67 (T_e + T_i) \frac{dn}{d\Phi} + 0.47n \frac{dT_e}{d\Phi} - 0.29n \frac{dT_i}{d\Phi} \right] \quad (2.23)$$

where the dominant harmonic is  $b_{n,m}$ . The  $g$  in this expression is the poloidal current outside of the flux surface, times the permeability of free space,  $\mu_0$ . Compare Eqn 2.23 for a traditional tokamak with dominant harmonic  $b_{0,1}$  to a quasi-helically symmetric system like HSX with  $b_{4,1}$ . The bootstrap current in HSX is reduced by a factor of  $n - mt \approx 3$  and the bootstrap current is in the opposite direction because the  $\nabla B$  and curvature drifts,  $\mathbf{b} \cdot \nabla \mathbf{b}$  are reversed, Figure 2.4.

The effects of the radial electric field and arbitrary collisionality are neglected in Eqn 2.23, and these both have significant consequences regarding the equilibrium neoclassical flows and currents in the plasma fluid [22] [23]. To address these effects, the drift kinetic equation, momentum conservation and radial electric field must be considered, self-consistently. The modifications to the transport coefficients are related to the monoenergetic transport coefficients solved for by DKES [22].

In a general 3-D toroidal configuration with non-symmetric field components, the particle and energy radial fluxes and in-surface flows are related in a complicated manner. In general, particle orbits and collisions will depend on temperatures, densities and their gradients. The Drift Kinetic Equation Solver (DKES) [19] uses a variational principle to find upper and lower bounds of the monoenergetic transport coefficients as a function of collisionality and radial electric field. A large database of coefficients have been generated to cover the regimes applicable to HSX plasmas, and the results have been extrapolated to the case of large  $E_r$  when necessary [24]. Neglecting conservation of momentum, and using the database of DKES transport coefficients, the parallel current for species ‘ $a$ ’ with electric charge  $q_a$  can be written as

$$J_{\parallel,a} = \frac{1}{B_0} \langle \mathbf{J}_a \cdot \mathbf{B} \rangle = q_a I_{3a} \quad (2.24)$$

where  $I_{3a}$  is the thermodynamic flow,

$$I_{3a} = -n_a \sum_{j=1}^3 L_{3j}^a A_{aj} \quad (2.25)$$

The thermodynamic forces are

$$A_{a1} = \frac{n'_a}{n_a} - \frac{3}{2} \frac{T'_a}{T_a} - \frac{q_a E_r}{T_a} \quad (2.26)$$

$$A_{a2} = \frac{T'_a}{T_a} \quad (2.27)$$

$$A_{a3} = -\frac{q_a}{T_a} \frac{\langle \mathbf{B} \cdot \mathbf{E} \rangle}{\langle B^2 \rangle} B_0 \quad (2.28)$$

The prime (') indicates a radial derivative.  $T_a$ ,  $n_a$ , and  $q_a$  are the temperature, density and electric charge of species ‘ $a$ ’.  $E_r$  is the radial electric field. The transport coefficients are found by

convolving the monoenergetic transport coefficients,  $D_{3j}^a$ , with appropriate energy moments:

$$L_{3j}^a = \frac{2}{\sqrt{\pi}} \int_0^\infty dK_a K_a^{1/2} e^{-K_a} h_j D_{3j}^a(K_a) \quad (2.29)$$

$$h_{1,3} = 1, \quad h_2 = K_a \quad (2.30)$$

$$K_a = \frac{m_a v^2}{2T_a} \quad (2.31)$$

The monoenergetic coefficients are calculated by DKES. They are defined such that  $D_{11}^a = D_{12}^a = D_{21}^a = D_{22}^a$ ,  $D_{13}^a = D_{23}^a$ ,  $D_{31}^a = D_{32}^a$ .  $D_{11}^a$  describes radial transport,  $D_{33}^a$  describes parallel transport,  $D_{13}^a$  is related to the Ware pinch, and  $D_{31}^a$  is related to the bootstrap current. By Onsager symmetry,  $D_{13}^a = -D_{31}^a$  [25].

The expression of the neoclassical bootstrap current in Eqn 2.24 neglects momentum conservation between different plasma species. This is acceptable if the plasma fluid flows are small, such as in the case of conventional stellarators. This is not the case for quasi-symmetric stellarators or tokamaks, which are expected to have a high level of flow because of a direction of symmetry in  $|B|$ . This flow has been measured in the quasi-helically symmetric stellarator, HSX [26] [27], and the measured ion flow exceeds that indicated by the model that neglects momentum conservation (MC) effects, Figure 2.11.

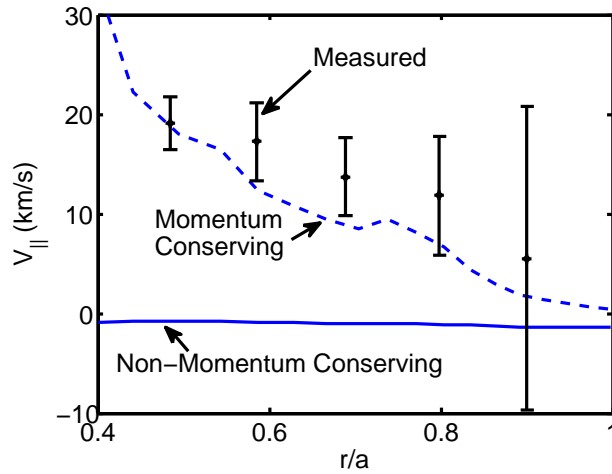


Figure 2.11 Measured parallel (to **B**) ion flow and calculated values that included and neglect momentum conservation. Figure courtesy A. Briesemeister [27].

A model that includes these effects has a few additional terms [22]. The parallel flows with MC are found by solving the following system of equations [24]:

$$\begin{aligned}
& m_a \sum_{k=0}^{j_{max}} \frac{\langle Bu_{\parallel ak} \rangle}{\langle B^2 \rangle} \left\| \nu_D^a F_a \left( \frac{v^2 \langle B^2 \rangle}{3\nu_D^a} - D_{33}^a B_0^2 \right) L_k^{3/2} \right\|_j \\
& + B_0 \| F_a D_{31}^a \|_j T_a A_{a1} + B_0 \| F_a D_{31}^a K_a \|_j T_a A_{a2} \\
& = \sum_b \sum_{k=0}^{j_{max}} \left[ l_{j+1,k+1}^{ab} \langle Bu_{\parallel bk} \rangle + \delta_{j0} n_a T_a \frac{\langle B^2 \rangle}{B_0} A_{a3} \right]
\end{aligned} \tag{2.32}$$

Here,  $L_j^{3/2}$  are the Sonine polynomials,  $\nu_D^a$  is the energy dependent perpendicular scattering frequency [19],  $l_{j+1,k+1}^{ab}$  are the classical friction coefficients [9], and

$$F_a(K_a) = \frac{2K_a \langle B^2 \rangle}{3B_0^2 D_{33}^a} \tag{2.33}$$

The  $\|A\|$  operator is a Sonine-weighted energy convolution over a Maxwellian distribution, defined as

$$\|A(K_a)\|_j \equiv n_a \frac{2}{\sqrt{\pi}} \int_0^\infty dK_a \sqrt{K_a} e^{-K_a} L_j^{3/2}(K_a) A(K_a) \tag{2.34}$$

The sum over  $k$  is truncated at some  $j_{max}$ , representing the truncation of the Sonine-expansion of the energy dependence of the velocity moment of the first order distribution function,  $f_{a1}^{l=1}$  [24]. In Eqn 2.32, the left side of the equation is the neoclassical parallel viscosity and the right side of the equation is the parallel friction and parallel electric field forces. The parallel flow of each species is found as a function of the radial electric field.

The radial particle and energy fluxes are a sum of contributions from the banana-plateau, non-axisymmetric, and Pfirsch-Schlüter fluxes. The sum of the first two contributions, banana-plateau and non-axisymmetric, is denoted as  $\Gamma_a^{bn}$  and  $Q_a^{bn}$ , respectively, for the particles and energy, while



the Pfirsch-Schlüter contribution is likewise denoted as  $\Gamma_a^{PS}$  and  $Q_a^{PS}$ . The fluxes are given by

$$\begin{bmatrix} \Gamma_a^{bn} \\ Q_a^{bn}/T_a \end{bmatrix} = B_0 \sum_{k=0}^{jmax} \begin{bmatrix} \|F_a D_{13}^a\|_k \\ \|F_a D_{13}^a K_a\|_k \end{bmatrix} \frac{\langle B u_{||,ak} \rangle}{\langle B^2 \rangle} - \begin{bmatrix} \|L_a\|_0 \\ \|L_a K_a\|_0 \end{bmatrix} A_{a1} - \begin{bmatrix} \|L_a K_a\|_0 \\ \|L_a K_a^2\|_0 \end{bmatrix} A_{a2} \quad (2.35)$$

$$\begin{bmatrix} \Gamma_a^{PS} \\ Q_a^{PS}/T_a \end{bmatrix} = \langle \tilde{U}^2 \rangle \sum_b \frac{T_b}{q_a q_b} \begin{bmatrix} l_{11}^{ab} & -l_{12}^{ab} \\ -l_{21}^{ab} & l_{22}^{ab} \end{bmatrix} \begin{bmatrix} (A_{b1} + \frac{5}{2} A_{b2}) \\ A_{b2} \end{bmatrix} \quad (2.36)$$

$L_a$  is the monoenergetic particle diffusion coefficient:

$$L_a = D_{11}^a - \frac{2m_a T_a K_a \nu_D^a}{3q_a^2} \langle \tilde{U}^2 \rangle + \frac{3B_0^2}{2\langle B^2 \rangle} \frac{(D_{13}^a)^2}{K_a} F_a \quad (2.37)$$

The factor  $\tilde{U}$  is related to the Pfirsch-Schlüter term,  $h$  in Eqn 2.7

$$\mathbf{B} \cdot \nabla \left( \frac{\tilde{U}}{B} \right) = \mathbf{B} \times \nabla r \cdot \nabla \frac{1}{B^2} \quad (2.38)$$

$$\langle B \tilde{U} \rangle = 0 \quad (2.39)$$

The fluxes are now calculated as a function of radial electric field. Ambipolarity is enforced to determine a unique set of solutions for the radial electric field ( $E_r$ ), fluxes ( $\Gamma$ ), and flows ( $u_{||}$ )

$$\Gamma_e^{bn} + \Gamma_e^{PS} = \sum_{b=ions} Z_b (\Gamma_b^{bn} + \Gamma_b^{PS}) \quad (2.40)$$

The parallel current density for each species is  $J_{||,a} = q_a n_a \langle b u_{||,a0} \rangle$  where  $b = B/B_0$  and the total parallel current is

$$J_{||} = \sum J_{||,a} \quad (2.41)$$

The bootstrap current is found by setting the parallel electric field force to 0:

$$J_{bootstrap} = J_{||} \Big|_{A_{a3}=0} \quad (2.42)$$

and the inductively driven current is found by setting the gradient forces to 0:

$$J_{inductive} = J_{||} \Big|_{A_{a1}=A_{a2}=0} \quad (2.43)$$

The parallel conductivity of the plasma, which accounts for the effects of trapped particles, can be solved for numerically by using

$$\sigma_{\parallel} = \frac{J_{inductive} \big|_{A_{a1}=A_{a2}=0, E_{\parallel}=E_{ind} \neq 0}}{E_{ind}} \quad (2.44)$$

For a two species plasma, this parallel conductivity reduces to the analytic results [16]

$$\sigma_{\parallel} = \frac{(n_e e)^2 l_{22}^{eb}}{l_{11}^{eb} l_{22}^{eb} - (l_{12}^{eb})^2} \quad (2.45)$$

In a stellarator, the flows and radial electric field are not independent. The radial fluxes are a function of the magnetic configuration, plasma temperature, density and their radial gradients. The radial electric field is determined by the ambipolarity constraint, and influences the fluid flows. The fluid flows, in turn, affect the radial fluxes. The PENTA code [23] calculates the neoclassical fluxes, flows, and  $E_r$  as outlined above, self-consistently. PENTA was adapted and extended for use at HSX [24], to predict the radial electric field and steady state fluid flows. The time required to perform a PENTA run for a plasma profile depends on the order of the Sonine polynomials to include in the expansion of the flow and flux equations, Eqns 2.32 and 2.36, ranging from 5 minutes for 35 surfaces and 2 Sonine polynomials, to 20 minutes for 35 surfaces and 6 Sonine polynomials, on a 2.13 GHz 64 bit Intel Core 2 Duo with 2 GB ram and running the GNU/Linux operating system. PENTA can be also be run in ‘DKES’ mode, where momentum conservation is not included in the solution.

The bootstrap current density is related to the monoenergetic transport coefficient,  $D_{31}^a$ . This coefficient is a complicated function of collisionality and  $E_r$ . The normalized transport coefficient,  $D_{31}^*$  is defined as

$$D_{31}^* = \frac{D_{31}^a}{m_a v^2 / 2 q_a^2 B_0} \quad (2.46)$$

Figures 2.12 and 2.13 show contour plots of  $D_{31}^*$  versus the normalized collisionality and normalized  $E_r$  for a surface near the mid-radius,  $\rho \simeq 0.5$ . For low-collisionality and small  $E_r$  (the lower left corner of each figure), the coefficient is nearly constant. In the high collisionality regime (the upper part of each figure) the coefficient approaches 0. The dependence on  $E_r$  is more complicated,

and can increase or decrease depending on the collisionality. The differences between the QHS and Mirror configuration are small in the high-collisionality regime, but are more pronounced in the low collisionality regime. Here, the coefficient is about 2-3 times larger in QHS than in Mirror for most  $E_r$  values, suggesting that higher parallel flows may be achieved in QHS than in Mirror for a similar set of conditions, if the effects of  $E_r$  and MC are not too large.

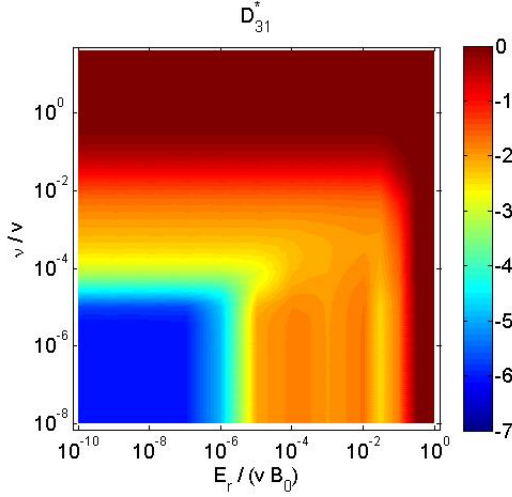


Figure 2.12 Normalized monoenergetic coefficient,  $D_{31}^*$  in the QHS configuration for  $\rho \simeq 0.5$ .

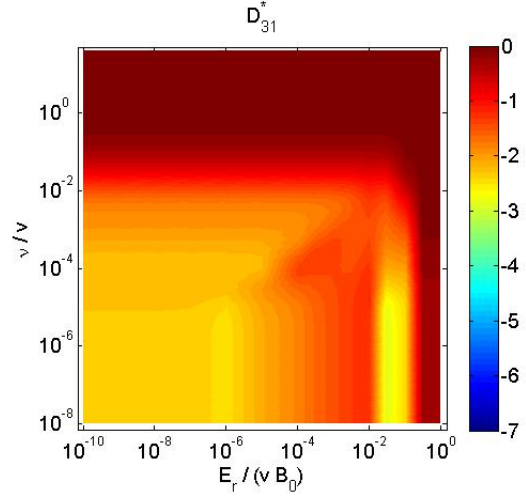


Figure 2.13 Normalized monoenergetic coefficient,  $D_{31}^*$  in the Mirror configuration for  $\rho \simeq 0.5$ .

## 2.4 Parallel currents with and without momentum conservation

To illustrate the effects of momentum conservation on the parallel currents, consider a simple two-species hydrogen-electron plasma with

$$n_e = n_i = 0.1 + 4.9(1 - \rho) \cdot 10^{18} \text{ m}^{-3} \quad (2.47)$$

$$T_e = 45 + 1050 \frac{1}{N_0} \left( \left( 1 + \left( \frac{\rho}{0.27} \right)^2 \right)^{-1} - c_0 \right) \text{ eV} \quad (2.48)$$

$$c_0 = (1 + 0.27^{-2})^{-1} \quad N_0 = 1 - c_0$$

$$T_i = 44 + 17(1 - \rho^2) \text{ eV} \quad (2.49)$$

The radial profiles, with  $\rho = \sqrt{\Phi/\Phi_{LCFS}}$  are shown in Figures 2.14 and 2.15. These profiles are similar to those achieved in the HSX stellarator in the QHS configuration with 50 kW ECRH,  $\rho_{ECRH} \lesssim 0.1$  and in the 11% Mirror configuration with 100kW ECRH,  $\rho_{ECRH} \lesssim 0.1$ .

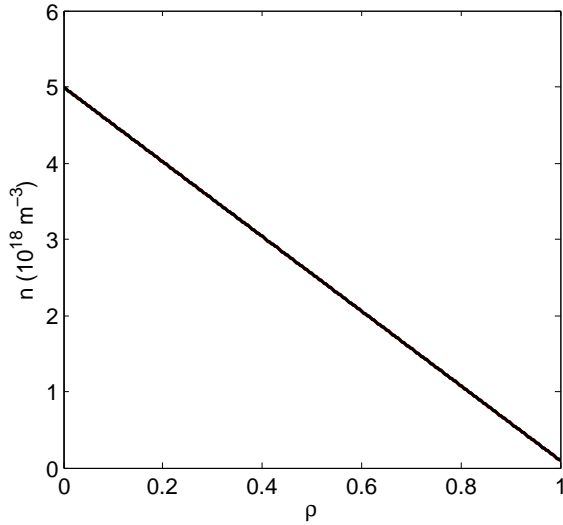


Figure 2.14 Example density profile.

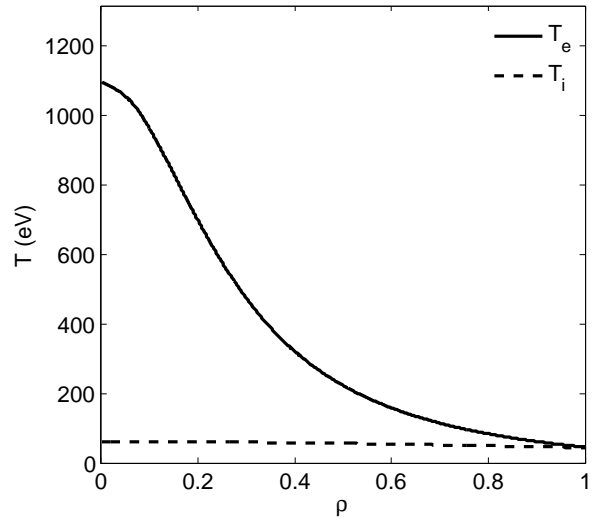


Figure 2.15 Example temperature profile.

The results of the PENTA calculation both including and neglecting the effects of momentum conservation are shown in Figures 2.16 - 2.19. The magnetic configuration for this set of calculations is the QHS configuration. The radial electric field solution varies with the radius, Figure 2.16, but has similar characteristics with or without momentum conservation. The neoclassical parallel current density (discussed below) is shown in Figure 2.17. The ion flows, Figure 2.18, are close to zero when momentum conservation is neglected and do not change significantly in the presence of the electron root. When momentum conservation is included in the modeling, the ion flows are non-zero. Near the core of the plasma, the flows are large when the  $E_r$  is in the ion-root solution and the flows are strongly reduced when  $E_r$  is in the electron-root. The electron flows constitute the majority of the parallel current when momentum conservation is neglected, Figure 2.19. Without momentum conservation, the flows are not very different when  $E_r$  is in either the ion- or electron- root. When momentum conservation is included, the electron contribution to the parallel current is similar to the ion contribution across the outer half of the plasma. The electron

flow near the core is a strong function of  $E_r$ . The flow is reversed and increased in magnitude when  $E_r$  is in the electron root.

The ion and electron fluxes for the cases with and without MC in QHS at  $\rho = 0.2$  are shown in Figure 2.20. The electron fluxes do not change much when MC is included. The ion flux experiences a helical particle resonance [28] near  $|E_r| \sim 65 \text{ V/cm}$ , where the  $E \times B$  drift causes the ions to experience an uncompensated radial drift, and hence, an increased radial flux [29]. When MC is included, the ion flux is altered slightly and the ambipolar root is different from the case without MC. The electron flow, ion flow and net current for  $\rho = 0.2$  are shown in Figure 2.21 as a function of  $E_r$ . Without MC, the ion flow is small for all  $E_r$ , and the electron flow is nearly linear with respect to  $E_r$ . When MC is included, the effects of the poloidal resonance alter the flow vs.  $E_r$  profile. For small  $E_r$ , the particle resonance effects described above alter both flows, although the net effect on the current is small. For large  $E_r$  (close to the electron root solution) the effect of MC between the species is a small increase in the magnitude of the ion flow and a larger increase in the electron flow. The net effect is a reversal of the total current.

With momentum conservation, the neoclassical parallel current density, Figure 2.17, is increased in the region where  $E_r$  is in the ion root, compared to the case without momentum conservation. The effect of momentum conservation is much more pronounced in the region where  $E_r$  is in the electric root. Without momentum conservation, the current density is slightly increased, but when momentum conservation is included, the current density reverses direction, due to a combination of ion flows being reduced and electron flows being reversed and increased in magnitude.

The results of the PENTA calculations with the 10% Mirror configuration, using density and temperature profiles shown in Figures 2.14 and 2.15, are shown in Figures 2.22 - 2.25. Again, the ambipolar  $E_r$  solutions, Figure 2.22, are similar with or without including momentum conservation. When momentum conservation is neglected, the ion flows are small, the majority of the current is carried by the electron flow, and the flows are not strongly affected by the different  $E_r$  roots. When momentum conservation is included, and  $E_r$  is in the ion root, the ion flows and electron flows are similar in magnitude. When  $E_r$  is in the electron root, the ion flows are reduced and the electron flows are increased in magnitude, leading to a reversal of the current density.

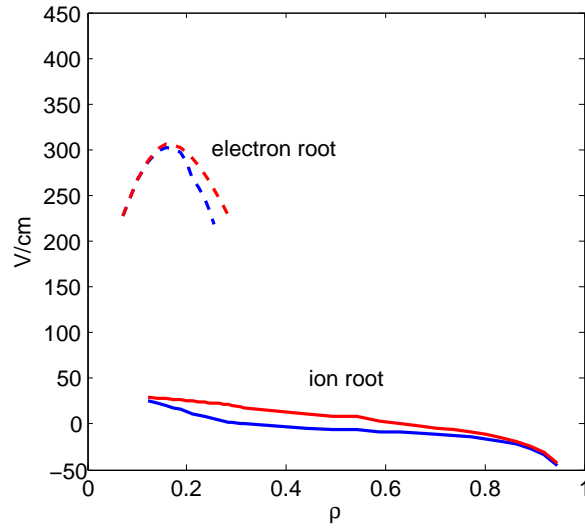


Figure 2.16 The radial electric field in QHS with (red) and without (blue) momentum conservation (MC). The ion root solution exists throughout across much of the plasma radius, while the electron root exists primarily near the core.

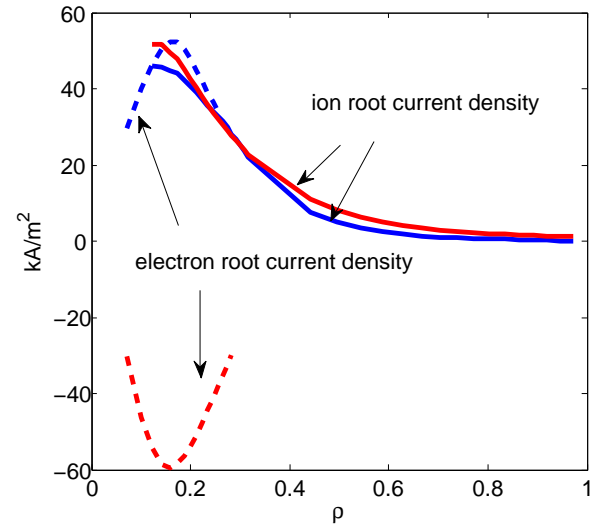


Figure 2.17 The parallel current density in QHS with (red) and without (blue) MC. With MC, the current density reverses in the electron root. Without MC, the current density shows little change.

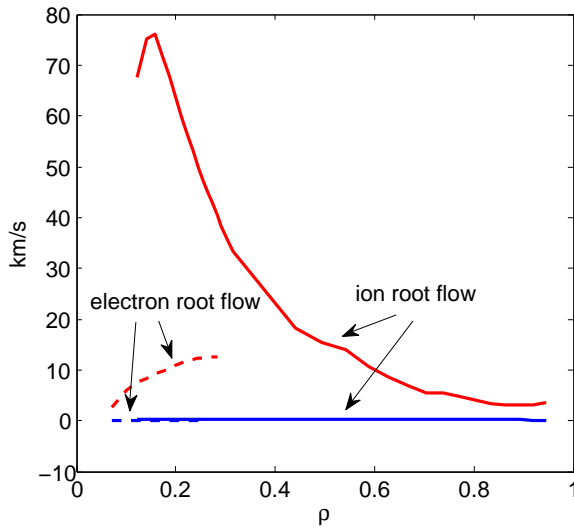


Figure 2.18 The parallel ion flow in QHS with (red) and without (blue) (MC). Without MC, the ion flow is near zero. With MC, the ion flow is non-zero and is reduced in the electron-root solution.

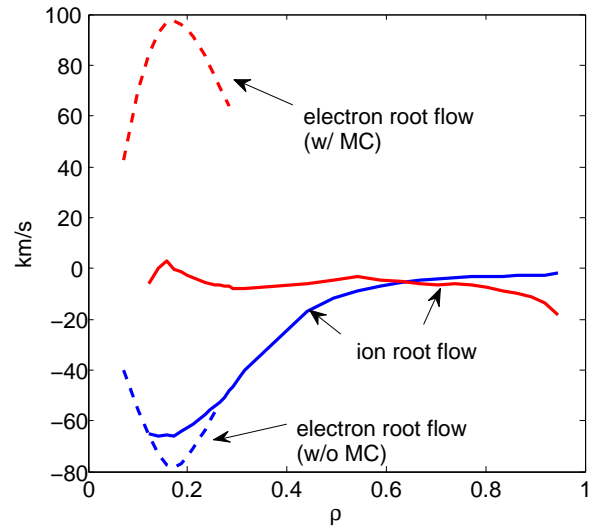


Figure 2.19 The parallel electron flow in QHS with (red) and without (blue) (MC). Without MC, the electron flow is the dominant component of the parallel current. With MC, the flow reverses in the electron root.

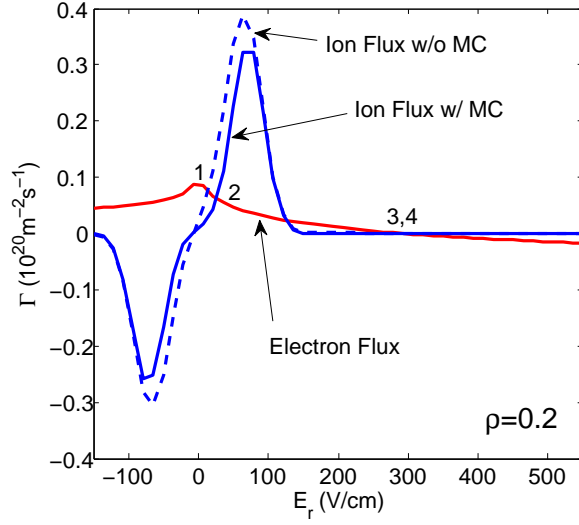


Figure 2.20 Ion and electron fluxes vs.  $E_r$  for QHS at  $\rho = 0.2$ . Ambipolar roots,  $\Gamma_i = \Gamma_e$ , are indicated as (1) ion root w/o MC, (2) ion root w/ MC, (3) electron root w/o MC, and (4) electron root w/ MC. (3) and (4) lie nearly on top of each other.

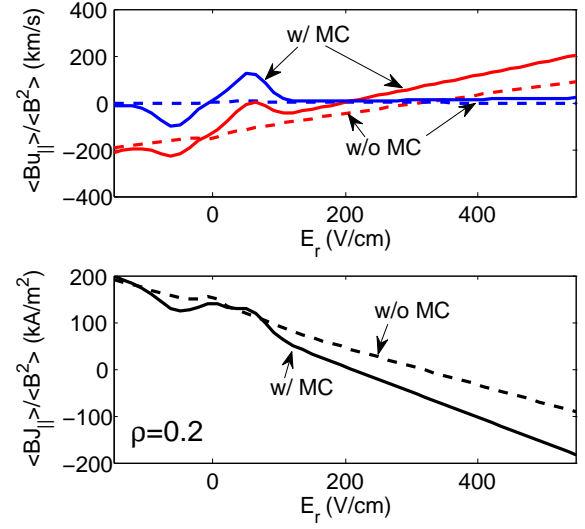


Figure 2.21 For QHS at  $\rho = 0.2$ : TOP: Parallel flow vs.  $E_r$  for ions (blue) and electrons (red) with and w/o MC. BOTTOM: Parallel bootstrap current with and w/o MC.

For  $\rho \gtrsim 0.5$ , the total current density is similar with or without momentum conservation, but for  $\rho \lesssim 0.5$ , the current density is reduced or reversed when momentum conservation is included.

The differences between the current density in the QHS and Mirror configurations are small when momentum conservation is neglected. The current density is reduced by about 30% for  $\rho \lesssim 0.2$ . When momentum conservation is included in the modeling, the currents are reduced for  $\rho \lesssim 0.4$ , where the ion flows and  $E_r$  effects play an important role.

The integrated current profiles for the cases shown in Figures 2.17 and 2.23 are shown in Figures 2.26 and 2.27, respectively. The profile of the ambipolar  $E_r$  is important, since it has a strong effect on the net current that is expected to be measured. Three limiting conditions are plotted. When the electron-root is the solution wherever it is a stable root, called the e-root dominant case, the integrated current profile is not monotonic and may switch signs at some radial location. A non-smoothing curve connects the current density,  $J_b$ , at the end of the electron-root, near  $\rho \sim 0.3$ , to the ion-root solution. If only a small portion of the electron-root is the stable solution, such as when the ion-root solution does not exist near the axis, then the ion-root solution accounts for most

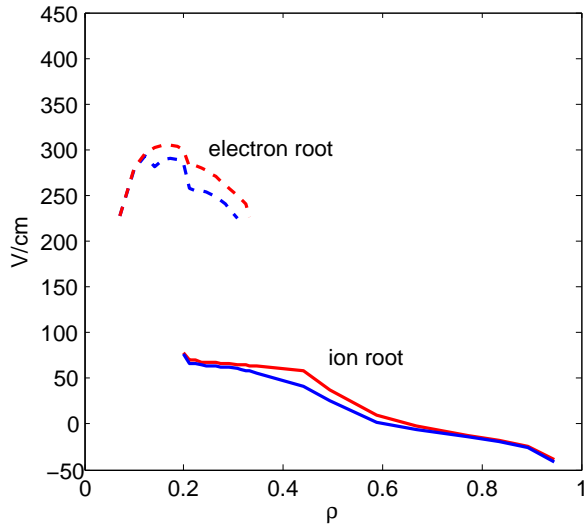


Figure 2.22 The radial electric field in Mirror with (red) and without (blue) momentum conservation (MC). The ion root solution exists throughout across much of the plasma radius, while the electron root exists primarily near the core.

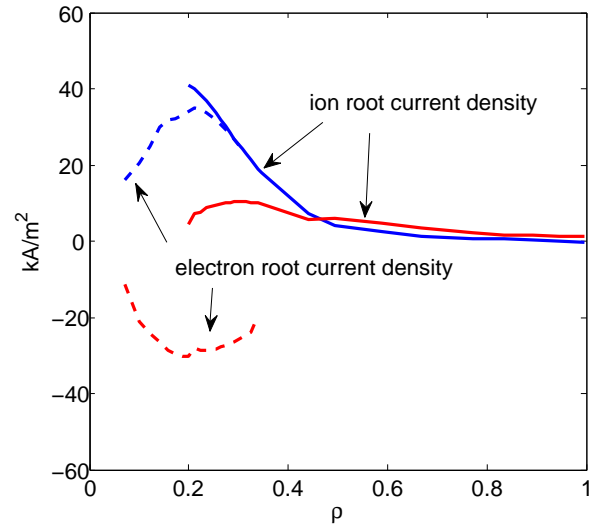


Figure 2.23 The parallel current density in Mirror with (red) and without (blue) MC. With MC, the current density reverses in the electron root. Without MC, the current density shows little change.

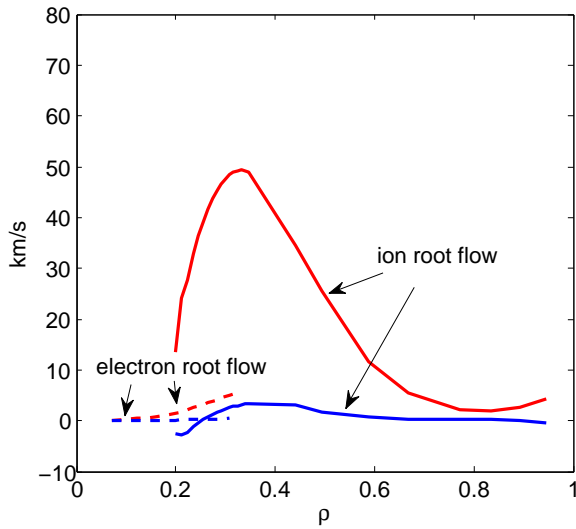


Figure 2.24 The parallel ion flow in Mirror with (red) and without (blue) MC. Without MC, the ion flow is near zero. With MC, the ion flow is non-zero and is reduced in the electron-root solution.

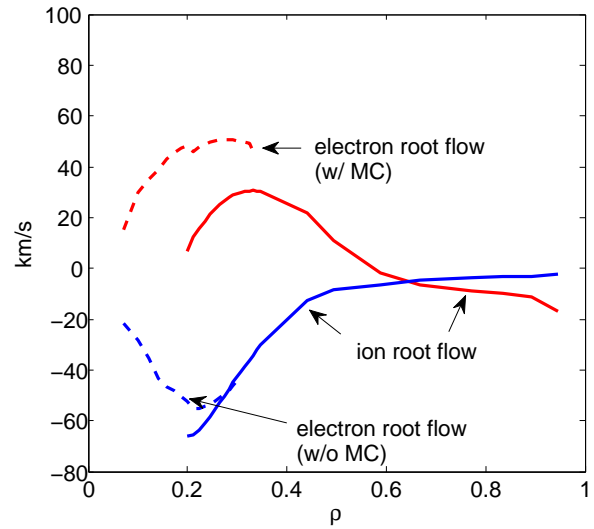


Figure 2.25 The parallel electron flow in Mirror with (red) and without (blue) MC. Without MC, the electron flow is the dominant component of the parallel current. With MC, the flow reverses in the electron root.



of the total current. If the ion-root is the solution wherever it is a stable root, the profile is called the i-root dominant case. An additional hypothetical case is shown, called the “ion-root only” solution. Here, in an attempt to mimic the existence of an ion-root solution, the current density is interpolated between 0 on the axis to whatever value is the closest radial ion-root solution.

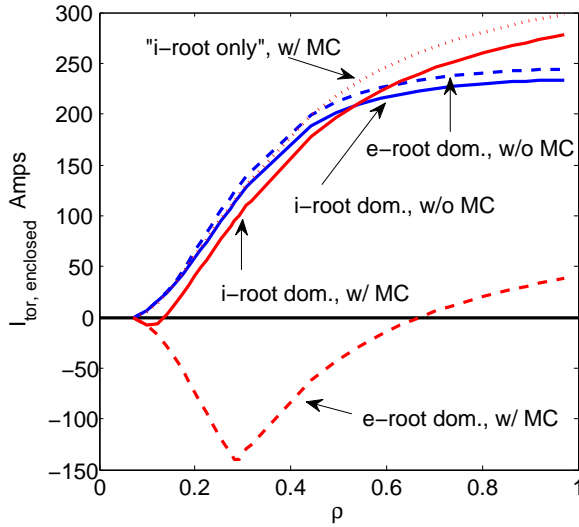


Figure 2.26 The enclosed parallel current profile for QHS. (The current density is shown in Figure 2.17.)

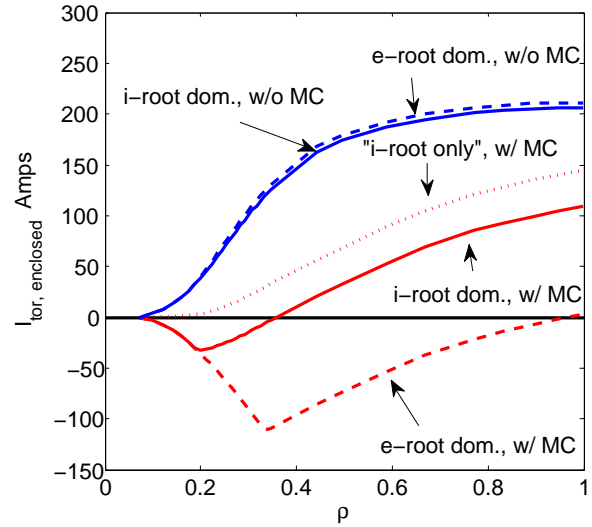


Figure 2.27 The enclosed parallel current profile for Mirror. (The current density is shown in Figure 2.23.)

The underlying reasons for the complicated dependency of the parallel currents on the radial electric field and magnetic spectrum are not well understood, as suggested by the results of benchmarking studies for several devices, including LHD, NCSX, HSX, and W7-X [30]. In those benchmarking studies for the HSX devices, for particles at low-collisionality and  $E_r = 0$ , even modest symmetry-breaking terms can dramatically affect the monoenergetic transport coefficient related to the bootstrap current,  $D_{31}^*$ , but even a small  $E_r$  can suppress the effects of the symmetry breaking.

## 2.5 Summary

This chapter has shown that with quasi-helical symmetry, the Pfirsch-Schlüter current profile rotates helically with the toroidal angle. The bootstrap current is in the opposite direction than

that of a tokamak, reducing the rotational transform. Also, each of these currents is reduced by a factor of  $\sim 1/3$  compared to an equivalent tokamak, and modifications to the net bootstrap current from  $E_r$  and MC effects are possible. The expected time evolution of the toroidal current profile in HSX is long compared to the experimental time, so a model of the time evolution of the toroidal current is required for meaningful comparisons to measured values. Trapped particle effects are included in the calculation of the parallel conductivity. The next step is to use one of the enclosed current profiles as a most-likely candidate for the plasma at hand. The choice is suggested by the extrapolated steady state current from the Rogowski coil. Usually, the profile that agrees best with the extrapolated steady state current is chosen. The candidate profile will be used in a time-evolution code that calculates the diffusion of the toroidal current across the plasma column, which is discussed in Chapter 3. The results of the simulation will provide the initial guess for the V3FIT reconstruction of the plasma pressure and current profiles, which is described in Chapter 4.

## References

- [1] J. P. Freidberg, Rev. Mod. Phys. **54**, 801 (1982).
- [2] V. V. Nemov, Nuclear Fusion **32**, 597 (1992).
- [3] A. H. Boozer, Phys. Fluids **24**, 1999 (1981).
- [4] A. H. Boozer, Phys. Fluids **25**, 520 (1982).
- [5] D. T. Anderson, et al., HSX: A Helically Symmetric Toroidal Experiment, Dept. of Energy Proposal (1992).
- [6] V. V. Nemov, et al., Physics of Plasmas **6**, 4822 (1999).
- [7] J. N. Talmadge and S. P. Gerhardt, Phys. Plasmas **12**, 072513 (2005).
- [8] Jeffrey Freidberg, “Plasma Physics and Fusion Energy”, Cambridge University Press, New York (2007).
- [9] S. P. Hirshman and D. J. Sigmar, Nuclear Fusion **21**, 1079 (1981).
- [10] Y. Nakamura, Plasma and Fusion Research:Rapid Comm **1**, 010 (2006).
- [11] S. P. Hirshman, Phys. Fluids **31**, 3150 (1988).
- [12] H. R. Wilson, Nuclear Fusion **22**, 257 (1992).
- [13] K. C. Shaing and J. D. Callen, Phys. Fluids **26**, 3315 (1983).
- [14] K. C. Shaing and J. D. Callen, Phys. Fluids **29**, 521 (1986).
- [15] K. C. Shaing, S. P. Hirshman, and J. S. Tolliver, Phys. Fluids **29**, 2548 (1986).
- [16] K. C. Shaing, et al., Phys. Fluids B **1**, 148 (1989).
- [17] Watanabe, et al., Nuclear Fusion **35**, 335 (1995).
- [18] A. H. Boozer and G. Kuo-Petravic, Phys. Fluids **24**, 851 (1981).

- [19] W. I. van Rij and S. P. Hirshman, *Phys. Fluids B* **1**, 563 (1989).
- [20] A. Masuyama, et al., *Physics of Plasmas* **16**, 052501 (2009).
- [21] Boozer and Gardner, *Phys. Fluids B* **2**, 2408 (1990).
- [22] H. Sugama and S. Nishimura, *Physics of Plasmas* **9**, 4637 (2002).
- [23] D. A. Spong, *Physics of Plasmas* **12**, 056115 (2005).
- [24] J. Lore, Ph. D. dissertation, University of Wisconsin-Madison (2010).
- [25] S. P. Hirshman, et al., *Phys. Fluids B* **29**, 2951 (1986).
- [26] S. G. Gerhardt, Ph. D. dissertation, University of Wisconsin-Madison (2004).
- [27] A. Briesemeister, et al., “Measured and neoclassically predicted intrinsic plasma flows and radial electric field in the HSX Stellarator”, Transport Task Force (TTF), San Diego, CA, (2011).
- [28] K. C. Shaing, *Physics of Fluids B* **5**, 3841 (1993).
- [29] A. Briesemeister, PhD Preliminary Report, University of Wisconsin, Madison, WI (2011).
- [30] C. D. Beidler, et al., *Nuclear Fusion* **51**, 076001 (2011).

## Chapter 3

### Temporal Modeling of Parallel Current

The evolution of the toroidal current in the HSX stellarator is described by the case of resistive relaxation of an induced electric field driven by the onset of non-inductive bootstrap current during the rapid pressure rise associated with the application of ECRH. The microwave heating source is turned on, the neutral gas ionizes and the plasma quickly reaches a quasi-equilibrium within a few *ms* with a relatively constant stored diamagnetic energy and line-averaged central density. The net toroidal current continues to rise throughout the shot, evolving on a timescale of 10's of ms, while the density and temperature profiles remain constant after the initial breakdown. Also known as the 'rapid heating scenario' [1], when the plasma pressure increases, the plasma current response is damped because of the finite conductivity of the plasma column. This is in contrast to a ohmic current drive, in which a loop voltage is enforced at the plasma edge, (i.e. using the plasma column itself as a winding in a transformer). The electric field at the edge diffuses into the plasma column and because the plasma has finite resistance, the current response is damped. In Section 3.1, the temporal evolution of the net toroidal current in a cylindrical geometry is presented. Section 3.2 extends this model to general nonaxisymmetric toroidal configurations.

#### 3.1 Plasma Current Evolution in a Cylindrical Geometry

In a toroidal confinement fusion experiment, the electron and ion flows on a flux surface,  $\mathbf{U}_e$  and  $\mathbf{U}_i$ , generate electric currents proportional to their densities,  $N_e$  and  $N_i$ , and, in the case of ions, the charge state,  $Z_i$ . This current distribution consists of both inductive and non-inductive

sources,  $\mathbf{J}_{ind}$  and  $\mathbf{J}_{n.i.}$ ,

$$\mathbf{J} = \mathbf{J}_{ind} + \mathbf{J}_{n.i.} = q_e N_e \mathbf{U}_e + q_i \sum_i N_i Z_i \mathbf{U}_i \quad (3.1)$$

The charges of the electron and proton are given by  $-q_e = q_i = 1.602 \cdot 10^{-19} \text{ C}$ . An example of an inductive source would be the ohmic current drive common to most tokamaks (not present on HSX) and examples of non-inductive sources include bootstrap current and electron-cyclotron current drive (ECCD). The current distribution generates a magnetic flux,  $\mathbf{B}$ , according to Ampere's law (neglecting displacement current)

$$\mu_0 \mathbf{J} = \nabla \times \mathbf{B} \quad (3.2)$$

When the current distribution changes (such as during rapid plasma heating or current-drive modulation), the magnetic flux also changes and an electric field,  $\mathbf{E}_{ind}$ , is induced (Faraday's law)

$$-\frac{\partial \mathbf{B}}{\partial t} = \nabla \times \mathbf{E}_{ind} \quad (3.3)$$

Due to the finite conductivity of the plasma,  $\sigma$ , a current is produced according to Ohm's law,

$$\mathbf{J}_{ind} = \sigma \mathbf{E}_{ind} \quad (3.4)$$

These three equations, along with appropriate initial and boundary conditions, must be solved self-consistently to describe the spatial and time evolution of the plasma current density as it diffuses throughout the column.

Consider a cylindrical geometry as shown in Figure 3.1. The current density directed in the z-direction has no azimuthal ( $\theta$ -) or height (z-) dependence and can be written as [2]

$$\mathbf{J}(r, t) = \hat{z} J_{cyl}(r, t) \quad (3.5)$$

$$J_{cyl}(r, t) = J_{cyl,n.i.}(r) + \sigma(r) E(r, t) \quad (3.6)$$

In Eqn 3.6, the variables  $J_{cyl,n.i.}(r)$ ,  $\sigma(r)$ , and  $E(r, t) = E_{cyl,ind}(r, t)$  are the non-inductive current density (bootstrap, ECCD, etc.), electrical conductivity and electric field, respectively. If changes in  $E(r, t)$  do not drastically change  $J_{cyl,n.i.}(r)$  over time, then by taking the time-derivative

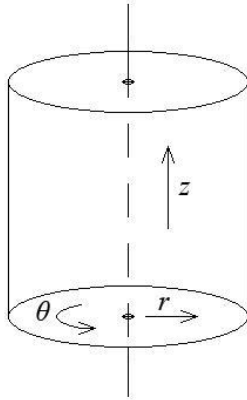


Figure 3.1 Cylindrical coordinate system.

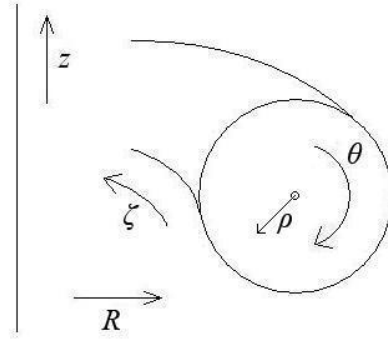


Figure 3.2 Toroidal coordinate system.

of Eqn 3.5 and substituting Eqn 3.2 for  $\mathbf{J}$  and Eqn 3.3 for  $\mathbf{B}$ , a 1-D radial diffusion equation for the electric field along the plasma column is [2]

$$\mu\sigma \frac{\partial E}{\partial t} = \frac{1}{r} \frac{\partial}{\partial r} \left( r \frac{\partial E}{\partial r} \right) \quad (3.7)$$

The magnetic permeability is given by  $\mu \approx \mu_0$ . The electric field diffuses radially across plasma with a characteristic time constant of  $(a_{cyl}^2 \sigma \mu_0)$ , where  $a_{cyl}$  is the radius of the plasma column.

If one provides the initial total and non-inductive current distributions along with the boundary conditions (constant current, constant loop voltage, or free relaxation), then the solution of the electric field,  $E(r, t)$  for the diffusion equation is readily computed numerically or analytically as the sum of Bessel or Bessel-like functions [2]. The radial profile of the current density can be determined as a function of time by Eqn 3.6. In this model, the azimuthal magnetic field is modified by the evolving current profile, but changes in the magnetic field along the z-direction do not occur.

The above model can be applied to axisymmetric tokamak configurations in the high aspect ratio limit by substituting the cylindrical coordinates with appropriate toroidal coordinates, Figure 3.2. Specifically, this is accomplished by equating the z-direction to the toroidal  $\phi$ -direction, the azimuthal  $\theta$ -direction to the poloidal  $\theta$ -direction, and the radial r-direction to the (minor) radial  $\rho$ -direction. In effect, the torus is ‘straightened’ into a cylinder. Modifications due to the aspect ratio and elongation of the flux surface have been considered [3] and changes, relative to the cylindrical

model, to the external inductance and V-s consumption were found to be important for machines with a small aspect ratio.

The helical 3-D shaping of the plasma column of HSX adds an additional ‘twist’: the equilibrium current profile has both toroidal and poloidal components and couples to both the poloidal and toroidal magnetic fluxes. The diffusion is not modeled adequately by Eqn 3.7 which only considers toroidal current and poloidal flux. These effects have been considered analytically for simple profile changes in stellarators with circular cross-sections [1], and more recently, numerically for general toroidal devices [4]. This modeling is presented next.

### **3.2 Plasma Current Evolution in a General Nonaxisymmetric Toroidal Configuration**

The modeling of the time evolution of the toroidal and poloidal currents and fluxes, relevant for general nonaxisymmetric toroidal configurations is presented here, following the method described in references [1] and [4]. A susceptance matrix relates the radial derivative of magnetic fluxes to plasma and coil currents (Ampere’s law). The components of the matrix are found for a VMEC [5] (Appendix A) representation of the magnetic field. With the addition of Faradays and Ohms laws, a 1-dimensional diffusion equation for the rotational transform is derived. Boundary conditions appropriate for HSX plasmas are given. Finally, the equations are recast into a form appropriate for a computational numerical solver.

The plasma formulary [6] and Prof. James D. Callen’s Plasma Physics text [7] are useful references for vector calculus identities and relations. The properties of curvilinear coordinates are summarized in references [1] and [7], and a very thorough review of the subject is provided in [8].

#### **3.2.1 Current and Magnetic Flux Relations via Ampere’s Law**

The notation in this section is as follows: A set of curvilinear coordinates is employed,  $(\rho, \theta, \zeta)$ , where  $\rho$  is the radial coordinate, and  $\theta$  and  $\zeta$  are general angular coordinates on a flux surface, but will be referred to as poloidal- and toroidal- like angles which vary from  $(0 \rightarrow 2\pi)$ , Figure 3.2. The radial coordinate is a flux surface label and is left unspecified at this point to maintain generality.



The flux surfaces are assumed to be well-defined closed toroidal surfaces. The magnetic field lines are written in contravariant form,

$$\mathbf{B} = B^\rho \mathbf{e}_\rho + B^\theta \mathbf{e}_\theta + B^\zeta \mathbf{e}_\zeta \quad (3.8)$$

with the contravariant components of the magnetic field defined as

$$B^\rho = \mathbf{B} \cdot \nabla \rho \quad B^\theta = \mathbf{B} \cdot \nabla \theta \quad B^\zeta = \mathbf{B} \cdot \nabla \zeta \quad (3.9)$$

The radial term,  $B^\rho = 0$ , because the field lines form closed surfaces and do not leave the surface. The field lines are assumed to be straight so that both  $B^\theta$  and  $B^\zeta$  are constant on a flux surface. The Cartesian coordinate system  $\mathbf{x} = (x, y, z)$  and the covariant basis vectors are

$$\mathbf{e}_\rho = \frac{\partial \mathbf{x}}{\partial \rho} \quad \mathbf{e}_\theta = \frac{\partial \mathbf{x}}{\partial \theta} \quad \mathbf{e}_\zeta = \frac{\partial \mathbf{x}}{\partial \zeta} \quad (3.10)$$

Covariant metric coefficients (or elements) are defined as:

$$g_{jk} = g_{kj} = \mathbf{e}_j \cdot \mathbf{e}_k \quad \text{for} \quad j, k = \{\rho, \theta, \zeta\} \quad (3.11)$$

The magnetic field lines can also be written in covariant form,

$$\mathbf{B} = B_\rho \nabla \rho + B_\theta \nabla \theta + B_\zeta \nabla \zeta \quad (3.12)$$

where the covariant components are defined as

$$B_\rho = \mathbf{B} \cdot \mathbf{e}_\rho \quad B_\theta = \mathbf{B} \cdot \mathbf{e}_\theta \quad B_\zeta = \mathbf{B} \cdot \mathbf{e}_\zeta \quad (3.13)$$

and the contravariant basis vectors are

$$\nabla \rho \quad \nabla \zeta \quad \nabla \theta \quad (3.14)$$

The Jacobian of the transformation from curvilinear to Cartesian coordinates is

$$\mathcal{J} = \frac{1}{\nabla \rho \cdot \nabla \zeta \times \nabla \theta} = \mathbf{e}_\rho \cdot \mathbf{e}_\theta \times \mathbf{e}_\zeta \quad (3.15)$$

and the basis vectors are related by the following relations:

$$\mathbf{e}_\rho = \mathcal{J} \nabla \theta \times \nabla \zeta \quad \mathbf{e}_\theta = \mathcal{J} \nabla \zeta \times \nabla \rho \quad \mathbf{e}_\zeta = \mathcal{J} \nabla \rho \times \nabla \theta \quad (3.16)$$

$$\nabla \rho = \frac{1}{\mathcal{J}} \mathbf{e}_\theta \times \mathbf{e}_\zeta \quad \nabla \theta = \frac{1}{\mathcal{J}} \mathbf{e}_\zeta \times \mathbf{e}_\rho \quad \nabla \zeta = \frac{1}{\mathcal{J}} \mathbf{e}_\rho \times \mathbf{e}_\theta \quad (3.17)$$

With the above definition of the Jacobian, the plasma volume is defined by the integral,

$$V = \int_0^\rho d\rho \int_0^{2\pi} d\theta \int_0^{2\pi} d\zeta \mathcal{J} \quad (3.18)$$

and the radial derivative of the volume is:

$$V' = \int_0^{2\pi} d\theta \int_0^{2\pi} d\zeta \mathcal{J} \quad (3.19)$$

The flux-surface-average operator,  $\langle \rangle$ , of the value  $Q$  is defined as

$$\langle Q \rangle = \frac{1}{V'} \int_0^{2\pi} d\theta \int_0^{2\pi} d\zeta \mathcal{J} Q \quad (3.20)$$

The toroidal and poloidal magnetic fluxes enclosed within the surface are, respectively:

$$\Phi(\rho) = \int_0^{2\pi} d\theta \int_0^\rho d\rho \mathcal{J} B^\zeta \quad (3.21)$$

$$\Psi(\rho) = \int_0^{2\pi} d\zeta \int_0^\rho d\rho \mathcal{J} B^\theta \quad (3.22)$$

The toroidal and poloidal components of the current density are

$$J^\zeta = \mathbf{J} \cdot \nabla \zeta \quad J^\theta = \mathbf{J} \cdot \nabla \theta \quad (3.23)$$

The current lies within a flux surface and so  $J^\rho = 0$ . The toroidal current enclosed within a flux surface is

$$I(\rho) = \int_0^{2\pi} d\theta \int_0^\rho d\rho \mathcal{J} J^\zeta \quad (3.24)$$

and the poloidal current *exterior* to a flux surface is

$$F(\rho) = \int_0^{2\pi} d\theta \int_{\rho}^{\infty} d\rho \mathcal{J} J^{\theta} \quad (3.25)$$

By writing the magnetic field in covariant form, Eqn 3.12, and using Eqn 3.2, the following relations between the currents and magnetic fields are found:

$$\begin{aligned} \mu_0 I(\rho) &= \int_0^{2\pi} d\theta \int_0^{\rho} d\rho \mathcal{J} J^{\zeta} \\ &= \int_0^{2\pi} d\theta \int_0^{\rho} d\rho \mathcal{J} (\mathbf{J} \cdot \nabla \zeta) \\ &= \int_0^{2\pi} d\theta \int_0^{\rho} d\rho \mathcal{J} (\nabla \times (B_{\rho} \nabla \rho + B_{\theta} \nabla \theta + B_{\zeta} \nabla \zeta)) \cdot \nabla \zeta \\ &= \int_0^{2\pi} d\theta \int_0^{\rho} d\rho \mathcal{J} (\nabla B_{\rho} \times \nabla \rho + \nabla B_{\theta} \times \nabla \theta + \nabla B_{\zeta} \times \nabla \zeta) \cdot \nabla \zeta \\ &= \int_0^{2\pi} d\theta \int_0^{\rho} d\rho \mathcal{J} (\nabla B_{\rho} \cdot (\nabla \rho \times \nabla \zeta) + \nabla B_{\theta} \cdot (\nabla \theta \times \nabla \zeta) + \nabla B_{\zeta} \cdot (\nabla \zeta \times \nabla \zeta)) \\ &= \int_0^{2\pi} d\theta \int_0^{\rho} d\rho (-\nabla B_{\rho} \cdot \mathbf{e}_{\theta} + \nabla B_{\theta} \cdot \mathbf{e}_{\rho}) \end{aligned} \quad (3.26)$$

The fourth step involves expanding the  $\nabla \times$  operation in the parenthesis and simplifying, the fifth step is a vector identity, and the last step comes from Eqn 3.16. The only component of  $\nabla B_{\rho}$  that is not orthogonal to  $\mathbf{e}_{\theta}$  is the  $\nabla \theta$ -term, and the only component of  $\nabla B_{\theta}$  that is not orthogonal to  $\mathbf{e}_{\rho}$  is the  $\nabla \rho$ -term, so

$$\begin{aligned} \mu_0 I(\rho) &= \int_0^{2\pi} d\theta \int_0^{\rho} d\rho \left( -\frac{dB_{\rho}}{d\theta} \nabla \theta \cdot \mathbf{e}_{\theta} + \frac{dB_{\theta}}{d\rho} \nabla \rho \cdot \mathbf{e}_{\rho} \right) \\ &= \int_0^{2\pi} d\theta \int_0^{\rho} d\rho \left( -\frac{dB_{\rho}}{d\theta} + \frac{dB_{\theta}}{d\rho} \right) \end{aligned} \quad (3.27)$$

The magnetic field is single-valued on a flux surface, so the first term vanishes after rearranging the order of the integrals:

$$\int_0^{2\pi} d\theta \left( -\frac{dB_\rho}{d\theta} \right) = 0 \quad (3.28)$$

and so,

$$\mu_0 I(\rho) = \int_0^{2\pi} d\theta (B_\theta(\rho) - B_\theta(0)) = \int_0^{2\pi} d\theta B_\theta(\rho) \quad (3.29)$$

Following an analogous set of steps for  $F(\rho)$ ,

$$\mu_0 F(\rho) = \int_0^{2\pi} d\zeta B_\zeta(\rho) \quad (3.30)$$

Using the metric coefficients, Eqn 3.11, the covariant components of the magnetic field can be written as:

$$B_\theta = (B^\theta \mathbf{e}_\theta + B^\zeta \mathbf{e}_\zeta) \cdot \mathbf{e}_\theta = B^\theta g_{\theta\theta} + B^\zeta g_{\zeta\theta} \quad (3.31)$$

$$B_\zeta = (B^\theta \mathbf{e}_\theta + B^\zeta \mathbf{e}_\zeta) \cdot \mathbf{e}_\zeta = B^\theta g_{\theta\zeta} + B^\zeta g_{\zeta\zeta} \quad (3.32)$$

With Eqns 3.19, 3.21 and 3.22, the radial derivatives of the magnetic fluxes are (recall that  $B^\zeta$  and  $B^\theta$  are constant on a flux surface):

$$2\pi\Phi'(\rho) = \int_0^{2\pi} d\theta \int_0^{2\pi} d\zeta \mathcal{J} B^\zeta = B^\zeta V' \quad (3.33)$$

$$2\pi\Psi'(\rho) = \int_0^{2\pi} d\theta \int_0^{2\pi} d\zeta \mathcal{J} B^\theta = B^\theta V' \quad (3.34)$$

The electric currents,  $I(\rho)$  and  $F(\rho)$ , can be related to the radial derivatives of the magnetic fluxes with Eqns 3.29 - 3.34:

$$\mu_0 I(\rho) = \frac{\Psi'}{V'} \int_0^{2\pi} d\theta \int_0^{2\pi} d\zeta g_{\theta\theta} + \frac{\Phi'}{V'} \int_0^{2\pi} d\theta \int_0^{2\pi} d\zeta g_{\zeta\theta} \quad (3.35)$$

$$\mu_0 F(\rho) = \frac{\Psi'}{V'} \int_0^{2\pi} d\theta \int_0^{2\pi} d\zeta g_{\theta\zeta} + \frac{\Phi'}{V'} \int_0^{2\pi} d\theta \int_0^{2\pi} d\zeta g_{\zeta\zeta} \quad (3.36)$$

Recalling the definition of the flux-surface-average operator, Eqn 3.20, Eqns 3.35 and 3.36 can be written as:

$$\mu_0 \begin{bmatrix} I \\ F \end{bmatrix} = \begin{bmatrix} S_{11} & S_{12} \\ S_{21} & S_{22} \end{bmatrix} \begin{bmatrix} \Psi' \\ \Phi' \end{bmatrix} \quad (3.37)$$

The components of the susceptance matrix are defined as:

$$\begin{aligned} S_{11} &= \left\langle \frac{g_{\theta\theta}}{\mathcal{J}} \right\rangle & S_{12} &= \left\langle \frac{g_{\zeta\theta}}{\mathcal{J}} \right\rangle \\ S_{21} &= \left\langle \frac{g_{\theta\zeta}}{\mathcal{J}} \right\rangle & S_{22} &= \left\langle \frac{g_{\zeta\zeta}}{\mathcal{J}} \right\rangle \end{aligned} \quad (3.38)$$

The susceptance matrix components, Eqn 3.38, describe the coupling between the toroidal and poloidal plasma currents to the radial derivatives of the toroidal and poloidal magnetic fluxes. In an axisymmetric tokamak, there is no coupling between poloidal currents and poloidal magnetic flux, and there is no coupling between the toroidal currents and toroidal magnetic flux;  $\mathbf{e}_\theta \perp \mathbf{e}_\zeta$ ,  $g_{\theta\zeta} = \mathbf{e}_\theta \cdot \mathbf{e}_\zeta = 0$  everywhere on a flux surface and  $S_{12} = S_{21} = 0$ . In HSX, and for stellarators in general,  $\mathbf{e}_\theta \cdot \mathbf{e}_\zeta \neq 0$  and  $S_{12} \neq 0$ ,  $S_{21} \neq 0$ .

### 3.2.2 Rotational Transform

The rotational transform,  $t$ , is defined as

$$t = \frac{\Psi'}{\Phi'} = \frac{\mu_0 I}{S_{11} \Phi'} - \frac{S_{12}}{S_{11}} \quad (3.39)$$

In the case of a vacuum magnetic field,  $I = 0$ , and

$$t_{vac} = -\frac{S_{12}}{S_{11}} \quad (3.40)$$

which for tokamaks with no toroidal current is 0, but for stellarators, because  $S_{12} \neq 0$ , there is a non-zero vacuum rotational transform.

### 3.2.3 VMEC Coordinates and Susceptance Matrix Components

Recall the contravariant form of the magnetic field, Eqn 3.8, and notice that it can be generalized to another form:

$$\mathbf{B} = B^\theta \mathbf{e}_\theta + B^\zeta \mathbf{e}_\zeta = \frac{1}{2\pi} (\nabla\zeta \times \nabla\Psi + \nabla\Phi \times \nabla\theta^*) \quad (3.41)$$

This is the choice that Variational Moments Equilibrium Code, or VMEC [5] code uses. A factor of  $\frac{1}{2\pi}$  is included in the definitions of the enclosed fluxes, so the Jacobian will be now  $\frac{V'}{4\pi^2}$  where  $V'$  is defined by Eqn 3.19. The value of  $\theta^*$  corresponds to the choice in determining the poloidal angle which results in a straight field line system. VMEC chooses the poloidal angle in such a way that the poloidal mode expansion of the inverse coordinates,  $R$  and  $Z$ , converges as rapidly as possible. This leads to the introduction of a magnetic stream function,  $\lambda$ , which is periodic in both  $\theta$  and  $\zeta$ :

$$\theta^* = \theta + \lambda(\rho, \theta, \zeta) \quad (3.42)$$

The magnetic field can now be written as

$$\mathbf{B} = \frac{1}{2\pi} \left( \nabla \zeta \times \nabla \Psi + \nabla \Phi \times \nabla \theta + \nabla \Phi \times \nabla \lambda(\rho, \theta, \zeta) \right) \quad (3.43)$$

$$= \frac{1}{2\pi \mathcal{J}} \left( \left( \Psi' - \Phi' \frac{d\lambda}{d\zeta} \right) \mathbf{e}_\theta + \Phi' \left( 1 + \frac{d\lambda}{d\theta} \right) \mathbf{e}_\zeta \right) \quad (3.44)$$

The contravariant components of  $\mathbf{B}$  in the VMEC representation are

$$B^\theta = \frac{1}{2\pi \mathcal{J}} \left( \Psi' - \Phi' \frac{d\lambda}{d\zeta} \right) \quad (3.45)$$

$$B^\zeta = \frac{1}{2\pi \mathcal{J}} \Phi' \left( 1 + \frac{d\lambda}{d\theta} \right) \quad (3.46)$$

With these definitions, the components of the susceptance matrix are given by:

$$\begin{aligned} S_{11} &= \frac{V'(\rho)}{4\pi^2} \left\langle \frac{g_{\theta\theta}}{\mathcal{J}^2} \right\rangle & S_{12} &= \frac{V'(\rho)}{4\pi^2} \left\langle \frac{g_{\zeta\theta} \left( 1 + \frac{d\lambda}{d\theta} \right) - g_{\theta\theta} \frac{d\lambda}{d\zeta}}{\mathcal{J}^2} \right\rangle \\ S_{21} &= \frac{V'(\rho)}{4\pi^2} \left\langle \frac{g_{\theta\zeta}}{\mathcal{J}^2} \right\rangle & S_{22} &= \frac{V'(\rho)}{4\pi^2} \left\langle \frac{g_{\zeta\zeta} \left( 1 + \frac{d\lambda}{d\theta} \right) - g_{\theta\zeta} \frac{d\lambda}{d\zeta}}{\mathcal{J}^2} \right\rangle \end{aligned} \quad (3.47)$$

Direct substitution shows that Eqn 3.37 is satisfied. The enclosed toroidal current is:

$$\begin{aligned}
S_{11}\Psi' + S_{12}\Phi' &= \frac{V'}{4\pi^2} \frac{1}{V'} \int_0^{2\pi} d\theta \int_0^{2\pi} d\zeta \frac{\mathcal{J}}{\mathcal{J}^2} \left[ g_{\theta\theta} \left( \Psi' - \Phi' \frac{d\lambda}{d\zeta} \right) + g_{\zeta\theta} \Phi' \left( 1 + \frac{d\lambda}{d\theta} \right) \right] \\
&= \frac{1}{4\pi^2} \int_0^{2\pi} d\theta \int_0^{2\pi} d\zeta 2\pi [g_{\theta\theta} B^\theta + g_{\zeta\theta} B^\zeta] \\
&= \frac{1}{2\pi} \int_0^{2\pi} d\theta \int_0^{2\pi} d\zeta B_\theta \\
&= \int_0^{2\pi} d\theta B_\theta = \mu_0 I
\end{aligned} \tag{3.48}$$

The poloidal current exterior to a flux surface is:

$$\begin{aligned}
S_{21}\Psi' + S_{22}\Phi' &= \frac{V'}{4\pi^2} \frac{1}{V'} \int_0^{2\pi} d\theta \int_0^{2\pi} d\zeta \frac{\mathcal{J}}{\mathcal{J}^2} \left[ g_{\theta\zeta} \left( \Psi' - \Phi' \frac{d\lambda}{d\zeta} \right) + g_{\zeta\zeta} \Phi' \left( 1 + \frac{d\lambda}{d\theta} \right) \right] \\
&= \frac{1}{4\pi^2} \int_0^{2\pi} d\theta \int_0^{2\pi} d\zeta 2\pi [g_{\theta\zeta} B^\theta + g_{\zeta\zeta} B^\zeta] \\
&= \frac{1}{2\pi} \int_0^{2\pi} d\theta \int_0^{2\pi} d\zeta B_\zeta \\
&= \int_0^{2\pi} d\zeta B_\zeta = \mu_0 F
\end{aligned} \tag{3.49}$$

Radial profiles of  $S_{11}$ ,  $S_{12}$ ,  $S_{21}$ , and  $S_{22}$ , for the standard QHS configuration of HSX and for an 'equivalent tokamak', Appendix A, are shown in Figure 3.3. The expressions in Eqn 3.47 were evaluated numerically with Matlab with the `calculate_susceptance` code. Each case is for a vacuum magnetic field. The diagonal terms,  $S_{11}$  and  $S_{22}$ , are similar in magnitude for each case, while the off-diagonal terms,  $S_{12}$  and  $S_{21}$ , are non-zero in the QHS case and zero for the equivalent tokamak, as expected.

In Figure 3.4, the radial profiles of the susceptance matrix components are shown for several different magnetic configurations that can be achieved in the HSX stellarator when energizing the

auxiliary field coils. The ‘Mirror’ configuration [9] adds a mirror ‘symmetry-breaking’ term to the QHS magnetic spectrum, but does not drastically alter the susceptance matrix. The ‘Well’ and ‘Hill’ configurations raise and lower the vacuum rotational transform, respectively. The effective minor radius is also smaller in each of these configurations. The  $S_{11}$ ,  $S_{12}$ , and  $S_{21}$  components are increased in magnitude in the Well configuration and are slightly decreased in the Hill configuration. The  $S_{22}$  component is not drastically altered in any of these configurations.

### 3.2.4 Parallel Electric Field: Faraday’s Law and Ohm’s Law

In the previous section, the relationship between the magnetic fluxes and electrical currents was found, leading to the susceptance matrix equation, 3.37. Now the relationships between the current, electric field and induced magnetic field will be used to derive the time evolution of the plasma current density, or more specifically, the rotational transform. Relationships, derived in Appendix C, between the magnetic energy density, Eqn C.32, parallel current density, Eqn C.33, and radial force balance, Eqn C.40, will be useful.

Returning to the notion for the general curvilinear coordinates, not those of VMEC, consider the integral form of Faraday’s law,  $\oint_C \mathbf{dl} \cdot \mathbf{E} = -\frac{\partial}{\partial t} \iint_S \mathbf{ds} \cdot \mathbf{B}$ , where the contour C is the boundary of surface S. With the electric field written in covariant form,

$$\mathbf{E} = E_\rho \nabla \rho + E_\theta \nabla \theta + E_\zeta \nabla \zeta \quad (3.50)$$

the time-rate-of-change of the poloidal magnetic flux is related to the toroidal electric field and loop voltage as:

$$\begin{aligned} \frac{d\Psi(\rho)}{dt} &= \int_0^{2\pi} d\zeta E_\zeta(\rho) - \int_0^{2\pi} d\zeta E_\zeta(0) \\ &= V_{\zeta-loop}(\rho) - V_{\zeta-loop}(0) \end{aligned} \quad (3.51)$$



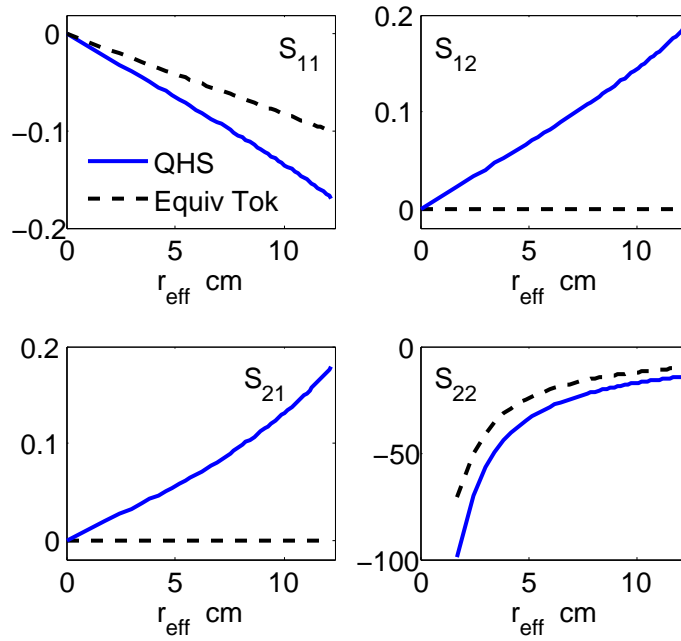


Figure 3.3 Radial profiles of susceptance matrix coefficients for the QHS magnetic configuration and an equivalent tokamak.

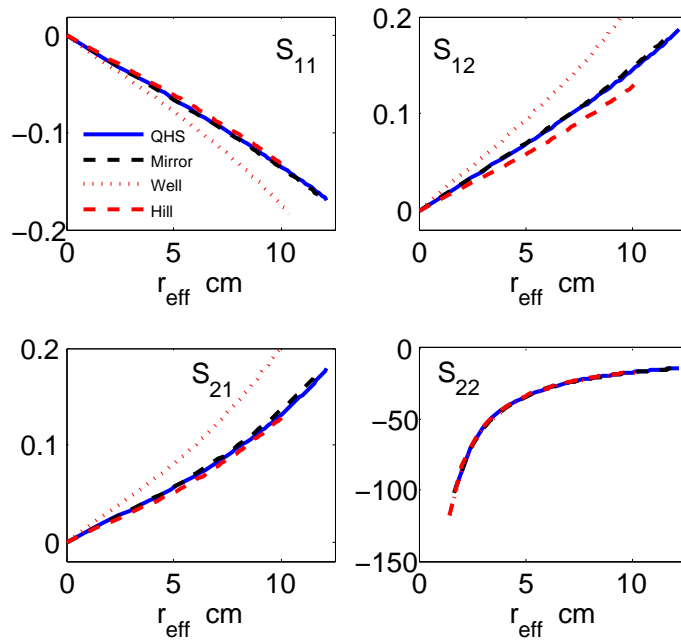


Figure 3.4 Radial profiles of susceptance matrix coefficients for several magnetic configurations possible in HSX when energizing the auxiliary field coils in different ways: QHS, 10% Mirror Flip14, 11% Well, and 11% Hill..

and the time-rate-of-change of the toroidal magnetic flux is related to the poloidal electric field and loop voltage as:

$$\begin{aligned}\frac{d\Phi(\rho)}{dt} &= - \int_0^{2\pi} d\theta E_\theta(\rho) + \int_0^{2\pi} d\theta E_\theta(0) = - \int_0^{2\pi} d\theta E_\theta(\rho) \\ &= -V_{\theta-loop}(\rho)\end{aligned}\quad (3.52)$$

The poloidal loop voltage is proportional to the circumference of the loop and vanishes as  $\rho \rightarrow 0$ .

The flux-surface-average of the parallel electric field relates the magnetic fluxes and loop voltages.

Using the contravariant form of  $\mathbf{B}$ , Eqn 3.8 and covariant form of  $\mathbf{E}$ , Eqn 3.50 :

$$\begin{aligned}\langle \mathbf{E} \cdot \mathbf{B} \rangle &= \langle B^\theta E_\theta + B^\zeta E_\zeta \rangle \\ &= \frac{1}{V'} \int_0^{2\pi} d\theta \int_0^{2\pi} d\zeta \mathcal{J} (B^\theta E_\theta + B^\zeta E_\zeta) \\ &= \frac{1}{V'} \int_0^{2\pi} d\theta \int_0^{2\pi} d\zeta \mathcal{J} (B^\theta E_\theta) + \frac{1}{V'} \int_0^{2\pi} d\theta \int_0^{2\pi} d\zeta \mathcal{J} (B^\zeta E_\zeta)\end{aligned}\quad (3.53)$$

With the following functions and differential definitions,

$$u = E_\theta \quad v = \Psi' \quad du = d\zeta \frac{\partial E_\theta}{\partial \zeta} \quad dv = d\zeta \mathcal{J} B^\theta \quad (3.54)$$

$$s = E_\zeta \quad t = \Phi' \quad ds = d\theta \frac{\partial E_\zeta}{\partial \theta} \quad dt = d\theta \mathcal{J} B^\zeta \quad (3.55)$$

Eqn 3.53 can be simplified by integrating by parts, twice:

$$\begin{aligned}\langle \mathbf{E} \cdot \mathbf{B} \rangle &= \frac{1}{V'} \int_0^{2\pi} d\theta \int_0^{2\pi} d\zeta \left( E_\theta \Psi' - \int_0^{2\pi} d\zeta \Psi' \frac{\partial E_\theta}{\partial \zeta} \right) \\ &\quad + \frac{1}{V'} \int_0^{2\pi} d\theta \int_0^{2\pi} d\zeta \left( E_\zeta \Phi' - \int_0^{2\pi} d\theta \Phi' \frac{\partial E_\zeta}{\partial \theta} \right)\end{aligned}\quad (3.56)$$

The terms involving derivatives of the electric field components vanish because of periodicity on the torus,

$$\langle \mathbf{E} \cdot \mathbf{B} \rangle = \frac{\Psi'}{V'} \int_0^{2\pi} d\theta E_\theta + \frac{\Phi'}{V'} \int_0^{2\pi} d\zeta E_\zeta \quad (3.57)$$

Substituting Eqns 3.51 and 3.52 into 3.57 and rearranging:

$$\langle \mathbf{E} \cdot \mathbf{B} \rangle V' = \Phi' \left( \frac{d\Psi}{dt} + V_{\zeta-loop}(0) \right) - \Psi' \frac{d\Phi}{dt} \quad (3.58)$$

The loop voltage dependence can be removed with rearranging and taking a toroidal flux derivative.

An equation for the time derivative of the rotational transform is found, after some algebra:

$$\begin{aligned} \frac{d\Psi}{dt} + V_{\zeta-loop}(0) &= \frac{\langle \mathbf{E} \cdot \mathbf{B} \rangle V'}{\Phi'} + \frac{\Psi'}{\Phi'} \frac{d\Phi}{dt} \\ \frac{d}{d\Phi} \frac{d\Psi}{dt} &= \frac{d}{d\Phi} \left( \langle \mathbf{E} \cdot \mathbf{B} \rangle \frac{dV}{d\Phi} \right) + \frac{d}{d\Phi} \left( \frac{d\Phi}{dt} \right) \\ \frac{d\iota}{dt} &= \frac{d}{d\Phi} \left( \langle \mathbf{E} \cdot \mathbf{B} \rangle \frac{dV}{d\Phi} \right) + \frac{d}{d\Phi} \left( \frac{d\Phi}{dt} \right) \end{aligned} \quad (3.59)$$

Next, consider Ohm's law. The parallel plasma resistivity is  $\eta_{\parallel} = \frac{1}{\sigma_{\parallel}}$ . Recalling that  $\mathbf{J}_{n.i.}$  is the non-inductive current density and  $\mathbf{J}$  is the total current density,

$$\begin{aligned} \langle \mathbf{E} \cdot \mathbf{B} \rangle V' &= \eta_{\parallel} \langle (\mathbf{J} - \mathbf{J}_{n.i.}) \cdot \mathbf{B} \rangle V' \\ &= \eta_{\parallel} \langle \mathbf{J} \cdot \mathbf{B} \rangle V' - \eta_{\parallel} \langle \mathbf{J}_{n.i.} \cdot \mathbf{B} \rangle V' \end{aligned} \quad (3.60)$$

With Eqn C.33 and  $\frac{dV}{d\rho} = \frac{V'}{\rho'}$ , this can be written as:

$$\begin{aligned} \langle \mathbf{E} \cdot \mathbf{B} \rangle V' &= \eta_{\parallel} \mu_0 (FI' - IF') - \eta_{\parallel} \langle \mathbf{J}_{n.i.} \cdot \mathbf{B} \rangle V' \\ &= \eta_{\parallel} \mu_0 F^2 \left( \frac{I}{F} \right)' - \eta_{\parallel} \langle \mathbf{J}_{n.i.} \cdot \mathbf{B} \rangle V' \end{aligned} \quad (3.61)$$

Substituting Eqn 3.61 into Eqn 3.59,

$$\frac{d\iota}{dt} = \frac{d}{d\Phi} \left[ \frac{1}{\Phi'} \left( \eta_{\parallel} \mu_0 F^2 \left( \frac{I}{F} \right)' - \eta_{\parallel} \langle \mathbf{J}_{n.i.} \cdot \mathbf{B} \rangle V' \right) \right] + \frac{d\iota}{d\Phi} \frac{d\Phi}{dt} \quad (3.62)$$

After substituting Eqn 3.37 for  $F$  and  $I$ , a 1-D diffusion equation for the rotational transform can be written as [4] :

$$\frac{d\iota}{dt} = \frac{d\iota}{d\Phi} \frac{d\Phi}{dt} + \frac{d}{d\Phi} \left( \Phi' \frac{\eta_{\parallel}}{\mu_0} (S_{21}\iota + S_{22})^2 \frac{d}{d\rho} \left( \frac{S_{11}\iota + S_{12}}{S_{21}\iota + S_{22}} \right) - \frac{\eta_{\parallel}}{\Phi'} \langle \mathbf{J}_{n.i.} \cdot \mathbf{B} \rangle V' \right) \quad (3.63)$$

This expression has mixed derivatives and requires calculation of the full susceptance matrix. Using the relations in Eqns C.32, C.33, and C.40,

$$FI' = \frac{\langle B^2 \rangle V'}{\mu_0 \Phi'} I' - II' \iota \quad (3.64)$$

$$-IF' = \frac{p' V'}{\Phi'} I + II' \iota \quad (3.65)$$

and  $F^2 \left(\frac{I}{F}\right)' = FI' - IF'$ ,

$$\frac{dt}{dt} = \frac{dt}{d\rho} \frac{d\rho}{d\Phi} \frac{d\Phi}{dt} + \frac{d\rho}{d\Phi} \frac{d}{d\rho} \left( \frac{\eta_{\parallel} \mu_0}{(\Phi')^2} \left( \frac{\langle B^2 \rangle V'}{\mu_0} I' + p' V' I \right) - \frac{\eta_{\parallel}}{\Phi'} \langle \mathbf{J}_{n.i.} \cdot \mathbf{B} \rangle V' \right) \quad (3.66)$$

$$= \frac{dt}{d\rho} \frac{d\rho}{d\Phi} \frac{d\Phi}{dt} + \frac{d\rho}{d\Phi} \frac{d}{d\rho} \dots \quad (3.67)$$

$$\left( \frac{\eta_{\parallel} V'}{(\Phi')^2} \left( \langle B^2 \rangle \frac{d}{d\rho} \left( \frac{\Phi'}{\mu_0} (S_{11}t + S_{12}) \right) + p' \Phi' (S_{11}t + S_{12}) \right) + - \frac{\eta_{\parallel}}{\Phi'} \langle \mathbf{J}_{n.i.} \cdot \mathbf{B} \rangle V' \right)$$

Two common choices for the radial variable are the normalized toroidal flux,  $\rho_s$  and square-root normalized toroidal flux,  $\rho_r$ , defined as

$$\rho_s = \Phi / \Phi_a \quad (3.68)$$

$$\rho_r = \sqrt{\Phi / \Phi_a} \quad (3.69)$$

Here,  $\Phi_a \equiv \Phi_{LCFS}$  is the flux enclosed within the last closed flux surface. These two choices lead to  $\frac{d\Phi}{d\rho_s} = \Phi_a$  and  $\frac{d\Phi}{d\rho_r} = 2\rho_r \Phi_a$ , respectively. For the term involving the time derivative of the toroidal flux, the two choices lead to  $\frac{d\Phi}{dt} = \frac{d(\Phi_a \rho_s)}{dt} = \rho_s \frac{d\Phi_a}{dt}$  and  $\frac{d\Phi}{dt} = \frac{d(\Phi_a \rho_r^2)}{dt} = \rho_r^2 \frac{d\Phi_a}{dt}$ . For the first choice of radial variable, the diffusion equation for  $t$  becomes

$$\frac{dt}{dt} = \frac{\rho_s}{\Phi_a} \frac{dt}{d\rho_s} \frac{d\Phi_a}{dt} + \frac{1}{\Phi_a^2} \frac{d}{d\rho_s} \left( \eta_{\parallel} V' \left( \frac{\langle B^2 \rangle}{\mu_0} \frac{d}{d\rho_s} (S_{11}t + S_{12}) + p' (S_{11}t + S_{12}) - \langle \mathbf{J}_{n.i.} \cdot \mathbf{B} \rangle \right) \right) \quad (3.70)$$

For the second choice, the diffusion equation is

$$\frac{dt}{dt} = \frac{\rho_r}{2\Phi_a} \frac{dt}{d\rho_r} \frac{d\Phi_a}{dt} + \frac{1}{4\rho_r \Phi_a^2} \frac{d}{d\rho_r} \left( \frac{\eta_{\parallel} V'}{\rho_r} \left( \frac{\langle B^2 \rangle}{\mu_0 \rho_r} \frac{d}{d\rho_r} (\rho_r (S_{11}t + S_{12})) + p' (S_{11}t + S_{12}) - \langle \mathbf{J}_{n.i.} \cdot \mathbf{B} \rangle \right) \right) \quad (3.71)$$

These expressions are similar to those in Refs [10] and [11], except these are dimensionally correct. The time-changing toroidal flux term, the 1st term on the RHS of Eqns 3.70 and 3.71, has a weak influence on the evolution and can be neglected in most cases, as will be done here. These last two equations use  $\langle B^2 \rangle$  and  $p'$  instead of  $S_{21}$  and  $S_{22}$ . During the numerical simulation of the diffusion equation, the MHD equilibrium quantities  $B^2$ ,  $p'$ ,  $S_{11}$ ,  $S_{12}$ , and  $\langle \mathbf{J}_{n.i.} \cdot \mathbf{B} \rangle$  are assumed to be slowly

varying or constant. This allows for the rotational transform profile to evolve for some time before a full recalculation of the equilibrium quantities is required. Studies on LHD have shown that an update interval of 100 ms is sufficient for their plasmas [11]. In the HSX plasmas studied here, the bootstrap current has small effect on the magnetic field geometry and so the MHD quantities are nearly constant during a simulation and no update is performed.

### 3.2.5 Boundary Conditions

A combination of Dirichlet and Neumann boundary conditions are used to complete the specification of the diffusion equation,

$$\alpha t + \beta t' = \gamma \quad (3.72)$$

At the center of the plasma column,  $\rho = 0$ , there is finite (or, non-infinite) current density so

$$\left. \frac{dt}{d\rho} \right|_{\rho=0} = 0 \quad (3.73)$$

At the edge of the plasma column,  $\rho = 1$ , the measured net toroidal current,  $I(\rho = 1)$  determines the value of  $t$  at the edge, Eqn 3.39

$$t|_{\rho=1} = \left( \frac{\mu_0 I}{S_{11} \Phi'} - \frac{S_{12}}{S_{11}} \right) \Big|_{\rho=1} \quad (3.74)$$

This is the boundary condition used for the work presented here. Other options for the boundary condition at the edge are discussed in Appendix D. The numerical implementation of the solution to the diffusion equation is given in Appendix E.

## References

- [1] V. D. Pustovitov and V. D. Shafranov, Rev. Plasma Phys. **15**, 163 (1990).
- [2] D. R. Mikkelsen, Phys. Fluids B **1**, 333 (1989).
- [3] S. P. Hirshman and G. H. Neilson, Phys. Fluids **29**, 790 (1986).
- [4] Strand and Houlberg, Phys. Plasmas **8**, 2782 (2001).
- [5] S. P. Hirshman and J. C. Whitson, Phys. Fluids **26**, 3553 (1983).
- [6] J. D. Huba, NRL Plasma Formulary, Naval Research Laboratory, NRL/PU/6790-06-491, Washington, DC (2006).
- [7] J. D. Callen, “Fundamentals of Plasma Physics”, Appendix D, 11 October 2002. <http://homepages.cae.wisc.edu/callen/book.html>.
- [8] W. D. D’haeseleer, et al, “Flux Coordinates and Magnetic Field Structure”, Springer, Berlin (1991).
- [9] J. M. Canik, et al., Phys. Plasmas **14**, 056107 (2007).
- [10] Nakamura, et al, 33rd EPS Conference on Plasma Physics, Rome, June 2006, P-4.122 (2006).
- [11] Nakamura, et al, Plasma and Fusion Research **3**, S1058 (2008).

## Chapter 4

### Magnetic Diagnostics and Equilibrium Reconstruction

This chapter presents the diagnostic set and computational tools implemented to reconstruct the plasma pressure and current profiles. A ‘flapper probe’, which sweeps out accelerated electrons during the rise in main field, is described in section 4.1. A set of magnetic diagnostics that measures changes in the magnetic field surrounding the plasma are described in section 4.2 and the signal analysis is discussed in section 4.3. The effects of the vacuum vessel are discussed briefly in section 4.4. In section 4.5, the V3RFUN code that calculate the expected signal response from plasma currents and external magnetic fields on a set of diagnostics is described. The V3FIT code performs the reconstruction of the plasma profiles, described in section 4.6.

#### 4.1 Flapper Probe

In HSX, a significant population of electrons can be accelerated in the confinement volume by the time-changing magnetic field during the main-field current ramp-up stage of the discharge. The presence of these  $dB/dt$  electrons has been seen on hard x-ray diagnostics [1], and they can constitute a significant toroidal current, even before any heating source has been applied, Figure 4.1. To remove this current source, and to simplify the analysis of the measured currents, a flapper probe has been installed on HSX. The probe is a 1 cm x 12 cm strip of titanium that extends into the confinement volume prior to the main field ramp-up. A sketch of the probe, along with Poincaré plots of the QHS magnetic configuration, are shown in Figure 4.2. The flap is completely removed from the confinement volume 50 - 100 ms before heating is applied. The flap remains out of the confinement volume until the next shot cycle begins.

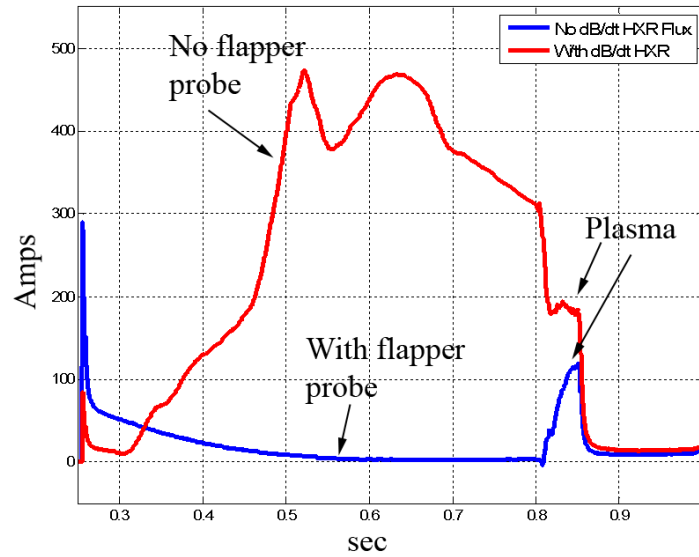


Figure 4.1 The toroidal current measurement with and without the presence of hard x-rays caused by  $dB/dt$  electrons (those accelerated during the main field ramp up). As the electrons leave the confinement field, they collide with the vessel and generate a hard x-ray flux [1]. The loss of these accelerated electrons results in a net toroidal current (red line). The flapper probe, Figure 4.2, prevents the generation of these particles, and the toroidal current is generated during the plasma discharge (blue), which occurs during  $0.800 < t < 0.850$ .

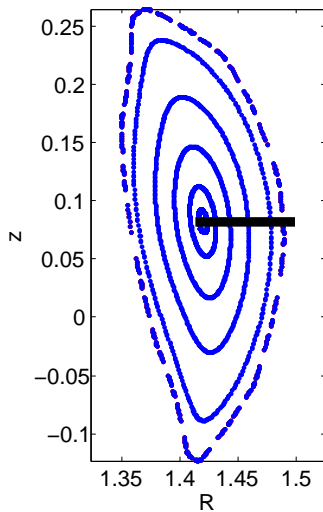


Figure 4.2 Sketch of the internal flapper probe in its extended position and Poincaré plots of vacuum magnetic surfaces in the QHS magnetic configuration.

## 4.2 Magnetic Diagnostics

The magnetic field in and around the plasma column of a magnetic fusion device has several sources. The currents in the external field coils generate a vacuum magnetic field which confines



the plasma. The plasma develops diamagnetic, Pfirsch-Schlüter, bootstrap and induced currents which generate magnetic fields. Eddy currents may be induced in the surrounding vacuum vessel and support structure which also generate magnetic fields. The magnetic field at any specific point is the sum of the contributions from all of these sources. Diagnostics can measure these ‘local’ changes in the magnetic field at a particular point in space. Diagnostics can also be designed to measure integral properties of the magnetic field in order to measure ‘global’ properties of the plasma, such as the total enclosed current or total flux. In this section, two types of magnetic diagnostics are described and the signal analysis techniques are in section 4.3.

#### 4.2.1 External Magnetic Vector Diagnostic Array

The external magnetic vector diagnostic array is a set of 32 individual cubes, or triplets, installed on the outside (atmospheric side) of the vacuum vessel. Each triplet measures the change in the local magnetic field vector. Each cube, Figure 4.3, is constructed from Delrin plastic, or polyoxymethylene, measuring 3/4” on a side. The cube is wrapped with three sets of insulated (Kapton coated) 35 AWG wire in such a way that each wire forms a square coil that measures flux in one of three orthogonal directions. A total of 160 turns of wire is wrapped in each orientation. The ends of the wire are then twisted together to avoid pickup from magnetic flux located away from the cube. The twisted wires are connected to an amplifier, where the signal is amplified, low-pass filtered at 3.2 kHz, and then digitized. A single layer of copper foil,  $\sim 2.5$  mil thick, is taped around the cube to protect the wires from damage, and is thin enough to not decrease the sensitivity or frequency response of the coil [2].

The output voltage,  $V$ , of a single axis of one of the triplets due to changes in the magnetic field  $\mathbf{B}$  is given by Faraday’s law and Stokes’ theorem:

$$V = GN \oint_C d\mathbf{l} \cdot \mathbf{E} = GN \int_S d\mathbf{s} \cdot (\nabla \times \mathbf{E}) = GN \int_S d\mathbf{s} \cdot \left( -\frac{\partial \mathbf{B}}{\partial t} \right) \quad (4.1)$$

$S$  is the face of the cube,  $C$  is the contour about the surface  $S$ ,  $G$  is the gain of the amplifier and  $N$  is the number turns of wire along the contour  $C$ . If the magnetic field does vary much over the

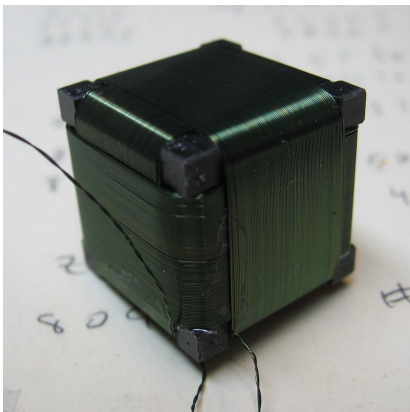


Figure 4.3 External magnetic diagnostic 'triplet'. Photo courtesy P. H.Probert.

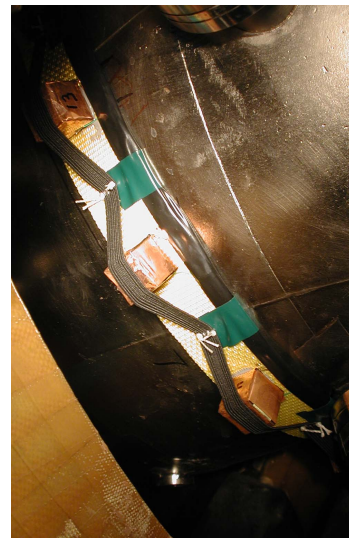


Figure 4.4 Triplets, covered with a protective copper shield, mounted on a nylon belt and wrapped around the vacuum vessel.

volume of the cube, then

$$V = -GNA \frac{\partial B}{\partial t} \quad (4.2)$$

where  $A$  is the area of the face of the surface  $S$  and  $B$  is the component of the magnetic field perpendicular to  $S$ . The time derivative of  $B$  is given by

$$\dot{B}(t) = \frac{\partial B}{\partial t} = -\frac{V}{GNA} \quad (4.3)$$

The  $GNA$  product of each axis of each triplet and amplifier was measured with a Helmholtz coil over the range of 30 Hz - 3 kHz and recorded for later use in the signal processing step.

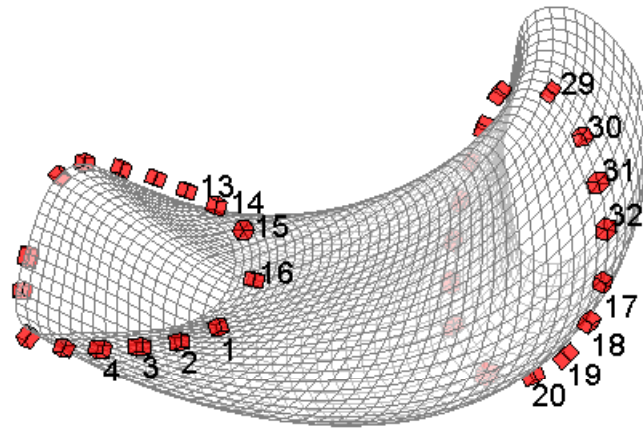


Figure 4.5 Outboard view of the external diagnostic array.

Two nylon belts each have 16 triplets mounted on them with epoxy and secured in place with elastic bands. Prior to the final installation on the HSX vessel, each belt was wrapped around a test section and tightened in place. This test section was created with the same forms as the rest of the HSX vacuum vessel and they share the same form markings and mechanical reference points etched into the stainless steel. In places where the belts do not touch the vacuum vessel, rubber shims were used to fill the gaps between the vessel and the belt in order to reduce mechanical vibrations. The location of each individual triplet, relative to the reference points on the vessel, was measured with a coordinate measuring machine (CMM), a Romer Cimcore, Model 5028 [3]. These are the coordinate points that are later used for input into V3RFUN to generate response functions,

section 4.5. The belts were then transferred from the test section to the HSX vacuum vessel using the machining marks and mechanical reference points to reproduce the same positioning.

The triplets are shown on the HSX vacuum vessel in Figure 4.4. The measured position of the 32 diagnostics and 1/2 of a field period of the vacuum vessel are shown in Figures 4.5 and 4.6. Each triplet is designated by a unique 'poloidal index', an integer between 1 and 32. The linear spacing along the nylon belt between the triplets is uniform except for triplets with poloidal indices 7-10. One of the main field coils makes an excursion close to the vacuum vessel in this location and there is not enough clearance in which to place a triplet. Each of the two sets of triplets lie nearly in plane. Each belt makes slight deviations due to the curvature of the vacuum vessel and the constraint of minimizing the belt length by wrapping the belt as tightly as possible around vessel. The position and alignment of each triplet was verified by comparing the measured response with the theoretical signal response while energizing the main field coil set and several individual auxiliary field coils. Details of this are in Appendix F. The misalignment in orientation is considered a systematic angular uncertainty in this thesis. This systematic error is typically a  $1\text{-}3^\circ$  for the majority of the triplets, with the maximum misalignment angle being  $5^\circ$ .

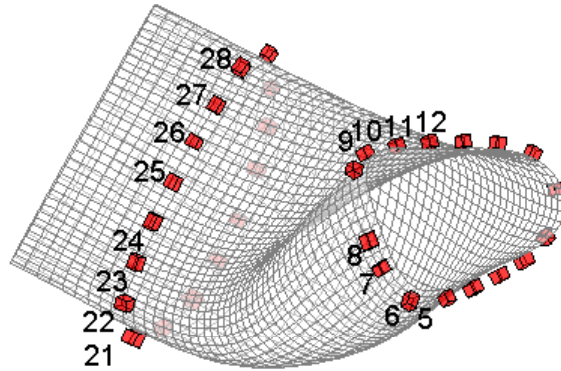


Figure 4.6 Inboard view of the external diagnostic array.

### 4.2.2 Internal Magnetic Diagnostics

A set of 15 coils, circularly wound on a polyethylene tube, and covered with electrostatic shielding and heat-shrink rubber are inside of a flexible helically-wound 10-mil stainless steel

hose. This hose is attached to the inside of the vacuum vessel by metal clips. The positions of the coils are known with respect to the ends of the tube, and the position of the hose was measured with the CMM. The calculated positions of each of the coils, are shown in Figure 4.7. A photograph of the hose is in Figure 4.8. These diagnostics are sensitive to mainly the poloidal component of the magnetic field, and are referred to as the internal poloidal array. The output voltage for these diagnostics is described by Equation 4.3. Each coil was calibrated with a Helmholtz coil in both free space and while inserted into the steel hose. The steel hose has negligible effect on the frequency response below 20 kHz. The signal from these coils is amplified and low-pass filtered at 3.3 kHz and digitized. The position and alignment of the array was verified by energizing the main field coil set. Details of this are in appendix F.

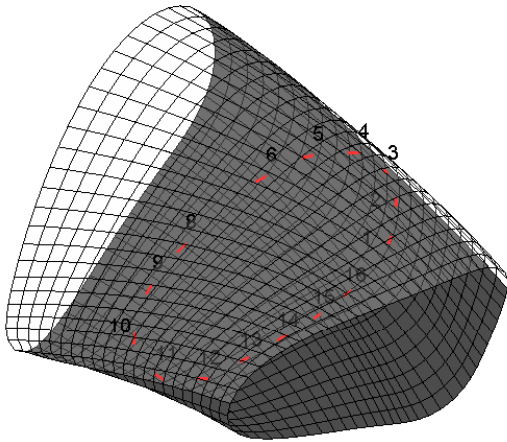


Figure 4.7 The calculated positions of the internal poloidal array.



Figure 4.8 Photograph of the steel hose of the internal poloidal array.

### 4.2.3 Rogowski Coil

The net toroidal current in HSX plasmas is measured by two Rogowski coils. An illustration of one is in Figure 4.9. This coil is essentially a solenoid inductor bent into the shape of a torus. The physical construction is identical to a helically-wound coil on a flexible tube, with a return wire traversing the center of the coil. The ends of the coil meet, and completely enclose a current,  $I$ . The magnetic field,  $B$  created by the enclosed current is linked by the cross-section area of the

coil,  $A$ . A change in  $I$  will induce a voltage at the ends of the coil. The purpose of the return wire is to minimize the effect of any background magnetic flux that may be enclosed by the loop.

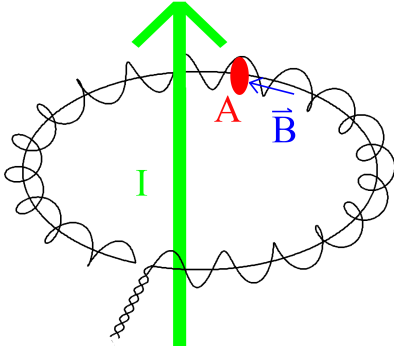


Figure 4.9 Illustration of a Rogowski coil. The current  $I$  generates magnetic field  $B$  which is linked by area  $A$ . Changes in  $I$  will induce a voltage across the ends of the coil.

The voltage appearing across the ends of the Rogowski coil is proportional to the time-derivative of the enclosed current,  $I$  [4]:

$$V = NA\mu \frac{dI}{dt} \quad (4.4)$$

$N$  is the number of turns in the coil,  $A$  is the cross-sectional area, and  $\mu$  is the permeability of the material inside the cross-section. The Rogowski coils on HSX are constructed with non-magnetic materials with a relative permeability of 1, so  $\mu = \mu_0$ . One of the Rogowski coils is mounted on the external side of the vacuum vessel, and the other one is installed on the internal side, inside of a helical steel tube identical in construction to the one shown in Figure 4.8. The signal from each coil is amplified with a gain factor,  $G$ , and low-pass filtered at 10 kHz. The time-derivative of  $I$  is given by

$$\frac{dI}{dt} = \frac{V}{GNA\mu} \quad (4.5)$$

The effective gain-area product,  $(GNA)$ , for each coil was determined while they were mounted in place by linking them with a multi-turn loop of wire which was driven by a signal generator and power amplifier. An independently calibrated Rogowski coil monitored the current in the multi-turn loop. The effective gain-area product of the internal coil is  $(GNA)_{internal} = 8.4 \pm 0.4 \text{ m}^2$ . For the external coil, it is  $(GNA)_{external} = 40. \pm 2. \text{ m}^2$ . The  $GNA$  factor for each coil has approximately 5% precision.

### 4.3 Magnetic Diagnostic Signal Processing

The reconstruction of the plasma pressure and current profiles depends on accurate measurements of the background vacuum magnetic field and of the magnetic field due to the plasma. The reconstruction also requires estimates of the uncertainties in these measurements. Data from several similar plasma shots are used to form ensemble averages. Calibration shots, similar to plasma shots except that there is no heating and no gas fueling, are also taken to measure the behavior of the vacuum magnetic field. The calibration shots help remove the largest components of the vacuum field, but small differences in the main field current from shot-to-shot exist and are accounted for in the data. The ultimate goal is to prepare the data for later use in V3FIT. The desired form for the magnetic diagnostic data is  $B_{total}$  and  $\sigma_{B_{total}}$ , where

$$B_{total}(t) = B_{vacuum} + B_{plasma}(t) \quad (4.6)$$

For simplicity, the main magnetic field is defined as a constant in time, where

$$B_{vacuum} = b_{d,1 \text{ Amp}} \times I_{Main \text{ Field}} \quad (4.7)$$

where  $b_{d,1 \text{ Amp}}$  is the calculated signal that diagnostic  $d$  would measure due to 1 amp of current in the main field coils for the particular magnetic configuration (i.e. from a Biot-Savart calculation or similar), and  $I_{Main \text{ Field}}$  is chosen as the mean value of the average current through the field coils, as measured by the main shunt resistor, during the time  $0.820 < t < 0.840 \text{ sec}$ . If  $\Delta t$  is the sampling time of the digitized signal,  $I_{MF,i}(t)$  is the main field current data at discrete time sample for shot  $i$ , and there are a total of  $n$  shots, then

$$I_{Main \text{ Field}} = \frac{1}{n} \sum_{i=1}^n \frac{1}{\# \text{ of } t \text{ samples}} \sum_{t=0.820}^{0.840} I_{MF,i}(t) \quad (4.8)$$

For a typical set of similar discharges that are analyzed, the main field current for a single shot,  $\left( \frac{1}{\# \text{ of } t \text{ samples}} \sum_{t=0.820}^{0.840} I_{MF,i}(t) \right)$ , varies no more  $\sim 0.30\%$  from the average,  $I_{Main \text{ Field}}$ . This point in time is approximately where the main field current has reached a ‘flat-top’ peak. The main field current is not used in the reconstruction process as a free parameter (section 4.6). It is treated as a ‘known quantity’ and is kept at the same value during each iteration of the minimization loop, and

has no uncertainty associated with it, so that  $\sigma_{B_{total}(t)} = \sigma_{B_{plasma}(t)}$  in the V3FIT reconstruction. Since the main field current is not a fit parameter in V3FIT, there is no need to estimate in an uncertainty in the main field signal.

$B_{plasma}(t)$  and  $\sigma_{B_{plasma}}(t)$  are needed. Relevant quantities that are measured by the diagnostics are  $\dot{B}_{d,i}(t)$  (the  $\dot{\phantom{x}}$  indicates a time derivative) for a typical magnetic diagnostic on shot  $i$ , and the time-derivative of the main field current,  $\dot{I}_{MF,i}$ . There is not an absolute measurement of  $B_d(t)$ . To account for this, the value of  $\Delta B_{d,i}(t)$  is defined as 0 for  $t \leq 0.800 \text{ sec}$ , and for  $t > 0.800 \text{ sec}$ , where  $\Delta t$  is the sampling time interval of the digitized signal

$$\Delta B_{d,i}(t) = \Delta t \sum_{t'=0.800}^t \dot{B}_{d,i}(t') \quad (4.9)$$

$$B_{total,i}(t) = B_{vacuum} + \Delta B_{d,i}(t) \quad (4.10)$$

After  $t = 0.800 \text{ sec}$ , the ECRH is turned on. This summation process, starting at  $t = 0.800 \text{ s}$ , acts as a numerical integrating ‘gate’ for the  $\Delta B_{d,i}(t)$  signal. The changes in the magnetic field,  $\Delta B_d(t)$  after  $t = 0.800$  are assumed to be from one of two sources: 1) Changes in the currents in the plasma, which generate  $\dot{B}_{plasma,i}$  or 2) Changes in the main field current,  $\dot{I}_{MF}$ , which we want to remove from the signal. Other sources of current, such as currents in the vacuum vessel or surrounding structure are not directly modeled at this point.

First, consider a set of calibration shots,  $j = 1 \dots m$ , and a diagnostic ‘d’

$$\dot{B}_{d,j,cal}(t) = b_{d,1 \text{ Amp}} \times \dot{I}_{MF,j,cal}(t) \quad (4.11)$$

An averaged calibration shot and variance are defined as

$$\overline{\dot{B}}_{d,cal}(t) = \frac{1}{m} \sum_{j=1}^m \dot{B}_{d,j,cal}(t) = b_{d,1 \text{ Amp}} \times \overline{\dot{I}}_{MF,cal}(t) \quad (4.12)$$

$$\sigma_{\overline{\dot{B}}_{d,cal}}^2(t) = \frac{1}{m-1} \sum_{j=1}^m \left( \overline{\dot{B}}_{d,cal}(t) - \dot{B}_{d,j,cal}(t) \right)^2 \quad (4.13)$$

For a set a plasma shots,  $i = 1 \dots n$ ,

$$\dot{B}_{d,i,pl}(t) = \dot{B}_{d,i,plasma}(t) + b_{d,1 \text{ Amp}} \times \dot{I}_{MF,i,pl}(t) \quad (4.14)$$



The difference between the plasma and average calibration shots is

$$\dot{B}_{d,i,pl}(t) - \bar{\dot{B}}_{d,cal}(t) = \dot{B}_{d,plasma,i}(t) + b_{d,1 \text{ Amp}} \times \dot{I}_{MF,i,pl}(t) - b_{d,1 \text{ Amp}} \times \bar{\dot{I}}_{MF,cal}(t) \quad (4.15)$$

$$\dot{B}_{d,i,plasma}(t) = \dot{B}_{d,i,pl}(t) - \bar{\dot{B}}_{d,cal}(t) - b_{d,1 \text{ Amp}} \left( \dot{I}_{MF,i,pl}(t) - \bar{\dot{I}}_{MF,cal}(t) \right) \quad (4.16)$$

Performing a time-integral

$$B_{d,i,plasma}(t) = \int_{t'=0.800}^t dt \left( \dot{B}_{d,i,pl}(t') - \bar{\dot{B}}_{d,cal}(t') - b_{d,1 \text{ Amp}} \left( \dot{I}_{MF,i,pl}(t) - \bar{\dot{I}}_{MF,cal}(t) \right) \right) \quad (4.17)$$

In terms of digitized data, the integral becomes a sum,

$$B_{d,i,plasma}(t) = \sum_{t'=0.800}^t \Delta t \left( \dot{B}_{d,i,pl}(t') - \bar{\dot{B}}_{d,cal}(t') - b_{d,1 \text{ Amp}} \left( \dot{I}_{MF,i,pl}(t) - \bar{\dot{I}}_{MF,cal}(t) \right) \right) \quad (4.18)$$

An average rate-of-change of the magnetic signals is

$$\begin{aligned} \bar{\dot{B}}_{d,plasma}(t) &= \frac{1}{n} \sum_{i=1}^n \left( \dot{B}_{d,i,pl}(t) - \bar{\dot{B}}_{d,cal}(t) - b_{d,1 \text{ Amp}} \left( \dot{I}_{MF,i,pl}(t) - \bar{\dot{I}}_{MF,cal}(t) \right) \right) \quad (4.19) \\ &= \frac{1}{n} \sum_{i=1}^n \left( \dot{B}_{d,i,pl}(t) - b_{d,1 \text{ Amp}} \dot{I}_{MF,i,pl}(t) \right. \\ &\quad \left. - \bar{\dot{B}}_{d,cal}(t) + b_{d,1 \text{ Amp}} \bar{\dot{I}}_{MF,cal}(t) \right) \quad (4.20) \end{aligned}$$

for which the variance is

$$\begin{aligned} \sigma_{\dot{B}_{d,plasma}}^2(t) &= \sigma_{\dot{B}_{d,cal}}^2(t) + b_{d,1 \text{ Amp}}^2 \sigma_{\dot{I}_{MF,cal}}^2(t) + \\ &\quad \frac{1}{n-1} \sum_{i=1}^n \left( \bar{\dot{B}}_{d,plasma}(t) - \left( \dot{B}_{d,i,pl}(t) - \bar{\dot{B}}_{d,cal}(t) - b_{d,1 \text{ Amp}} \left( \dot{I}_{MF,i,pl}(t) - \bar{\dot{I}}_{MF,cal}(t) \right) \right) \right)^2 \end{aligned} \quad (4.21)$$

The magnetic field due to the plasma on diagnostic ‘d’ is

$$\bar{B}_{d,plasma}(t) = \Delta t \sum_{t'=0.800}^t \bar{\dot{B}}_{d,plasma}(t) \quad (4.22)$$

The variance of the magnetic field due to the plasma is

$$\sigma_{B_{d,plasma}}^2(t) = \sum_{t'=0.800}^t \left( \Delta t \sigma_{\bar{\dot{B}}_{d,plasma}}(t') \right)^2 \quad (4.23)$$

The current in the main field coils is measured by two separate methods. The first method, a shunt resistor, measures a signal that is directly proportional to the current in the main field coils. The second method, a Rogowski coil wrapped around one of the field coils, measures the time derivative of the current in the field coils. Each main field coil has 14 turns. The shunt resistor is digitized by a 12-bit digitizer and a single bit in the measurement is on the order of 150 amps. The Rogowski coil, with a sensitivity of  $3.31 \cdot 10^{-7} \frac{V-s}{A}$  is amplified with a gain of 50  $V/V$  and digitized with a 16-bit digitizer with an effective signal range of  $\pm 1V$ . With this configuration the Rogowski coil is sensitive to changes as small as 0.007  $A$  over the length of the shot, 50  $ms$ . During the field ramp up and ramp down, the digitized Rogowski signal is saturated, so the time-integrated signal is scaled to fit the shunt signal from  $t = 0.6 \rightarrow 0.9$  sec, Figure 4.10. The Rogowski is a more precise measurement of the time-derivative of the main field current, but still needs to be calibrated against the main shunt to determine the absolute value. It is the Rogowski signal that is used as  $\dot{I}_{MF}$ , above.

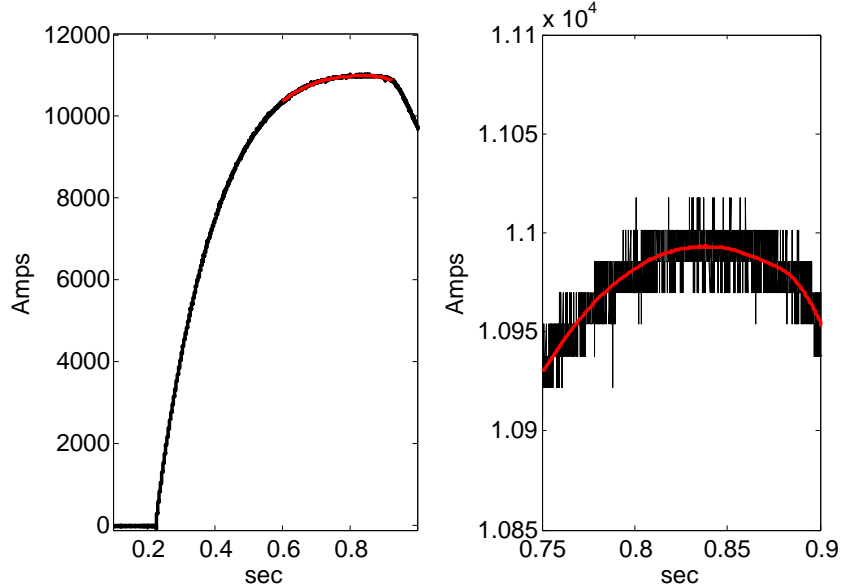


Figure 4.10 Main field current measured by the shunt resistor (black) and Rogowski coil (red).

For each triplet,  $i$ , the uncertainty in the magnitude of the measured field,  $\sigma_{i,Mag}$ , was estimated in appendix F. The uncertainty in each channel of triplet  $i$ , due to this is

$$\sigma_{i,k,Mag}(t) = \sigma_{i,Mag} \cdot \bar{B}_{i,k}(t) \quad (4.24)$$

where  $k = (x, y, z)$ . To account for the uncertainty in the location and orientation of the external magnetic vector diagnostics, an estimate of the angular misalignment is used to calculate the uncertainty for each channel, Eqn F.11:  $\sigma_{B_{i,k,MA}}(t)$ . The total uncertainty in the measured signal for each channel,  $k = (x, y, z)$ , of a triplet with poloidal index  $i$  is

$$\sigma_{i,k}(t) = \sqrt{\sigma_{B_{i,k,plasma}}^2(t) + \sigma_{B_{i,k,MA}}^2(t) + \sigma_{i,k,Mag}^2(t)} \quad (4.25)$$

The measured magnetic field components and uncertainties on a triplet are shown in Figure 4.11. The orthogonal x-, y-, and z- components are shown separately.

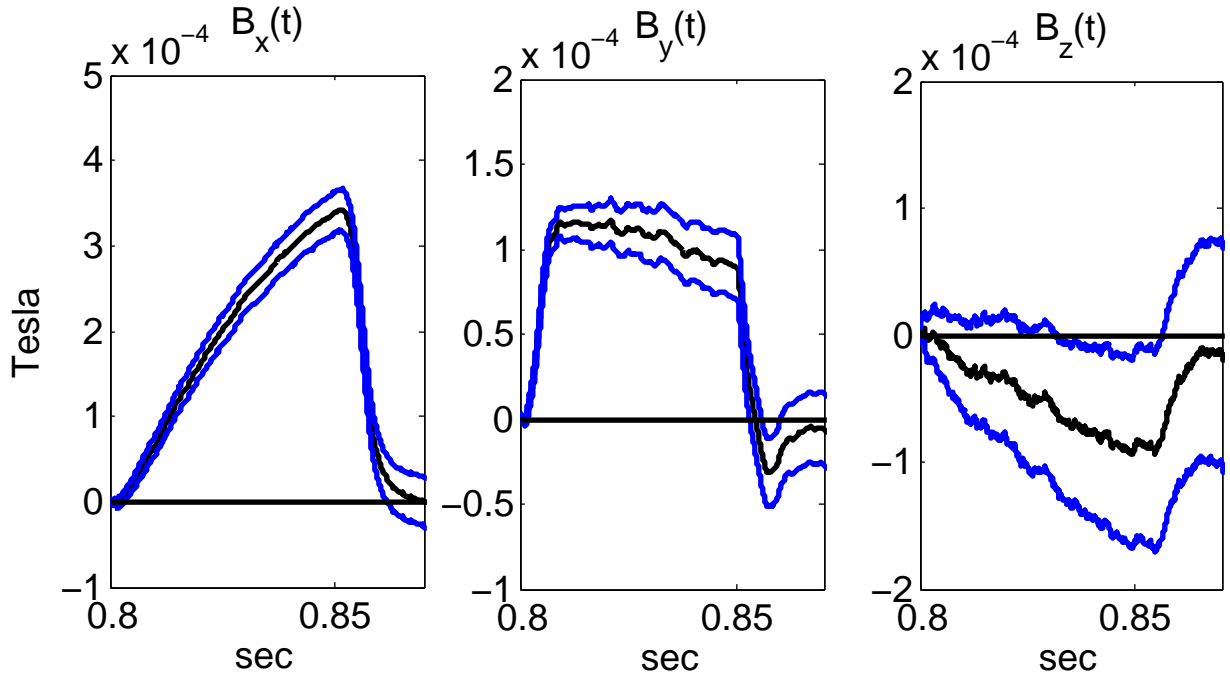


Figure 4.11 The x-, y-, and z- components of the calculated magnetic vector,  $\vec{B}_i$  (black) along with  $1-\sigma$  uncertainties for an external magnetic diagnostic triplet (blue).

The magnitude of the magnetic field component and uncertainty measured by the internal magnetic diagnostics are given by Eqns 4.22 and 4.23. The alignment of the internal diagnostics has

been discussed in appendix F, and no reliable estimate has been made. The uncertainty in the gain of the coil+amplifier system is estimated, conservatively at 5%. However, the internal diagnostics gain an additional signal drift during the plasma discharge. It is related to the presence of the plasma, but a direct correlation with other measurable plasma quantities has not been determined. This drift appears to occur while the electron cyclotron heating is applied and only after plasma breakdown occurs. Additional signal processing is applied to remove this drift. First, a linear offset is matched to the signal after the plasma signal decays. This line is projected back in time to a point at ECH turn-off. Next, a line is calculated to connect this value to the zero value at ECH turn-on. These two lines are subtracted from the integrated signal to arrive at a post-processed magnetic signal for that poloidal channel. Figure 4.12 shows the original signal, the linear offsets and final signal. This drift is only significant on a few of the internal diagnostics. For most coils, the drift is  $0.25 - 0.4 \times 10^{-4} T$  or less, as shown in Figure 4.13. No uncertainty is estimated for this drift. An example of the magnetic field component measured by the poloidal array and the standard deviation of the signal is shown in Figure 4.14.

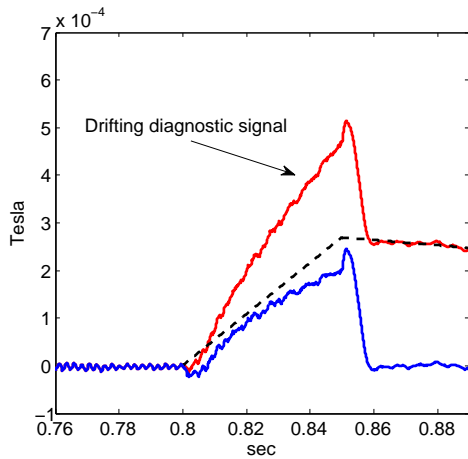


Figure 4.12 The measured field due to the plasma before offset removal (red) and after (blue). The offset line is shown (black, dashed). A large drift occurs during the plasma on this diagnostic.

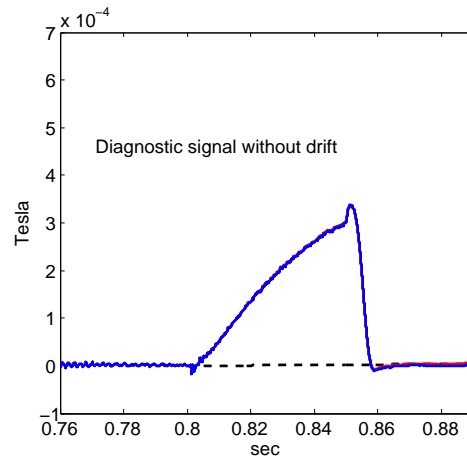


Figure 4.13 The measured field due to the plasma before offset removal (red) and after (blue). The offset line is shown (black, dashed). No significant drift appears on this diagnostic.

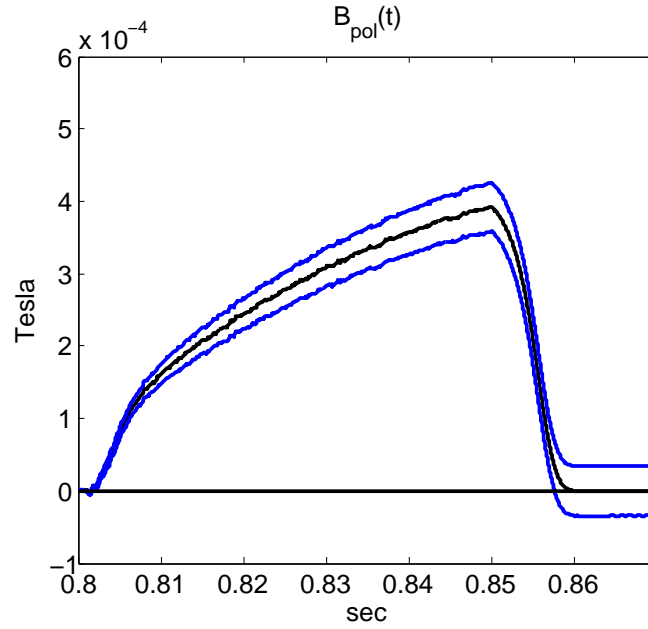


Figure 4.14 Calculated poloidal magnetic field for an internal poloidal diagnostic (black) and 1- $\sigma$  uncertainties (blue).

Two Rogowski coils measure the net plasma current in HSX. One of the coils is mounted on the external side of the vacuum vessel and the other other is internal to the vacuum vessel, installed inside of a flexible steel hose similar to that of the internal poloidal array, Figure 4.8. The signal for each coil is time-integrated for each plasma and calibration shot. With Eqn 4.5, the current measured by each coil is

$$I_{Rog} = \int dt \frac{V}{GNA\mu} \quad (4.26)$$

The Rogowski coils are not perfect and pick up some signal due to the vacuum field from the main field coils, so the mean and variance of the  $n$  calibration signals is calculated:

$$\bar{I}_{Rog,Cal}(t) = \frac{1}{n} \sum_{i=1}^n I_{Rog}(t) \quad (4.27)$$

$$\sigma_{\bar{I}_{Rog,Cal}}^2(t) = \frac{1}{n-1} \sum_{i=1}^n (\bar{I}_{Rog,Cal}(t) - I_{Rog}(t)) \quad (4.28)$$

The mean and variance of the current for the  $m$  plasma shots is calculated, after subtracting the calibration signal:

$$\bar{I}_{Rog,Plasma}(t) = \frac{1}{m} \sum_{i=1}^m I_{Rog}(t) - \bar{I}_{Rog,Cal}(t) \quad (4.29)$$

$$\begin{aligned} \sigma_{\bar{I}_{Rog,Plasma}}^2(t) &= \frac{1}{m-1} \sum_{i=1}^m (\bar{I}_{Rog,Plasma}(t) - I_{Rog}(t) - \bar{I}_{Rog,Cal}(t))^2 \\ &+ \sigma_{\bar{I}_{Rog,Cal}}^2(t) \end{aligned} \quad (4.30)$$

Finally, an arbitrary integration constant is removed from this signal to set the net current to 0 at  $t = 0.800 \text{ sec}$ , when the ECH is turned on.

$$I_{Rog,Plasma,Comp}(t) = \bar{I}_{Rog,Plasma}(t) - \bar{I}_{Rog,Plasma}(t = 0.800) \quad (4.31)$$

Because one of the coils lies on the inside of the vessel and one is on the outside, the net toroidal current in the vacuum vessel is

$$I_{Vessel}(t) = I_{Ext.Rog,Plasma,Comp}(t) - I_{Int.Rog,Plasma,Comp}(t) \quad (4.32)$$

$$\sigma_{I_{Vessel}}^2(t) = \sigma_{\bar{I}_{Ext.Rog,Plasma}}^2(t) + \sigma_{\bar{I}_{Int.Rog,Plasma}}^2(t) \quad (4.33)$$

The compensated signals for the external and internal Rogowski coils, Eqn 4.31, and the current in the vessel, Eqn 4.32 are shown in Figure 4.15 for a set of similar plasma discharges in QHS. After ECH turn-on, the net current measured by the internal coil increases faster than that measured by the external coil. After ECH turn-off, the current decreases faster on the internal coil. The difference between the internal and external Rogowskis indicates that several 10's of amps are induced in the vacuum vessel and decays during the shot. Long after ECH turn-off, the measured currents have returned to 0.

#### 4.4 Effects of the Vacuum Vessel

Fast fluctuations or changes in magnetic flux due to currents in the plasma are attenuated by the type 304 stainless steel vessel [5]. The skin frequency of the vacuum vessel, which is a good conductor with permeability  $\mu \approx \mu_0 = 4\pi \cdot 10^{-7} \text{ H/m}$ , conductivity  $\sigma = (72\mu\Omega\text{-cm})^{-1}$ , and

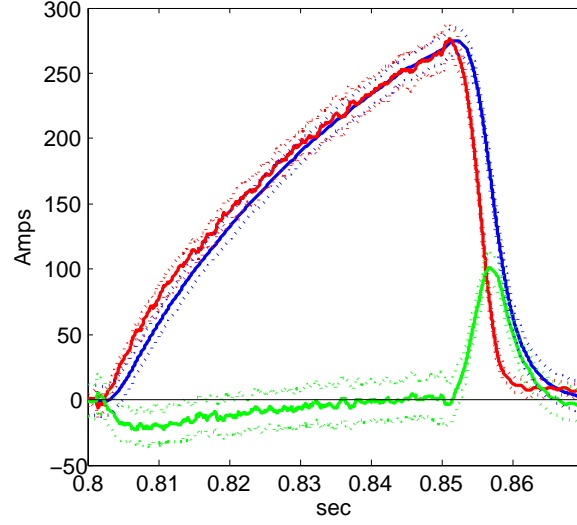


Figure 4.15 The compensated net current during a set of plasma discharges in QHS as measured by the internal Rogowski (red) and external Rogowski (blue). The difference of these two signals is the vessel current (green). 1- $\sigma$  uncertainties are shown as dotted lines.

width  $d = 6.35 \text{ mm}$ , is given by [6]:  $f_{1/e} = (\pi\mu\sigma d^2)^{-1} \text{ Hz}$ . Variations in magnetic flux above this frequency are effectively filtered with a 3-dB frequency of  $f_{3dB} \approx 0.693f_{1/e} = 3.1 \text{ kHz}$ .

Net toroidal currents in the vessel are inferred from measurements, but the magnitude is small and tend to decay during the plasma discharge, Figure 4.15. The magnetic field generated by this current in the vessel can be estimated by approximating the vacuum vessel as a cylinder. The diagnostics lie on this cylinder along a contour with a circumference of  $\approx 1.2 \text{ m}$ . The poloidal magnetic field due to the current in the vessel in the axial direction can be calculated from Ampere's law,  $\int dl B_{pol} = \mu_0 I_{vessel}$ . If the current is distributed uniformly in the poloidal direction around the vessel, then

$$\int dl B_{pol} \approx B_{pol} \int dl = 1.2 B_{pol} = \mu_0 I_{vessel} \quad (4.34)$$

$$B_{pol} \approx \frac{\mu_0 I_{vessel}}{1.2} \quad (4.35)$$

This estimate gives  $B_{pol} \approx 2 \times 10^{-5} \text{ T}$  early in the discharge and  $B_{pol} \leq 5 \times 10^{-6} \text{ T}$  after 30 ms.

Local eddy currents which produce no net current are not considered, but will be discussed in section 6.3.

## 4.5 Response Functions to Rapidly Calculate Magnetic Signals

The generation of Green's function responses for a set of magnetic diagnostics is described here. The V3RFUN code [7], written in Fortran, is used to perform the numerical calculations presented. The outline here follows the method outlined in Ref. [7].

Consider a current-carrying wire described by the curve  $\mathbf{l}_i(s)$ . The magnetic diagnostic response of this loop of wire is determined by the flux that it encloses:

$$\Psi^i \equiv \iint_{S_i} d\mathbf{s}_i \cdot \mathbf{B} = \oint_{\mathbf{l}_i} d\mathbf{l}_i \cdot \mathbf{A} \quad (4.36)$$

$\mathbf{B}$  is the magnetic field and  $d\mathbf{s}$  is the differential surface area. The integration is taken over a surface enclosed by the loop,  $S_i$ . The second equality follows from Stokes' theorem where  $\mathbf{A}$  is the magnetic vector potential,  $d\mathbf{l}$  is the differential length vector and the integral is taken along the contour of the loop,  $\mathbf{l}_i$ . The vector potential is comprised of two parts. The first part is due to the current in the external field coils that generate the vacuum field and the second part is from currents in the plasma itself.

$$\mathbf{A} = \mathbf{A}_{coil} + \mathbf{A}_{plasma} \quad (4.37)$$

A third contribution would be from currents in other diagnostic loops around the machine, but the current in these loops is negligible compared to these first two sources and can be neglected.

The vector potential from the field coils can be written as a linear combination of coil currents,  $I_j$  and vector potentials due to unit current in each coil,  $\mathbf{a}_{coil}^j$ .

$$\mathbf{A}_{coil} = \sum_{j=coils} I_j \mathbf{a}_{coil}^j \quad (4.38)$$

The flux can also be expressed as a linear combination of mutual inductances,

$$\Psi_{coil}^i = \sum_{j=coils} I_j L_{ij} \quad (4.39)$$

where the mutual inductance between an external coil,  $j$ , and magnetic diagnostic,  $i$ , is defined as

$$L_{ij} = \oint_{\mathbf{l}_i} \mathbf{a}_{coil}^j \cdot d\mathbf{l}_i^{diag} \quad (4.40)$$



The vector potential in terms of an arbitrary current density,  $\mathbf{J}(\mathbf{x}')$ , is

$$\mathbf{A}(\mathbf{x}) = \frac{\mu_0}{4\pi} \int d^3\mathbf{x}' \frac{\mathbf{J}(\mathbf{x}')}{r} \quad (4.41)$$

Here,  $r = |\mathbf{x} - \mathbf{x}'|$ . Here, the diagnostic and external coils are modeled as thin elements, so the current density can be replaced by a line density,  $\mathbf{I} = I d\mathbf{l}$  and the volume integral changes to a contour integral:

$$\mathbf{A}(\mathbf{x}) = \frac{I\mu_0}{4\pi} \oint \frac{d\mathbf{l}'}{r} \quad (4.42)$$

For unit current, the vector potential is

$$\mathbf{a}(\mathbf{x}) = \frac{\mu_0}{4\pi} \oint \frac{d\mathbf{l}'}{r} \quad (4.43)$$

Now the mutual inductance,  $L_{ij}$ , can be written as

$$L_{ij} = \frac{\mu_0}{4\pi} \oint_{\mathbf{l}_i} \oint_{\mathbf{l}_j} \frac{d\mathbf{l}_i^{diag} \cdot d\mathbf{l}_j^{coil}}{|\mathbf{l}_i - \mathbf{l}_j|} \quad (4.44)$$

By reciprocity, the flux through diagnostic  $i$  due to a unit current in coil  $j$  is the same as the flux through coil  $j$  due to a unit current in diagnostic loop  $i$ :

$$L_{ij} = \oint_{\mathbf{l}_j} \mathbf{a}_{diag}^i \cdot d\mathbf{l}_j^{coil} \quad (4.45)$$

This expression shows that the response of the diagnostic due to currents in the coils can be determined from the vector potential of the diagnostic coil evaluated along the contour of the external coils:

$$\mathbf{a}_{diag}^i(\mathbf{x}) = \frac{\mu_0}{4\pi} \oint_{\mathbf{l}_i} \frac{d\mathbf{l}_i^{diag}}{|\mathbf{l}_i - \mathbf{x}|} \quad (4.46)$$

In V3RFUN, an expansion for Eqn 4.46 [8] involving elliptical integrals is evaluated numerically [9].

A Rogowski coil is constructed of many small loops wound on a guiding curve,  $\mathbf{m}_i$ . For one of these small loops, assumed to lie in a plane, the dominant component of a multipole expansion of Eqn 4.46 gives

$$\mathbf{a}_{diag}^i(\mathbf{x}) = \frac{\mu_0}{4\pi} \mathbf{w}_i \times \frac{\mathbf{x} - \mathbf{x}_i}{r^3} \quad (4.47)$$

where  $\mathbf{w}_i$  is the area of the loop times the unit vector normal to the surface of the loop and  $\mathbf{x}_i$  is the center of the loop. The vector  $\mathbf{w}_i$  is assumed to be tangent to the guide curve. If  $n_R$  is the number of turns, or loops of the Rogowski coil per unit length, and the quantity  $(n_R |\mathbf{w}_i|)$  is constant along  $\mathbf{m}_i$ , then the vector potential of the Rogowski coil can be written as

$$\mathbf{a}_{Rogowski}^i(\mathbf{x}) = n_R |\mathbf{w}_i| \frac{\mu_0}{4\pi} \int_{\mathbf{m}_i} d\mathbf{m}_i \times \frac{\mathbf{x} - \mathbf{m}_i}{|\mathbf{x} - \mathbf{m}_i|^3} \quad (4.48)$$

A unit current along the guide path will generate a magnetic field of

$$\mathbf{b}_{Rogowski}^i(\mathbf{x}) = \frac{\mu_0}{4\pi} \int_{\mathbf{m}_i} d\mathbf{m}_i \times \frac{\mathbf{x} - \mathbf{m}_i}{|\mathbf{x} - \mathbf{m}_i|^3} \quad (4.49)$$

so the magnetic vector potential for a Rogowski coil is simply

$$\mathbf{a}_{Rogowski}^i(\mathbf{x}) = n_R |\mathbf{w}_i| \mathbf{b}_{Rogowski}^i(\mathbf{x}) \quad (4.50)$$

The plasma contribution to the total magnetic vector potential, the second part in Eqn 4.37, can also be found using a similar procedure. Using Eqns 4.36 and 4.41, the magnetic flux enclosed by a diagnostic coil due to the current,  $\mathbf{J}_{plasma}$ , in the volume of the plasma,  $V_p$ , is

$$\Psi_{plasma}^i = \frac{\mu_0}{4\pi} \oint_{\mathbf{l}_i} d\mathbf{l}_i^{diag} \cdot \int_{V_p} d^3\mathbf{x}' \frac{\mathbf{J}_{plasma}(\mathbf{x}')}{|\mathbf{l}_i - \mathbf{x}'|} \quad (4.51)$$

$$= \int_{V_p} d^3\mathbf{x}' \mathbf{J}_{plasma}(\mathbf{x}') \cdot \frac{\mu_0}{4\pi} \oint_{\mathbf{l}_i} \frac{d\mathbf{l}_i^{diag}}{|\mathbf{l}_i - \mathbf{x}'|} \quad (4.52)$$

$$= \int_{V_p} d^3\mathbf{x}' \mathbf{J}_{plasma}(\mathbf{x}') \cdot \mathbf{a}_{diag}^i(\mathbf{x}') \quad (4.53)$$

The plasma equilibrium is solved by VMEC which uses a set of coordinates  $(\Phi, \theta, \zeta)$  where  $\Phi$  is the enclosed toroidal flux,  $\theta$  is a poloidal flux coordinate angle, and  $\zeta$  is the geometric toroidal angle. The current distribution is expressed in contravariant form:

$$\mathbf{J}_{plasma} = J^\theta \mathbf{e}_\theta + J^\zeta \mathbf{e}_\zeta \quad (4.54)$$

VMEC assumes well-defined closed flux surfaces, so the MHD equilibrium requires that the radial current is 0,  $J^\Phi = 0$ . The inverse mapping of the flux surfaces between cylindrical and flux

coordinates is also calculated by VMEC:  $R(\Phi, \theta, \zeta)$  and  $Z(\Phi, \theta, \zeta)$ . The magnetic vector potential in Eqn 4.53 is expressed in a cylindrical coordinate  $(R, \phi, Z)$  covariant form and converted to flux coordinate covariant form:

$$\mathbf{a}_{diag}^i(\mathbf{x}') = a_R^i \mathbf{e}^R + R a_\phi^i \mathbf{e}^\phi + a_Z^i \mathbf{e}^Z \quad (4.55)$$

$$\begin{aligned} &= a_R^i \left( \frac{dR}{d\Phi} \mathbf{e}^\Phi + \frac{dR}{d\theta} \mathbf{e}^\theta + \frac{dR}{d\zeta} \mathbf{e}^\zeta \right) \\ &\quad + R a_\phi^i \left( \frac{d\phi}{d\Phi} \mathbf{e}^\Phi + \frac{d\phi}{d\theta} \mathbf{e}^\theta + \frac{d\phi}{d\zeta} \mathbf{e}^\zeta \right) \\ &\quad + a_Z^i \left( \frac{dZ}{d\Phi} \mathbf{e}^\Phi + \frac{dZ}{d\theta} \mathbf{e}^\theta + \frac{dZ}{d\zeta} \mathbf{e}^\zeta \right) \end{aligned} \quad (4.56)$$

The  $_{diag}$  subscript has been suppressed on the terms of the right hand side. The terms involving  $\mathbf{e}^\Phi$  do not survive the dot product in Eqn 4.53,  $\frac{d\phi}{d\theta} \equiv 0$ , and  $\phi = \zeta$  (defined in VMEC), so

$$\Psi_{plasma}^i = \int_{V_p} d^3\mathbf{x}' \left[ J^\theta \left( a_R^i \frac{dR}{d\theta} + a_Z^i \frac{dZ}{d\theta} \right) + J^\zeta \left( a_R^i \frac{dR}{d\zeta} + R a_\phi^i + a_Z^i \frac{dZ}{d\zeta} \right) \right] \quad (4.57)$$

In general, the plasma current density, flux coordinates and inverse coordinates in Eqn 4.57 all vary with different equilibrium solutions. However, the vector potential components,  $(a_R^i, a_Z^i, a_\phi^i)$ , are calculated once and stored by V3RFUN. The domain is a cylindrical coordinate grid that covers all possible location of current density and shares the same geometric toroidal angle as the VMEC equilibrium. Once the equilibrium is solved, the vector potential components are interpolated with a bilinear formula and Eqn 4.57 is evaluated.

The mutual inductances between the diagnostic coils and external field coils, Eqn 4.45 and response functions for plasma currents,  $(a_R^i, a_Z^i, a_\phi^i)$ , are calculated once for each diagnostic and stored by V3RFUN. The external magnetic vector diagnostics are each modeled as three orthogonal circular magnetic probes with the same surface area as the square face of the triplet. The calculated flux is divided by the area, so the final output is a signal in units of Tesla. The internal diagnostics are also modeled as circular magnetic probes, but with a radius of  $1/4'' = 3.175 \text{ mm}$ . The V3RFUN code does not use the information about the number of turns or size of the Rogowski coils, so the signal that is returned is just  $(\int d\mathbf{l} \cdot \mathbf{B}) / (\int dl)$  which also has units in Tesla. This means that the Rogowski signal and uncertainty are multiplied by  $\mu_0/L$  where  $L$  is the length of

the Rogowski coil.

$$B_{Rog,Plasma,Comp}(t) = \frac{\mu_0}{L} I_{Rog,Plasma,Comp}(t) \quad (4.58)$$

$$\sigma_{\tilde{B}_{Rog,Plasma,Comp}}^2(t) = \frac{\mu_0}{L} \sigma_{\tilde{I}_{Rog,Plasma,Comp}}^2(t) \quad (4.59)$$

The equilibrium is calculated by VMEC and then the V3FIT [13] code evaluates Eqns 4.39 and 4.57 to determine the total magnetic signal for a diagnostic coil. This process of calculating the expected magnetic signals for a plasma equilibrium is called the ‘forward-problem’. The V3FIT code is also capable of reconstructing the plasma profile properties (current and pressure) based on the signals measured by the diagnostics. That process is described next.

#### 4.6 Modeling and Reconstruction of Plasma Pressure and Current Profiles

The solution of the 3D-MHD equilibrium is provided by VMEC, discussed in Appendix A. VMEC uses the lab coordinates of the magnetic field coil set and main field current to determine the vacuum magnetic field. Each field coil is modeled as a set of current filaments which are directed along the contour of the coil. To model the plasma profiles in HSX, the Lorentz-type profile (see Appendix A) with  $AM(0) = AM(1) = AM(2) = AM(4) = 1$  is chosen. The pressure profile has 2 free parameters:  $PRES\_SCALE$  and  $AM(3)$ :

$$p(s) = PRES\_SCALE \left[ \frac{1}{N_0} \left( (1 + s^{AM(3)})^{-1} - c_0 \right) \right] \quad (4.60)$$

The normalization terms are

$$c_0 = (1 + s^{AM(3)})^{-1} \quad (4.61)$$

$$N_0 = 1 - c_0 \quad (4.62)$$

The enclosed toroidal current profile is described by an arctangent function (see Appendix A) with  $AC(0) = AC(5) = AC(9) = AC(13) = AC(17) = 0$ ,  $AC(1) = AC(4) = 1$ , and  $AC(3) = 3/2$ . This profile has 2 free parameters:  $CURTOR$  and  $AC(2)$ :

$$I_{enclosed}(s) = CURTOR \frac{2}{\pi} \arctan \left( \frac{AC(2)s^{3/2}}{1 - s} \right) \quad (4.63)$$

The net toroidal flux enclosed by the last flux surface,  $PHIEDGE$  is also a free parameter. There are a total of 5 free parameters to describe the plasma equilibrium. The free parameters are denoted as the set  $\mathbf{p}$ . The magnetic diagnostic signals calculated by V3FIT [13] for this set of parameters is  $S_{m,i}(\mathbf{p})$ . The observed diagnostic signals,  $S_{o,i}$ , are the sum of the plasma and vacuum field contributions, Eqns 4.6 and 4.22. The uncertainty of the observed signals is  $\sigma_i$ , given by either Eqn 4.23 or 4.25.

V3FIT also includes information about a limiter. The ‘signal’ associated with the limiter is the distance from the last closed flux surface to the edge of the limiter. The position of the limiter during the experiment is at the calculated vacuum last closed flux surface,  $S_{o,limiter} = 0$  with an uncertainty of  $\sigma_{limiter} = 1 \text{ mm}$ .

The reconstruction process that V3FIT employs is a nonlinear least-squares minimization routine and uses singular value decomposition (SVD) to approximate a quasi-newton algorithm for choosing new parameters. Non-linear minimization is a nontrivial problem, one that has encompassed many decades of work and continues to be an active field of research. Many excellent references cover the basic challenges of nonlinear minimization, including References [10], [11] and [12]. The technique involved here is described in reference [13] and [14].

The quantity that is minimized to find an optimal solution is the mismatch between the measured and observed signals, weighted by their respective uncertainty:

$$\chi^2(\mathbf{p}) = \sum_i \kappa_i \left( \frac{S_{o,i} - S_{m,i}(\mathbf{p})}{\sigma_i} \right)^2 \quad (4.64)$$

The quantity,  $\kappa_i$ , is a weighting function to allow one to emphasize certain diagnostics during the reconstruction process. For the work here,  $\kappa_i \equiv 1, \forall i$ . By defining a dimensionless error vector,

$$e_i = \frac{\sqrt{\kappa_i}}{\sigma_i} (S_{o,i} - S_{m,i}(\mathbf{p})) \quad (4.65)$$

the  $\chi^2$  can be written as

$$\chi^2(\mathbf{p}) = \sum_i e_i e_i = \mathbf{e} \cdot \mathbf{e} \quad (4.66)$$

The components of a normalized parameter vector,  $\mathbf{a}$ , and the Jacobian matrix,  $\mathbf{J} = \nabla \mathbf{e}$ , are defined,

$$a_j = \frac{p_j}{\pi_j} \quad (4.67)$$

$$J_{ik} = -\frac{\partial e_i}{\partial a_k} \quad (4.68)$$

The number of columns in the Jacobian matrix is the same as the number of free parameters,  $m$ , and the number of rows is the same as the number of signals,  $n$ . The matrix is calculated as a single-sided finite difference for each parameter, where the finite difference for each parameter is  $\pi_j$ . A total of  $m + 1$  VMEC calculations are performed, one for each fit parameter and one for the initial state.

A Taylor-series expansion of  $\chi^2(\mathbf{a})$  is

$$\chi^2(\mathbf{a} + \delta \mathbf{a}) \approx \chi^2(\mathbf{a}) - 2\boldsymbol{\beta} \cdot \delta \mathbf{a} + \delta \mathbf{a} \cdot \boldsymbol{\alpha} \cdot \delta \mathbf{a} \quad (4.69)$$

The gradient vector,  $\boldsymbol{\beta}$ , and Hessian matrix,  $\boldsymbol{\alpha}$ , are defined as

$$\boldsymbol{\beta} = -\frac{1}{2} \nabla \chi^2 = \mathbf{J}^T \cdot \mathbf{e} \quad (4.70)$$

$$\boldsymbol{\alpha} = \frac{1}{2} \nabla \nabla \chi^2 = \mathbf{J}^T \cdot \mathbf{J} - \mathbf{e} \cdot \nabla \mathbf{J} \approx \mathbf{J}^T \cdot \mathbf{J} \quad (4.71)$$

A quasi-Newton method attempts to minimize  $\chi^2$  by locating where the gradient is 0,

$$\nabla \chi^2(\mathbf{a} + \delta \mathbf{a}) = -2\boldsymbol{\beta} + 2\boldsymbol{\alpha} \cdot \delta \mathbf{a} = 0 \quad (4.72)$$

which leads to

$$\boldsymbol{\alpha} \cdot \delta \mathbf{a} = \boldsymbol{\beta} \quad (4.73)$$

or,

$$\mathbf{J}^T \cdot \mathbf{J} \cdot \delta \mathbf{a} = \mathbf{J}^T \cdot \mathbf{e} \quad (4.74)$$

The change in parameters that is predicted to minimize  $\chi^2$  is  $\delta \mathbf{a}$ . The Hessian,  $\mathbf{J}^T \cdot \mathbf{J}$ , tends to be ill-conditioned, but SVD provides a useful way to deal with this situation.

The SVD decomposes a matrix,  $\mathbf{D}$ , of size  $n \times m$  into three matrices:

$$\mathbf{D} = \mathbf{U} \cdot \mathbf{W} \cdot \mathbf{V}^T \quad (4.75)$$

The matrix  $\mathbf{U}$  is orthonormal and has size  $n \times n$ .  $\mathbf{V}$  is also orthonormal and has size  $m \times m$ . The matrix  $\mathbf{W}$  is a diagonal matrix with the same size as  $\mathbf{D}$ , whose elements are sorted in decreasing order,  $W_{i,i} \geq W_{i+1,i+1}$ . A k-SVD inverse,  $\mathbf{D}^{(k)\sim 1}$  is defined such that the largest  $k$  elements in  $\mathbf{W}$  are replaced with their reciprocals, and the rest are set to 0.

$$W_{i,i}^{(k)\sim 1} = (W_{i,i})^{-1} \quad 1 \leq i \leq k \quad (4.76)$$

$$= 0 \quad i > k \quad (4.77)$$

Now, rather than solving Eqn 4.74 directly,  $\delta \mathbf{a} = (\mathbf{J}^T \cdot \mathbf{J})^{-1} \cdot \mathbf{J}^T \cdot e$ , the k-SVD inverse of  $(\mathbf{J}^T \cdot \mathbf{J})$ , is applied to find an approximate solution [15],

$$\delta \mathbf{a} \approx (\mathbf{J}^T \cdot \mathbf{J})^{(k)\sim 1} \cdot \mathbf{J}^T \cdot e \quad (4.78)$$

$$= (\mathbf{V} \cdot \mathbf{W} \cdot \mathbf{U}^T \cdot \mathbf{U} \cdot \mathbf{W} \cdot \mathbf{V}^T)^{(k)\sim 1} \cdot \mathbf{V} \cdot \mathbf{W} \cdot \mathbf{U}^T \cdot e \quad (4.79)$$

$$= (\mathbf{V} \cdot \mathbf{W}^2 \cdot \mathbf{V}^T)^{(k)\sim 1} \cdot \mathbf{V} \cdot \mathbf{W} \cdot \mathbf{U}^T \cdot e \quad (4.80)$$

$$= \mathbf{V} \cdot (\mathbf{W}^2)^{(k)\sim 1} \cdot \mathbf{V}^T \cdot \mathbf{V} \cdot \mathbf{W} \cdot \mathbf{U}^T \cdot e \quad (4.81)$$

$$= \mathbf{V} \cdot \mathbf{W}^{(k)\sim 1} \cdot \mathbf{U}^T \cdot e \quad (4.82)$$

$$= \mathbf{J}^{(k)\sim 1} \cdot \mathbf{e} \quad (4.83)$$

It is not necessary to calculate the Hessian, rather, only the k-SVD inverse of the Jacobian. Once  $\delta \mathbf{a}$  is calculated, the next guess of the normalized parameter vector that minimizes  $\chi^2$  is  $\mathbf{a} + \delta \mathbf{a}$ . The Jacobian is calculated, etc. The process is repeated until the value of  $\chi^2$  is no longer getting smaller and a minimum value is found.

If the errors on input signals are uncorrelated, and diagonal signal covariance matrix is given by  $\mathbf{C}$  with  $C_{ij} = \sigma_i^2 \delta_{ij}$ . The parameter covariance or posterior covariance matrix is then defined as [16]

$$\mathbf{C}_p = (\mathbf{J}^T \cdot \mathbf{C}^{-1} \cdot \mathbf{J})^{-1} \quad (4.84)$$

A measure of the confidence for fit parameter  $p_j$  is the

$$\sigma_{p,j} = \sqrt{(\mathbf{C}_p)_{jj}} \quad (4.85)$$

A measure of the effectiveness of a signal, simply called the "Signal Effectiveness" is defined as

$$R_{ji} = \frac{d \ln \sigma_{p,j}}{d \ln \sigma_i} \quad (4.86)$$

This quantity indicates how much the posterior confidence,  $\sigma_{p,j}$ , improves when the uncertainty on the  $i$ th diagnostic,  $\sigma_i$  is reduced. This is a local, in parameter space, estimate of the importance for a particular diagnostic and is not necessarily representative of the how useful a diagnostic is for reconstructing a particular parameter for a general profile.

Several parameters may be adjusted by the user of the V3FIT code to control its behavior. These include: the fit parameters,  $p_j$ , the finite difference variance,  $\pi_j$ , the threshold for the minimum  $W_{i,i}$  to include in the k-SVD inverse. A maximum threshold on the magnitude of the change in parameters,  $\delta a_{max}$  is an optional parameter. The maximum number of iterations to seek a minimum in  $\chi^2$  is also specified.

After the V3FIT code is completed and a set of reconstructed fit parameters is found, a reduced- $\chi^2$  value is calculated

$$\chi_{\nu,\min}^2 = \chi^2 / \nu \quad (4.87)$$

where  $\nu = n - m - 1$ . If  $\chi_{\nu}^2 \approx 1$ , then this indicates that the profile descriptions, i.e. the fit functions and fit parameters, are a good approximation of the actual profiles and agree well with the experimental data. If  $\chi_{\nu}^2 \gg 1$ , then the profile descriptions are a poor fit to the data and are not an appropriate description. If  $\chi_{\nu}^2 \ll 1$ , then the fit is not necessarily a better fit. It may indicate that there are too many free parameters in the model, or that the signal uncertainties have been overestimated.

The number of degrees of freedoms in a profile description can be adjusted simply by adding or removing fit parameters. Let's denote the value of  $\chi^2$  with a set of functions with  $m$  fit parameters as  $\chi^2(m)$ . If an additional fit parameter is added, the value is  $\chi^2(m + 1)$ . The  $F_{\chi}$  statistic



can provide an indication of whether or not the addition of an additional parameter significantly improves the fit.

$$F_\chi = \frac{\chi^2(m) - \chi^2(m+1)}{\chi^2(m+1)/(n-m-1)} = \frac{\Delta\chi^2}{\chi_\nu^2(m+1)} \quad (4.88)$$

If the addition of an additional term has improved the fit, then the value of  $F_\chi$  will be large. If the additional term does not significantly improve the fit, then  $\Delta\chi^2 \approx 0$  and  $F_\chi$  will be small.

One practical problem with this definition of Eqn 4.85 is that the Jacobian matrix,  $\mathbf{J}$ , is calculated with single-sided finite differences, so the 2nd order mixed partial derivatives are not directly calculated and the nonlinear relationship among the parameters is not captured very well. This leads to an overestimation of the parameter uncertainties. To overcome this limitation, the parameter space around the solution is scanned to determine the  $\chi_\nu^2$  value for a large variety of parameters. When the parameter space around the pressure profile is scanned, the current profile is held at the reconstructed parameterization. When the current profile is scanned, the pressure profile is also held constant. Profiles that satisfy

$$\chi_\nu^2 \lesssim \chi_{\nu,\min}^2 + 1 \quad (4.89)$$

are considered to fall within a single standard deviation interval of the reconstructed solution. This is not the traditional definition according to multivariate statistics. The more exact definition [17] would require all of the parameters for the pressure and current profile to be scanned simultaneously, but that is not done here because of the large amount of computational time that would be required to scan the 5-D parameter space ( $PRES\_SCALE$ ,  $AM(3)$ ,  $CURTOR$ ,  $AC(2)$ ,  $PHIEDGE$ ).

## References

- [1] Ali Abdou, Ph. D. dissertation, University of Wisconsin-Madison (2005).
- [2] P. H. Probert, private communication.
- [3] Romer Cimcore Model 5028, <http://us.romer.com>
- [4] I. H. Hutchinson, “Principles of Plasma Diagnostics”, Cambridge University Press, Cambridge, 1994.
- [5] 304/304L Stainless Steel Data Sheet, AK Steel, 2000, <http://www.aksteel.com>
- [6] Balanis, “Advanced Engineering Electromagnetics”, John Wiley & Sons, New York, 1989.
- [7] S. P. Hirshman, E. A., Lazarus, J. D. Hanson, S. F. Knowlton, & L. L. Lao, *Phys Plasmas* **11**, 595 (2004).
- [8] J. D. Jackson, “Classical Electrodynamics”, John Wiley & Sons, Inc., Hoboken, NJ, 1999.
- [9] W. H. Press, et al., “Numerical Recipes in FORTRAN”, Cambridge University Press, New York, NY, 1992.
- [10] Dennis Schnabel, “Numerical Methods for Unconstrained Optimization and Nonlinear Equations”, Prentice-Hall, Inc., Englewood Cliffs, New Jersey, 1983.
- [11] Kenneth Lange, “Optimization”, Springer-Verlag NY, LLC, New York, NY, 2004.
- [12] Jorge Nocedal and Stephen J. Wright, “Numerical Optimization”, Springer, Science+Business Media, New York, NY, 2006.
- [13] J. D. Hanson, et al., *Nucl. Fusion* **49**, 075031 (2009).
- [14] W. H. Press, S. A. Teukolsky, W. T. Vetterling, B. P. Flannery, “Numerical Recipes in FORTRAN, Second Edition”, Cambridge University Press, New York, NY, 1992.
- [15] Emanuele Trucco, Alessandro Verri, “Introductory Techniques for 3-D Computer Vision”, Prentice Hall, Upper Saddle River, NJ, 1998.

- [16] J.D. Hanson, et al., “Three-Dimensional Equilibrium Reconstruction: The V3FIT Code”, 2009 International Stellarator/Heliotron Workshop, Invited Talk (2009).
- [17] Philip R. Bevington, “Data Reduction and Error Analysis for the Physical Sciences”, McGraw-Hill, New York, NY, 2003.

## Chapter 5

### 3-D Equilibrium Reconstruction

The 3-D equilibrium reconstruction procedure begins with a set of plasma realizations that have similar measurements of: line-averaged central density, main field current, radiated power, and magnetic signals, including the diamagnetic flux loop, Rogowski coil and the rest of the diagnostics presented in Chapter 4. Examples of these will be shown in this chapter. These shots are also used to calculate the electron temperature and density profiles from the Thomson scattering data. A set of magnetic calibration shots provide data to characterize and remove the effects of the small changes in the vacuum field over time, Eqn 4.22. Once the signals due to the plasma currents are known, Section 4.3, the data is entered into the V3FIT input files as the observed data,  $S_{o,i}$ , (see Eqn 4.64).

Next, the measured  $T_e$ ,  $N_e$ , and  $T_i$  are used as input into PENTA, Section 2.3.2, to determine radial profiles of the radial electric field,  $E_r$ , bootstrap current density,  $J_b$ , and parallel conductivity,  $\sigma_{\parallel}$ . Multiple stable  $E_r$  roots may exist across regions of the plasma, and the  $J_b$  will vary between the regions of different  $E_r$ . The total bootstrap current is calculated for a set of limiting conditions: an electron-root dominant solution, an ion-root dominant solution and a ion-only solution, as discussed in the end of Section 2.4. A candidate for the ‘most-likely’ steady-state solution is selected by choosing the profile that has a total current that is closest to that extrapolated from the Rogowski data (discussed below). The selected bootstrap current density, parallel conductivity, and measured net toroidal current are then used as input for the codes `iota_evolution_generate` (IEG, Appendix E) to simulate the time evolution of the rotational transform, plasma current and plasma current density, Eqn 3.70. The results of the simulation is a current profile that serves as an ‘initial guess’ for the reconstruction process, Section 4.6. The initial guess of the plasma pressure

is calculated from the measured  $T_e$ ,  $N_e$ , and  $T_i$ . The V3FIT code is then executed to search for a set of plasma parameters that minimize the  $\chi^2$  statistic, Eqn 4.64, by applying SVD to the Jacobian matrix to estimate the minimization search vector, Eqn 4.83. A flowchart of this process is shown in Figure 5.1.

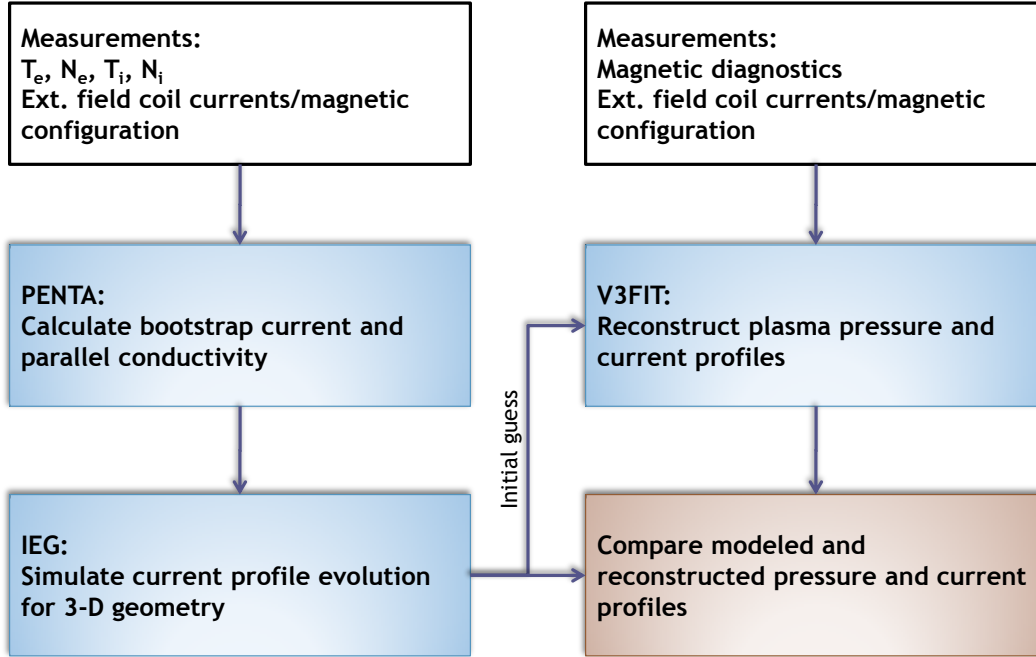


Figure 5.1 Flowchart showing the process from measured data to reconstructed plasma profiles.

For the data presented in this dissertation, the vacuum vessel was conditioned prior to plasma operations by depositing a layer of boron on the interior (vacuum-side) of the vessel by evaporating O-carborane into a helium glow discharge. In the past, before boron-conditioning was available, methane glow discharges were used to deposit a layer of carbon on the vacuum vessel. Each of these conditioning methods were found to be beneficial for plasma operations. Without this conditioning, impurity radiation and density would rise throughout the discharge until the plasma would reach a density cutoff, where the ECH waves would no longer penetrate and heat the plasma. The plasma profiles (temperature, density and current evolution) are different for these two cases of

Field Configuration	$\rho_{ECRH}$	$P_{ECRH,launched}$	$\bar{N}_e \times 10^{18}/m^3$	$I_{tor}(t = \infty)$
QHS CCW*	$\rho \lesssim 0.1$	50 kW	4.1	386. $\pm$ 23. A
QHS CW	$\rho \lesssim 0.1$	50 kW	4.2	-411. $\pm$ 46. A
QHS CCW*	$\rho \lesssim 0.1$	100 kW	4.1	352. $\pm$ 21. A
QHS CW	$\rho \lesssim 0.1$	100 kW	4.0	-343. $\pm$ 20. A
QHS CCW	$\rho \sim 0.3$	50 kW	3.1	167. $\pm$ 14. A
QHS CW*	$\rho \sim 0.3$	50 kW	3.0	-164. $\pm$ 11. A

Table 5.1 Configuration space explored with balanced fueling in the QHS configuration.

\* Reconstruction is presented in this chapter.

vessel conditioning. Typically, the temperatures and net current are higher with carbon conditioning, compared to boron conditioning. However, the radiated power is also higher with carbon, and fewer shots could be taken before a glow discharge cleaning cycle was necessary.

The plasma is heated by a 28 GHz gyrotron operated in 1st-harmonic O-mode. The microwaves are launched perpendicular to the magnetic axis from the outboard midplane at the symmetric boxport location, Figure 5.2. No direct ECH-driven current is expected with this configuration. To check for the possibility of an ECH-driven current, similar plasmas are generated with the main magnetic field in both the CCW and in the CW direction. In these ‘flip-field’ experiments, the bootstrap current is expected to reverse with the field direction and any differences may indicate the presence of ECH-driven current. The fueling location for these experiments is at the puff valve at field period A’ (A-prime), Figure 5.2. This is referred to as ‘balanced fueling’ in the sense that the gas fuel source is as far from the launch mirror as physically possible. Table 5.1 summarizes the parameter space explored under these conditions. For a particular heating power,  $P_{ECRH,Launched}$ , and resonance location,  $\rho_{ECRH}$ , the extrapolated steady state current was similar in magnitude but of opposite sign when the direction of the main magnetic field was reversed. The case with the largest level of steady state current is 50 kW,  $\rho \lesssim 0.1$  with  $|I_{tor}(t = \infty)| \sim 400$  A. The case with 100 kW,  $\rho \lesssim 0.1$  is estimated to have a steady state current of 50 A less, or  $|I_{tor}(t = \infty)| \sim 350$  A. The off-axis 50 kW heating case could not be controlled with  $\bar{N}_e \sim$

$4.0 \times 10^{18}/m^3$ , but  $\bar{N}_e \sim 3.0 \times 10^{18}/m^3$  was controllable, so the data comes from this latter case and the steady state current is  $|I_{tor}(t = \infty)| \sim 165$  A. For all of the cases, the fueling gas was hydrogen, and  $Z_{eff} \approx 1$  was assumed in the analysis. This is suggested by the low levels of carbon and oxygen impurity radiation observed during plasmas made with the boron-conditioned vacuum vessel walls, compared to the carbon-conditioned walls.

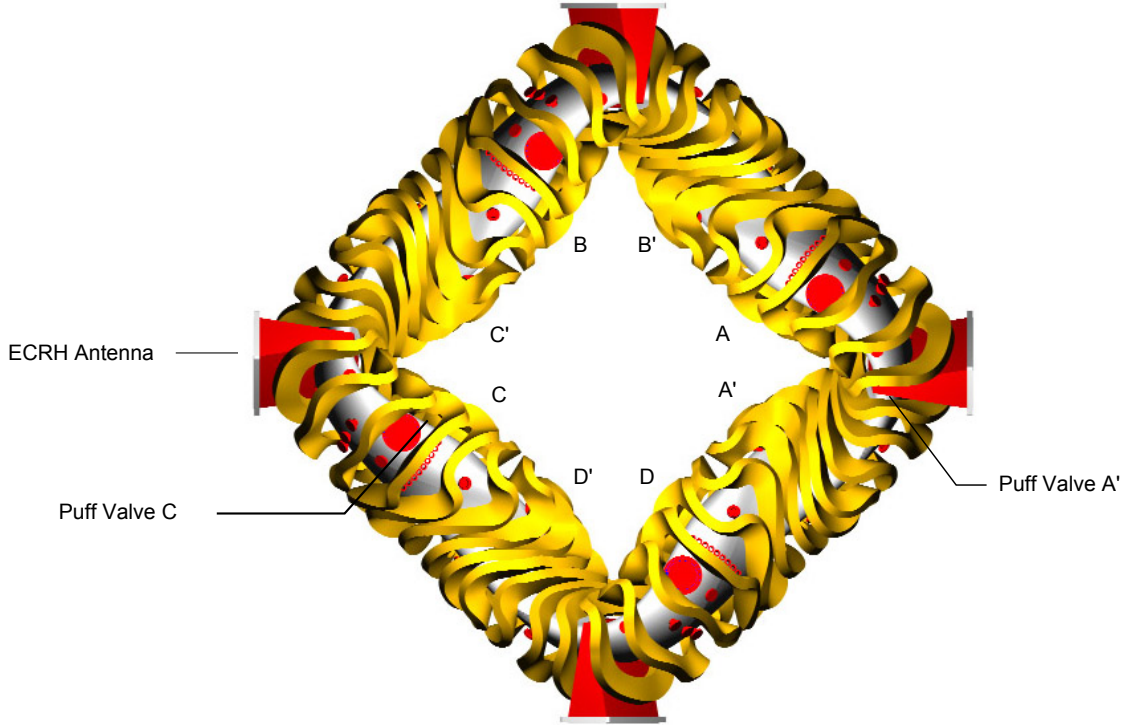


Figure 5.2 The HSX stellarator, viewed from above. The ECRH launch mirror is located at boxport C. One of two fueling valves can be used at a time. One is located near the ECRH launch point, in field period C, and the other is located far away, near boxport A.

## 5.1 QHS 50 kW with Balanced Fueling

The net toroidal current and loop voltage for the both the CCW (blue) and CW (red) plasmas are shown in Figures 5.3 and 5.4. The steady state estimate of the net toroidal current,  $I_\infty$ , and decay time,  $\tau$ , is extrapolated by fitting the measurement to

$$I(t) = I_\infty (1 - e^{-t/\tau}) \quad (5.1)$$

The measured current and voltage are reversed, and nearly identical in magnitude. The measured

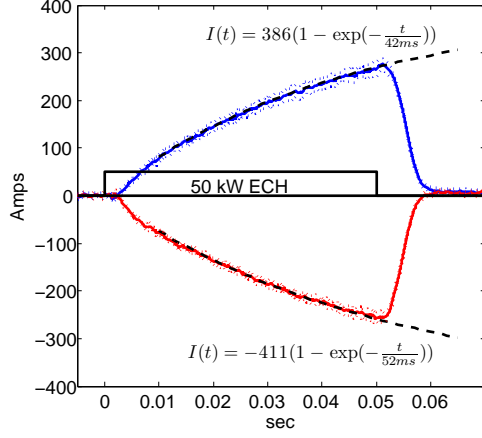


Figure 5.3 QHS, 50 kW,  $\rho_{ECRH} \lesssim 0.1$ : Measured net toroidal current for an ensemble average of 6 shots with the magnetic field in the CCW (blue) and CW (red) directions.

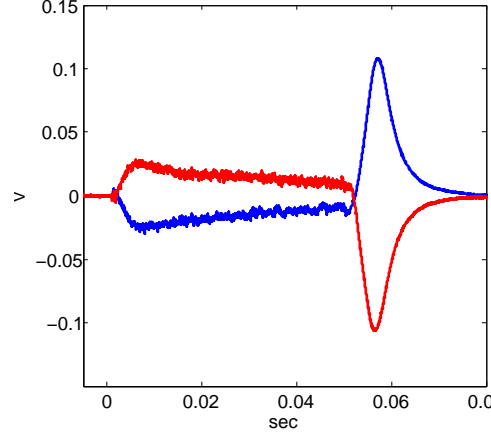


Figure 5.4 QHS, 50 kW,  $\rho_{ECRH} \lesssim 0.1$ : Measured loop voltage (ens. avg.).

net current at ECH turn off, the extrapolated decay time, and steady state current for the cases listed in Table 5.1 are shown in Figure 5.5. By doubling the heating power from 50 kW to 100 kW, the stored energy increases by about 50%.

The measured electron temperature and density profiles from the Thomson system at  $t = 0.030$  s for the shots from Figure 5.3 are in Figures 5.6 and 5.7. An estimate of the ion temperature, based on Doppler-broadening of a carbon-impurity emission line measured by the ChERS spectrometer is also shown. The temperatures and densities are very similar in both CCW and CW. The line averaged central density measured by the microwave interferometer for each case is  $\sim 4.1 \times 10^{18}/m^3$ , Figure 5.8. The diamagnetic signal for an internal flux loop is shown in Figure 5.9. The signals are reversed because the main field is reversed. There is about 54 J of stored energy in the CCW case and 45 J in the CW case. From the measured profiles, the calculated stored energy for the CCW and CW cases are 51 J and 49 J, which agrees well.

A subset of the magnetic diagnostic signals at the ECRH turn-off time, 50 ms, is shown in Figures 5.10 and 5.11. Every signal is very close in magnitude and flipped in sign. This also holds



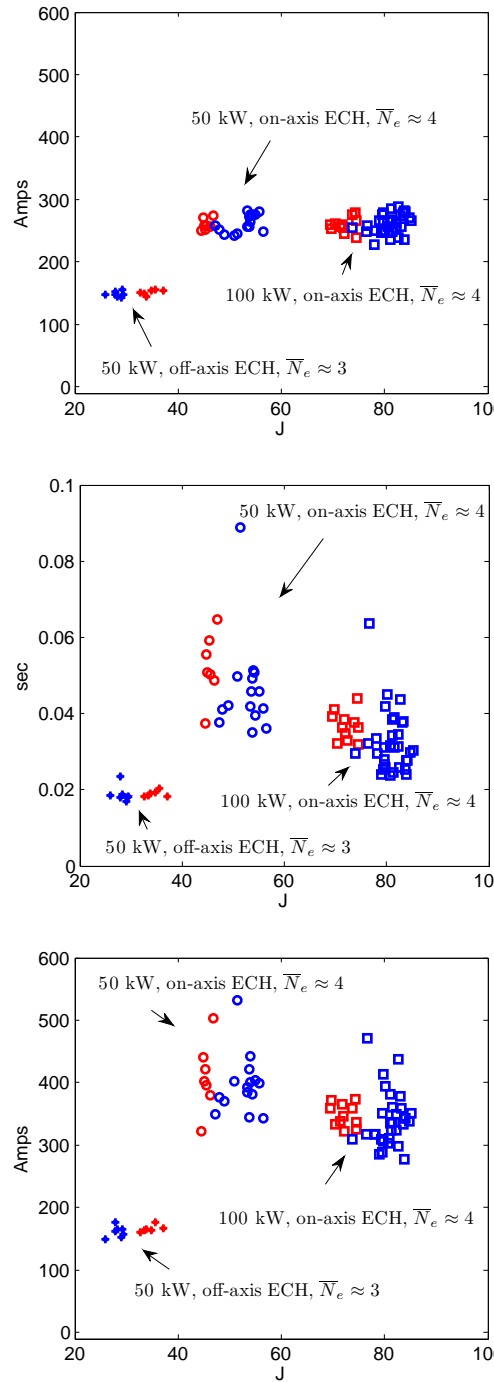


Figure 5.5 The net toroidal current at ECH turn-off (top), the estimated decay time (center), and the extrapolated steady state value (bottom) for conditions indicated. CCW cases are in blue, and CW cases are in red.

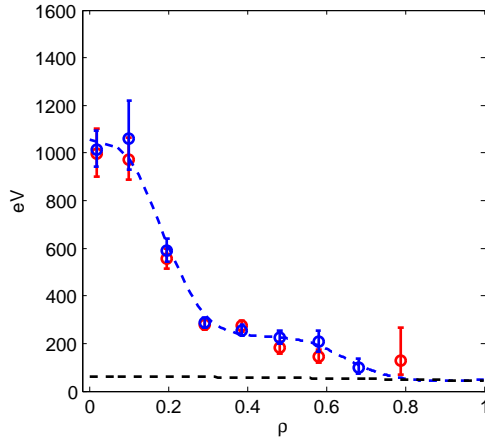


Figure 5.6 QHS,  $50\text{ kW}$ ,  $\rho_{ECRH} \lesssim 0.1$ :  $T_e$  for CCW (blue) and CW (red).  $T_i$  from ChERS (black, dashed).

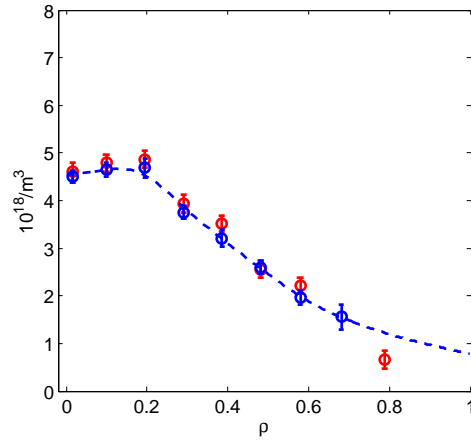


Figure 5.7 QHS,  $50\text{ kW}$ ,  $\rho_{ECRH} \lesssim 0.1$ :  $N_e$  for CCW (blue) and CW (red).

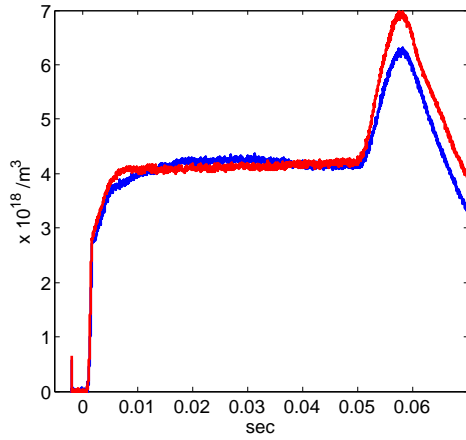


Figure 5.8 QHS,  $50\text{ kW}$ ,  $\rho_{ECRH} \lesssim 0.1$   
Line-averaged central chord density measurement for two shots of the subset used in Figure 5.3. CCW (blue) and CW (red).

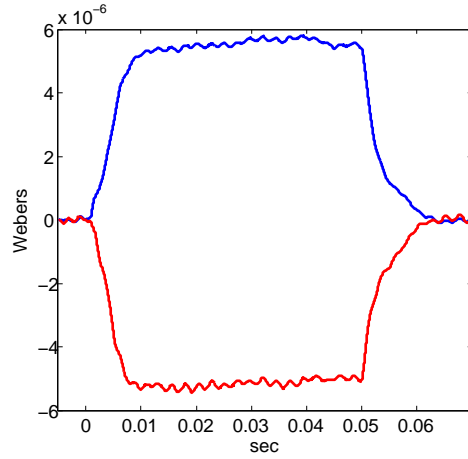


Figure 5.9 QHS,  $50\text{ kW}$ ,  $\rho_{ECRH} \lesssim 0.1$ .  
Diamagnetic flux loop measurement (ens. avg.) CCW (blue) and CW (red).

for the rest of the diagnostic signals (not shown). From the viewpoint of the Thomson scattering, interferometer, flux loop, Rogowski coil, loop voltage and magnetic diagnostic signals, these two sets of QHS plasmas appear to be identical with the exception of the direction of the main magnetic field. If the ECH antenna were misaligned, it may be possible to drive a current in either the CCW

or CW direction, regardless of the main field direction, and the net toroidal current would be different for the two directions of the main field. Since that is not case, it is assumed that the ECH antenna is well aligned (perpendicular to the magnetic axis) and does not directly drive a parallel plasma current. For the rest of this section, only the data for the CCW case will be shown. The results for the CW case are nearly identical.

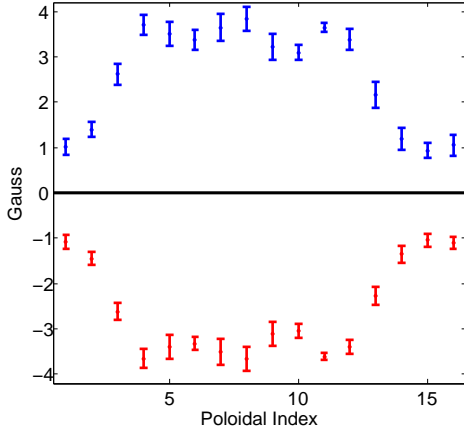


Figure 5.10 QHS, 50 kW,  $\rho_{ECRH} \lesssim 0.1 B_\theta$  component of the magnetic field due to the plasma for CCW (blue) and CW (red).

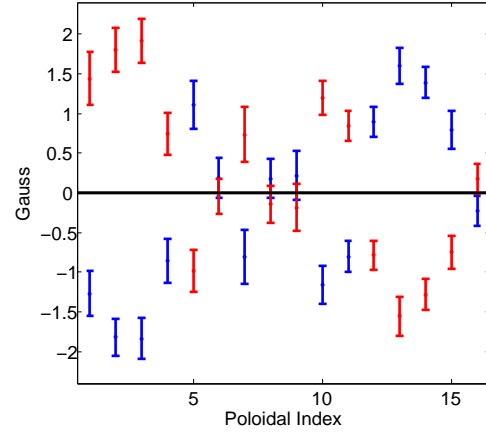


Figure 5.11 QHS, 50 kW,  $\rho_{ECRH} \lesssim 0.1 B_r$  component of the magnetic field due to the plasma for CCW (blue) and CW (red).

Based on the Thomson profiles, above, the PENTA code calculates the neoclassical radial fluxes, parallel flows and radial electric field. With the assumption that the plasma is a two-component, hydrogen-electron plasma, the stable ambipolar radial electric field  $E_r$  for the CCW case is shown in Figure 5.12. Regardless if momentum conservation (MC) is included or not, the  $E_r$  solution is similar. Note that the radial coordinate is the normalized flux,  $s = \Phi/\Phi_{LCFS}$ , not the normalized effective radius,  $\rho \equiv \sqrt{\Phi/\Phi_{LCFS}}$ . Across the majority of the plasma column, the stable ‘ion-root’ case is the only possible solution for  $E_r$  and  $|E_r| < 50 \text{ V/cm}$ . Near the core of the plasma, where  $T_e \gg T_i$ , the ‘electron-root’ is also stable, and  $E_r \sim 300 \text{ V/cm}$ . The electron and ion portion of the parallel current,  $J_e$  and  $J_i$ , along with the total parallel current,  $J_b = J_e + J_i$ , for both ambipolar roots are shown in Figures 5.13 (with MC) and 5.14 (without MC).

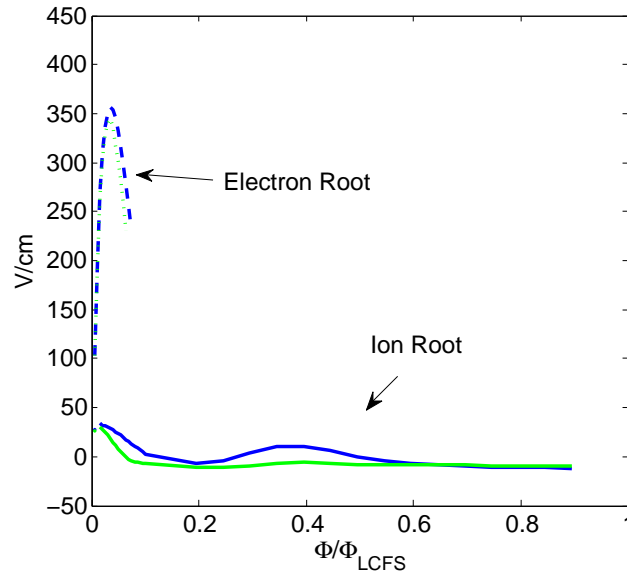


Figure 5.12 QHS,  $50 \text{ kW}$ ,  $\rho_{ECRH} \lesssim 0.1$ : Stable ambipolar  $E_r$  solutions with MC (blue) and without MC (green). Calculation by PENTA.

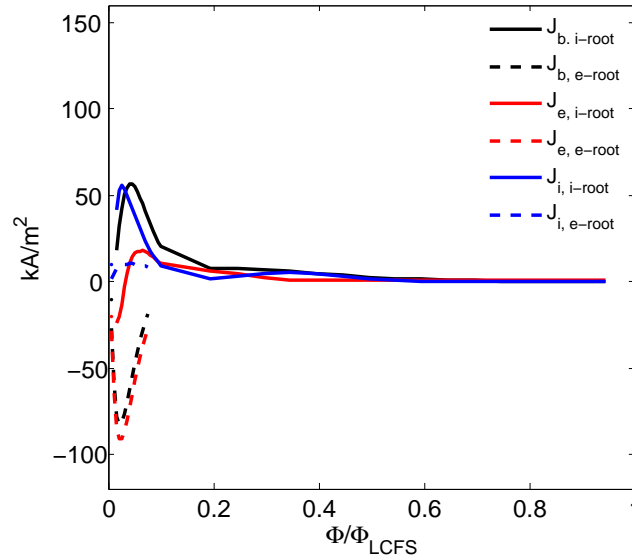


Figure 5.13 QHS,  $50 \text{ kW}$ ,  $\rho_{ECRH} \lesssim 0.1$ , With MC: Ion (blue), electron (red) and total (black) parallel current. Solid lines coincide with the ion root solution and dashed lines coincide with the electron root solution. Calculation by PENTA.

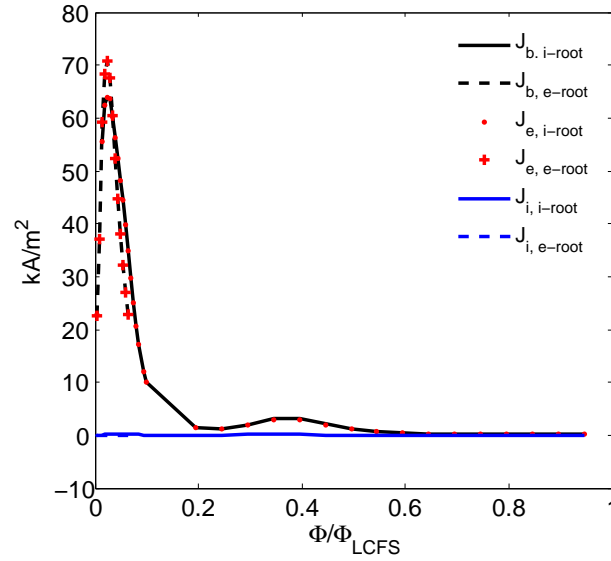


Figure 5.14 QHS, 50 kW,  $\rho_{ECRH} \lesssim 0.1$ , Without MC: Ion (blue), electron (red) and total (black) parallel current. Solid lines coincide with the ion root solution and dashed lines coincide with the electron root solution. The ion current is nearly zero for each case. Calculation by PENTA.

With MC, when  $E_r$  is in the ion-root solution, the electron and ion currents are close in magnitude across most of the radius,  $(\Phi/\Phi_{LCFS}) \gtrsim 0.1$ . Near the axis, in the ion-root, the ion current is the majority of the current density and the electron current is reduced and even reverses direction. This arises because of the ‘poloidal resonance’ (discussed in Sections 2.4 and 6.1 and shown in Figures 2.20 and 6.1). The radial ion transport near this resonance condition increases rapidly and is strongly suppressed when  $|E_r|$  is raised. In contrast, in the electron-root near the axis, the ion flows are reduced to a level comparable to that across the rest of the plasma and the electron current is reversed and increased in magnitude. Near the core, the total parallel current is dominated by the electron current, is reversed in direction, and is larger than that in the ion root. Without MC, the ion current is small, relative to the electron current. The electron current makes up most of the current, and is not changed much when  $E_r$  is in the electron-root solution.

The current enclosed by the flux surface  $I(s) \sim \int ds J_b(s)$  is shown in Figure 5.15. For the cases that include MC, if  $E_r$  is in the ion-root across the plasma profile where it is a stable  $E_r$ -root, then the net toroidal current in steady state is expected to be about 260 A (i-root dominant). If

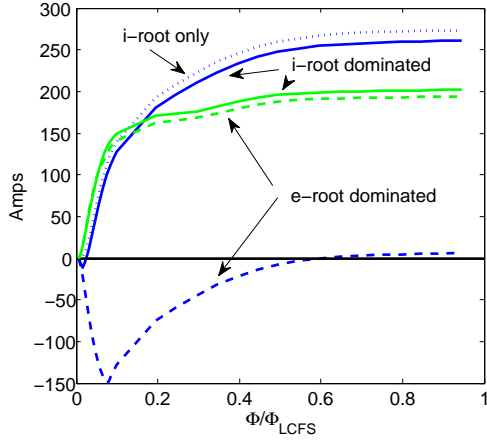


Figure 5.15 QHS 50 kW,  $\rho_{ECRH} \lesssim 0.1$ :  
Enclosed current profile for different  
possible scenarios of current density. With  
MC (blue) and without MC (green).

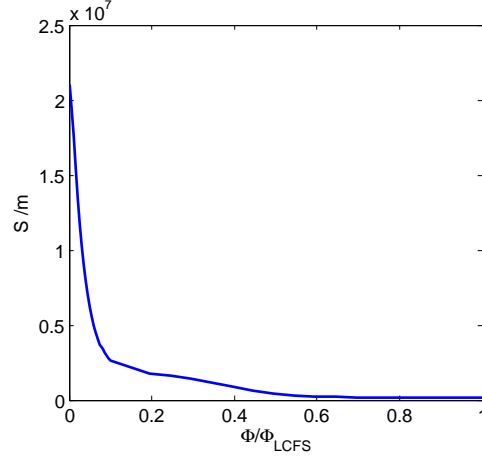


Figure 5.16 QHS 50 kW,  $\rho_{ECRH} \lesssim 0.1$ :  
Parallel conductivity of the plasma,  
including trapped particle effect. Calculation  
by PENTA.

$E_r$  is in the electron-root everywhere that it is a stable root, then the net current is greatly reduced to about 5 A (e-root dominant). There is a small region near the core that does not have a stable ion-root solution. If the current density in the ion-root is extrapolated to 0 at the axis, then the net current would be near 275 A (i-root only). If MC is not included in the PENTA calculations, the current density profile is not strongly affected by the electron-root region, and the net current is near 200 A. In the experiment, the net toroidal current is  $\sim 270$  A at the end of the shot, and the extrapolated current is  $\sim 386$  A. This suggests that  $E_r$  is not in the electron-root. The ‘i-root dominant’ MC solution is chosen as the most likely candidate for the steady-state current density profile and will be used in the time evolution modeling of the current density profile. The calculation of the parallel conductivity, including the effects of trapped particles, is shown in Figure 5.16. The conductivity is highest near the core where  $T_e$  is the hottest. This conductivity profile is also used in the time evolution modeling. The edge boundary condition for the modeling is provided by the measured net toroidal current, Figure 5.3.

The time-evolved net current density, (radial derivative of Eqn 3.24) and induced current density profiles are shown in Figures 5.17 and 5.18. Early in the simulation,  $t_{sim} = 10$  ms, the induced current density is large near the axis. By the end of the shot,  $t_{sim} = 50$  ms, most of the induced

current has diffused out of the column. The current density profile is approaching the assumed neoclassical current density profile,  $J_{b,ion-root}$ . The simulated and measured loop voltage signal, Eqn 3.61 is shown in Figure 5.19. The behavior is similar, but the measured value is larger. The extrapolated current measurement suggests that the total current will exceed the total bootstrap current. Since the boundary condition on the simulation uses the measured net toroidal current, and the measured toroidal current exceeds that of the ‘i-root dominant’ solution, the simulation requires an extra parallel electric field to drive this current. The direction of this extra parallel electric field is in the same direction as the net current, opposite to that of the bootstrap-induced electric field. This excess parallel electric field reduces the simulated loop voltage below that of the measurement.

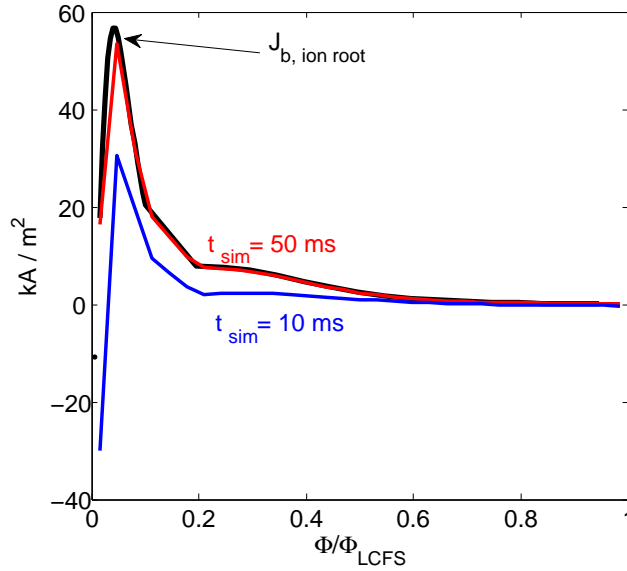


Figure 5.17 QHS 50 kW,  $\rho_{ECRH} \lesssim 0.1$ : Simulated evolving current density profile. Steady state solution shown in black. Calculation by IEG.

## 5.2 Helical rotation of Pfirsch-Schlüter current

At  $t_{sim} = 10 \text{ ms}$ , the line-averaged density and diamagnetic flux loop signal have both reached a stationary value, and the net toroidal current is about 75 A. The pressure profile derived from

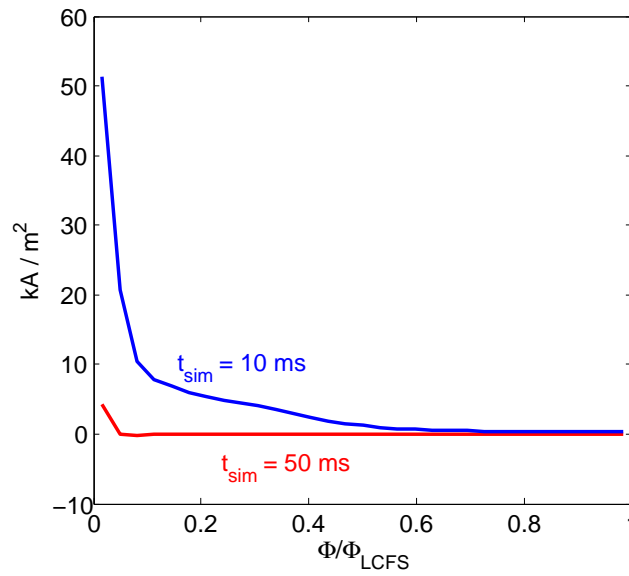


Figure 5.18 QHS 50 kW,  $\rho_{ECRH} \lesssim 0.1$ : Simulated induced current density profile. Calculation by ige+igv.

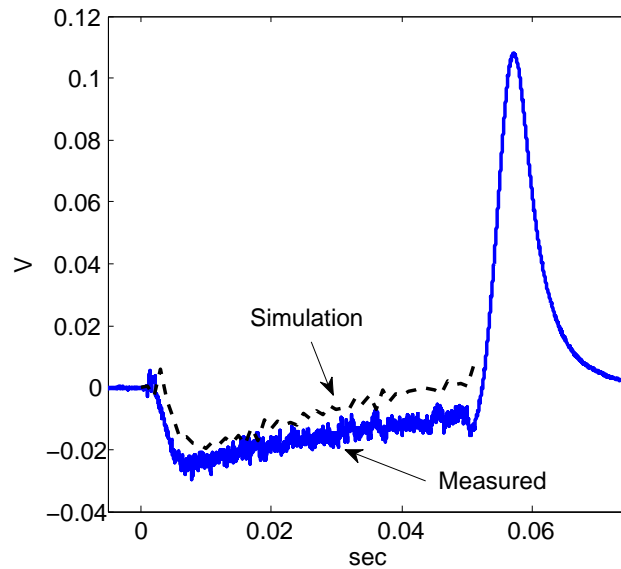


Figure 5.19 QHS 50 kW,  $\rho_{ECRH} \lesssim 0.1$ : Simulated and measured loop voltage.

the measured temperature and densities is shown in Figure 5.20. A best-fit Lorentz profile, Eqn A.17, is shown, with  $AM(0) = AM(1) = AM(2) = AM(4) = 1$ ,  $PRES\_SCALE = 803$  and



$AM(3) = 0.395$ . The simulated enclosed current profile is in Figure 5.21. The *SUM\_ATAN* fitline, Eqn A.20, at  $t_{sim} = 10\text{ ms}$ , is parameterized  $AC(0) = 0$ ,  $AC(1) = AC(4) = 1$ ,  $AC(2) = 10$ ,  $CURTOR = 77$ . and  $AC(3) = 1.5$ .

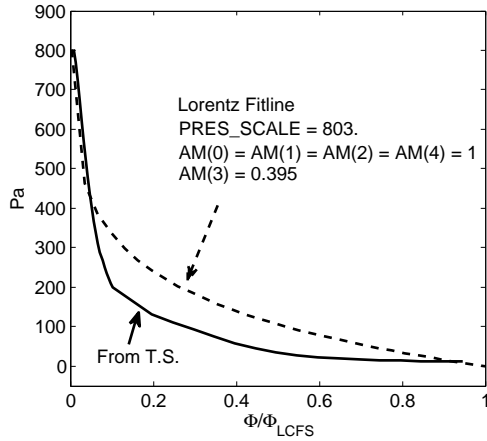


Figure 5.20 QHS 50 kW,  $\rho_{ECRH} \lesssim 0.1$ : Plasma pressure profile and *TWO\_LORENTZ* fitline.

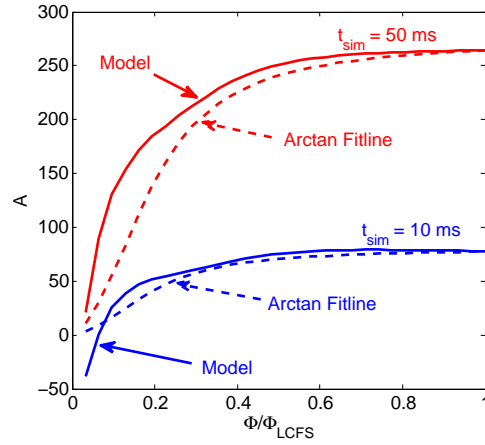


Figure 5.21 QHS 50 kW,  $\rho_{ECRH} \lesssim 0.1$ : Enclosed current calculated by IEG, and arctan fitlines.  $AC(0) = 0$ ,  $AC(1) = AC(4) = 1$ ,  $AC(2) = 10$ ,  $AC(3) = 1.5$  for both, and  $CURTOR = 77$ (blue),  $CURTOR = 264$ (red).

V3FIT was used to calculate the expected magnetic diagnostic response for a 'Pressure Only' case, where the pressure profile was specified by the Lorentz fitline in Figure 5.20 and the net toroidal current was identically 0 across the entire plasma. The diagnostic response was also calculated for the case with the same pressure profile, but with the current density profile specified by the arctan fitline for  $t_{sim} = 10\text{ ms}$  in Figure 5.21. The expected diagnostic responses for the radial and poloidal channels of the external magnetic diagnostic array are shown in Figure 5.22 as dashed lines. The experimentally measured values are also shown in the figures as points with uncertainties.

An illustrative sketch of the Pfirsch-Schlüter current density at the location of the two external diagnostic belts is shown in Figure 5.23. (This sketch does not show the Pfirsch-Schlüter current density for this case, but for a parabolic pressure profile.) Early in the shot, before the net toroidal

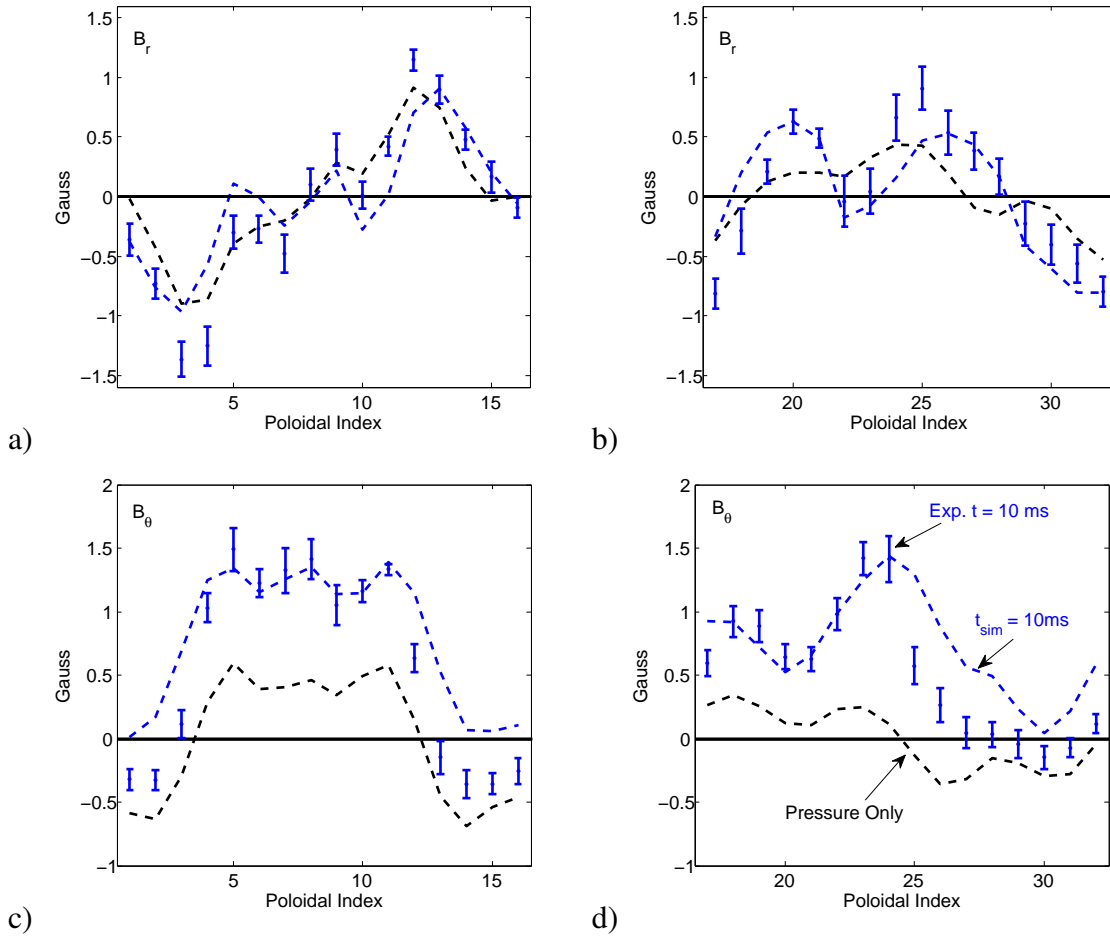


Figure 5.22 QHS 50 kW,  $\rho_{ECRH} \lesssim 0.1$ .  $B_r$  and  $B_\theta$  components of the external magnetic diagnostic signals: Measured (blue, with unc.), Pressure profile only, no toroidal current (black, dashed), and Pressure profile with evolved current profile at  $t_{sim} = 10$  ms (blue, dashed).

current becomes the largest part of the signal, the largest contribution to the signals is expected to be a dipole-like field generated by the Pfirsch-Schlüter current. Near the 1/2-field period location, the radial signal,  $B_r$ , is expected to be largest near diagnostics with poloidal indices 3-4 and 12-13. It should be negative near 3-4 and positive for 12-13, Figure 5.22a. The poloidal signal,  $B_\theta$ , is expected to be positive for diagnostics 5-11 and negative for 13-16 and 1-3. As seen in Figure 5.22c, this is the case with no net toroidal current, but the toroidal current produces an offset in the poloidal magnetic field is expected even at  $t_{sim} = 10$  ms. Near the 1/6-field period location,  $B_r$ , is expected to be largest near diagnostics 24-25 and 32-17. The signal is expected to be positive

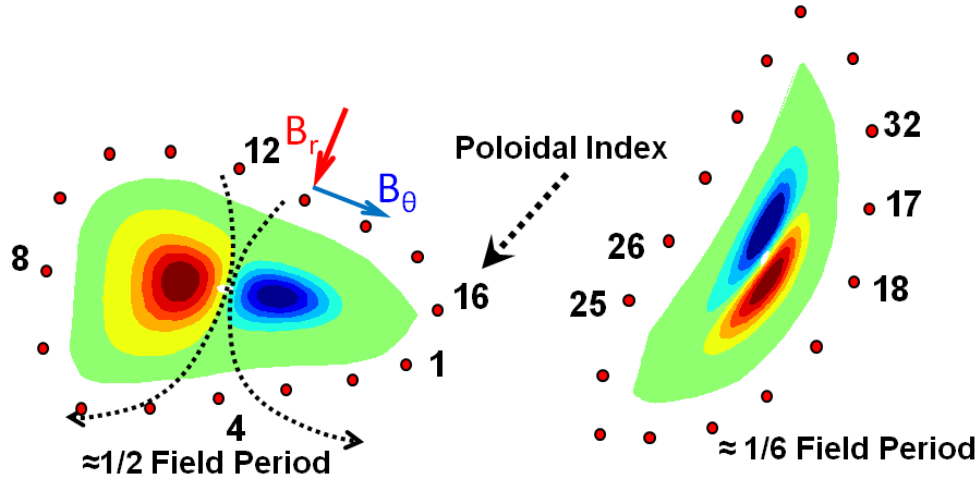


Figure 5.23 Sketch of the Pfirsch-Schlüter current density at the location of the two external magnetic vector diagnostic belts. The regions of red indicate current density going into the page and regions of blue indicate current density directed out of the page. Each diagnostic has a unique poloidal index and measures the magnetic field components in its own local coordinate system.

See section 4.2.1 for details of the diagnostic array.

near 24-25 and negative near 32-17, Figure 5.22b. The values of  $B_\theta$  are expected to be positive for diagnostics 17-23, negative for diagnostics 25-31, and be near zero at diagnostics 24 and 32. This is clearly the case for no net toroidal current, Figure 5.22d, but even at  $t_{sim} = 10 \text{ ms}$ , the poloidal drift from the toroidal current is evident. The magnetic diagnostic data from the external array agrees qualitatively with the simulated calculations and demonstrates the helical nature of the Pfirsch-Schlüter current density. This confirms that the toroidal curvature is largely reduced in QHS magnetic configuration.

### 5.3 Reconstruction of Plasma Pressure and Current Profiles

The reconstruction of the plasma pressure and enclosed current profiles at the ECH turn-off time,  $t = 50 \text{ ms}$ , are discussed here. The initial guess for the plasma pressure profile is the Lorentz fitline in Figure 5.20 and the initial guess for the enclosed current profile is the arctan fitline in Figure 5.21. Reconstructions are performed with two different sets of diagnostics. The first set of diagnostics includes the internal poloidal array, section 4.2.2, the Rogowski Coil, section

4.2.3, and a limiter placed at the calculated last-closed flux surface in the QHS configuration. The second set of diagnostics includes all of the first set, with the addition of the external magnetic vector diagnostics array, section 4.2.1.

### 5.3.1 Reconstruction with the Internal Poloidal Array and Rogowski Coil

The reconstruction with the internal poloidal array was performed several times, adjusting the number of fit parameters. For Reconstruction #1, the free parameters were *PRES\_SCALE*, *AM*(3), *CURTOR*, *AC*(3), and *PHIEDGE*. *AC*(3) kept at 1.5. For Reconstruction #2, the free parameters included all of those previously listed, with the addition of *AC*(3). Reconstruction #3 includes the previous set and includes *AM*(2) as a fit parameter. The initial guess of the parameters and the results of the reconstruction are listed in table 5.2. The modeled profiles, best-fit initial guess profiles, and reconstructed profiles are shown in Figures 5.24 and 5.26. The magnetic diagnostic signals for the initial guess and reconstructions, along with the measured diagnostic data are in Figure 5.28. The overall change between the initial guess and reconstruction signals is small, and the differences between the different reconstructions is even smaller.

As seen in the figures, the reconstructed pressure profile for each case agrees well with measured one. The enclosed current profile for case #1 does not change much from the initial guess, while the profile from case #2, with the extra free fit parameter in the profile description actually agrees very well with that of the initial model profile. The  $\chi^2_\nu$  for each case is smaller than 1, but not too close to 0, indicating that the fit profiles are probably reasonable reconstructions for both cases. While the value of  $F_\chi$ , Eqn 4.88, is larger than 1, indicating that the addition of the extra fit parameter, *AC*(3) improves the overall fit, the value of  $\chi^2_\nu$  is already small, so the additional fit parameter and improvement of the fit is not significant.

The values of  $\sigma$  for each parameter were calculated by V3FIT according to Eqn 4.85. Since the Jacobian matrix is calculated by a single-sided finite difference (see Eqn 4.68 and the discussion above Eqn 4.89), the non-linear relationship between the fit parameters is not well resolved and the uncertainty for each parameter is overestimated. To get an idea of what types of profiles would produce similar magnetic diagnostic signals, two scans of the parameter space are performed. The

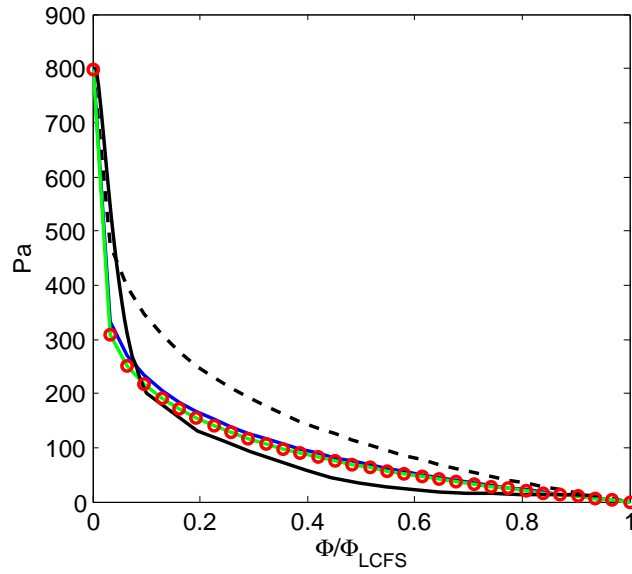


Figure 5.24 QHS 50  $kW$ ,  $\rho_{ECRH} \lesssim 0.1$ : Measured plasma pressure profile (black), the Lorentz-fit initial guess (black, dashed), **Reconstruction #1**, **Reconstruction #2**, and **Reconstruction #3** (o). See Table 5.2.

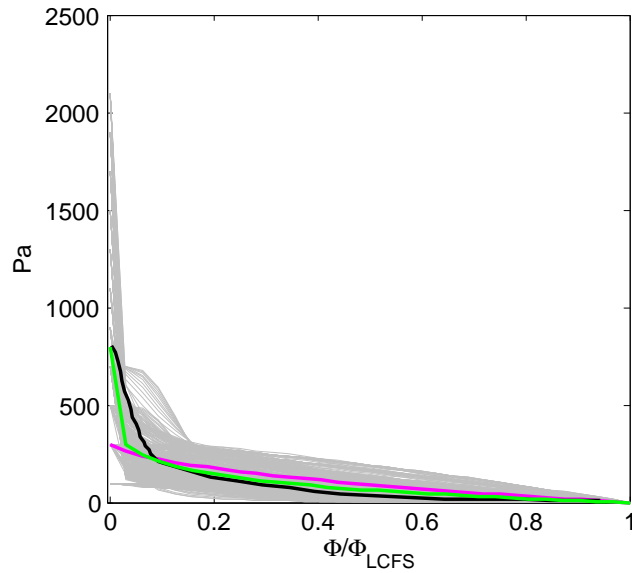


Figure 5.25 QHS 50  $kW$ ,  $\rho_{ECRH} \lesssim 0.1$ : Measured plasma pressure profile (black), **Reconstruction #2**, and the profile with the minimum  $\chi^2$  found during **Parameter scan #1**. The pressure profiles from the scan that satisfy  $\chi^2_\nu \leq \chi^2_{\nu,\min} + 1$  are indicated in gray. See Table 5.2.

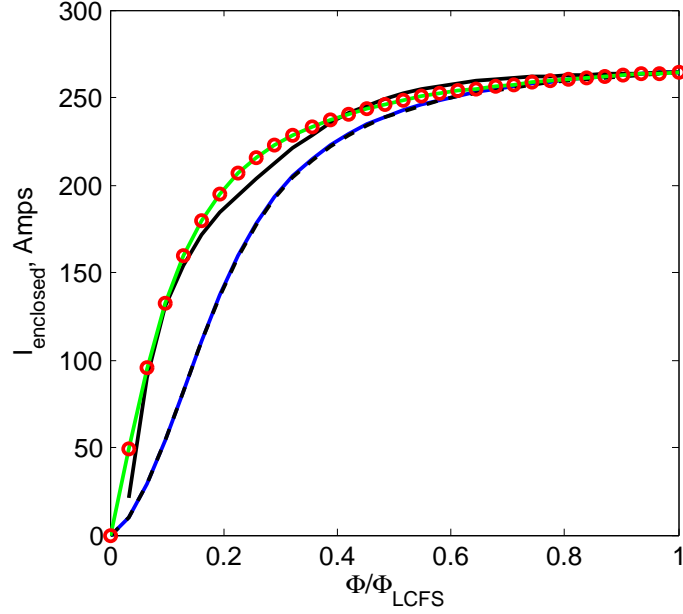


Figure 5.26 QHS 50 kW,  $\rho_{ECRH} \lesssim 0.1$ : The calculated enclosed current profile (black), the arctan-fit initial guess (black, dashed), **Reconstruction #1**, **Reconstruction #2**, and **Reconstruction #3** (o). See Table 5.2.

first scan varies the parameters involving the pressure profile, ( $PRES\_SCALE$ ,  $AM(2)$ ,  $AM(3)$ ), while holding the current profile at its reconstructed value from Reconstruction #1. The second scan varies the parameters involving the current profile, ( $CURTOR$ ,  $AC(2)$ ,  $AC(3)$ ), while holding the pressure profile at its reconstructed value. Profiles that produce magnetic diagnostics signals such that  $\chi^2_\nu \lesssim \chi^2_{\nu,\min} + 1$ , Eqn 4.89, are considered to be within a single standard deviation of the reconstructed solution. Here, the  $\chi^2_{\nu,\min}$  used is the one found during the parameter scan. There are a total of  $(15 \times 15 \times 21) = 4725$  grid points for each scan. The pressure scan included 15 linear points for each of the  $AM(2)$  and  $AM(3)$  from 0.25 to 5.0, and 21 pressure values from 100 to 2100 Pa. A 2-D cross-section of  $\chi^2$  for a scan of  $AM(2)$  and  $PRES\_SCALE$  from 100 to 2100 Pa is shown in Figure 5.29. For each grid point that satisfies Eqn 4.89, that pressure profile is plotted in Figure 5.25. Likewise, current profiles that satisfies Eqn 4.89 are plotted in 5.27.

The profile parameter scan provide a sense of pressure and current profiles that produce diagnostic signals that are close to the reconstructed ones. There are a variety of pressure profiles

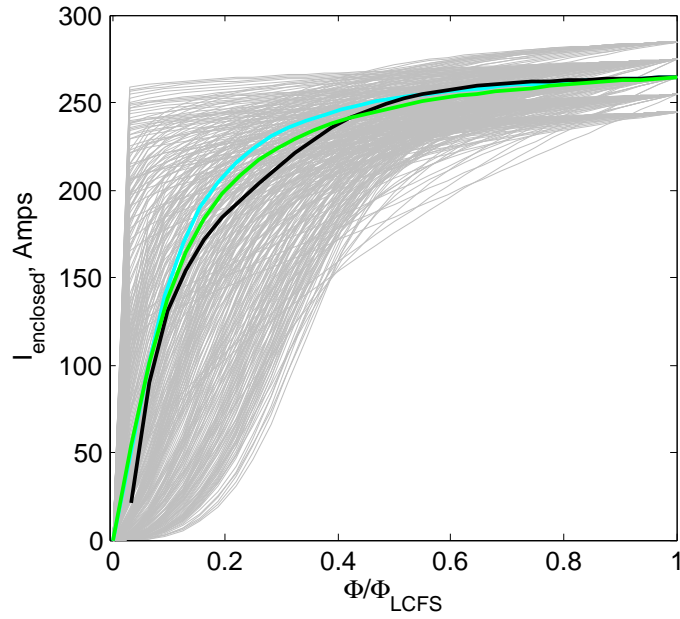


Figure 5.27 QHS 50 kW,  $\rho_{ECRH} \lesssim 0.1$ : The calculated enclosed current profile (black), **Reconstruction #2**, and the profile with the minimum  $\chi^2$  found during **Parameter scan #2**. The current profiles from the scan that satisfy  $\chi^2_\nu \leq \chi^2_{\nu,\min} + 1$  are indicated in gray. See Table 5.2.

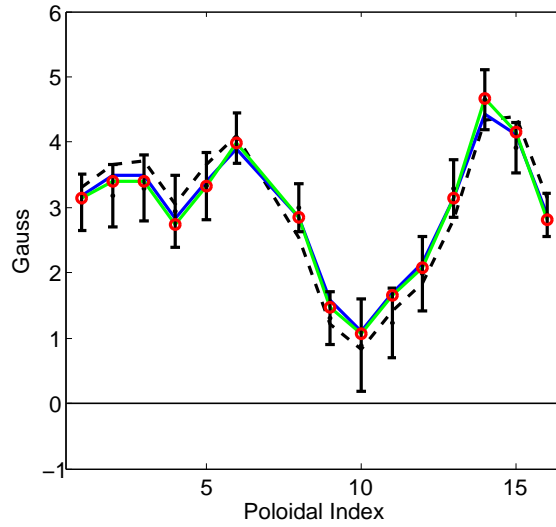


Figure 5.28 QHS 50 kW,  $\rho_{ECRH} \lesssim 0.1$ : Signals for the internal poloidal diagnostic array at  $t_{exp} = t_{sim} = 50$  ms. Measurements (black, with unc.), initial guess (black, dashed), **Reconstruction #1**, **Reconstruction #2**, and **Reconstruction #3** (o), each listed in Table 5.2.

Parameter		PRES_SCALE		AM(2)		AM(3)		PHIEDGE	
		Value	$\sigma$	Value	$\sigma$	Value	$\sigma$	Value	$\sigma$
Initial Guess		803.	-	1.	-	0.395	-	0.0424	-
Reconstruction #1		797.	5450.	1.*	-	0.252	1.828	0.0409	0.0113
Reconstruction #2		798.	5715.	1.*	-	0.230	1.703	0.0409	0.0172
Reconstruction #3		798.	8455.	0.981	83.1	0.231	2.414	0.0409	0.0334
Parameter Scan #1 **		300.	-	2.329	-	0.657	-	0.0409*	-
Parameter Scan #2 **		797.*	-	1.*	-	0.252*	-	0.0409*	-
CURTOR		AC(2)		AC(3)		$\chi^2$	$\nu$	$\chi_\nu^2$	$F_\chi$
Value	$\sigma$	Value	$\sigma$	Value	$\sigma$				
264.	-	10.	-	1.5	-	13.1	-	-	-
265.	7.	9.98	7.62	1.5*	-	4.16	11	0.38	-
264.	7.	10.00	16.1	1.00	1.14	2.70	10	0.27	5.4
264.	7.	10.00	16.8	1.00	1.34	2.70	9	0.30	$\sim 0$
265.*	-	9.98*	-	1.5*	-	3.71	10	0.37	—
265.	-	15.00	-	1.15	-	2.73	10	0.27	—

Table 5.2 QHS,  $50kW$ ,  $\rho_{ECRH} \lesssim 0.1$ . V3FIT reconstruction results using the internal poloidal array, Rogowski coil, and limiter signal. Black: Initial guess. Reconstruction with 5 free parameters. Reconstruction with 6 free parameters. Reconstruction with 7 free parameters. Scan of pressure profile parameters, holding the current profile constant. Scan of current profile parameters, holding the pressure profile constant. The  $\chi^2$ ,  $\chi_\nu^2$  and  $F_\chi$  values are also shown, where relevant. (\*) Quantity was not a fit parameter for this case. (\*\*) The limiter signal was disabled and PHIEDGE was not a fit parameter.

that produce similar signals, but most of the ambiguity is near the axis, where a profile that is strongly peaked is indistinguishable from one that has a lower and broader pressure profile. The reconstructed and measured pressure profiles all lie near the middle of the scan, indicating that the model and the reconstruction agree quite well. The calculated and reconstructed current profiles all lie near the profile with the minimum  $\chi^2$  found during the parameter scan. However, there is a large variation of possible enclosed current profiles for  $\rho \lesssim 0.5$ , and so the current density is poorly resolved in this region.



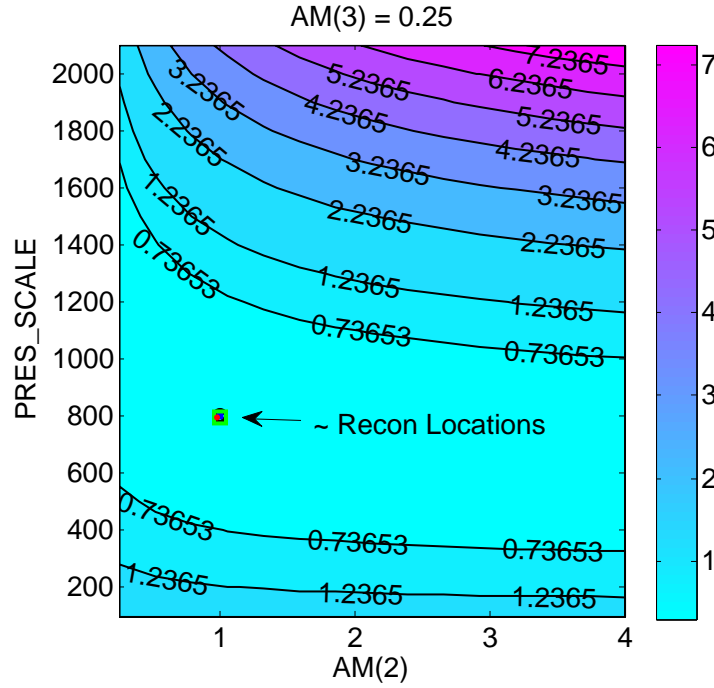


Figure 5.29 QHS,  $50kW$ ,  $\rho_{ECRH} \lesssim 0.1$ :  $\chi^2_\nu$  for pressure profile parameter scan. One plane of the 3-D scan is shown. The point in space near where the 3 reconstructions found the minimum  $\chi^2$  is indicated.

The number of parameters that can reasonably be used to model the pressure and current profiles is around 5. This is consistent with the estimate of the number of significant eigenvalues that the internal diagnostic array can measure when the typical noise is around  $\pm 0.25G - \pm 0.5G$ , as shown in Figure G.6. If the noise level could be reduced to  $\pm 0.05G$ , it is expected that the number of reconstruction parameters could be increased to 8 or 9.

### 5.3.2 Reconstruction with the External Magnetic Diagnostic Array, Internal Poloidal Array and Rogowski Coil

The above reconstruction process was repeated for a set of reconstructions that included the signals from the external magnetic diagnostic array. The parameter scan was repeated to find profiles that satisfy  $\chi^2_\nu \leq \chi^2_{\nu, \min} + 1$ . The profile specifications for the initial guess and reconstructions, along with the parameter scan results, are listed in table 5.3. The magnetic diagnostics signals for the initial guess and reconstructions, along with the measured signals is in Figure 5.34.

Parameter		PRES_SCALE		AM(2)		AM(3)		PHIEDGE	
		Value	$\sigma$	Value	$\sigma$	Value	$\sigma$	Value	$\sigma$
Initial Guess		803.	-	1	-	0.395	-	0.0424	-
Reconstruction #1		807.	463.	1*	-	0.704	0.530	0.0411	0.0015
Reconstruction #2		804.	486.	1*	-	0.722	0.609	0.0409	0.0028
Parameter Scan #1 **		700.	-	2.33	-	0.657	-	0.0411*	-
Parameter Scan #2 **		807.*	-	1.*	-	0.704*	-	0.0411*	-
CURTOR		AC(2)		AC(3)		$\chi^2$	$\nu$	$\chi_\nu^2$	$F_\chi$
Value	$\sigma$	Value	$\sigma$	Value	$\sigma$				
264.	-	10.	-	1.5	-	220.8	-	-	-
253.	3.	9.98	2.04	1.5*	-	114.4	107	1.07	-
253.	3.	9.94	3.74	1.71	0.45	113.4	106	1.07	0.93
253.*	-	9.98*	-	1.5*	-	113.7	106	1.07	—
253.	-	12.87	-	1.85	-	113.1	106	1.07	—

Table 5.3 QHS,  $50kW$ ,  $\rho_{ECRH} \lesssim 0.1$ . V3FIT reconstruction results using the signals from the external magnetic diagnostic array, internal poloidal array, Rogowski coil, and limiter signal.

Black: Initial guess. Reconstruction with 5 free parameters. Reconstruction with 6 free parameters. Scan of pressure profile parameters, holding the current profile constant. Scan of current profile parameters, holding the pressure profile constant. The  $\chi^2$ ,  $\chi_\nu^2$  and  $F_\chi$  values are also shown, were relevant. (\*) Quantity was not a fit parameter for this case. (\*\*) The limiter signal was disabled and PHIEDGE was not a fit parameter.

Using the external diagnostic array, the reconstructed pressure profiles and the profile with the minimum  $\chi^2$  found during the parameter scan exceed the measured profile by about a factor of 2. The total stored energy from the reconstructed profile is about twice that of the measured profile, which does not even lie within profiles found during the parameter scan. The reconstructed current profiles and the profile with the minimum  $\chi^2$  found during the parameter scan agree with each other, and lie near the middle of the profiles found during the scan. However, the calculated profile lies near the edge of the parameter scan. Again, the current profile is not well resolved for  $\rho \lesssim 0.5$ . For these reconstructions,  $\chi_\nu^2 \approx 1$ , which indicates that the model reasonably represents the data

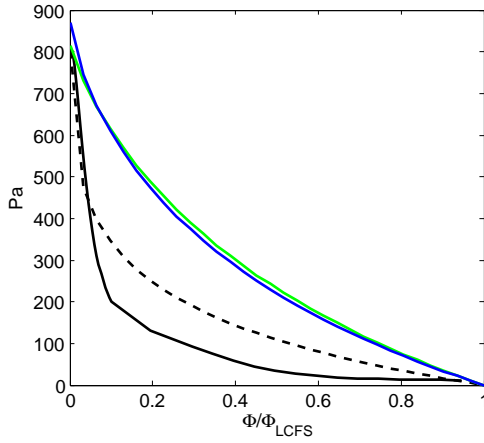


Figure 5.30 QHS 50 kW,  $\rho_{ECRH} \lesssim 0.1$ : Measured plasma pressure (black), the Lorentz-fit initial guess (black, dashed), **Reconstruction #1**, and **Reconstruction #2**. See Table 5.3.

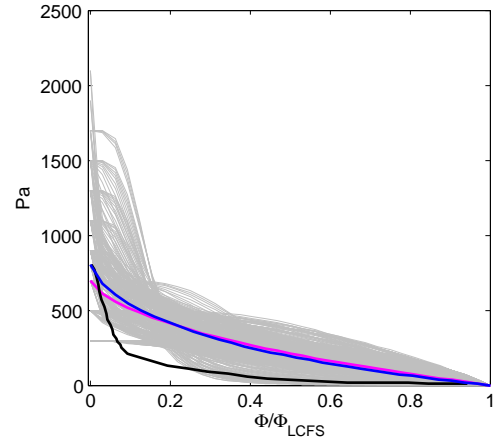


Figure 5.31 QHS 50 kW,  $\rho_{ECRH} \lesssim 0.1$ : Measured plasma pressure (black), **Reconstruction #1**, and the profile with the minimum  $\chi^2$  found during **Parameter scan #1**. The pressure profiles from the scan that satisfy  $\chi^2_{\nu} \leq \chi^2_{\nu, \min} + 1$  are indicated in gray. See Table 5.3.

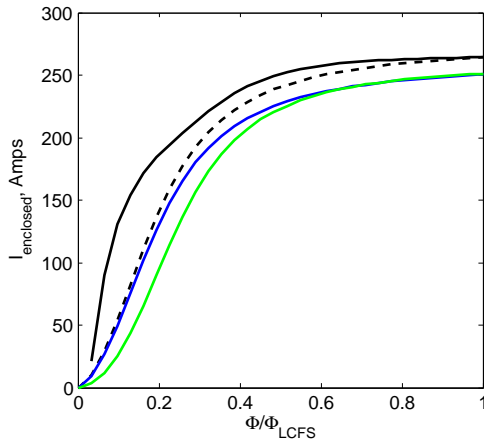


Figure 5.32 QHS 50 kW,  $\rho_{ECRH} \lesssim 0.1$ : The calculated enclosed current profile (black), the arctan-fit initial guess (black, dashed), **Reconstruction #1**, and **Reconstruction #2**. See Table 5.3.

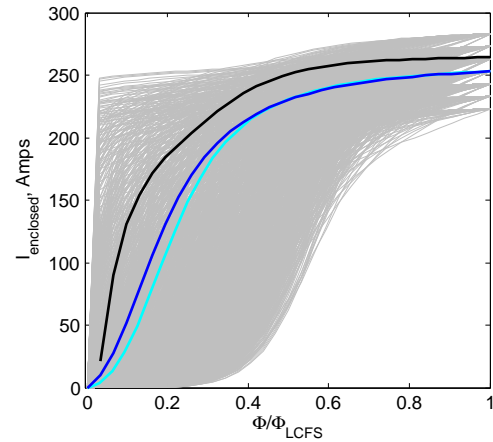


Figure 5.33 QHS 50 kW,  $\rho_{ECRH} \lesssim 0.1$ : The calculated enclosed current profile (black), **Reconstruction #1**, and the profile with the minimum  $\chi^2$  found during **Parameter scan #2**. The current profiles from the scan that satisfy  $\chi^2_{\nu} \leq \chi^2_{\nu, \min} + 1$  are indicated in gray. See Table 5.3.

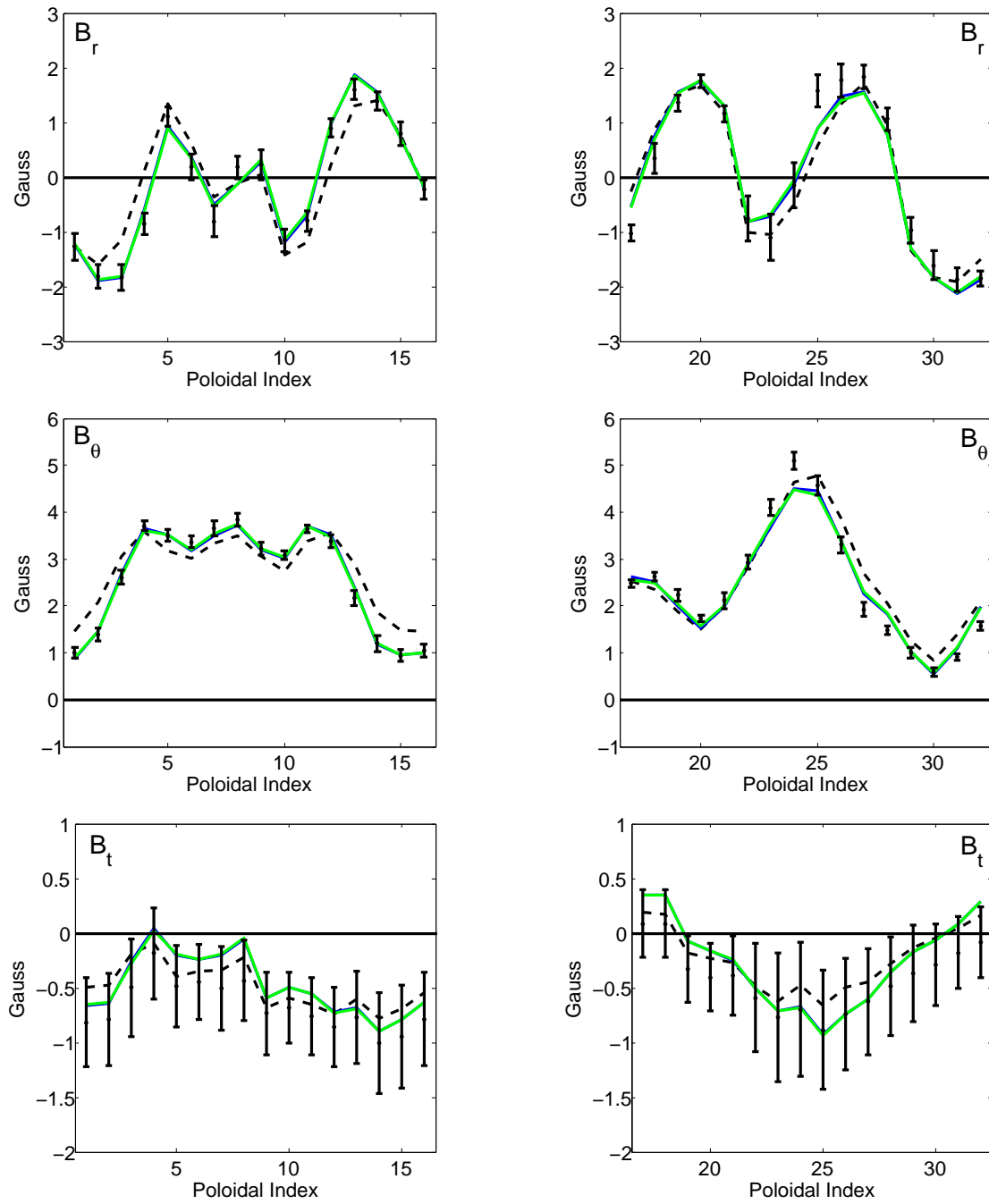


Figure 5.34 QHS 50 kW,  $\rho_{ECRH} \lesssim 0.1$ :  $B_r$ ,  $B_\theta$ , and  $B_t$  signal components of all 32 triplets of the external diagnostic array: Measured (black, with unc.), initial guess (black, dashed), **Reconstruction #1**, **Reconstruction #2**, listed in Table 5.3. The green line lies nearly on top of the blue line.

The reconstruction process does a good job at minimizing the differences between the measured and modeled signals for the external diagnostic array, Figure 5.34. To do so, the reconstruction increases the plasma pressure. The clearest way to see this is by inspecting the magnetic signals due to the plasma pressure and current profile individually. This is done with V3FIT by calculating the magnetic field due to the pressure profile while the current profile is set to zero, and then calculating the magnetic field due to only the current profile by setting the pressure profile to zero. Since HSX is a low beta machine, neither the plasma pressure nor plasma current drastically alter the magnetic configuration. This allows the magnetic signals due to the plasma pressure and current to be calculated approximately independently with V3FIT.

$$B_{plasma,total} \approx B_{plasma,pressure\ only} + B_{plasma,current\ only} \quad (5.2)$$

This is done for both the initial guess and the reconstructed profiles and the signals for  $B_r$  and  $B_\theta$  for diagnostics with poloidal index 1-16 are shown in Figure 5.35. The pressure profile is responsible for generating a dipole-like magnetic field, which appears as a  $m = 1$  poloidal variation in the  $B_r$  and  $B_\theta$  signals. The current profile contributes a net offset ( $m = 0$ ) to the  $B_\theta$  component. In addition to this, the net current produces an  $m = 2$  variation in the  $B_r$  and  $B_\theta$  signals. This difference between the plasma pressure and plasma current signals is what allows the V3FIT to reconstruct the details of both the plasma pressure and current profile. To go from the initial guess to the measured signals, Figure 5.36, adjusting the current profile alone will not improve the fit, but, increasing the pressure profile, while also slightly decreasing the current, improves the match for most of the diagnostic signals.

While the majority of the external diagnostics show better agreement with the reconstructions, the signals for the internal poloidal array show better agreement with the initial guess than with the reconstructions, Figure 5.37. V3FIT tries to minimize the total  $\chi^2$ , and the contribution to  $\chi^2$  from the 96 external diagnostic signals is larger than that from 15 internal diagnostics. The reconstruction with the internal diagnostics alone, Table 5.2, Figures 5.24 and 5.26, also reinforces this. The reason for the difference in reconstruction results based on the internal poloidal array compared to ones including the external diagnostic set is not known at this point. This will be discussed more in Chapter 6.

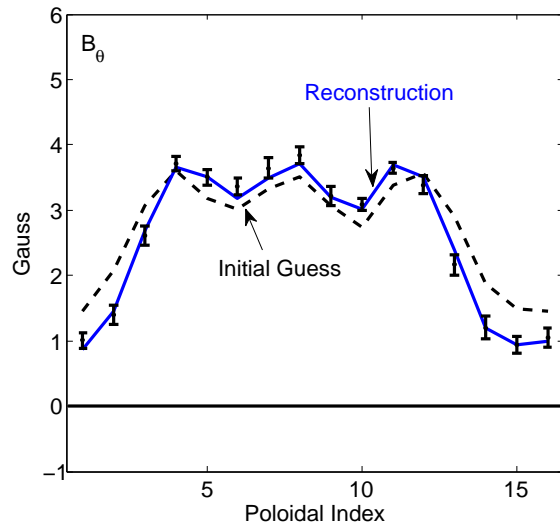
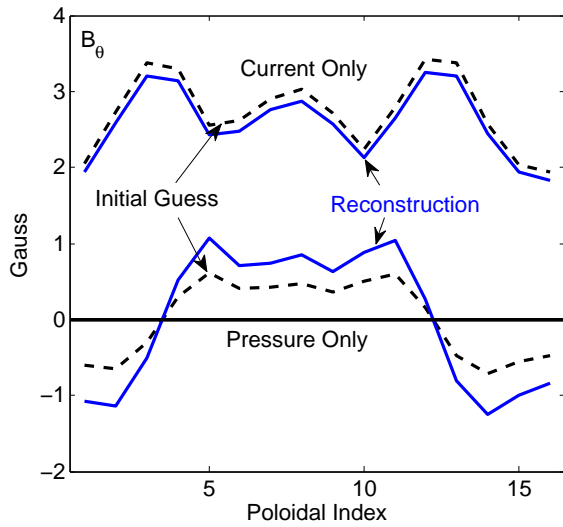
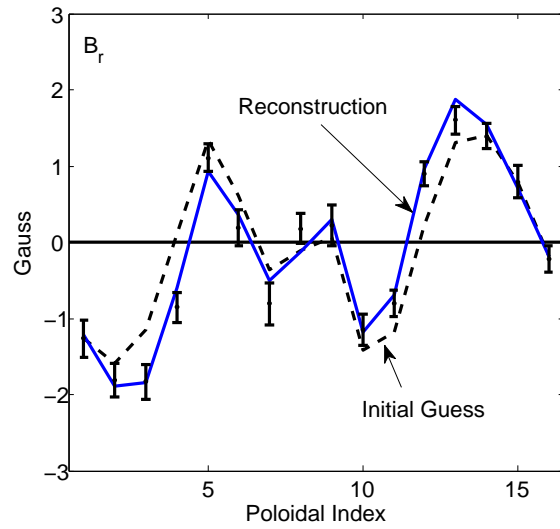
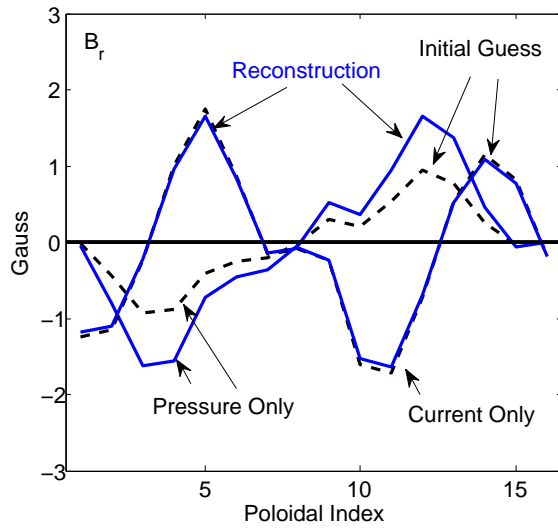


Figure 5.35 Magnetic diagnostic signals due to the current profile and pressure profile, calculated separately. Initial guess (black, dashed) and reconstruction (blue) signals.

Figure 5.36 The total magnetic signal for the initial guess (black, dashed) and reconstruction (blue), from Figure 5.34.

## 5.4 100 kW QHS with Balanced Fueling

The Thomson profiles for QHS, 100 kW ECRH,  $\rho_{ECRH} \lesssim 0.1$  are shown in Figure 5.38 and 5.39. Plasmas made with the magnetic field in both CCW and CW direction are shown. The stored

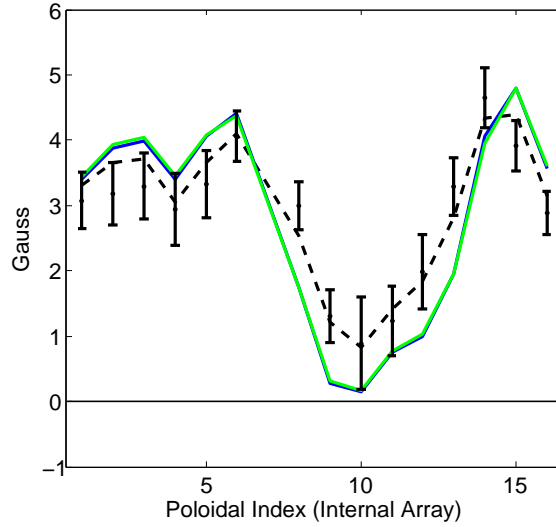


Figure 5.37 QHS 50  $kW$ ,  $\rho_{ECRH} \lesssim 0.1$ : Signal components for the internal poloidal array: Measured (black, with unc.), initial guess (black, dashed), Reconstruction #1, Reconstruction #2, listed in Table 5.3.

energy calculated from the measured profiles for the CCW and CW cases is, respectively, 80  $J$  and 85  $J$ . The measured stored energy from the flux loop (not shown) for the two cases is 78  $J$  and 72  $J$ , respectively. There is good agreement, for the CCW case, and for the CW case, about a 15% difference, which may indicate the presence of a small suprathermal population of well-confined electrons. The net toroidal current and loop voltage for the both the CCW (blue) and CW (red) plasmas are shown in Figures 5.40 and 5.41. The measured current and voltage are reversed, and nearly identical in magnitude. The extrapolated steady state current,  $|I_{tor}(t = \infty)| \sim 350$  A, and  $\bar{N}_e \sim 4 \times 10^{18} \text{ \#}/m^3$ , listed in Table 5.1, are within a few percent of each other in magnitude, and, for the current, of opposite sign.

The measured temperature and density profiles are used as input for PENTA, which calculates the neoclassical ambipolar solutions for  $E_r$  both with and without MC, shown in Figure 5.42. The parallel current density profile for each case is shown in Figure 5.43 (with MC) and Figure 5.44 (without MC).

Compared to the QHS 50  $kW$ ,  $\rho_{ECRH} \lesssim 0.1$  case, the basic features of the radial electric field are similar, except that the value of  $E_r$  in the electron root solution is increased by about 100 A in

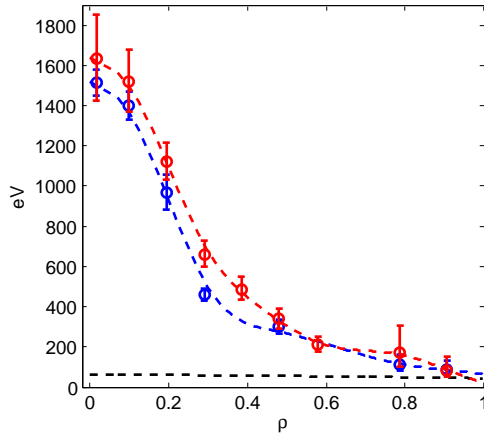


Figure 5.38 QHS 100 kW,  $\rho_{ECRH} \lesssim 0.1$ :  
 $T_e$  for CCW (blue) and CW (red).  $T_i$   
 measurement from ChERS (black, dashed).

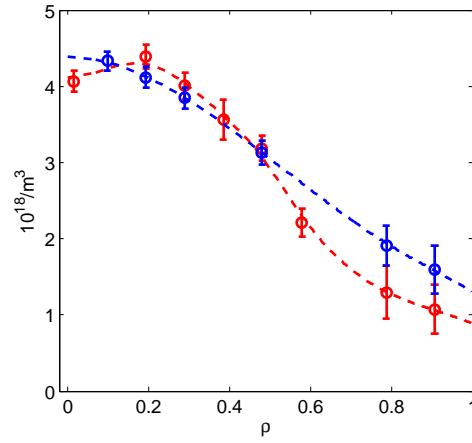


Figure 5.39 QHS 100 kW,  $\rho_{ECRH} \lesssim 0.1$ :  
 $N_e$  for CCW (blue) and CW (red).

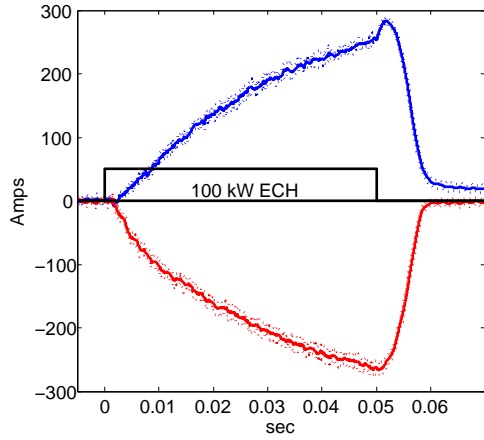


Figure 5.40 QHS, 100 kW,  $\rho_{ECRH} \lesssim 0.1$ :  
 Measured net toroidal current for an  
 ensemble average of 6 shots with the  
 magnetic field in the CCW (blue) and CW  
 (red) directions.

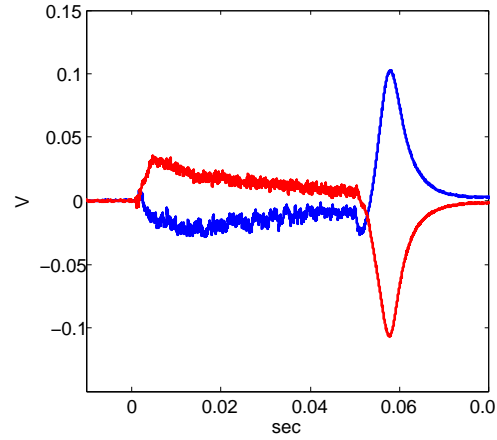


Figure 5.41 QHS, 100 kW,  $\rho_{ECRH} \lesssim 0.1$ :  
 Measured loop voltage (ens. avg.).

the 100kW case. In previous 100 kW experiments, [1], it was found that no stable ion-root solution existed for  $\Phi/\Phi_{LCFS} \lesssim 0.04$  ( $\rho \lesssim 0.2$ ), and the shear in the radial electric field was suggested to be responsible for suppressing turbulent transport near the core in QHS plasmas. For this case the no stable ion-root exists for  $\Phi/\Phi_{LCFS} \lesssim 0.02$  ( $\rho \lesssim 0.14$ ). The current density without MC is



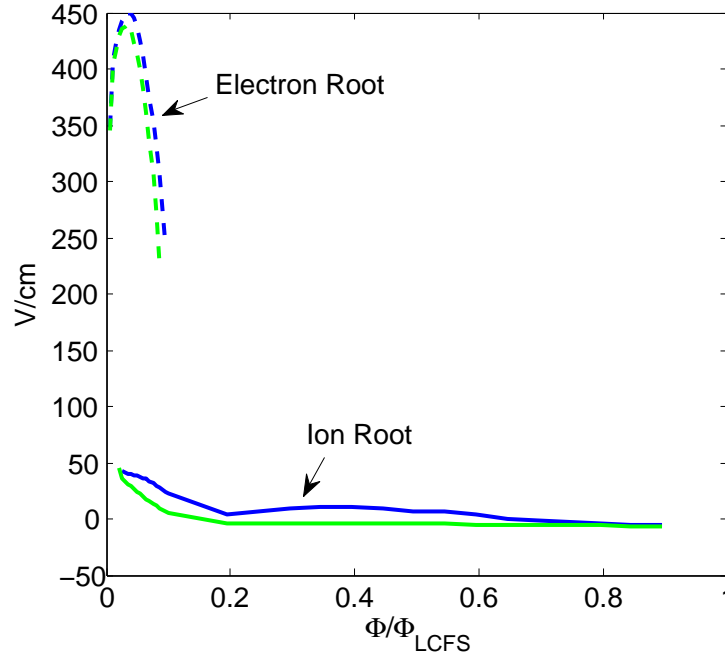


Figure 5.42 QHS 100  $kW$ ,  $\rho_{ECRH} \lesssim 0.1$ : Stable ambipolar  $E_r$  solutions with MC (blue) and without MC (green). Calculation by PENTA.

about 3 times higher in the 100  $kW$  case, Figure 5.44, and again, the total current is almost entirely electron current. When MC is included, Figure 5.43, the current density profile has the same basic characteristics with 100  $kW$  ECHR as it did with 50  $kW$ , i.e., relative magnitude of the ion and electron parallel current, and behavior in the ion root an electron root, with small differences in the electron current for  $\rho \lesssim 0.1$  (see figure). In the 100  $kW$  case, compared to the 50  $kW$  case, there is slightly larger region near the axis that has no stable ion-root solution and only a stable electron root. This electron-root current density is the opposite sign of the ion-root current density and will reduce the total enclosed current profile a small amount, relative to the 50  $kW$  case. The conductivity with 100  $kW$  is shown in Figure 5.46, which is about 1.6 – 1.8 times higher than the 50  $kW$  case, mostly because of the  $\sim 1.5$  times increase in  $T_e$  with 100  $kW$  and  $\sigma_{\parallel} \sim T_e^{3/2}$ .

The enclosed current profile both with and without MC is shown in Figure 5.45. The total enclosed current without MC is around 500  $A$  for i-root dominant current density profiles, and reduced by about 100  $A$  in the e-root dominant profile. With MC, the total current would be about

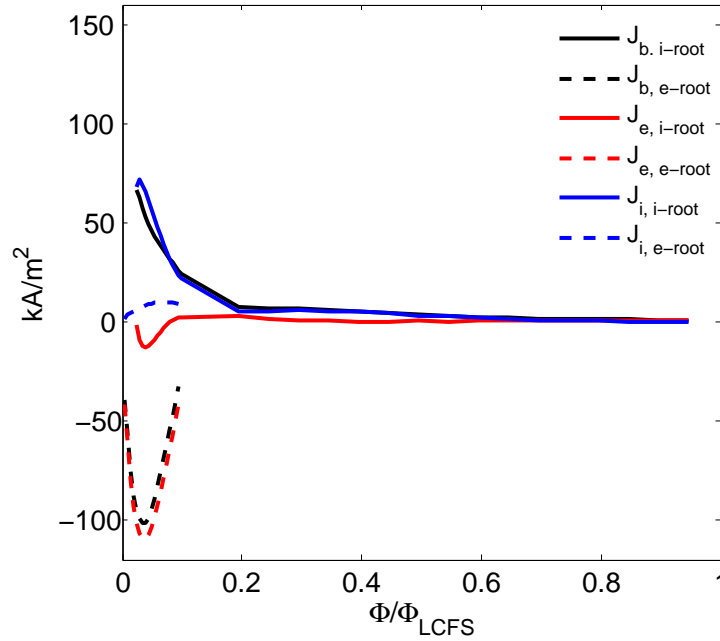


Figure 5.43 QHS 100  $kW$ ,  $\rho_{ECRH} \lesssim 0.1$ , with MC: Ion (blue), electron (red) and total (black) parallel current. Solid lines coincide with the ion root solution and dashed lines coincide with the electron root solution. Calculation by PENTA.

$-100 \text{ A}$  in the e-root dominant case, a complete reversal from the i-root dominant case, which would have about  $250 \text{ A}$ . If the current density for the ion-root solution is extrapolated to 0 on the axis, the ion-root only case, then the total current would be about  $305$ . The extrapolated steady state current was around  $350 \text{ A}$ , exceeding all of estimates that include MC. Regardless, the i-root only solution, with MC, is chosen for the time evolution. The only difference is the current density near the magnetic axis where the reconstruction is unlikely to be sensitive enough to be able to resolve the current profile well enough to discern the difference.

The IEG code takes the conductivity and the current density profiles and simulates the current profile, from which the current density and  $t$  profile are calculated, Eqn 3.39. The measured and simulated toroidal loop voltage are shown in Figure 5.47. Neither simulation matches the measurement, but the one with the higher net steady state current (i-root only) comes closer. This is

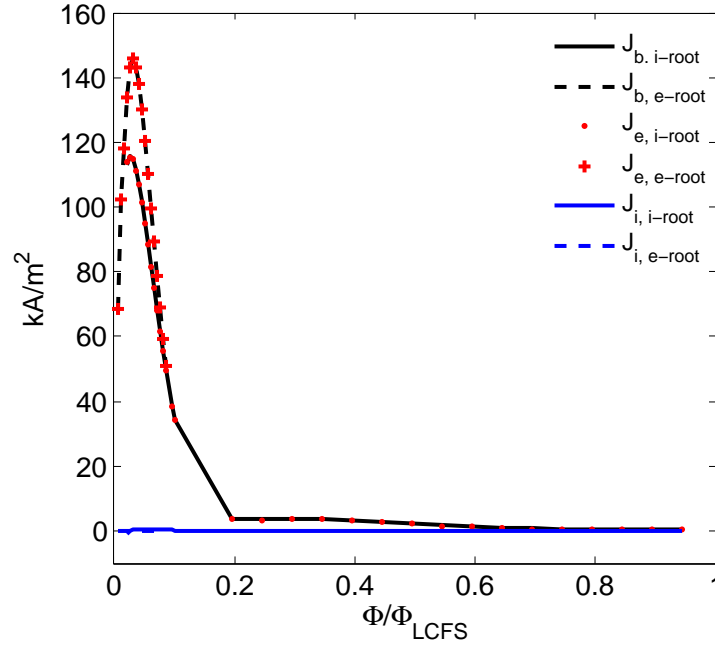


Figure 5.44 QHS 100 kW,  $\rho_{ECRH} \lesssim 0.1$ , without MC: Ion (blue), electron (red) and total (black) parallel current. Solid lines coincide with the ion root solution and dashed lines coincide with the electron root solution. The ion current is nearly zero in each case. Calculation by PENTA.

because of the extra parallel loop voltage that would be required to continue driving an increasing current after the net amount exceeds that of the predicted bootstrap current.

The simulated current profile and pressure profile at  $t_{sim} = 50 \text{ ms}$  are shown in Figures 5.52 and 5.54. A Lorentz-fitline is shown in the pressure profile, which serves as the initial guess in the reconstruction process. An arctan-fitline is shown for the current profile, which also serves as the initial guess profile. The reconstruction results are shown in each figure, as are the profiles found during parameter scans that satisfy  $\chi_\nu^2 \leq \chi_{\nu,min}^2 + 1$ . The reconstruction in this case uses only the internal poloidal array, Rogowski, and the limiter as reconstruction data. The parameters for the initial guess, reconstruction, and both parameter scans are shown in Table 5.4.

The reconstructions with the internal array agree well with the initial guess. Again there is some ambiguity regarding the pressure and pressure density near the core, and the current density is not well constrained for  $\rho \lesssim 0.5$ . The reconstruction completed with  $\chi_\nu^2 = 0.75$ .

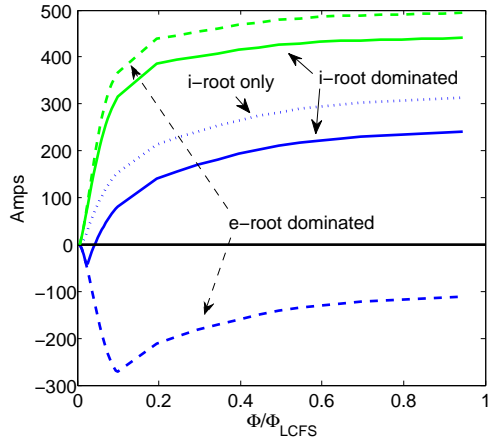


Figure 5.45 QHS 100 kW,  $\rho_{ECRH} \lesssim 0.1$ : Enclosed current profile for different possible scenarios of current density. With MC (blue) and without MC (green).

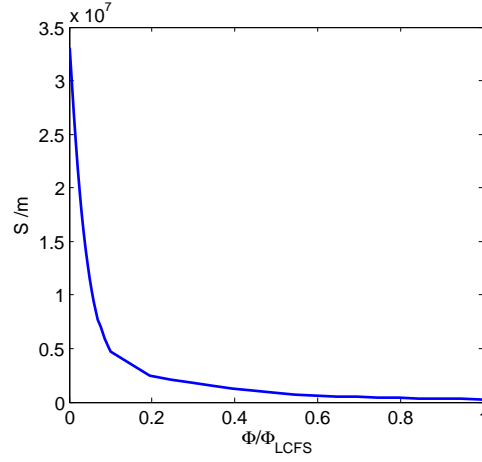


Figure 5.46 QHS 100 kW,  $\rho_{ECRH} \lesssim 0.1$ : Parallel conductivity of the plasma, including the effects of trapped particles, for QHS 100 kW near-axis heating. Calculation by PENTA.

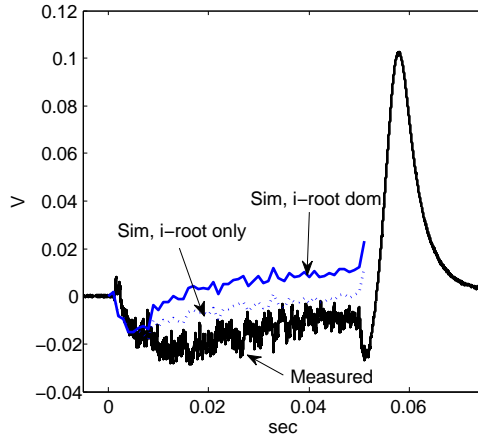


Figure 5.47 QHS 100 kW,  $\rho_{ECRH} \lesssim 0.1$ : Measured and simulated loop voltage for the i-root dominant and i-root only profiles of the bootstrap current. Calculation by IEG.

Figures 5.52, 5.54, and Table 5.5 show the same information with reconstructions using all of the external diagnostic signals along with the internal array, Rogowski and limiter. The reconstructions find solutions for which the pressure profiles do not satisfy  $\chi_\nu^2 \leq \chi_{\nu,\min}^2 + 1$ . The reconstructed pressure profiles are higher than the measured profile by a factor of  $\sim 2$ . The reconstructed total

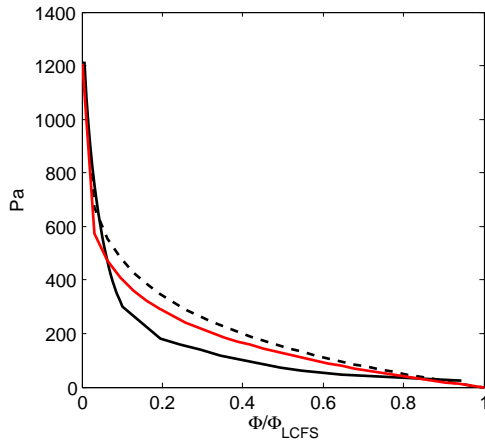


Figure 5.48 QHS 100 kW,  $\rho_{ECRH} \lesssim 0.1$ : Measured plasma pressure profile (black), the Lorentz-fit initial guess (black, dashed), and **Reconstruction**. See Table 5.4.

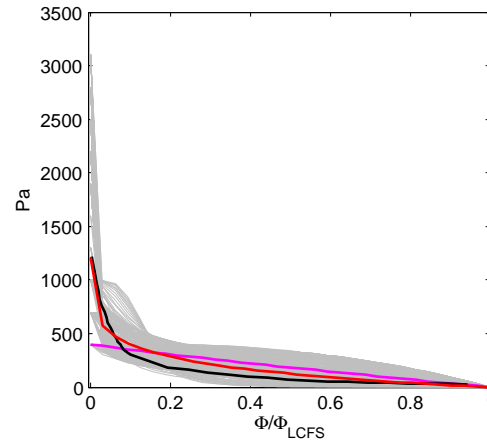


Figure 5.49 QHS 100 kW,  $\rho_{ECRH} \lesssim 0.1$ : Measured plasma pressure profile (black), **Reconstruction**, and the profile with the minimum  $\chi^2$  found during **Parameter scan #1**. The pressure profiles from the scan that satisfy  $\chi_\nu^2 \leq \chi_{\nu,\min}^2 + 1$  are indicated in gray. See Table 5.4.

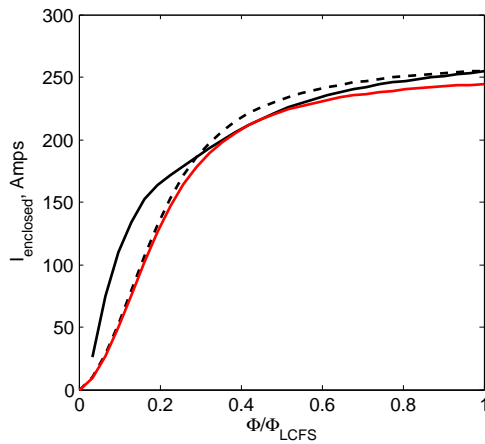


Figure 5.50 QHS 100 kW,  $\rho_{ECRH} \lesssim 0.1$ : The calculated enclosed current profile (black), the arctan-fit initial guess (black, dashed), and **Reconstruction**. See Table 5.4.

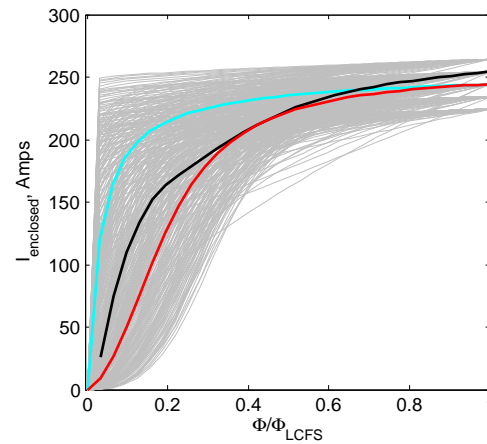


Figure 5.51 QHS 100 kW,  $\rho_{ECRH} \lesssim 0.1$ : The calculated enclosed current profile (black), **Reconstruction**, and the profile with the minimum  $\chi^2$  found during **Parameter scan #2**. The current profiles from the scan that satisfy  $\chi_\nu^2 \leq \chi_{\nu,\min}^2 + 1$  are indicated in gray. See Table 5.4.

Parameter		PRES_SCALE		AM(2)		AM(3)		PHIEDGE	
		Value	$\sigma$	Value	$\sigma$	Value	$\sigma$	Value	$\sigma$
Initial Guess		1214.	-	1	-	0.361	-	0.0424	-
Reconstruction		1209.	4944.	1. *	-	0.300	1.312	0.0408	0.0108
Parameter Scan #1 **		400.	-	4.	-	0.936	-	0.0408*	-
Parameter Scan #2 **		1209.*	-	1. *	-	0.300*	-	0.0408*	-
CURTOR		AC(2)		AC(3)		$\chi^2$	$\nu$	$\chi_\nu^2$	$F_\chi$
Value	$\sigma$	Value	$\sigma$	Value	$\sigma$				
255	-	10.	-	1.5	-	14.6	-	-	-
244.	8.	9.98	8.90	1.5*	-	8.3	11	0.75	-
244.*	-	9.98*	-	1.5*	-	7.1	10	0.71	-
244.	-	15.00	-	0.8	-	4.8	10	0.48	-

Table 5.4 QHS, 100kW,  $\rho_{ECRH} \lesssim 0.1$ . V3FIT reconstruction results using internal poloidal array, Rogowski coil, and limiter signal. Black: Initial guess. **Reconstruction with 5 free parameters.** Scan of pressure profile parameters, holding the current profile constant. Scan of current profile parameters, holding the pressure profile constant. The  $\chi^2$ ,  $\chi_\nu^2$  and  $F_\chi$  values are also shown, were relevant. (\*) Quantity was not a fit parameter for this case. (\*\*) The limiter signal was disabled and PHIEDGE was not a fit parameter.

enclosed current is smaller than that measured by the Rogowski coil by  $\sim 25$  A. The reconstruction completed with  $\chi_\nu^2 = 1.24$ , which indicates that the model is in reasonably agreement with the measurements.

## 5.5 50 kW QHS, $\rho_{ECRH} \sim 0.3$

The Thomson profiles for QHS, 50 kW ECRH,  $\rho_{ECRH} \sim 0.3$  are shown in Figure 5.56 and 5.57. Plasmas made with the magnetic field in both CCW and CW direction are shown. In the CCW case, the calculated stored energy from the measured profiles is 34 J, and the stored energy from the flux loop measurement (not shown) is 35 J. In the CW direction, the calculated and measured stored energy are 33 J and 28 J, respectively. The net toroidal current and loop voltage for the both the CCW (blue) and CW (red) plasmas are shown in Figures 5.58 and 5.59. The measured current and voltage are reversed, and nearly identical in magnitude. The extrapolated

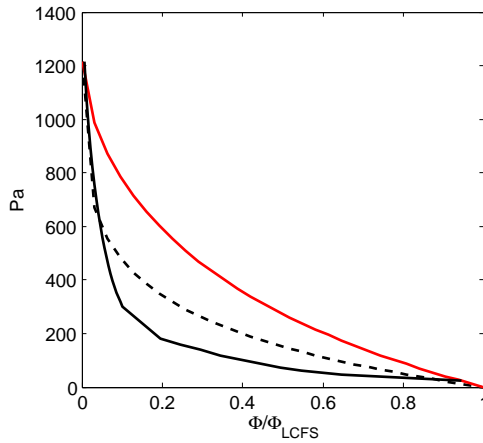


Figure 5.52 QHS 100 kW,  $\rho_{ECRH} \lesssim 0.1$ : Measured plasma pressure profile (black), the Lorentz-fit initial guess (black, dashed), and **Reconstruction**. See Table 5.5.

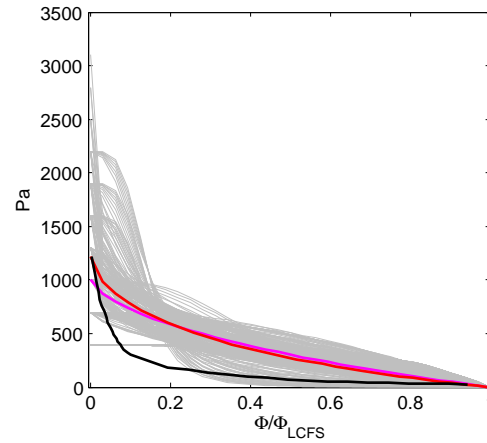


Figure 5.53 QHS 100 kW,  $\rho_{ECRH} \lesssim 0.1$ : Measured plasma pressure profile (black), **Reconstruction**, and the profile with the minimum  $\chi^2$  found during **Parameter scan #1**. The pressure profiles from the scan that satisfy  $\chi_\nu^2 \leq \chi_{\nu,\min}^2 + 1$  are indicated in gray. See Table 5.5.

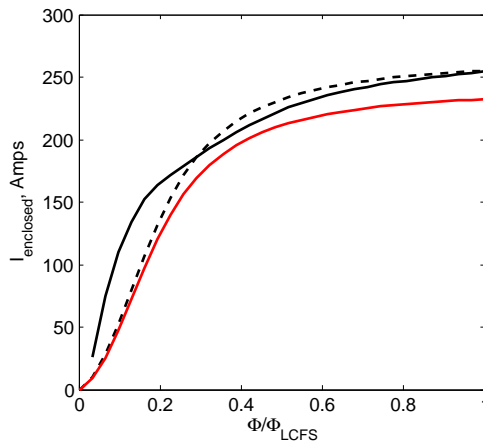


Figure 5.54 QHS 100 kW,  $\rho_{ECRH} \lesssim 0.1$ : The calculated enclosed current profile (black), the arctan initial guess (black, dashed), and **Reconstruction**. See Table 5.5.

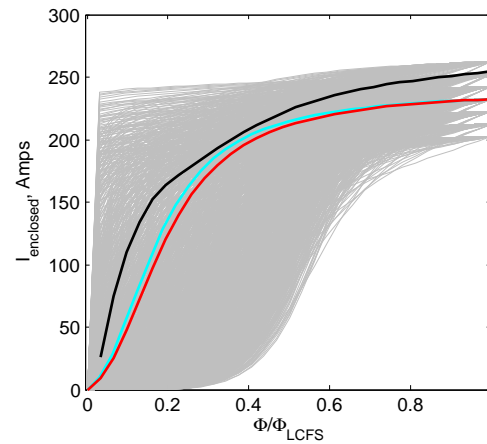


Figure 5.55 QHS 100 kW,  $\rho_{ECRH} \lesssim 0.1$ : The calculated enclosed current profile (black), **Reconstruction**, and the profile with the minimum  $\chi^2$  found during **Parameter scan #2**. The current profiles from the scan that satisfy  $\chi_\nu^2 \leq \chi_{\nu,\min}^2 + 1$  are indicated in gray. See Table 5.5.

Parameter		PRES_SCALE		AM(2)		AM(3)		PHIEDGE	
		Value	$\sigma$	Value	$\sigma$	Value	$\sigma$	Value	$\sigma$
Initial Guess		1214.	-	1.	-	0.361	-	0.0424	-
Reconstruction		1213.	542.	1. *	-	0.662	0.376	0.0408	0.0016
Parameter Scan #1 **		1000.	-	2.32	-	0.657	-	0.0408*	-
Parameter Scan #2 **		1213.*	-	1. *	-	0.662*	-	0.0408*	-
CURTOR		AC(2)		AC(3)		$\chi^2$	$\nu$	$\chi_\nu^2$	$F_\chi$
Value	$\sigma$	Value	$\sigma$	Value	$\sigma$				
255.	-	10.	-	1.5	-	342.5	107	-	-
232.	3.2	9.97	2.32	1.5*	-	132.8	107	1.24	-
232.*	-	9.97*	-	1.5*	-	132.6	106	1.25	-
232.	-	11.81	-	1.5	-	132.3	106	1.25	-

Table 5.5 QHS,  $100kW$ ,  $\rho_{ECRH} \lesssim 0.1$ . V3FIT reconstruction results using the signals from the external magnetic diagnostic array, internal poloidal array, Rogowski coil, and limiter signal. Black: Initial guess. **Reconstruction with 5 free parameters.** Scan of pressure profile parameters, holding the current profile constant. Scan of current profile parameters, holding the pressure profile constant. The  $\chi^2$ ,  $\chi_\nu^2$  and  $F_\chi$  values are also shown, were relevant. (\*) Quantity was not a fit parameter for this case. (\*\*) The limiter signal was disabled and PHIEDGE was not a fit parameter.

steady state current,  $I_{tor}(t = \infty) \sim 160 A$ , and  $\bar{N}_e \sim 3 \times 10^{18}/m^3$ , listed in Table 5.1, are within a few percent of each other in magnitude, and, for the current, of opposite sign. An operational density as high as  $\bar{N}_e \sim 4 \times 10^{18}/m^3$  was not possible for this resonance location. Compared to  $50 kW$ ,  $\rho_{ECRH} \lesssim 0.1$  case, the electron temperature is reduced in the core region,  $\rho \lesssim 0.25$ . and the density is slightly reduced. The profiles are used as input for PENTA, which calculates the neoclassical ambipolar solutions for  $E_r$  both with and without MC, shown in Figure 5.60. The parallel current density profile for each case is shown in Figure 5.61 (with MC) and Figure 5.62 (without MC).

In the QHS  $50kW$ ,  $\rho_{ECRH} \sim 0.3$  case, there is only a single stable ambipolar  $E_r$  root across the plasma profile. Compared to the  $50 kW$ ,  $\rho_{ECRH} \lesssim 0.1$  case, the current density is reduced in both MC and non-MC calculations, but the reduction is much larger in the non-MC case. The enclosed current profiles with and without MC, shown in Figure 5.63 show that the net toroidal current is



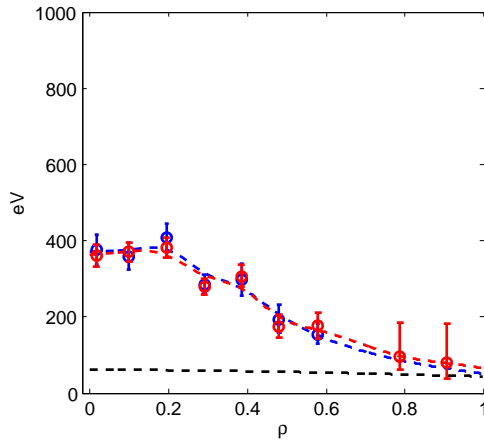


Figure 5.56 QHS,  $50kW$ ,  $\rho_{ECRH} \sim 0.3$ :  $T_e$  for CCW (blue) and CW (red).  $T_i$  estimate from ChERS (black, dashed).

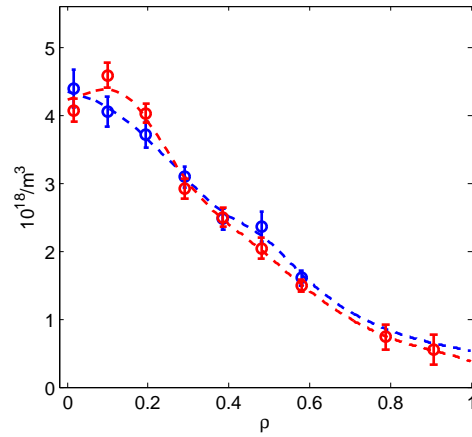


Figure 5.57 QHS,  $50kW$ ,  $\rho_{ECRH} \sim 0.3$ :  $N_e$  for CCW (blue) and CW (red).

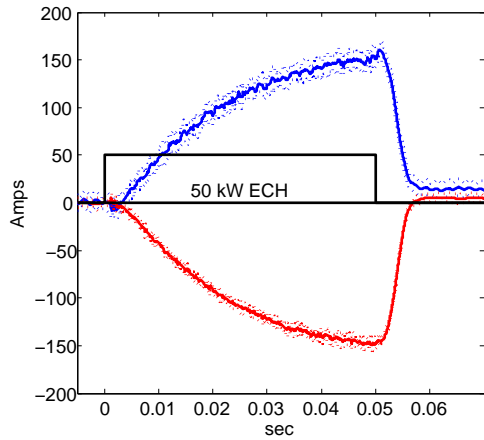


Figure 5.58 QHS,  $50kW$ ,  $\rho_{ECRH} \sim 0.3$ : Measured net toroidal current for an ensemble average of 7 shots with the magnetic field in the CCW (blue) and CW (red) directions.

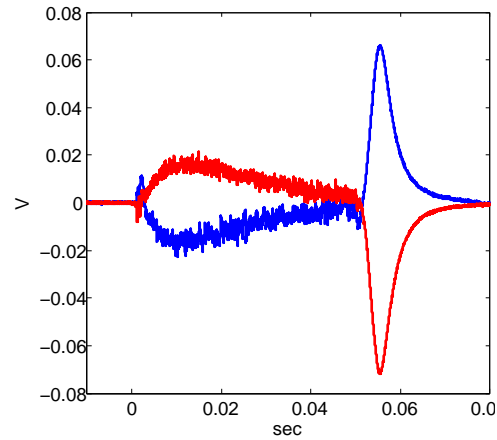


Figure 5.59 QHS,  $50kW$ ,  $\rho_{ECRH} \sim 0.3$ : Measured loop voltage (ens. avg.).

expected to be around 180 A when MC is included, and only about 55 A when MC is not included in the model. The extrapolated net current from the Rogowski measurement is  $\sim 165$  A, which agrees better with the calculation that includes MC. This is the profile used in the time evolution simulation. The parallel conductivity profile is shown in Figure 5.64.

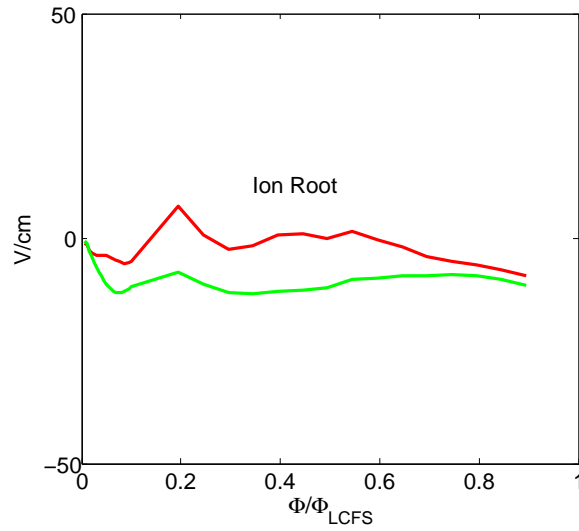


Figure 5.60 QHS,  $50kW$ ,  $\rho_{ECRH} \sim 0.3$ : Stable ambipolar  $E_r$  with MC (red) and without MC (green). Calculation by PENTA.

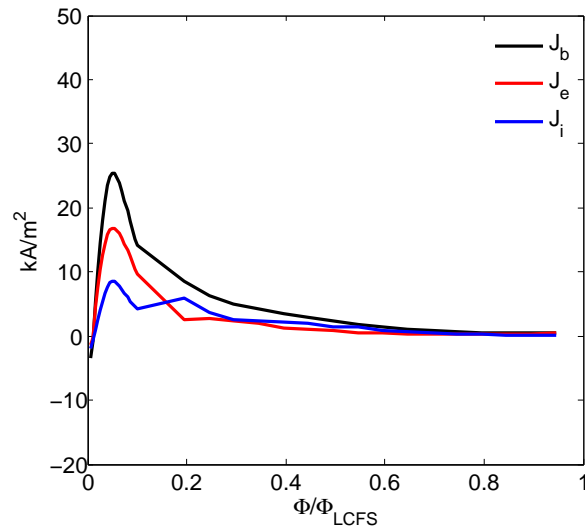


Figure 5.61 QHS,  $50kW$ ,  $\rho_{ECRH} \sim 0.3$ , with MC: Ion (blue), electron (red) and total (black) parallel current. Only ion root solutions exist for this case. Calculation by PENTA.

The measured and simulated loop voltage signals are shown in Figure 5.65, and they are in excellent agreement. The simulated current profile and pressure profile at  $t_{sim} = 50 \text{ ms}$  are shown in Figures 5.66 and 5.68. A Lorentz-fitline is shown in the pressure profile, which serves

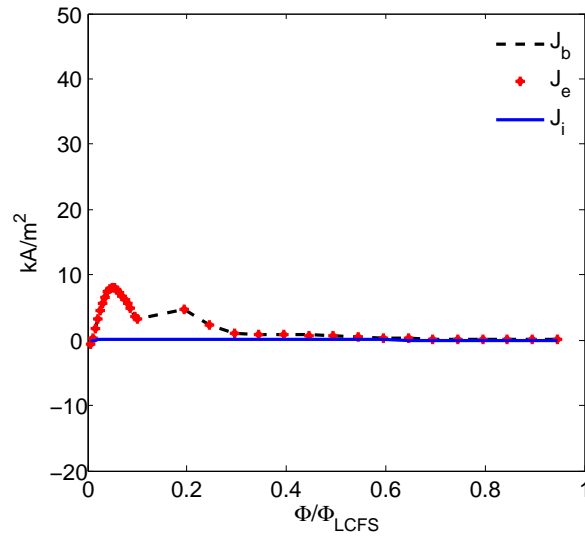


Figure 5.62 QHS,  $50kW$ ,  $\rho_{ECRH} \sim 0.3$ , without MC: Ion (blue), electron (red) and total (black) parallel current. Only ion root solutions exist for this case. Calculation by PENTA.

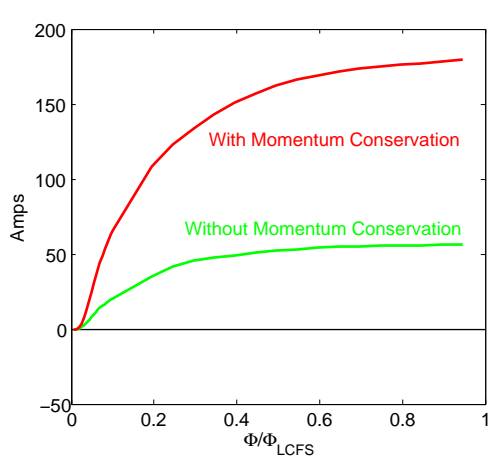


Figure 5.63 QHS,  $50kW$ ,  $\rho_{ECRH} \sim 0.3$ : Enclosed current profile for different possible scenarios of current density.

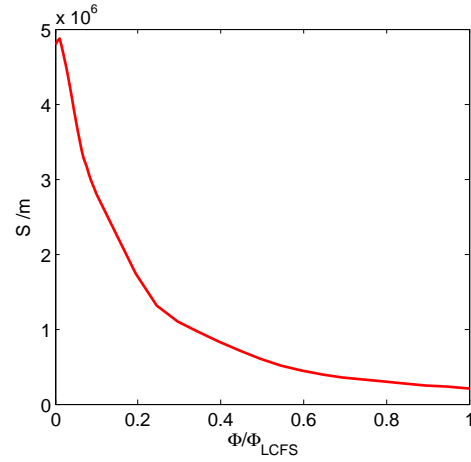


Figure 5.64 QHS,  $50kW$ ,  $\rho_{ECRH} \sim 0.3$ : Parallel conductivity of the plasma, including the effects of trapped particles. Calculation by PENTA.

as the initial guess in the reconstruction process. An arctan-fitline is shown for the current profile, which serves as the initial guess profile for the reconstruction. The reconstruction here uses only the Rogowski, limiter, and the  $B_r$  and  $B_\theta$  signals from the external diagnostic array. The internal

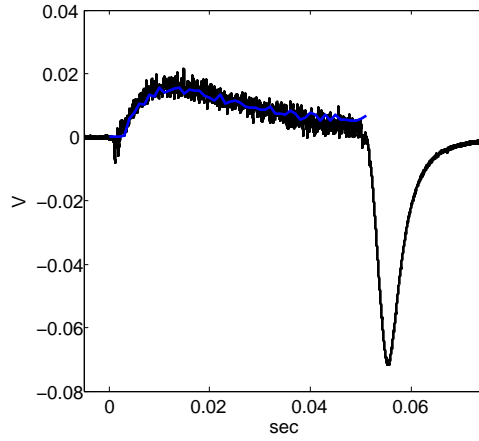


Figure 5.65 QHS, 50kW,  $\rho_{ECRH} \sim 0.3$ : Measured (black) and simulated (blue) loop voltage. Calculation by IEG.

poloidal array was not configured for equilibrium reconstruction measurements at the time this data was taken. The reconstruction results are shown in each figure, as are the profiles found during parameter scans that satisfy  $\chi_\nu^2 \leq \chi_{\nu, \min}^2 + 1$ . The parameters for the initial guess, reconstruction, and both parameter scans are shown in Table 5.6.

Similar to the previous reconstructions using the signals from the external array, the reconstructed plasma pressure is  $\sim 1.8$  times larger than the measured profile, and the measured pressure profile is on the edge of the  $\chi_\nu^2 \leq \chi_{\nu, \min}^2 + 1$  set. The net toroidal current is predicted well, but, as with the pressure profile, the calculated current profile is on the edge of the  $\chi_\nu^2 \leq \chi_{\nu, \min}^2 + 1$  parameter scan. The reconstructed profiles have  $\chi_\nu^2 = 0.68$ .

## 5.6 Summary

For the 6 cases in Table 5.1, the total enclosed current was calculated for the limiting cases listed in Table 5.7. The cases are, with MC, i-root dominant, e-root dominant, and without MC, i-root dominant. The estimate of the steady state current that is closest to the extrapolated value with the estimate that includes MC and is in the ion-root wherever the ion-root is a stable ambipolar  $E_r$  solution. The MC i-root dominant solution also correctly predicts little change or even a small reduction in current going from the 50 kW,  $\rho_{ECRH} \lesssim 0.1$  case to the 100 kW,  $\rho_{ECRH} \lesssim 0.1$ . This

Parameter		PRES_SCALE		AM(2)		AM(3)		PHIEDGE	
		Value	$\sigma$	Value	$\sigma$	Value	$\sigma$	Value	$\sigma$
Initial Guess		301.	-	1	-	0.625	-	-0.0400	-
Reconstruction		373.	180.	1.*	-	1.177	0.985	-0.0419	0.0011
Parameter Scan #1 **		900.	-	0.38	-	0.657	-	-0.0419*	-
Parameter Scan #2 **		373.*	-	1.*	-	1.177*	-	-0.0419*	-
CURTOR		AC(2)		AC(3)		$\chi^2$	$\nu$	$\chi_\nu^2$	$F_\chi$
Value	$\sigma$	Value	$\sigma$	Value	$\sigma$				
-147	-	10.	-	1.5	-	152.	60	-	-
-148.	3.	1.00	4.13	1.5*	-	41.	60	0.68	-
-148.*	-	1.00*	-	1.5*	-	40.	59	0.67	-
-148.	-	0.47	-	2.2	-	28.	59	0.47	-

Table 5.6 QHS, 50kW,  $\rho_{ECRH} \sim 0.3$ . V3FIT reconstruction results using the signals from the external magnetic diagnostic array, Rogowski coil, and limiter signal. Black: Initial guess.

Reconstruction with 5 free parameters. Scan of pressure profile parameters, holding the current profile constant. Scan of current profile parameters, holding the pressure profile constant. The  $\chi^2$ ,  $\chi_\nu^2$  and  $F_\chi$  values are also shown, were relevant. (\*) Quantity was not a fit parameter for this case. (\*\*) The limiter signal was disabled and PHIEDGE was not a fit parameter.

was because in the 100 kW case, the ion-root was not stable for a slightly larger region near the axis. The electron-root current density is the opposite sign to that in the ion-root, and since it is the only stable root in this region, increasing the radial extent of this region decreases the total current a small amount. The e-root dominant case tends to underestimate the total current. The estimates from the non-MC solution exceeds the measurement in the 100 kW,  $\rho_{ECRH} \lesssim 0.1$  case by 100 A or more, while it is smaller than the measurement by 100 A or more in the 50 kW,  $\rho_{ECRH} \sim 0.3$  case and by about 200 A in the 50 kW,  $\rho_{ECRH} \lesssim 0.1$  case.

For each of the reconstruction cases presented here, either the i-root dominant or i-root only current profile and parallel conductivity profile were used in the IEG code to simulate the current profile. The reconstructions based on the internal diagnostics show good agreements with measured pressure profile and calculated (time-evolved) current profile. When the diagnostics signals from the external array are used in the reconstruction, the reconstructed pressure profile is about

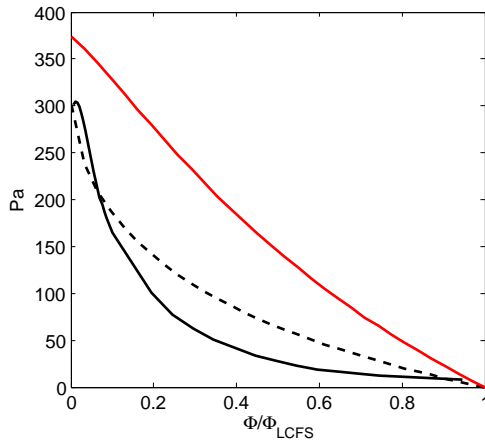


Figure 5.66 QHS 50 kW,  $\rho_{ECRH} \sim 0.3$ : Measured plasma pressure profile (black), the Lorentz-fit initial guess (black, dashed), and **Reconstruction**. See Table 5.6.

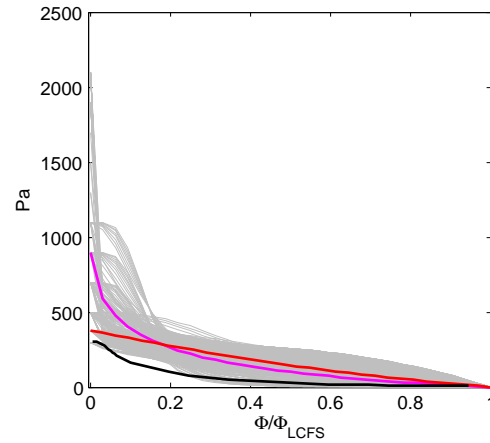


Figure 5.67 QHS 50 kW,  $\rho_{ECRH} \lesssim 0.1$ : Measured plasma pressure profile (black), **Reconstruction**, and the profile with the minimum  $\chi^2$  found during **Parameter scan #1**. The pressure profiles from the scan that satisfy  $\chi^2_{\nu} \leq \chi^2_{\nu, \min} + 1$  are indicated in gray. See Table 5.6.

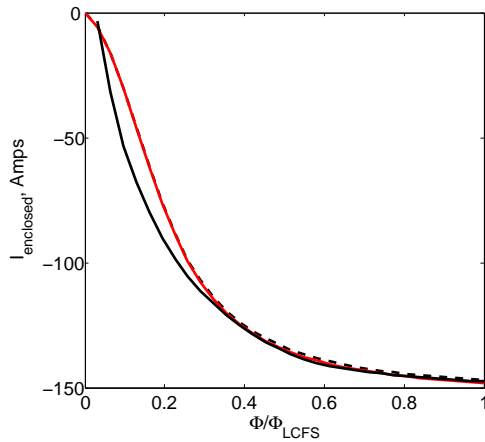


Figure 5.68 QHS 50 kW,  $\rho_{ECRH} \sim 0.3$ : The calculated enclosed current profile (black), the arctan initial guess (black, dashed), and **Reconstruction**. See Table 5.6.

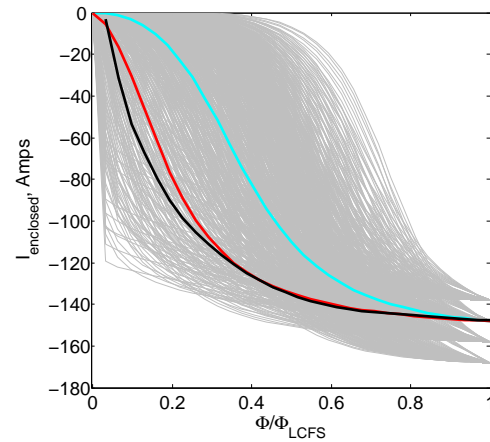


Figure 5.69 QHS 50 kW,  $\rho_{ECRH} \lesssim 0.1$ : The calculated enclosed current profile (black), **Reconstruction**, and the profile with the minimum  $\chi^2$  found during **Parameter scan #2**. The current profiles from the scan that satisfy  $\chi^2_{\nu} \leq \chi^2_{\nu, \min} + 1$  are indicated in gray. See Table 5.6.

Field Configuration	$\rho_{ECRH}$	$P_{ECRH}$ , launched	$\bar{N}_e$	$I_{tor}(t = \infty)$	I.b, w/ MC, i-root dom	I.b, w/ MC, e-root dom	I.b, w/o MC, i-root dom
QHS CCW*	$\rho \lesssim 0.1$	50 kW	4.1	386. $\pm$ 23. A	261.	6.	202.
QHS CW	$\rho \lesssim 0.1$	50 kW	4.2	-411. $\pm$ 46. A	-285.	60.	- 173.
QHS CCW*	$\rho \lesssim 0.1$	100 kW	4.1	352. $\pm$ 21. A	242.	-110.	440.
QHS CW	$\rho \lesssim 0.1$	100 kW	4.0	-343. $\pm$ 20. A	-243.	281.	-593.
QHS CCW	$\rho \sim 0.3$	50 kW	3.1	167. $\pm$ 14. A	162.	-	64.
QHS CW*	$\rho \sim 0.3$	50 kW	3.0	-164. $\pm$ 11. A	-179.	-	56.

Table 5.7 Configuration space explored with balanced fueling in the QHS configuration. Resonance location, heating power and operating  $\bar{N}_e (\times 10^{18}/m^3)$ , extrapolated steady state current, and net current with MC in i-root and e-root dominant solution, and without MC in the i-root dominant solution. \* Reconstruction is presented in this chapter.

twice the measured profile, and the calculated current profile is near the edge or outside of the  $\chi^2_{\nu} \leq \chi^2_{\nu, \min} + 1$  boundary found from the parameter scans around reconstructed current profile, indicating that the the model and reconstruction only agree marginally. A possible reason for the poor agreement with the external diagnostics will be discussed in Section 6.3.

## References

- [1] W. Guttentfeller, J. Lore, D. T. Anderson, F. S. B. Anderson, J. M. Canik, W. Dorland, K. M. Likin, and J. N. Talmadge, PRL **101**, 215002 (2008).



## Chapter 6

### Conclusions and Future Work

In the previous chapter, results of the neoclassical modeling of the bootstrap current, the time-evolution of the net toroidal current, and the reconstruction of the equilibrium plasma pressure and current profile in the quasi-helically symmetric (QHS) magnetic configuration were presented. The helical rotation of the Pfirsch-Schlüter current due to the lack of toroidal curvature was confirmed by measurements with two ‘belts’ of magnetic diagnostic triplets separated by  $1/3$  of a field period and mounted on the external side of the vacuum vessel. The reversal of the neoclassical bootstrap current in QHS, compared to a tokamak, was confirmed with measurements by a Rogowski coil. The measured radial profiles of the electron temperature and density and ion temperature in hydrogen plasmas were used as inputs for the neoclassical transport code, PENTA, which includes the effects of momentum conservation between the electron and ion flows. The 3-D inductive response of the plasma was simulated and the calculated current profile was used as the initial guess for the 3-D equilibrium reconstruction code, V3FIT. V3FIT used the measured magnetic diagnostic signals as constraints to reconstruct the plasma pressure and current profiles. Using the internal magnetic diagnostics, the reconstructed pressure profile agreed well with measurements from Thomson scattering. The reconstruction of the current profile is consistent with the calculated neoclassical bootstrap current. Because of the high effective transform, the magnitude of both the Pfirsch-Schlüter and bootstrap currents are reduced by  $\sim 3$ . The level of uncertainty in the reconstructed pressure and current profiles is largest near the core of the plasma.

In the remainder of this chapter, possible topics for future research and unresolved questions are discussed.

## 6.1 Benchmarking PENTA

The PENTA code [1] calculates the neoclassical transport fluxes, radial electric field, and parallel flows, including the effects of momentum conservation between different plasma species. It has been shown to reproduce intrinsic ambipolarity in symmetric devices. [2]. The PENTA code is applicable for a large range of toroidal configurations with vastly different effective ripple, from ITER which is estimated to have an effective ripple as low as  $10^{-5}$  near the magnetic axis to conventional stellarators with an effective ripple of  $\sim 1$ .

The PENTA codes uses the DKES transport coefficients [3] in its calculation [4] of the neoclassical quantities above. The DKES code has been benchmarked against several other codes [5], including field-line integration codes, such as NEO [6], [7],  $full - f$  and  $\delta f$  Monte Carlo simulations [8], [9], [10], [11], [12], and GSRAKE [13]. The results of the benchmarking show that DKES does a good job accurately calculating the monoenergetic transport calculations in most cases. DKES is limited in the sense that it takes a long time for DKES results to converge in the extremely low-collisionality regime. DKES is also sensitive to a region near a ‘poloidal-resonance’, [14],

$$E_r^{res} = \frac{|n - mt|}{mt} v_{Ta} B_\theta \quad (6.1)$$

When this condition is satisfied, the poloidal precession of particles is reduced to zero, increasing the particle diffusion, and for larger  $E_r$ , the particles are detrapped [15] [16], and the diffusion and flows are reduced. This condition is easily achieved in HSX plasmas. For example [17], at  $\rho \sim 0.2$  with  $T_i \sim 50$  eV,  $B_\theta \sim \epsilon_{41} B_0$ ,  $\epsilon_{41} \sim 0.003$ , and  $E_r^{res} \sim 70 - 90$  V/cm, as shown in Figure 6.1. It is this resonance condition that is responsible for predicting large parallel ion flows and small parallel electron flows near the core of QHS plasmas. This predicted resonance is seen in the DKES transport calculations, but it is known that the calculations are inaccurate near this region (the  $\mathbf{E} \times \mathbf{B}$  drift is modeled as incompressible, which may not necessarily be true [18]). The validity of this calculation near this regime is of some concern, since the non-locality of the transport near this condition violates the single-surface assumption of the DKES code, and changes the results of subsequent calculations, i.e. PENTA.

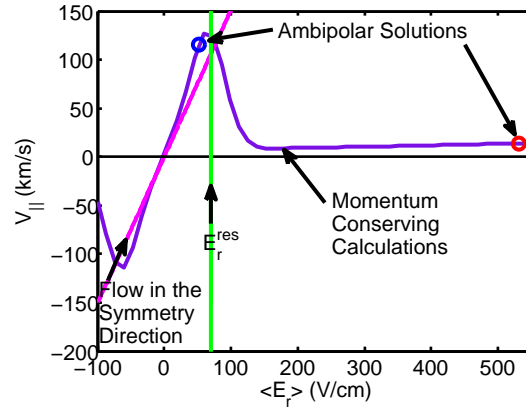


Figure 6.1 The relationship between parallel flow velocity and the radial electric field at  $r/a=0.2$  as calculated by PENTA is plotted in purple. The ambipolar solutions, resonant value of  $E_r$  and relationship between  $V_{||}$  and  $E_r$  that would result in a net flow in the direction of symmetry are shown for that radial location. Figure courtesy A. Briesemeister [17].

The PENTA code has not been benchmarked against other codes that include momentum conservation. One other such code is the VENUS+ $\delta f$  code [19], which uses a  $\delta f$  Monte Carlo method to calculate  $D_{31}$  and  $D_{33}$ , the transport coefficients related to the parallel flow (current) and conductivity. In the future, some effort should be made to benchmark PENTA against VENUS+ $\delta f$  (or similar code) to check under which conditions the PENTA calculations are valid and where they need further refinement.

## 6.2 Improving the Reconstruction

For the reconstructions presented in this thesis, it is clear the certainty of the plasma pressure gradient and the current density profile near the axis is low. This section will discuss ways to improve the reconstruction and to increase the level of certainty on the reconstructed profiles.

### 6.2.1 Improve S/N ratio

As the SVD study in Appendix G suggests, the reconstruction of the plasma profiles with the internal diagnostic array, where the typical uncertainty for each signal is  $\pm 0.25 - 0.5 G$ , is probably

limited to 5 or 6 reconstruction parameters, Figure G.6. This was seen in Section 5.3.1, where the number of parameters was adjusted from 5 to 7. The reconstruction with 6 free parameters was only marginally better than that with 5 free parameters, and adding a 7th parameter did not improve the reconstruction any better. To increase the number of parameters that can be used in the reconstruction, improving the signal-to-noise ratio (S/N) for the diagnostics may help, although only marginally. Even with only  $\pm 0.05 G$  of noise, the number of parameters that can be extracted from the data will only increase to 7 or 8. For this same level of noise ( $\pm 0.05 G$ ), the SVD study shows that reconstructions with the external diagnostic array may be able to resolve up to 9 parameters in the reconstruction. This result holds even for a diagnostic set consisting of the entire ‘virtual triplets’, Figure G.3, indicating that even a small level of noise, or uncertainty in the signal has a large impact in the ability to reconstruct the plasma profiles.

### 6.2.2 Optimize the Diagnostic Set

In the design of National Compact Stellarator Experiment (NCSX), an optimized set of magnetic diagnostics were chosen to accurately reconstruct the plasma pressure and current profiles [20]. The process began by calculating the magnetic signal normal to the vacuum vessel on a dense mesh ( $20 \times 60$ ) of points for  $\sim 2500$  different plasma pressure and current profiles. It was predicted that 19 unique eigenvalues, each corresponding to a reconstruction parameter, could be extracted from the data collected by the diagnostics. Starting with a trial set of 600 diagnostics covering the vacuum vessel and measuring the flux normal to the vacuum vessel, the magnetic signal for each diagnostic for the  $\sim 2500$  equilibria were calculated. A selection process was performed to rank the diagnostics according to how effective each was in determine the reconstruction, and diagnostics were eliminated if they were redundant or ineffective. It was found that there was a high correlation between important (low rank #) diagnostics and the distance from the vacuum vessel to the plasma. Diagnostics located closer to the plasma were better suited for reconstruction. At the end of the ranking process, 225 diagnostic loops were selected for reconstruction purposes.

V3FIT calculates the signal effectiveness of a diagnostic, which is defined as [21]

$$R_{ji} = \frac{d \log \sigma_{pj}}{d \log \sigma_i} \quad (6.2)$$

Here,  $j$  refers to the reconstruction parameter index,  $i$  is the diagnostic index,  $\sigma_{pj}$  is the uncertainty in the reconstructed parameter, Eqn 4.85, and  $\sigma_i$  is the signal uncertainty.  $R_{ji}$  is a measure of how much the uncertainty of the reconstructed parameter improves (decreases) if the noise level on the  $i$ th signal is reduced.  $R$  is dimensionless and non-negative, and  $\sum_i R_{ji} = 1$ .  $R_{ji}$  provides a measure of how effective a diagnostic is for reconstructing a fit parameter. For instance, for the reconstruction of the net toroidal current,  $CURTOR$  in VMEC, the  $R_{ij}$  parameter is largest for the Rogowski signal. The value of  $R_{ji}$  is local in parameter space, i.e. for a particular plasma pressure and current profile, and so different diagnostics may be more significant for different equilibrium. By inspecting the signal effectiveness matrix, it may be possible to identify specific locations on the vacuum vessel that are important for reconstruction, and either improve the diagnostics at that location, or install better ones.

### 6.2.3 Other Methods of Measuring Magnetic Fields

As discussed in the Chapter 1, there are other methods to measure the magnetic field strength in toroidal plasmas. Two methods making use of polarimetry are possible. Measuring the Faraday rotation of a probe beam [22] and another is to measure the polarization due to the motional Stark effect [23]. These do not appear feasible in HSX.

### 6.2.4 Other Reconstruction Constraints

V3FIT is an on-going project and the types of diagnostics that can be used for reconstruction constraints is being expanded [24]. Soft x-ray and Thomson scattering data are in the process of being included in the reconstruction routine, which should improve the reconstruction of the plasma pressure profile.

### 6.3 Vessel Eddy Currents

The reconstructions with the internal diagnostics agreed better with the measured pressure and calculated current profiles than did the reconstructions with the external diagnostics. In particular, the pressure profile from the reconstructed profile based on the external diagnostics had about  $2\times$  the total stored energy than measured. The effects of the vacuum vessel were not included in the modeling. It's possible that eddy currents are produced in the vacuum vessel by the parallel electric field induced in the plasma by the bootstrap current.

The parallel current density,  $J \cdot B$ , at three toroidal locations along a 1/2-field period is shown in Figure 6.2 for  $t_{sim} = 10 \text{ ms}$  and  $t_{sim} = 50 \text{ ms}$  for the plasmas discussed in Section 5.1. Early in the shot the dipole Pfirsch-Schlüter current density is the dominant current density, but by the end of the shot the bootstrap current has become the largest component, making most of the current density unidirectional. The magnetic field generated by the evolving current profile was calculated for a dense mesh of points covering the vacuum vessel and plotted for several times during the simulation, Figure 6.3. The figure shows the  $|B|$  and  $\vec{B}$  caused by the plasma current (the main field contribution has been suppressed). As the simulation moves forward in time, helical 'stripes' in  $|B|$  can be seen grow in intensity on the vessel. The direction of the magnetic field is predominately in a poloidal-like direction. The magnetic field is changing in time because of an induced electric field,

$$\frac{\partial \mathbf{B}}{\partial t} = -\nabla \times \mathbf{E} \quad (6.3)$$

Since the vessel itself is conductive, a current in the vessel will be

$$\mathbf{J} = \sigma \mathbf{E} \quad (6.4)$$

This current will generate a magnetic field

$$\mathbf{J} = \nabla \times \frac{\mathbf{B}}{\mu} \quad (6.5)$$

By substituting Eqn 6.5 into 6.4 and then into 6.3,

$$\frac{\partial \mathbf{B}}{\partial t} = -\nabla \times \nabla \times \frac{\mathbf{B}}{\sigma \mu} \quad (6.6)$$

By solving Eqn 6.6 on the vacuum vessel, and then for  $\mathbf{J}$ , modifications to the measured field outside of the vacuum vessel due to the eddy currents in the vessel can be determined. By including the effect of the conductive vacuum vessel, the reconstruction with the external diagnostics should improve.

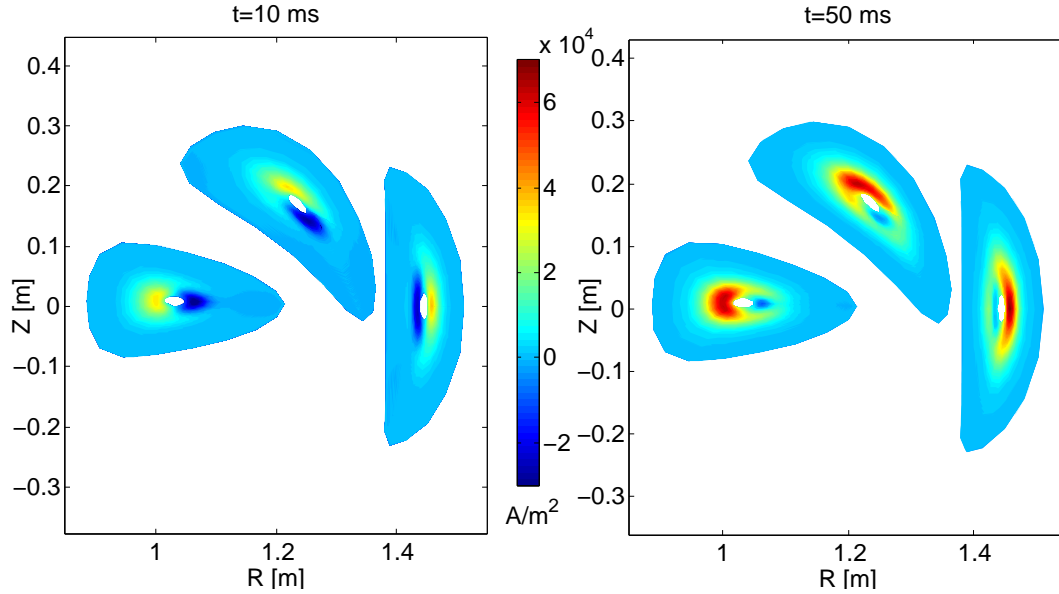


Figure 6.2  $J \cdot B$  at three toroidal locations during the plasma evolution. Calculation by VMEC.

Eddy currents due to changes in current in external field coils have been modeled on the W7-AS stellarator [25] and on the NSTX spherical tokamak [26]. In each of those cases, the modeling improved the measurement of the plasma beta. Eddy currents from the plasma column shift has been detected by vibrational measurements with accelerometers in the vacuum vessel of LHD, but the analysis indicates that more sensors are required to determine the distribution of the eddy current in the vacuum vessel [27].

## 6.4 Magnetic Islands

Magnetic islands can have detrimental effects on plasma confinement. Islands have the potential to form near rational surfaces, where  $t = n/m$  and  $n$  and  $m$  are low-order integers. When an island is present in the plasma volume, it forms a region with its own separatrix. The field

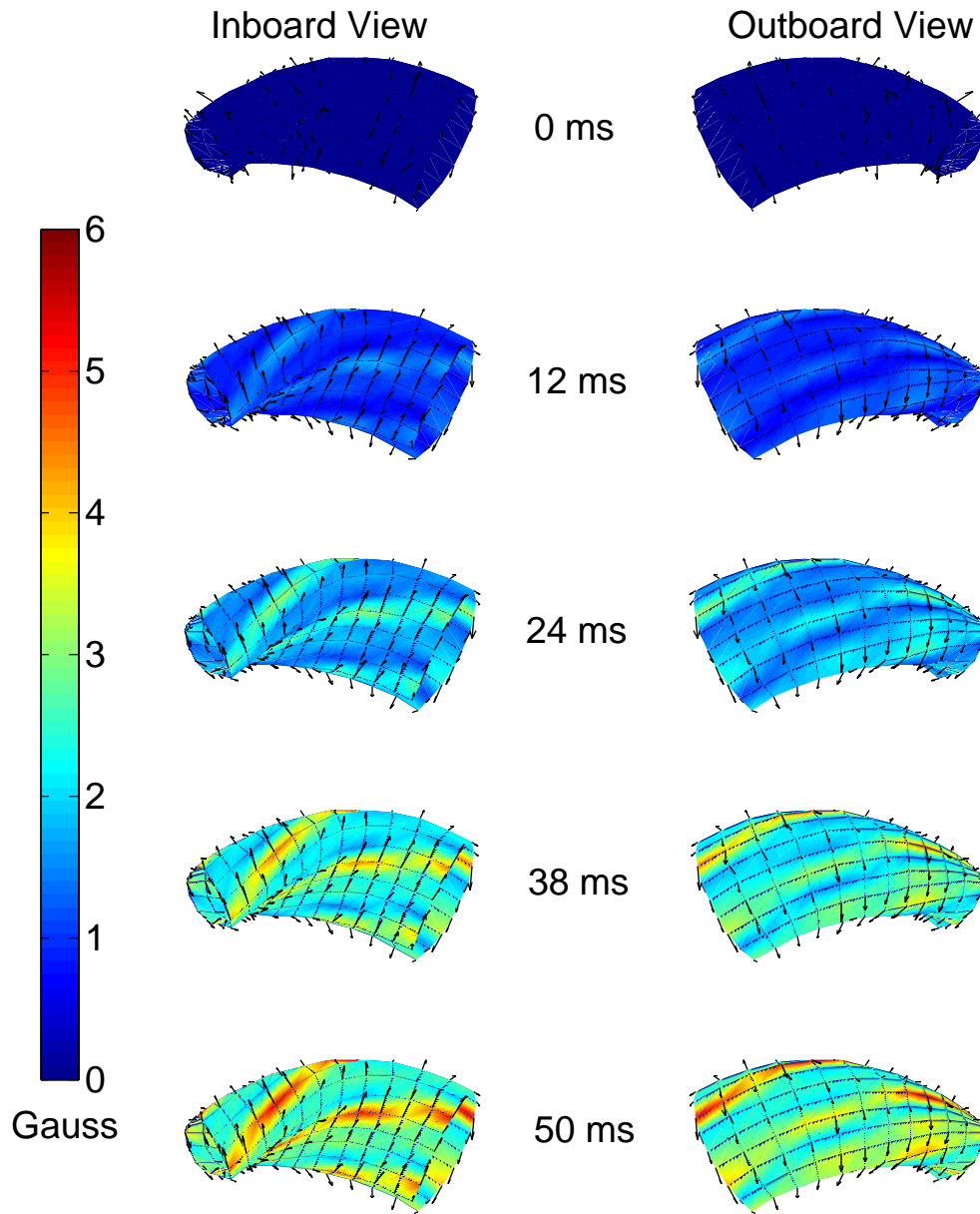


Figure 6.3  $|B|$  and  $\vec{B}$  on the vacuum vessel during the plasma evolution.



lines on the separatrix travel along the surface and eventually sample the space on every side of the island. They are short-circuiting or connecting the region just inside and just outside of the location of the island. This increases the radial transport in the area around the island, decreasing the confinement [28]. In some cases, islands have been found to be beneficial for confinement, particularly when located near the last-closed flux surface. In W7-AS, an improved confinement regime, an H-mode, was found when rational surfaces were located just outside the last-closed flux surface [29]. It is of interest to be able to detect and identify the presence of island.

The V3FIT code uses VMEC as its equilibrium solver, which does not allow for the possibility of magnetic islands on the computational grid. V3FIT is modular and can be adapted to use any equilibrium solver. The Scalable Island Equilibrium Solver for Toroidal Applications code, or SIESTA, is designed to be a 3-D MHD equilibrium solver that resolves islands and stochastic regions [30]. SIESTA uses the same background coordinates system and spectral representation as VMEC, so it well suited to be used with V3FIT.

With SIESTA and V3FIT, the expected response for magnetic diagnostics can be calculated for the case when islands are in the plasma. HSX has ability to lower and raise the rotational transform of the QHS configuration. By lowering the rotational transform to  $t = 1$ , a set of  $n/m = 4/4$  islands can form in the vacuum field, Figure 6.4. If the islands produce a unique signature in the diagnostic signals, it may be possible to study the effects that islands have on plasma in HSX, i.e. changes in confinement or transport properties.

## 6.5 Mirror Flip Field

In Appendix H, the results of plasmas made in the Mirror configuration are presented. An attempt was made to match the temperature and density profiles achieved in QHS to study the effects that the Mirror magnetic spectrum, which has symmetry-breaking terms, as shown in Figure 1.7, has on the bootstrap current. The results of the Mirror flip-field experiments indicate that the net toroidal current depends on the direction of the main magnetic field. The reason for this is not understood.

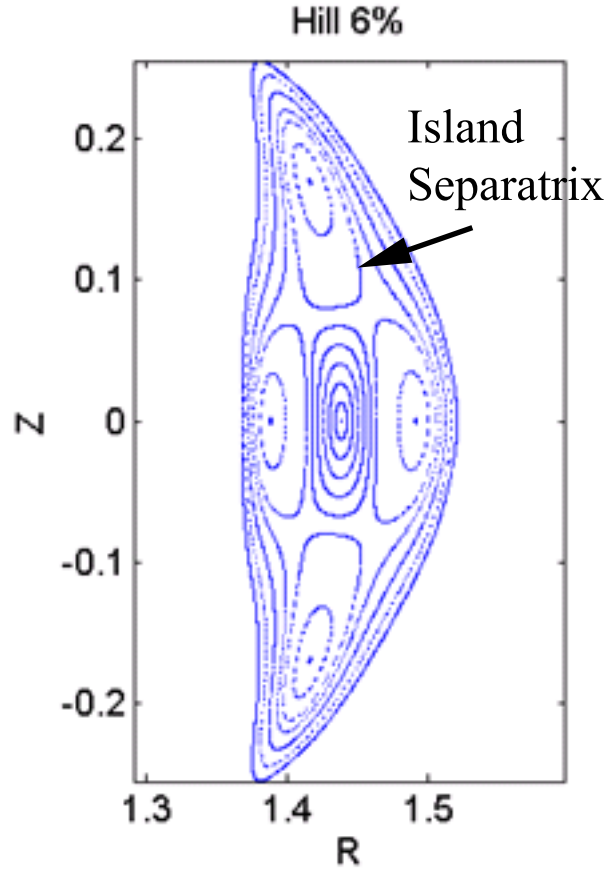


Figure 6.4 Poicaré plot of surfaces in the Hill 6% configuration with 4/4 island structure.

## 6.6 Near-ECH Fueling

The fueling source for the plasmas discussed in this dissertation was the puff valve located far away from the ECH launch mirror, at the opposite side of the machine near boxport A, Figure 5.2. In Appendix I, the results of flip field experiments with the fueling provided by a puff valve in field period C, located only a short distance away toroidally from the ECH antenna, are presented. For four different operating line-averaged operating densities,  $\bar{N}_e = (2, 3, 4, 5) \times 10^{18}/m^3$ , differences in the measured density profiles and net toroidal current were observed when the direction of the main field was switched from CCW to CW. At present, only speculative ideas regarding the interaction of the neutral fueling gas with the plasma have been made.

## References

- [1] D. A. Spong, Physics of Plasmas **12**, 056115 (2005).
- [2] J. Lore, Ph. D. dissertation, University of Wisconsin-Madison (2010).
- [3] W. I. van Rij and S. P. Hirshman, Phys. Fluids B **1**, 563 (1989).
- [4] H. Sugama and S. Nishimura, Physics of Plasmas **9**, 4637 (2002).
- [5] C. D. Beidler, et al., “Results From the International Collaboration on Neoclassical Transport in Stellarators (ICNTS)”, 22nd IAEA Fusion Energy Conference, TH/P8-10 (2008).
- [6] V. V. Nemov, et al., Phys. Plasmas **6**, 4622 (1999).
- [7] W. Kernbichler, et al., Plasma Fusion Res. **3**, S1061 (2008).
- [8] C. D. Beidler, J. Comput. Phys **72**, 220 (1987) .
- [9] A. Wakasa, et al., J. Plasma Fusion Res. Series **4**, 408 (2001).
- [10] V. Tribaldos, Phys. Plasmas **8**, 1229 (2001).
- [11] M. Yu Isaev, et al., Fusion Sci. Technology **50**, 440 (2006).
- [12] K. Allmaier, Phys. Plasma **15**, 072512 (2008).
- [13] C. D. Beidler and W. D. D’haeseleer, Plasma Phys. Control. Fusion **37**, 463 (1995).
- [14] M. Yokoyama, M. Wakatani, and K. C. Shaing, Nuclear Fusion **35**, 153 (1995).
- [15] H. Maassberg, et al., Phys. Fluids B **5**, 3627 (1993).
- [16] H. Maassberg, et al., Phys. of Plasmas **16**, 072504 (2009).
- [17] A. Briesemeister, Ph. D. Preliminary Report, University of Wisconsin, Madison, WI (2011).
- [18] C. D. Beidler, et al., Proceedings of the 16th ISHW, Ceratopia Toki, Toki, Japan (2007).
- [19] M. Yu Isaev, et al., Nuclear Fusion **49**, 075013 (2009).

- [20] N. Pomphrey, E. Lazarus, M. Zarnstorff, A. Boozer, A. Brooks, *Phys. Plasmas* **14**, 056103 (2007).
- [21] J. D. Hanson, et al., “Three-Dimensional Equilibrium Reconstruction: The V3FIT Code”, 2009 International Stellarator/Heliotron Workshop, Invited Talk (2009).
- [22] D. L. Brower, et al., *PRL* **88**, 185005 (2002).
- [23] C. C. Petty, et al., *Plasma Physics and Controlled Fusion* **43**, 1077 (2005).
- [24] J. D. Hanson, personal communication.
- [25] H. Laqua and F. Schneider, *Fusion Engineering and Design* **48**, 143 (2000).
- [26] D. A. Gates, et. al, *Review of Scientific Instruments* **75**, 5090 (2004).
- [27] K. Nakamura, “Inference of Eddy Current Distribution by Vibration Measurement of Vacuum Vessel”, Annual Report of National Institute of Fusion Science, Japan, 111 (2010).
- [28] F. Wagner, et al, *Proc. 25th EPS Conf. Control. Fusion and Plasma Physics*, B049PR, (1998).
- [29] H. Wobig and J. Kisslinger, *Plasma Physics and Controlled Fusion* **42**, 823 (2000).
- [30] S. P. Hirshman, R. Sanchez and C. R. Cook, *Physics of Plasmas* **18** (2011), to be published.

## Appendix A: Variational Moments Equilibrium Code

### A.1 VMEC Overview

The MHD equilibrium code, VMEC [1], solves the MHD force balance equation, Ampere's and Gauss's laws in a 3D-toroidal geometry:

$$\mathbf{F} = -\mathbf{J} \times \mathbf{B} + \nabla p = 0 \quad (\text{A.1})$$

$$\nabla \times \mathbf{B} = \mu_0 \mathbf{J} \quad (\text{A.2})$$

$$\nabla \cdot \mathbf{B} = 0 \quad (\text{A.3})$$

The code assumes a set of nested, closed flux surfaces exist. The plasma pressure,  $p(s)$ , is constant on each surface. The innermost surface is the magnetic axis and the outermost surface is the last closed flux surface (LCFS). The radial coordinate is  $s = \Phi/\Phi_{LCFS}$ , where  $\Phi$  is the toroidal flux enclosed within a surface. Two angular coordinates are defined:  $\zeta$  and  $\theta$  are toroidal and poloidal angles, respectively. Each has a range of  $(0 \rightarrow 2\pi)$ . The toroidal angle,  $\zeta$ , is the same as the geometric (laboratory) toroidal angle. The surfaces are defined by the inverse coordinate transformation

$$R = R(s, \theta, \zeta) \quad (\text{A.4})$$

$$Z = Z(s, \theta, \zeta) \quad (\text{A.5})$$

A magnetic stream function,  $\lambda(s, \theta, \zeta)$ , is introduced to define another poloidal angle,  $\theta^* = \theta + \lambda$ , which makes the magnetic field lines straight in the coordinate system. The magnetic field lines can be written as

$$\mathbf{B} = \frac{t}{2\pi} \nabla \zeta \times \nabla \Phi + \frac{1}{2\pi} \nabla \Phi \times \nabla \theta^* \quad (\text{A.6})$$

With the toroidal and poloidal mode numbers given by  $n$  and  $m$ , respectively, a general Fourier series expansion in the VMEC coordinate system is

$$f(s, \theta, \zeta) = \sum_m \sum_n [f_{mn,\sin} \sin(m\theta - n\zeta) + f_{mn,\cos} \cos(m\theta - n\zeta)] \quad (\text{A.7})$$

Stellarator symmetry implies that at some toroidal plane, say  $\zeta = 0$ , the vacuum symmetry of the external coils system imposes vertical symmetry, such that  $R(s, \theta, 0) = R(s, -\theta, 0)$  and  $Z(s, \theta, 0) = -Z(s, -\theta, 0)$ . This implies that the inverse coordinate transformation can be written as the sums

$$R(s, \theta, \zeta) = \sum_m \sum_n R_{mn,cos}(s) \cos(m\theta - n\zeta) \quad (\text{A.8})$$

$$Z(s, \theta, \zeta) = \sum_m \sum_n Z_{mn,sin}(s) \sin(m\theta - n\zeta) \quad (\text{A.9})$$

This also has the consequence that the stream function can be written as [1]

$$\lambda(s, \theta, \zeta) = \sum_m \sum_n \lambda_{mn,sin}(s) \sin(m\theta - n\zeta) \quad (\text{A.10})$$

The plasma energy in the volume of the plasma is defined as the sum of magnetic and kinetic energy:

$$W = \int_{V_{pl}} dV \left( \frac{|B|^2}{2\mu_0} + \frac{p}{\gamma - 1} \right) \quad (\text{A.11})$$

Here,  $\gamma$  is the adiabatic index. Minimizing the variation of the energy,  $\delta W$ , leads to a volume-averaged residual force of

$$\mathbf{F} = -\mathbf{J} \times \mathbf{B} + \nabla p = 0 \quad (\text{A.12})$$

The selection of the poloidal angle,  $\theta$ , accelerates the convergence with minimal spectral content [2]. The boundary conditions at the plasma edge are that the total pressure is continuous across the LCFS, and that the normal component of the magnetic field is 0:

$$\frac{|B_{in}|^2}{2\mu_0} + \frac{p}{\gamma - 1} = \frac{|B_{out}|^2}{2\mu_0} \quad \mathbf{B} \cdot \nabla \Phi = 0 \quad (\text{A.13})$$

The numerical minimization is performed by a conjugate gradient steepest descent method.

## A.2 VMEC Input file

The VMEC input file, *input.configuration* contains a list of the following (it is generally not case-sensitive except in the specification of filenames):

- RBC, ZBS: Initial guess of Fourier spectrum of  $R$ - and  $Z$ - components of the last closed flux surface, or boundary
- RAXIS, ZAXIS: Initial guess of the Fourier spectrum of the magnetic axis.
- NS\_ARRAY: The number of radial surfaces in the computation grid.
- NFP: The number of field periods.
- MPOL: The number of poloidal harmonics to include in the Fourier series.
- NTOR: The number of toroidal harmonics to include in the Fourier series.
- NTHETA: The number of poloidal grid points in the computational grid.
- NZETA: The number of toroidal grid points in the computational grid.
- PHIEDGE: The toroidal magnetic flux enclosed by the last closed flux surface.
- FTOL\_ARRAY: The minimum value which the volume-averaged residual force,  $F$ , must reach before the equilibrium is considered to have reached convergence.
- PMASS\_TYPE: The type of specification of the radial pressure profile.
- AM: Parameters or coefficients of the pressure profile.
- PRES\_SCALE: A scaling factor of the pressure profile (default = 1).
- PCURR\_TYPE: The type of specification of the radial current profile.
- AC: Parameters of coefficients of the current profile.
- CURTOR: The toroidal current enclosed by the LCFS.
- LFREEB: Logical flag to indicate if the equilibrium is a free-boundary, 'T', or fixed boundary, 'F'.

- **MGRID\_FILE:** A string in single quotes “ ” for the path to the mgrid file for the magnetic configuration. This is required for free-boundary calculations.

There is also a set of parameters that deal with the minimization algorithm and preconditioners, which will not be discussed here. The logical flag, **LFREEB**, which is set to 'T' (true) to indicate that the equilibrium represents a free-boundary solution where the VMEC code permits the  $R$  and  $Z$  spatial coordinates to evolve. If the flag is set to 'F' (false), then the LCFS is fixed. This is often desirable when calculating vacuum equilibria  $p(s) \equiv 0$ ,  $J(s) \equiv 0$ . However, when the pressure and current profiles are non-zero, clamping the LCFS to its vacuum value results in poorly understood inconsistencies in the calculations of the magnetic field, via V3FIT, and this is undesirable and avoided by using the free-boundary solution. Two of the parameters, **NS\_ARRAY** and **FTOL\_ARRAY** must be the same length. In general, VMEC allows one to specify an **NS\_ARRAY** with an increasing number of radial surfaces. But, when V3FIT is controlling the VMEC calls, only the first element of the **NS\_ARRAY** is used.

The default specifications of the pressure and current density profiles are power series, explicitly specified by **PMASS\_TYPE** = 'POWER\_SERIES' or **PCURR\_TYPE**='POWER\_SERIES'. In each of these cases, the coefficients of the power series are contained in the **AM** and **AC** arrays. The pressure profile is

$$p(s) = PRES\_SCALE \cdot (AM(0) + AM(1) \cdot s + AM(2) \cdot s^2 + AM(3) \cdot s^3 + \dots) \quad (\text{A.14})$$

and the current density profile and normalization is

$$J(s) \propto ac(0) + AC(1) \cdot s + AC(2) \cdot s^2 + AC(3) \cdot s^3 + \dots \quad (\text{A.15})$$

$$\int_0^1 ds J(s) = CURTOR \quad (\text{A.16})$$

The power series expansions are convenient for simple profile specifications, but for the purposes of representing realistic experimental profiles, they are not ideal. Many terms are required to reproduce the typically peaked pressure profiles in QHS plasmas, and often the power-series fit will have regions of negative plasma pressure. The current density profile also suffers from similar



problems. In addition to the ill-fitting characteristics, the reconstruction process of V3FIT does not perform well with the large number of free parameters required to model the profiles.

Another possible specification of the pressure profiles is a Lorentz-type profile, `PMASS_TYPE = 'TWO_LORENTZ'`.

$$\begin{aligned} \frac{p(s)}{PRES\_SCALE \cdot AM(0)} = & \frac{AM(1)}{N_0} \left( \frac{1}{\left(1 + \left(\frac{s}{AM(2)^2}\right)^{AM(3)}\right)^{AM(4)}} - c_0 \right) \\ & + \frac{1 - AM(1)}{N_0} \left( \frac{1}{\left(1 + \left(\frac{s}{AM(5)^2}\right)^{AM(6)}\right)^{AM(7)}} - c_1 \right) \end{aligned} \quad (\text{A.17})$$

The normalization terms are

$$\begin{aligned} c_0 &= \left(1 + \left(\frac{1}{AM(2)^2}\right)^{AM(3)}\right)^{-AM(4)} \\ c_1 &= \left(1 + \left(\frac{1}{AM(5)^2}\right)^{AM(6)}\right)^{-AM(7)} \\ N_i &= 1 - c_i \end{aligned} \quad (\text{A.18})$$

With  $AM(0) \equiv 1$ , The number of free parameters is 8. The number of free parameters can be reduced to 4 if  $AM(1) \equiv 1$ . This specification is positive-definite, and does a good job of approximating pressure profiles derived from Thomson Scattering, either with 4 or 8 free parameters.

Figures A.1 - A.3 show example pressure profiles made by the 'TWO\_LORENTZ' pressure profile with  $AM(0) = AM(1) = AM(5) = AM(6) = AM(7) = 1$ , while the parameters  $AM(2)$ ,  $AM(3)$  and  $AM(4)$  are scanned around the value of unity. The scan of  $AM(3)$  shows the widest variation of achievable plasma pressure profiles for a 1-parameter scan. The scans of the  $AM(2)$  and  $AM(4)$  values show that if the rest of the parameters are set to 1, flat pressure profiles (near the plasma core) are unlikely to be modeled well.

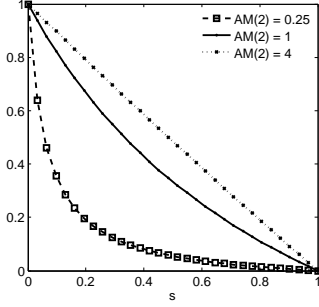


Figure A.1  $P(s)$  for  $AM(0) = AM(1) = AM(3) = AM(4) = 1$ ,  $AC(5) = AC(6) = AC(7) = 1$  and  $AM(2) = (0.25, 1, 4)$ .

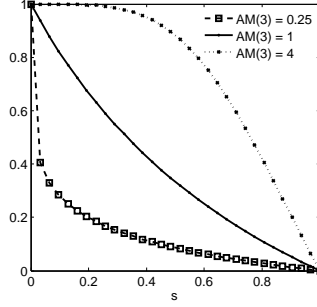


Figure A.2  $P(s)$  for  $AM(0) = AM(1) = AM(2) = AM(4) = 1$ ,  $AC(5) = AC(6) = AC(7) = 1$  and  $AM(3) = (0.25, 1, 4)$ .

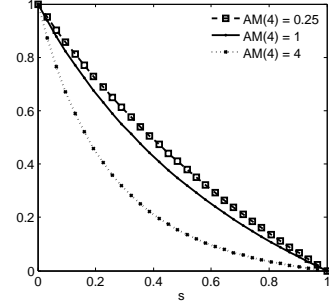


Figure A.3  $P(s)$  for  $AM(0) = AM(1) = AM(2) = AM(3) = 1$ ,  $AC(5) = AC(6) = AC(7) = 1$  and  $AM(4) = (0.25, 1, 4)$ .

An alternate current profile specification is `PCURR_TYPE = 'SUM_ATAN'`, where the enclosed toroidal current profile is described by a sum of arctangent functions:

$$I_{enclosed}(s) \propto AC(0) + \sum_{i=1}^5 AC(1 + 4(i-1)) \frac{2}{\pi} \arctan \left( \frac{AC(2 + 4(i-1)) s^{AC(3+4(i-1))}}{(1-s)^{AC(4+4(i-1))}} \right) \quad (\text{A.19})$$

The normalization is determined by the total enclosed toroidal current:

$$I_{enclosed}(s=1) = CURTOR \quad (\text{A.20})$$

Figures A.4 - A.6 are examples of enclosed current and current density profiles modeled by the 'SUM\_ATAN' basis function, with only a single arctan-function in the sum. In each, the location of the current and current density is compared for different function parameters near unity. In Figure A.4,  $AC(0) = 0$ ,  $AC(1, 4) = 1$ , and two parameters are varied:  $AC(2) = (0.25, 1, 4)$ ,  $AC(3) = (1, 1.5, 2)$ . The current density profiles for this case show that it can represent situations where the current density is peaked, near-axis, mid-radius, or near the edge of the plasma. When  $AC(0) = 0$ ,  $AC(1) = AC(2) = AC(4) = 1$ ,  $AC(3) = (0.25, 1, 4)$ , Figure A.2, current density profiles that are peaked near-axis or the mid-radius may not be modeled very well with this set of parameters. In Figure A.6,  $AC(0) = 0$ ,  $AC(1) = AC(2) = AC(3) = 1$ , and  $AC(4) = (0.25, 1, 4)$ . Here, current density profiles that are not peaked on-axis or that are not flat may not be modeled very well.

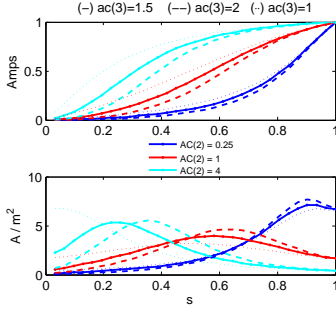


Figure A.4  $I(s)$  and  $I'(s)$  for  
 $AC(0) = 0$ ,  $AC(1, 4) = 1$ ,  
 $AC(2) = (0.25, 1, 4)$ ,  
 $AC(3) = (1, 1.5, 2)$ .

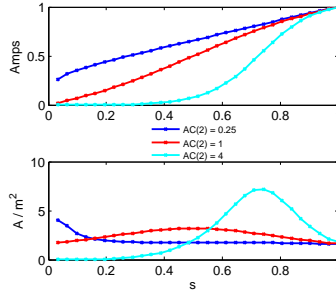


Figure A.5  $I(s)$  and  $I'(s)$  for  
 $AC(0) = 0$ ,  
 $AC(1) = AC(2) = AC(4) = 1$ .  
 $AC(3) = (0.25, 1, 4)$ .

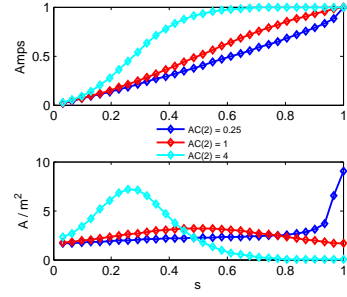


Figure A.6  $I(s)$  and  $I'(s)$  for  
 $AC(0) = 0$ ,  
 $AC(1) = AC(2) = AC(3) = 1$ .  
 $AC(4) = (0.25, 1, 4)$ .

### A.3 VMEC Input file: QHS

The RBC and ZBS coefficients in the input file serve as an initial guess of the last closed flux surface of the plasma column. If the initial guess is too far away from the final converged solution, the VMEC solver may not be able to find the solution by the steepest decent method and it will not converge. It is important to start from a reasonable initial guess of the LCFS. The vacuum last closed flux surface serves as a good starting point.

To determine the Fourier series of the last closed flux surface, Poincaré plots were generated for a set of 200 surfaces separated equiangular in the laboratory toroidal angle, 50 surfaces per field period. The Poincaré plots used a field-line following code that calculated the magnetic field of the QHS magnetic configuration using a Biot-Savart code, without using magnetic field interpolation. The field line was followed for a total of 200 orbits around the machine and because of the 4 symmetric field periods, 800 points were generated for each of the 50 surfaces in a field period. Next, these points are used in the DESCUR/SCRUNCH [2] code to calculate the VMEC-compatible Fourier series expansion that best fits these points in a least-squares sense.

The level of agreement between the Poincaré plots and the Fourier expansion depends strongly on the presence of vacuum magnetic islands or island remnants, as seen in Figures A.7 and A.8. In Figure A.8, the surfaces are labeled by the  $R$ -value of the launch point of the field-line following ( $Z = 0$  for all launch points). Near the LCFS of the QHS configuration, a  $(n, m) = (12, 11)$  island

chain lies between the surfaces with starting launch points of  $R = 1.509\text{ m}$  and  $1.510\text{ m}$ . Outside of the  $R = 1.5161\text{ m}$  surface, a  $(n, m) = (20, 18)$  island chain causes significant corrugation of that flux surface. The effect of the ability to closely match the magnetic surfaces with a finite Fourier series with only a few terms is limited due to these corrugations. The surface with  $R = 1.513\text{ m}$  is chosen as the initial guess for the LCFS in the QHS VMEC input file.

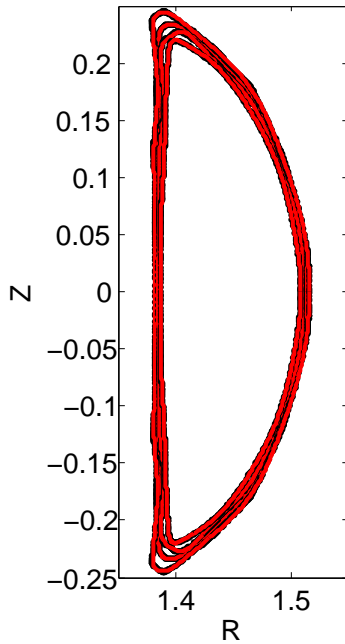


Figure A.7 Poincaré plot of flux surfaces (black) and Fourier series expansions (red) for surfaces near the LCFS of the QHS magnetic configuration.

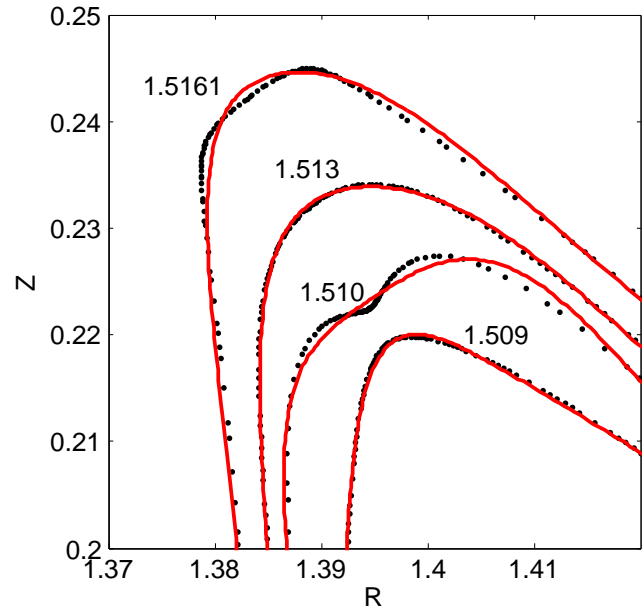


Figure A.8 The same surfaces as in Figure A.7, zoomed in to the region near the top of the D-shape. The R-value of the launch point of each flux surface labels each set of points.

Like the initial guess of the LCFS, VMEC also converges faster and more consistently if the initial guess of the magnetic axis is close to the actual one. The DESCUR code finds an initial guess of the magnetic axis by calculating the Fourier series expansion of the geometric center of the points that define the LCFS. For the highly shaped surfaces of the QHS plasma, this tends to be a poor estimate. A better initial guess of the magnetic axis is generated by running DESCUR with a set of surfaces that were generated with a launch point very close the the magnetic axis,  $R = 1.4454\text{ m}$ ,  $Z = 0\text{ m}$ . The location of the magnetic axis along one half of a field period

calculated with these two method is compared in table A.1. The axis generated from LCFS points is several mm to cm away from the axis generated by near-axis points.

The VMEC equilibrium and subsequent calculations depend on the choice of the LCFS. In particular, the Boozer coordinate transformation and DKES and PENTA transport calculations are modified depending on which LCFS is chosen. These effects are discussed elsewhere [3].

The magnetic diagnostic signals from V3FIT depend strongly on the minimum tolerance level achieved by the VMEC code. Figure A.9 shows how the magnetic signals for a single triplet due to the plasma currents varies with the inverse residual force balance,  $1/FTOL$ . A linear pressure gradient (in s) and a constant toroidal current density were chosen for this equilibrium:  $p(s) = 2000 \cdot (1 - s) \text{ Pa}$ , and  $J(s) = 400 \text{ A/s}$ ,  $I_{total} = 400 \text{ A}$ . In practice, the minimum FTOL is set to  $1e-15$  to ensure that the VMEC equilibrium and magnetic signals are well converged.

The number of poloidal and toroidal harmonics and the number of radial surfaces in the equilibrium has a large effect on the minimum residual force balance that can be achieved. To consistently reach a value of  $FTOL \leq 1e-15$ , and to maintain reasonable radial resolution of the plasma column, the VMEC input file has the following settings:

- NS\_ARRAY = 32
- MPOL = 6
- NTOR = 8

#### A.4 Information generated by VMEC

VMEC generates a set of output files. The spectrum and spectral coefficients of the inverse coordinate transformation, Eqns A.8 and A.9, magnetic field strength, current density, are stored in output files *wout\_configuration.nc* and *jxbout\_configuration.nc*. For example, the inverse coordinates are used to find the location of the computation grid. In the *wout\_configuration.nc* file, the poloidal and toroidal mode numbers are stored in arrays respectively as

$$xm(1 : mn\_mode) \quad \quad \quad xn(1 : mn\_mode) \quad \quad \quad (A.21)$$

	$R = 1.513 \text{ m}$		$R = 1.4454 \text{ m}$		Difference	
Toroidal Angle [* $\pi/(2 * 50)$ ]	R [m]	Z [m]	R [m]	Z [m]	$\Delta R$ [m]	$\Delta Z$ [m]
0	1.426E+00	1.157E-04	1.445E+00	-3.750E-09	0.019	-1.157e-05
1	1.424E+00	2.341E-02	1.443E+00	2.498E-02	0.019	0.00157
2	1.417E+00	4.612E-02	1.437E+00	4.939E-02	0.02	0.00327
3	1.406E+00	6.759E-02	1.426E+00	7.266E-02	0.02	0.00507
4	1.392E+00	8.718E-02	1.411E+00	9.423E-02	0.019	0.00705
5	1.374E+00	1.045E-01	1.393E+00	1.136E-01	0.019	0.0091
6	1.353E+00	1.192E-01	1.372E+00	1.305E-01	0.019	0.0113
7	1.330E+00	1.311E-01	1.349E+00	1.446E-01	0.019	0.0135
8	1.306E+00	1.400E-01	1.323E+00	1.555E-01	0.017	0.0155
9	1.281E+00	1.459E-01	1.297E+00	1.634E-01	0.016	0.0175
10	1.255E+00	1.490E-01	1.269E+00	1.681E-01	0.014	0.0191
11	1.230E+00	1.494E-01	1.242E+00	1.697E-01	0.012	0.0203
12	1.206E+00	1.472E-01	1.215E+00	1.683E-01	0.009	0.0211
13	1.182E+00	1.428E-01	1.189E+00	1.640E-01	0.007	0.0212
14	1.160E+00	1.364E-01	1.165E+00	1.573E-01	0.005	0.0209
15	1.140E+00	1.284E-01	1.142E+00	1.485E-01	0.002	0.0201
16	1.121E+00	1.189E-01	1.121E+00	1.379E-01	0	0.019
17	1.104E+00	1.083E-01	1.102E+00	1.256E-01	-0.002	0.0173
18	1.089E+00	9.675E-02	1.085E+00	1.122E-01	-0.004	0.01545
19	1.077E+00	8.445E-02	1.071E+00	9.780E-02	-0.006	0.01335
20	1.066E+00	7.148E-02	1.059E+00	8.267E-02	-0.007	0.01119
21	1.057E+00	5.789E-02	1.049E+00	6.688E-02	-0.008	0.00899
22	1.050E+00	4.381E-02	1.042E+00	5.055E-02	-0.008	0.00674
23	1.045E+00	2.939E-02	1.036E+00	3.386E-02	-0.009	0.00447
24	1.042E+00	1.476E-02	1.033E+00	1.697E-02	-0.009	0.00221
25	1.041E+00	2.255E-05	1.032E+00	-5.000E-09	-0.009	-2.2555e-05

Table A.1 Comparison between the  $(R, Z)$ -coordinates of the magnetic axis calculated by DESCUR for two set of flux surfaces with different launch points. The  $R = 1.513 \text{ m}$  is the launch point that generates the LCFS, while the  $R = 1.4454 \text{ m}$  is a launch point close to the vacuum magnetic axis. The extent of the toroidal angle starts at toroidal cut near the boxport (0) and ends at a vertical cut at the joint flange region (25).

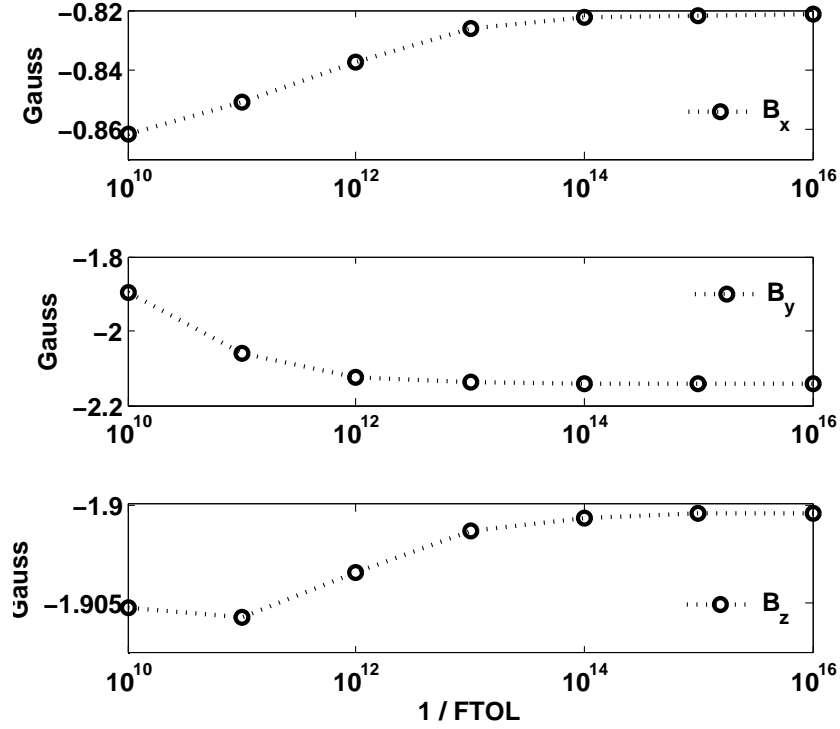


Figure A.9 The magnetic signals due to plasma currents for an external magnetic diagnostic triplet. The signal varies with the residual force balance tolerance achieved by VMEC. In practice, FTOL=1e-15 is chosen for reconstruction attempts.

The coefficients are stored in arrays

$$rmnc(1 : ns, 1 : mn\_mode) \quad (\text{A.22})$$

for the R-coordinate, and

$$zmns(1 : ns, 1 : mn\_mode) \quad (\text{A.23})$$

for the Z-coordinate. Now, the sums A.8 and A.9 for any surface can be calculated as the cumulative sum over the poloidal and toroidal mode numbers. The derivatives of  $R$  and  $Z$  as a function

of the VMEC coordinates, for radial surface number  $s$  is,

$$R_{s,\zeta_V}(s, \theta_V, \zeta_V) = \frac{\partial R}{\partial \zeta_V} = \sum_{mn=1:mn\_mode} n \cdot rmnc^*(s, mn) \sin(m\theta_V - n\zeta_V) \quad (A.24)$$

$$R_{s,\theta_V}(s, \theta_V, \zeta_V) = \frac{\partial R}{\partial \theta_V} = \sum_{mn=1:mn\_mode} -m \cdot rmnc^*(s, mn) \sin(m\theta_V - n\zeta_V) \quad (A.25)$$

$$R_{s,\theta_V}(s, \theta_V, \zeta_V) = \frac{\partial R}{\partial s} = \sum_{mn=1:mn\_mode} \frac{d(rmnc^*(s, mn))}{ds} \cos(m\theta_V - n\zeta_V) \quad (A.26)$$

$$Z_{s,\zeta_V}(s, \theta_V, \zeta_V) = \frac{\partial Z}{\partial \zeta_V} = \sum_{mn=1:mn\_mode} -n \cdot zmns^*(s, mn) \cos(m\theta_V - n\zeta_V) \quad (A.27)$$

$$Z_{s,\theta_V}(s, \theta_V, \zeta_V) = \frac{\partial Z}{\partial \theta_V} = \sum_{mn=1:mn\_mode} m \cdot zmns^*(s, mn) \cos(m\theta_V - n\zeta_V) \quad (A.28)$$

$$Z_{s,\theta_V}(s, \theta_V, \zeta_V) = \frac{\partial Z}{\partial s} = \sum_{mn=1:mn\_mode} \frac{d(zmns^*(s, mn))}{ds} \cos(m\theta_V - n\zeta_V) \quad (A.29)$$

where  $rmnc^*(s, mn) = s^{xm/2} \cdot rmnc^\dagger(s, mn)$  and  $zmns^*(s, mn) = s^{xm/2} \cdot zmns^\dagger(s, mn)$  are derived from a radial spline fit to the normalized coefficients

$$rmnc^\dagger(s, mn) = \text{splinefit} \left( \frac{rmnc(s, mn)}{s^{xm/2}} \right) \quad (A.30)$$

$$zmns^\dagger(s, mn) = \text{splinefit} \left( \frac{zmns(s, mn)}{s^{xm/2}} \right) \quad (A.31)$$

where the poloidal mode number,  $xm$ , is used as a normalization factor. This radial derivatives are also evaluated from the spline fit coefficient, and the derivatives found this way are more accurate than from an unnormalized spline fit or partial differences [4].

The Jacobian on this ‘full-mesh’ is

$$\mathcal{J} = \mathbf{e}_\rho \cdot \mathbf{e}_\theta \times \mathbf{e}_\zeta \quad (A.32)$$

$$= \left( R_s \hat{R} + Z_s \hat{Z} \right) \cdot \left( R_{\theta_V} \hat{R} + Z_{\theta_V} \hat{Z} \right) \times \left( R_{\zeta_V} \hat{R} + Z_{\zeta_V} \hat{Z} + R \hat{\zeta} \right) \quad (A.33)$$

$$= R (Z_s R_{\theta_V} - R_s Z_{\theta_V}) \quad (A.34)$$

The  $(s, \theta_V, \zeta_V)$  part is suppressed, but each of the quantities in the expression varies on the flux surface.



## A.5 QHS-Equivalent Tokamak

The VMEC input code for a tokamak with a circular cross-section that has the same average minor and major radius, and same effective transform as HSX is below:

```
&INDATA
MGRID_FILE='NONE'
DELT=0.99
NFP=1
NCURR=0
MPOL=10 NTOR=20
NS_ARRAY=16 101
NITER=4000
NSTEP=250
NVACSKIP=4
GAMMA=0.E+0
FTOL_ARRAY=1.0E-06 1.E-11
CURTOR=0.E+0
PHIEDGE=-0.039418
AM=0.E+0
AI=1.0604E+00 -4.72E-02 1.058E-01 -2.16E-02
AC=0.E+0
RAXIS=1.2138E+00
ZAXIS=0.00E+00
RBC(0,0) = 1.2138E+00 ZBS(0,0) = 0.000000E+00
RBC(0,1) = 1.215076937910504e-001 ZBS(0,1) = 1.215076937910504e-001
/
```

## Appendix A: References

- [1] S. P. Hirshman and J. C. Whitson, *Phys. Fluids* **26**, 3553 (1983).
- [2] S. P. Hirshman and D. K. Lee, *Comp. Phys. Comm.* **39**, 161 (1985).
- [3] Jeremy Lore, Ph. D. dissertation, University of Wisconsin-Madison (2010).
- [4] S. E. Attenberger, W. A. Houlberg and S. P. Hirshman, *Journal of Comp. Physics* **72**, 435 (1987).

## Appendix B: Limiter Specification for V3FIT

The V3FIT reconstruction can include a specification of a limiter in a number of ways, such as concave polynomials, lines, circles and more through the use of a function,  $f$ , and an auxiliary function,  $g$  [1]:

$$f(R, Z) \equiv \frac{g(R, Z)}{|\nabla g(R, Z)|} \quad (\text{B.1})$$

$$g(R, Z) \equiv \sum_{i,j=0}^4 a_{RZ}(i, j) (R - R_C)^i (Z - Z_c)^j \quad (\text{B.2})$$

$$\begin{aligned} \nabla g(R, Z) \equiv & \hat{R} \left( \sum_{i,j=0}^4 a_{RZ}(i, j) i (R - R_C)^{i-1} (Z - Z_c)^j \right) \\ & + \hat{Z} \left( \sum_{i,j=0}^4 a_{RZ}(i, j) j (R - R_C)^i (Z - Z_c)^{j-1} \right) \end{aligned} \quad (\text{B.3})$$

The upper limit of 4 is arbitrary and can be changed in the source code. As it is, there are 27 free parameters for the specification of  $f$ :  $R_C$ ,  $Z_c$ ,  $a_{RZ}(i, j)$ .

The plasma edge, as calculated by following field-line launched at 20 different poloidal angles, at a single toroidal angle. As long as the value along the field line, which is tracing out the last-closed flux surface, of  $f(R, Z) < 0$ , the plasma edge has not intersected the limiter. If  $f(R, Z) > 0$  along the field-line at some point, then it has intersected the limiter and the value of  $\chi^2$  increase. Two examples [1] of simple limiters are circles and lines. A circular zero-contour with radius  $a$  centered at  $R = R_C$ ,  $Z = Z_c$  is given by

$$\begin{aligned} a_{RZ}(0, 0) &= -a^2 & a_{RZ}(2, 0) &= a_{RZ}(0, 2) = 1 \\ a_{RZ}(i, j) &= 0 & \text{for all other} & \\ g(R, Z) &= (R - R_C)^2 + (Z - Z_c)^2 - a^2 \end{aligned} \quad (\text{B.4})$$

The interior of the circle has negative values for  $f$ .

A line segment on the  $R - Z$  plane that connects points  $(R_C, Z_C)$  and  $(R_2, Z_2)$  is given by

$$\begin{aligned}
 a_{RZ}(0,0) &= 0 & a_{RZ}(1,0) &= (Z_2 - Z_C) & a_{RZ}(0,1) &= -(R_2 - R_C) \\
 a_{RZ}(i,j) &= 0 & & \text{for all other} & & \\
 g(R,Z) &= (Z_2 - Z_C)(R - R_C) - (R_2 - R_C)(Z - Z_C)
 \end{aligned} \tag{B.5}$$

The values of  $f$  on the left side of the segment directed from  $(R_C, Z_C)$  to  $(R_2, Z_2)$  are negative.

Multiple limiters may be defined. Concave polygons can be constructed by using multiple lines to define/construct the outside edge of the polygon.

## B.1 HSX Limiter

A graphite limiter mounted on an adjustable feed-through is installed on HSX at a single field period [2]. The limiter is installed at the boxport location and intersects the plasma column along a chord that perpendicular to the helical axis, and can be adjusted, Figure B.1. Figure B.2 shows the calculated outline of the limiter, without the stainless steel support tube, in a retracted position in red. The outline with the limiter positioned so that its inner edge is at the calculated last closed flux surface is shown in black, and strike points of field lines launched just outside the last closed flux surface are marked as blue  $\times$ 's. An  $(n, m) = (8, 7)$  island remnant is partially resolved in the pattern.

The V3FIT limiter specification does not permit a limiter that does not lie at a single laboratory toroidal angle. Instead, the limiter used in this dissertation was defined to lie on a vertical plane at a toroidal angle of  $0^\circ$  (the boxport), to be up-down symmetric and follow a contour similar to the QHS LCFS at this location. The V3FIT description of the limiter is:

```

n_lif = 1,
n_phi_lif = 1,
lif_rc = 1.44585,
lif_zc = 0,
lif_on_edge = T,
lif_sigma = 0.0010,
lif_arz(1,0,0) = -0.0003818,
lif_arz(1,0,2) = 0.008286,

```

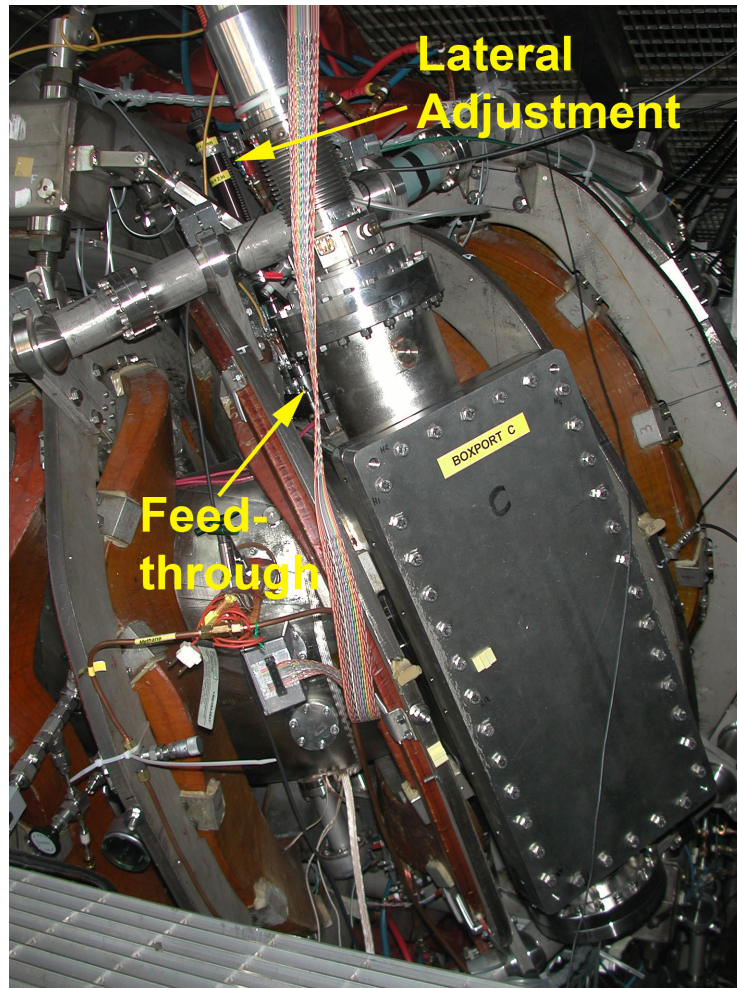


Figure B.1 The limiter at the boxport location.

```

lif_arz(1,0,4) = 0.02888,
lif_arz(1,1,0) = -0.0006503,
lif_arz(1,1,2) = 0.1527,
lif_arz(1,1,4) = 0.009945,
lif_arz(1,2,0) = 0.08481,
lif_arz(1,2,2) = -0.005776,
lif_arz(1,2,4) = 0.009752,
lif_arz(1,3,0) = 0.01129,
lif_arz(1,3,2) = 0.0003575,
lif_phi_degree(1,1) = 0.0,

sdo_data_a(66)=0.0,  ! \mathrm{the limiter is the 66th signal for this example}
sdo_sigma_a(66)=1e-3,

```

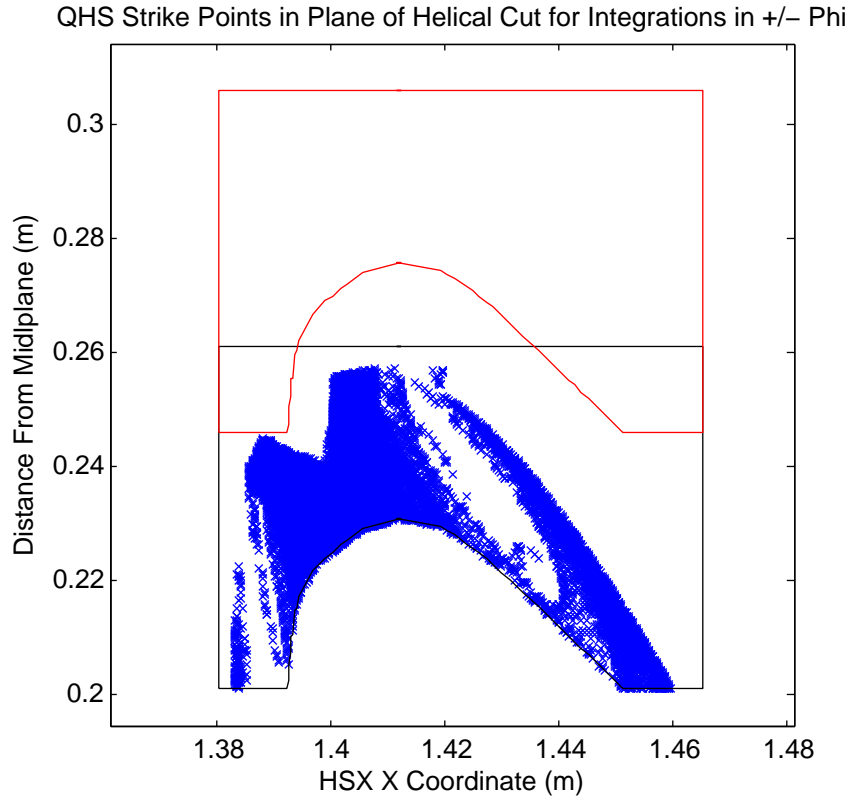


Figure B.2 Outline of graphite limiter in a retracted position (red) and with its inner edge at the LCFS of the QHS configuration (black). Strikes points of field lines launched from points outside of the LCFS are indicated by blue  $\times$ 's. Image courtesy C.Clark

A contour plot of  $f(R, Z)$  is shown in Figure B.1, showing negative values in the plasma column region and negative values outside of the LCFS. A Poincaré plot with the field lines launched at  $(R, Z, \Phi) = (1.514, 0, 0)$  is also shown (note, the surface used to define the LCFS for VMEC was derived from the surface with launch point  $(R, Z, \Phi) = (1.513, 0, 0)$ , but the differences are imperceptible). The uncertainty was chosen to be  $1e-3$ . The limiter is touches the LCFS at certain location, but does not intersect the plasma column significantly.

The presence of the limiter in the numerical calculation is useful because it prevents the reconstruction from increasing the net toroidal flux to the point where the plasma volume exceeds the dimensions of the computational grid. Experimentally, no significant change in plasma parameters were observed with the limiter at the LCFS or in its retracted position. All results shown in this

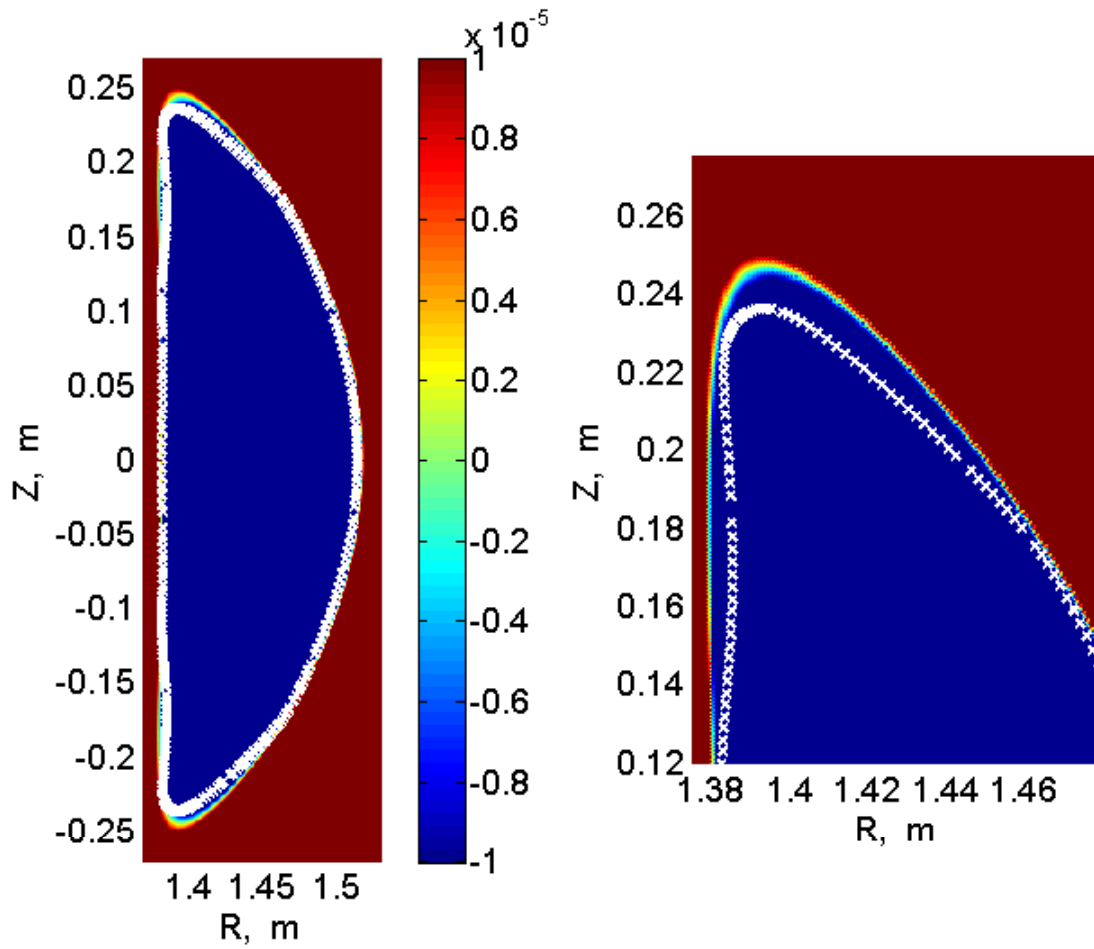


Figure B.3 Contour plot of  $f(R, Z)$  on a vertical slice at the boxport location and Poincaré plot of the LCFS (white x's).

thesis were obtained with the limiter located with its edge near the calculated QHS LCFS, with about 5 mm of uncertainty.

## **Appendix B: References**

- [1] J. D. Hanson, “Limiters in V3FIT 2009-10-21.nb”, personal communication (2009).
- [2] C. Clark, “Limiter Simulation Results”, HSX Group meeting, 5/1/2008.



## Appendix C: MHD Relationships

The standard magnetohydrodynamic (MHD) equations are stated here and relations among the various surface quantities are derived. These will be useful in the derivation of the time-evolution of the toroidal current in the plasma column. The original form of these equations, presented in a left-handed coordinate system, appear in a paper by Kruskal and Kulsrud [1]. The derivation here uses slightly different definitions of surface quantities and is in a right-handed coordinate system.

The fundamental MHD equations relate the plasma pressure gradient,  $\nabla p$ , plasma current density,  $\mathbf{J}$ , and the magnetic field (more precisely, the magnetic flux density),  $\mathbf{B}$ .

$$\nabla p = \mathbf{J} \times \mathbf{B} \quad (\text{C.1})$$

$$\mu_0 \mathbf{J} = \nabla \times \mathbf{B} \quad (\text{C.2})$$

$$\nabla \cdot \mathbf{B} = 0 \quad (\text{C.3})$$

The last equation is not a property of plasma, but of magnetic fields in general: In the absence of magnetic monopoles, the magnetic field is divergence-free. By taking the dot products,  $\mathbf{B} \cdot$  and  $\mathbf{J} \cdot$  (Eqn C.1),

$$\mathbf{B} \cdot \nabla p = 0 \quad (\text{C.4})$$

$$\mathbf{J} \cdot \nabla p = 0 \quad (\text{C.5})$$

If  $p$  is continuous and constant on some surface, then by Eqns C.4 and C.5 the surface is also a magnetic surface and a current surface, in that the magnetic field lines and current lines do not leave that surface. If this surface is 1) closed and continuous (no edges), 2) exists within a bounded region of space, and 3) if either  $\mathbf{B}$  or  $\mathbf{J}$  are non-zero on the surface, then, if it is to be realizable in physical 3-D space, the surface is a toroid [2]. A ‘toroidal’,  $\zeta$  and ‘poloidal’ angle,  $\theta$ , can be defined. Each angle increases by  $2\pi$  after one passing around the torus in some direction. The direction for the  $\zeta$ -loop is along the direction of the magnetic axis, and the direction of the  $\theta$ -loop is the ‘short way’ around the torus, which is, in general, orthogonal to the toroidal direction. See Figure C.1. The pressure,  $p$ , is assumed to increase monotonically going in toward the axis of the

torus. The pressure can be parameterized by  $p = p(\rho)$ , where  $\rho$  is some radial coordinate.  $\rho = 0$  at the magnetic axis and increases in an outward direction from the axis. The three values,  $(\rho, \theta, \zeta)$  form a right-handed coordinate system. The Jacobian is defined as

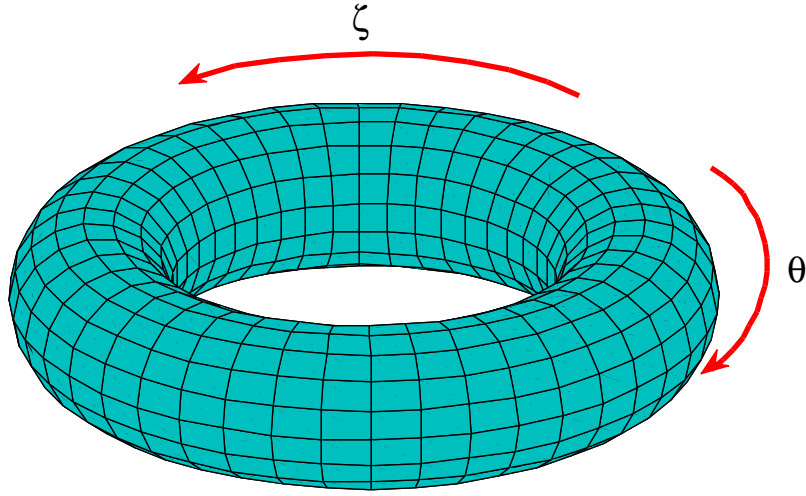


Figure C.1 A torus.

$$\mathcal{J} = \frac{1}{\nabla \rho \cdot \nabla \zeta \times \nabla \theta} \quad (\text{C.6})$$

The volume of interior to a toroidal surface with radius  $\rho$  is

$$V = \int_0^\rho d\rho \int_0^{2\pi} d\theta \int_0^{2\pi} d\zeta \mathcal{J} \quad (\text{C.7})$$

The radial derivative of the volume is

$$V' = \int_0^{2\pi} d\theta \int_0^{2\pi} d\zeta \mathcal{J} \quad (\text{C.8})$$

The flux-surface-average operator,  $\langle \rangle$ , of the value  $Q$  is defined as

$$\langle Q \rangle = \frac{1}{V'} \int_0^{2\pi} d\theta \int_0^{2\pi} d\zeta \mathcal{J} Q \quad (\text{C.9})$$

The following surface quantities are defined:

$$\begin{aligned} 2\pi\Phi(\rho) &= \int_0^\rho d\rho \int_0^{2\pi} d\theta \int_0^{2\pi} d\zeta \mathcal{J} \mathbf{B} \cdot \nabla \zeta \\ &= \int_0^\rho d\rho V' \langle \mathbf{B} \cdot \nabla \zeta \rangle \end{aligned} \quad (\text{C.10})$$

$$2\pi\Psi(\rho) = \int_0^\rho d\rho V' \langle \mathbf{B} \cdot \nabla \theta \rangle \quad (\text{C.11})$$

$$2\pi I(\rho) = \int_0^\rho d\rho V' \langle \mathbf{J} \cdot \nabla \zeta \rangle \quad (\text{C.12})$$

$$2\pi F(\rho) = \int_0^\rho d\rho V' \langle \mathbf{J} \cdot \nabla \theta \rangle \quad (\text{C.13})$$

$$2\pi U(\rho) = \int_\rho^\infty d\rho V' \langle \mathbf{B} \cdot \mathbf{B} \rangle \quad (\text{C.14})$$

$$2\pi K(\rho) = \int_0^\rho d\rho V' \langle \mathbf{J} \cdot \mathbf{B} \rangle \quad (\text{C.15})$$

Suppose that  $\mathbf{w}$  is some single valued vector field that satisfies

$$\nabla p \cdot (\nabla \times \mathbf{w}) = 0 \quad (\text{C.16})$$

Let the vector  $\mathbf{z}(\rho)$  be a set of points defined on the toroidal surfaces. For each point in the toroidal volume,  $\mathbf{x}$ , define the integral

$$\nu(\mathbf{x}) = \int_{\mathbf{z}(\rho)}^{\mathbf{x}} d\mathbf{x} \cdot \mathbf{w} \quad (\text{C.17})$$

The integration path is on a surface. For any two paths that can be continuously deformed into one another, Stokes' theorem,  $\int_S d\mathbf{S} \cdot (\nabla \times \mathbf{A}) = \oint_C d\mathbf{l} \cdot \mathbf{A}$ , and Eqn C.16, show that  $\nu(\mathbf{x})$  is independent of the path connecting the starting and finishing points and is single valued with value  $\lambda$ . If the path wraps around the torus one or more times in either the poloidal or toroidal direction, additional

contributions to the integral exists:

$$\nu(\mathbf{x}) = \lambda + \frac{\zeta}{2\pi} \oint_{\theta=0} d\mathbf{x} \cdot \mathbf{w} + \frac{\theta}{2\pi} \oint_{\zeta=0} d\mathbf{x} \cdot \mathbf{w} \quad (\text{C.18})$$

The value of  $\nabla\nu$  has a component in the  $\nabla\rho$ -direction and a component that is equal to  $\mathbf{w}$ . The  $\nabla\rho$ -part arises because the points  $\mathbf{z}$  are a function of  $\rho$ . Since  $\nabla p \times \nabla\rho = 0$ ,

$$\nabla p \times (\nabla\nu - \mathbf{w}) = 0 \quad (\text{C.19})$$

The quantity  $(\nabla\nu - \mathbf{w})$  is parallel to  $\nabla p$ . By Eqns C.4 and C.5,

$$\mathbf{B} \cdot (\nabla\nu - \mathbf{w}) = 0 \quad (\text{C.20})$$

$$\mathbf{J} \cdot (\nabla\nu - \mathbf{w}) = 0 \quad (\text{C.21})$$

Two more surface quantities may be defined:

$$2\pi Q(\rho) = \int_0^\rho d\rho V' \langle \mathbf{B} \cdot \mathbf{w} \rangle \quad (\text{C.22})$$

$$2\pi R(\rho) = \int_0^\rho d\rho V' \langle \mathbf{J} \cdot \mathbf{w} \rangle \quad (\text{C.23})$$

Radial derivatives are found by using Eqns C.10-C.13, C.18, C.20, and C.21:

$$2\pi Q' = V' \langle \mathbf{B} \cdot \mathbf{w} \rangle = V' \langle \mathbf{B} \cdot \nabla\nu \rangle \quad (\text{C.24})$$

$$= \frac{V'}{2\pi} \left\langle \mathbf{B} \cdot \nabla\zeta \oint_{\theta=0} d\mathbf{x} \cdot \mathbf{w} + \mathbf{B} \cdot \nabla\theta \oint_{\zeta=0} d\mathbf{x} \cdot \mathbf{w} \right\rangle \quad (\text{C.25})$$

$$= \Phi' \oint_{\theta=0} d\mathbf{x} \cdot \mathbf{w} + \Psi' \oint_{\zeta=0} d\mathbf{x} \cdot \mathbf{w} \quad (\text{C.26})$$

$$2\pi R' = I' \oint_{\theta=0} d\mathbf{x} \cdot \mathbf{w} - F' \oint_{\zeta=0} d\mathbf{x} \cdot \mathbf{w} \quad (\text{C.27})$$

Now, consider two possible options for the quantity  $\mathbf{w}$ :

$$\mathbf{w} = \mathbf{B} \quad (\text{C.28})$$

$$\mathbf{w} = \frac{\mathbf{B} \times \nabla p}{(\nabla p)^2} \quad (\text{C.29})$$

For the first option,  $Q = U$  and  $R = K$ . Ampere's law can be applied to the loop integrals above:

$$\oint_{\zeta=0} d\mathbf{x} \cdot \mathbf{B} = \mu_0 I \quad (\text{C.30})$$

$$\oint_{\theta=0} d\mathbf{x} \cdot \mathbf{B} = \mu_0 F \quad (\text{C.31})$$

Then, the radial derivatives can be written as:

$$2\pi U' = \langle B^2 \rangle V' = \mu_0 (F\Phi' + I\Psi') \quad (\text{C.32})$$

$$2\pi R' = \langle \mathbf{J} \cdot \mathbf{B} \rangle V' = \mu_0 (FI' - IF') \quad (\text{C.33})$$

For the second option,  $Q = 0$  and  $2\pi R = V$ . The loop integrals in this case are

$$\oint_{\zeta=0} d\mathbf{x} \cdot \mathbf{w} = \frac{1}{2\pi} \oint_{\zeta=2\pi} d\mathbf{x} \cdot \mathbf{w} \zeta - \oint_{\zeta=0} d\mathbf{x} \cdot \mathbf{w} \zeta \quad (\text{C.34})$$

$$= \frac{1}{2\pi} \int_0^{2\pi} d\theta \int_0^{2\pi} d\zeta (\nabla \times (\mathbf{w}\zeta)) \cdot \frac{\nabla p}{|\nabla p|} \quad (\text{C.35})$$

The first step is a simple construction, and the next step uses Stokes' theorem. With Eqn C.16,

$$\oint_{\zeta=0} d\mathbf{x} \cdot \mathbf{w} = \frac{1}{2\pi} \int_0^{2\pi} d\theta \int_0^{2\pi} d\zeta (\mathbf{w} \times \nabla \zeta) \cdot \frac{\nabla p}{|\nabla p|} \quad (\text{C.36})$$

For this case,  $\nabla p \times \mathbf{w} = \mathbf{B}$ , and so

$$\oint_{\zeta=0} d\mathbf{x} \cdot \mathbf{w} = \frac{1}{2\pi} \int_0^{2\pi} d\theta \int_0^{2\pi} d\zeta \frac{\mathbf{B} \cdot \nabla \zeta}{|\nabla p|} \quad (\text{C.37})$$

$$= \frac{\Phi'}{p'} \quad (\text{C.38})$$

Likewise,

$$\oint_{\theta=0} d\mathbf{x} \cdot \mathbf{w} = -\frac{\Psi'}{p'} \quad (\text{C.39})$$

The radial derivative,  $2\pi R'$ , is then

$$2\pi R' = V' = -I' \frac{\Psi'}{p'} - F' \frac{\Phi'}{p} \quad \text{or} \quad -p'V' = I'\Psi' + F'\Phi' \quad (\text{C.40})$$

## Appendix C: References

- [1] M. D. Kruskal and R. M. Kulsrud, Phys. Fluids **1**, 265 (1958).
- [2] P. Alexandroff and H. Hopf, “Topologie”, Verlag Von Julius Springer, Berlin, Germany, 1935, p. 552, Satz III.

## Appendix D: Boundary Conditions for Current Diffusion Equation

The boundary condition for the diffusion equation of the rotational transform, Eqn 3.67, is specified by a combination of Dirichlet and Neumann boundary conditions,

$$\alpha t + \beta t' = \gamma \quad (\text{D.1})$$

At the center of the plasma column,  $\rho = 0$ , there is finite current density so

$$\left. \frac{dt}{d\rho} \right|_{\rho=0} = 0 \quad (\text{D.2})$$

At the edge of the plasma column,  $\rho = 1$ , a few options exist. The measured net toroidal current,  $I(\rho = 1)$  can be used to set the value of  $t$  at the edge, Eqn 3.39

$$t|_{\rho=1} = \left( \frac{\mu_0 I}{S_{11} \Phi'} - \frac{S_{12}}{S_{11}} \right) \Big|_{\rho=1} \quad (\text{D.3})$$

Another option is to use the measured loop voltage to determine the edge condition. From Eqn 3.51,

$$V_{Loop} = V_{\zeta-loop}(\rho = 1) = \left. \frac{d\Psi}{dt} \right|_{\rho=1} + V_{\zeta-loop}(\rho = 0) \quad (\text{D.4})$$

After substitutions with Eqns 3.58 and 3.60,

$$V_{Loop} = \eta_{\parallel} \langle (\mathbf{J} - \mathbf{J}_{n.i.}) \cdot \mathbf{B} \rangle \left. \frac{dV}{d\Phi} \right|_{\rho=1} + t(\rho = 1) \left. \frac{d\Phi}{dt} \right|_{\rho=1} \quad (\text{D.5})$$

If the net toroidal flux is constant, which is correct to within 1% for 1 Tesla QHS plasmas (HSX is a low  $\beta$  machine), then last term is zero and

$$\frac{V_{Loop}}{\eta_{\parallel}} + \langle \mathbf{J}_{n.i.} \cdot \mathbf{B} \rangle \left. \frac{dV}{d\Phi} \right|_{\rho=1} = \langle \mathbf{J} \cdot \mathbf{B} \rangle \left. \frac{dV}{d\Phi} \right|_{\rho=1} \quad (\text{D.6})$$

With Eqn C.33

$$\frac{V_{Loop}}{\eta_{\parallel}} + \langle \mathbf{J}_{n.i.} \cdot \mathbf{B} \rangle \left. \frac{dV}{d\Phi} \right|_{\rho=1} = \frac{\mu_0}{\Phi'} (FI' - IF') \Big|_{\rho=1} \quad (\text{D.7})$$

Using Eqns 3.64 and 3.65 for  $(FI' - IF')$  and simplifying:

$$\frac{V_{Loop}}{\eta_{\parallel}} + \langle \mathbf{J}_{n.i.} \cdot \mathbf{B} \rangle \frac{dV}{d\Phi} \Big|_{\rho=1} = \frac{\mu_0}{\Phi'} \frac{dV}{d\Phi} \left( \frac{\langle B^2 \rangle}{\mu_0} I' + p' I \right) \Big|_{\rho=1} \quad (D.8)$$

and then using Eqn 3.37 for  $I$ ,

$$\begin{aligned} \frac{V_{Loop}}{\eta_{\parallel}} + \langle \mathbf{J}_{n.i.} \cdot \mathbf{B} \rangle \frac{dV}{d\Phi} \Big|_{\rho=1} &= \frac{\mu_0}{\Phi'} \frac{dV}{d\Phi} \left( \frac{\langle B^2 \rangle}{\mu_0} I' + p' I \right) \Big|_{\rho=1} \\ &= \frac{\mu_0}{\Phi'} \frac{dV}{d\Phi} \left( \frac{\langle B^2 \rangle}{\mu_0^2} \frac{d}{d\rho} (\Phi' (S_{11}t + S_{12})) + \frac{p'\Phi'}{\mu_0} (S_{11}t + S_{12}) \right) \Big|_{\rho=1} \\ &= \frac{dV}{d\Phi} \left( \frac{\langle B^2 \rangle}{\mu_0 \Phi'} \frac{d}{d\rho} (\Phi' (S_{11}t + S_{12})) + p' (S_{11}t + S_{12}) \right) \Big|_{\rho=1} \end{aligned} \quad (D.9)$$

Applying the radial derivative, simplifying and separating the terms for  $t$  and  $t'$ :

$$\begin{aligned} \frac{V_{Loop}}{\eta_{\parallel}} + \langle \mathbf{J}_{n.i.} \cdot \mathbf{B} \rangle \frac{dV}{d\Phi} \Big|_{\rho=1} &= \\ \left[ t \left( p' S_{11} + \frac{\langle B^2 \rangle}{\mu_0} \left( S'_{11} + \frac{\Phi''}{\Phi'} S_{11} \right) \right) + t' \frac{\langle B^2 \rangle S_{11}}{\mu_0} + p' S_{12} + \frac{\langle B^2 \rangle}{\mu_0} \left( S'_{12} + \frac{\Phi''}{\Phi'} S_{12} \right) \right] \frac{dV}{d\Phi} \Big|_{\rho=1} \end{aligned} \quad (D.10)$$

In this last expression, all quantities are calculated on the last closed flux surface (LCFS).

If the radial variable is the square-root normalized flux,  $\rho_r$ , Eqn 3.69, then  $\Phi' = \Phi'' = 2\Phi_a$ , where  $\Phi_a$  is the flux enclosed by the LCFS and Eqn D.10 simplifies to:

$$\begin{aligned} \frac{V_{Loop}(2\Phi_a)}{\eta_{\parallel} V'} + \langle \mathbf{J}_{n.i.} \cdot \mathbf{B} \rangle &= \\ t \left( p' S_{11} + \frac{\langle B^2 \rangle}{\mu_0} (S'_{11} + S_{11}) \right) + t' \frac{\langle B^2 \rangle S_{11}}{\mu_0} + p' S_{12} + \frac{\langle B^2 \rangle}{\mu_0} (S'_{12} + S_{12}) \end{aligned} \quad (D.11)$$

If the radial variable is the normalized flux,  $\rho_s$ , Eqn 3.68, then  $\Phi' = \Phi_a$  and  $\Phi'' = 0$ , and Eqn D.10 simplifies to

$$\frac{V_{Loop}\Phi_a}{\eta_{\parallel} V'} + \langle \mathbf{J}_{n.i.} \cdot \mathbf{B} \rangle = t \left( p' S_{11} + \frac{\langle B^2 \rangle}{\mu_0} S'_{11} \right) + t' \frac{\langle B^2 \rangle S_{11}}{\mu_0} + p' S_{12} + \frac{\langle B^2 \rangle}{\mu_0} S'_{12} \quad (D.12)$$

Eqns D.11 and D.12 are the boundary conditions for the diffusion equation in which the loop voltage,  $V_{Loop}$  is specified.  $V'$  is the radial derivative of the plasma volume. Each of the quantities are evaluated on the LCFS.



Another boundary condition, relevant to free resistive decay, is determined by the external inductance of the plasma column. In a toroidal conductor, the measured loop voltage is related to the change in net toroidal current by Faraday's Law. The direction of the induced voltage is opposite to the non-inductive current.

$$V_{Loop} = -L_{Ext} \frac{d}{dt} I (\rho = 1) \quad (D.13)$$

The external inductance for a cylindrical toroid is [1]

$$L_{Ext} \simeq \mu_0 R_{eff} \left[ \ln \left( 8 \frac{R_{eff}}{r_{eff}} \right) - 2 + F_{shaping} \right] \quad (D.14)$$

$R_{eff}$  and  $r_{eff}$  are the effective major and minor radii of the torus, respectively. The shaping factor,  $F_{shaping}$ , varies from 0 when the current is distributed along the surface of the conductor (the plasma column, in this case) to 1/4 when the current is uniformly distributed over the cross section of the conducting region.  $F_{shaping} = 0.25$  is closer to the actual case in most toroidal fusion experiments.

Non-inductive changes in the current profile induce currents that diffuse and decay resistively. The loop voltage associated with the change in net current, Eqn D.13, can be substituted in Eqn D.11 or D.12.

$$\begin{aligned} & -\frac{L_{Ext}}{\eta_{\parallel}} \frac{d}{dt} I (\rho = 1) + \langle \mathbf{J}_{n.i.} \cdot \mathbf{B} \rangle = \\ & t \left( p' S_{11} + \frac{\langle B^2 \rangle}{\mu_0} (S'_{11} + S_{11}) \right) + t' \frac{\langle B^2 \rangle S_{11}}{\mu_0} + p' S_{12} + \frac{\langle B^2 \rangle}{\mu_0} (S'_{12} + S_{12}) \end{aligned} \quad (D.15)$$

$$\begin{aligned} & -\frac{L_{Ext}}{\eta_{\parallel}} \frac{d}{dt} I (\rho = 1) + \langle \mathbf{J}_{n.i.} \cdot \mathbf{B} \rangle = \\ & t \left( p' S_{11} + \frac{\langle B^2 \rangle}{\mu_0} S'_{11} \right) + t' \frac{\langle B^2 \rangle S_{11}}{\mu_0} + p' S_{12} + \frac{\langle B^2 \rangle}{\mu_0} S'_{12} \end{aligned} \quad (D.16)$$

Eqn D.15 corresponds to the choice of the radial variable,  $\rho_r$ , and Eqn D.16 is for the choice of radial variable,  $\rho_s$ .

## **Appendix D: References**

- [1] F. W. Grover, “Inductance calculations: working formulas and tables”, Research Triangle Park, N.C. : Instrument Society of America, 1981.

## Appendix E: Numerical Implementation of the Diffusion Equation

In this appendix, the numerical implementation of the radial diffusion equation for the toroidal current is presented. The software package, MATLAB [1] and its partial differential equation solver, pdepe, is used to perform the calculation. A set of codes called ‘iota\_evolution\_generate’ and ‘iota\_evolution\_view’ (IEG+IEV) evaluate, save, and display the information about the time-evolution of quantities such as toroidal current profile, parallel electric field and rotation transform.

Recall the 1-D radial diffusion equation and boundary conditions, Eqns 3.70, 3.73 and 3.74, reprinted here for convenience, with the explicit variable substitution of  $s \equiv \rho_s$  and the time-varying net toroidal flux set to 0:

$$\frac{dt}{dt} = \frac{1}{\Phi_a^2} \frac{d}{ds} \left( \eta_{\parallel} V' \left( \frac{\langle B^2 \rangle}{\mu_0} \frac{d}{ds} (S_{11}t + S_{12}) + p' (S_{11}t + S_{12}) - \langle \mathbf{J}_{n.i.} \cdot \mathbf{B} \rangle \right) \right) \quad (\text{E.1})$$

$$\left. \frac{dt}{ds} \right|_{s=0} = 0 \quad (\text{E.2})$$

$$t|_{s=1} = \left( \frac{\mu_0 I}{S_{11} \Phi'} - \frac{S_{12}}{S_{11}} \right) \Big|_{s=1} \quad (\text{E.3})$$

For the pdepe solver, the diffusion equation needs to be cast into the form given by [2]:

$$c \left( x, t, u, \frac{du}{dx} \right) \frac{du}{dt} = x^{-m} \frac{d}{dx} \left( x^m f \left( x, t, u, \frac{du}{dx} \right) \right) + s \left( x, t, u, \frac{du}{dx} \right) \quad (\text{E.4})$$

Here,  $u$  is the diffusing quantity of interest. The spatial coordinate is  $x$  and time is  $t$ . The initial condition is set as  $u(x, t_0) = u_0(x)$  and the boundary conditions are satisfied by  $p$  and  $q$  such that:

$$p(x, t, u) + q(x, t) f \left( x, t, u, \frac{du}{dx} \right) = 0 \quad (\text{E.5})$$

The following definitions are appropriate to recast the diffusion equation into the form required for pdepe ( $x \equiv s$ ):

$$m = 0 \quad (\text{E.6})$$

$$u = S_{11}t + S_{12} = \frac{\mu_0 I}{\Phi'} \quad (\text{E.7})$$

$$c = \frac{\Phi_a^2}{S_{11}} \quad (\text{E.8})$$

$$f = \eta_{\parallel} V' \left( p' u + \frac{\langle B^2 \rangle}{\mu_0} \frac{du}{dx} - \langle \mathbf{J} \cdot \mathbf{B} \rangle \right) \quad (\text{E.9})$$

$$s = 0 \quad (\text{E.10})$$

$$u(x, t = 0) = 0 \quad (\text{E.11})$$

$$p(x = 0, t) = u(x = 0, t) \quad (\text{E.12})$$

$$q(x = 0, t) = 0 \quad (\text{E.13})$$

$$p(x = 1, t) = u(x = 1, t) - \frac{\mu_0 I}{\Phi'} \quad (\text{E.14})$$

$$q(x = 1, t) = 0 \quad (\text{E.15})$$

For the case of free inductive-resistive relaxation of the net current, the above definitions hold, with the exception of the last two. These are replaced with:

$$p(x = 1, t) = 2\Phi' \eta_{\parallel} \frac{R_{eff}}{r_{eff}^2} I_{\infty} \exp^{-t/\tau_{L/R}} \quad (\text{E.16})$$

$$q(x = 1, t) = 1 \quad (\text{E.17})$$

Here,  $I_{\infty}$  is the net toroidal current in steady state,  $R_{eff}$  and  $r_{eff}$  are the effective major and minor radii, respectively, and

$$\tau_{L/R} = \frac{L_{ext} r_{eff}^2}{2\eta_{\parallel} R_{eff}} \quad (\text{E.18})$$

where  $L_{ext}$  is the external inductance defined in Eqn D.14 and the resistivity,  $\eta_{\parallel}$  is evaluated at the edge of the plasma column.

## Appendix E: References

- [1] MATLAB R2010a, The MathWorks, Natick, MA.
- [2] The MathWorks, “Solve initial-boundary value problems for parabolic-elliptic PDEs in 1-D”,  
<http://www.mathworks.com/help/techdoc/ref/pdepe.html>

## Appendix F: Alignment of the Magnetic Diagnostics

### F.1 External Magnetic Vector Diagnostic Array

The location and orientation of the external magnetic vector diagnostic array is known by measuring their location with a coordinate measurement machine (cmm) Romer Cimcore, Model 5028 [1]. The measurements are made on the test vessel section and the diagnostics are then transferred to the vacuum vessel by using the form marking and mechanical reference points. To check the alignment in-situ, the magnetic fields generated by main coil set and individual coils of the auxiliary field coil set were measured by the triplets. The measurement was compared to the calculated response calculated from a Biot-Savart code. For the tests here, the following auxiliary coils were charged: A3, A4, A6, D1, and D6. These coils are indicated in Figure F.1. The different magnetic fields generated provide a variety of fields at the location of each of the triplets, allowing each of the orthogonal channels of the triplets to be tested.

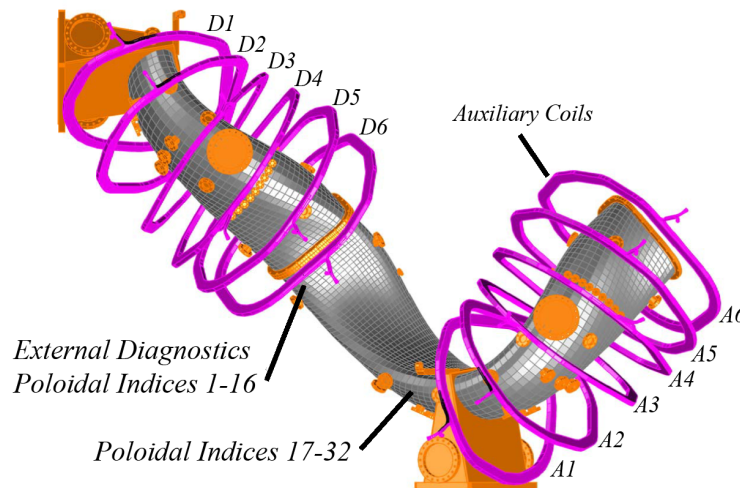


Figure F.1 A subset of the auxiliary coil set, the vacuum vessel and diagnostic ports. The approximate locations of the external magnetic diagnostic belts are indicated.

A capacitor bank is used to apply  $\approx 30$  A of current through the auxiliary coils. The time trace of the current through auxiliary coil A3 is shown in Figure F.2. The components of the magnetic field vector for triplet #17, as a function of time, are shown in Figure F.3. The  $B_x$ ,  $B_y$ ,

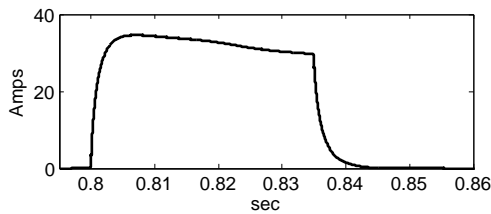


Figure F.2 Typical current waveform applied to the auxiliary coils.

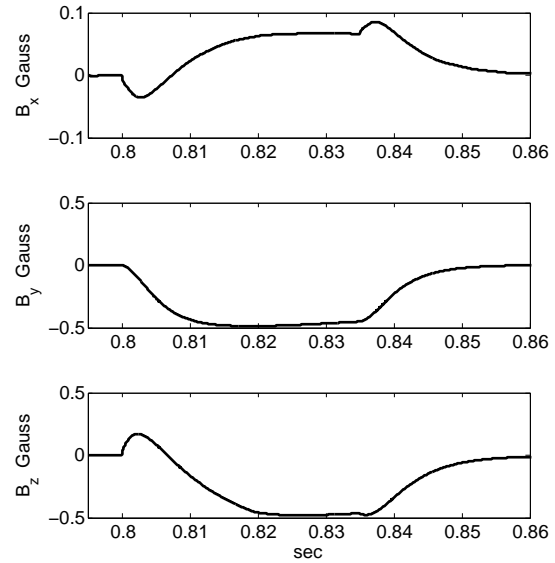


Figure F.3 Signal response on triplet #17 due to the applied current in Figure F.2 on auxiliary coil A3.

$B_z$  components approximately correspond, respectively, to the local poloidal, radial, and toroidal components of the magnetic field with respect to the vacuum vessel. The field components take several 10's of ms to reach steady state. The input current pulse is not quite constant, so the field has a small drift. The mean values of the current and magnetic field vector are calculated during the window from  $t = 0.830 \rightarrow 0.835$  sec. The calculated magnetic field at each triplet, excluding the effects of any eddy currents, are calculated for the measured mean current. This field value is then compared to the actual measurement. This comparison for the 32 triplets is shown in Figure F.4. Each component and the total magnitude of the field vector is compared for each triplet location. From the comparison, it can be seen that there is good agreement among the  $B_x$  and  $B_y$  components, but for the  $B_z$  component, the measured value tends to a few percent smaller than the calculated value. This is likely due to eddy currents in the vacuum vessel and structure causing the toroidal component of the field to slowly approach steady state. The magnitude of the measured and calculated magnetic field vectors are also compared, and measurement is smaller than the calculation, as seen in Figure F.4.

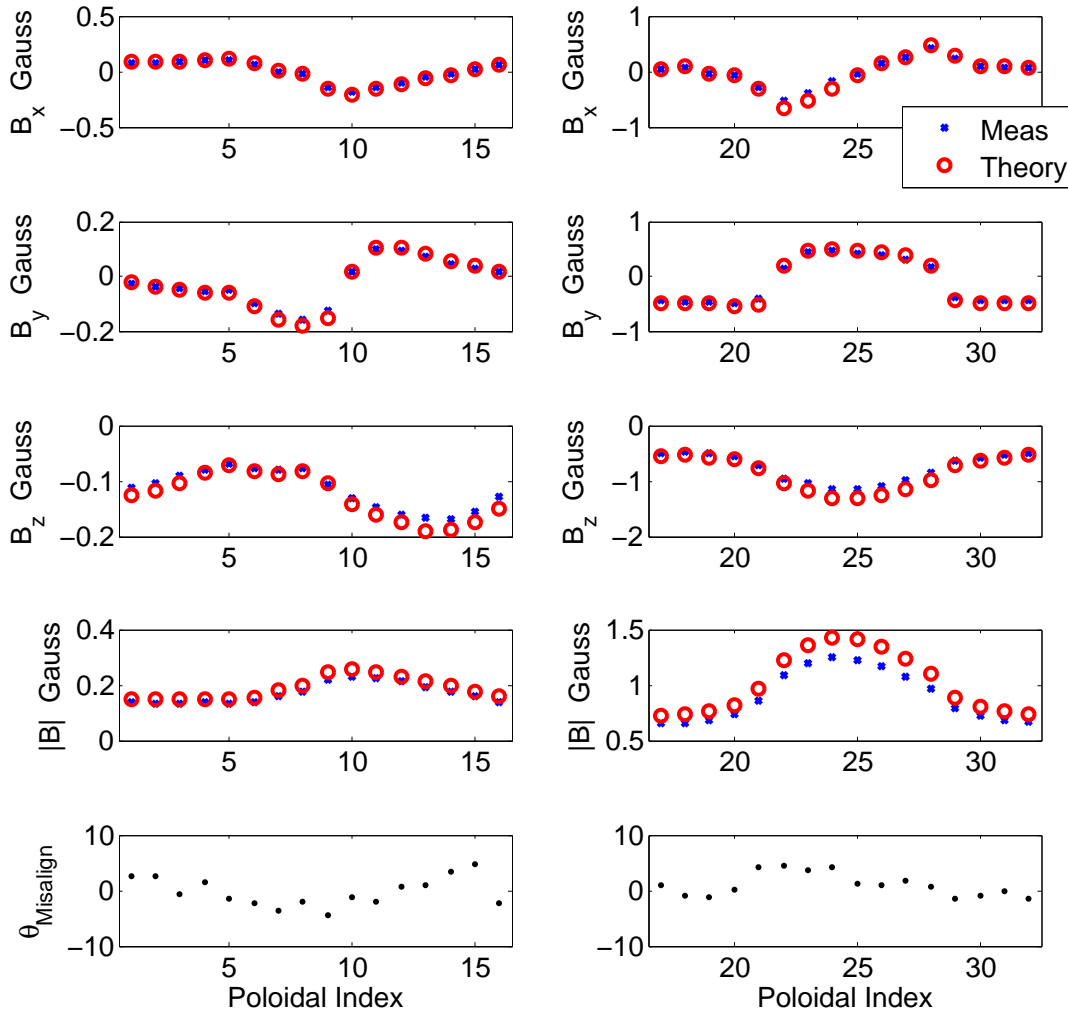


Figure F.4 Comparison between calculated and measured signals of the external magnetic diagnostic array.

The main field coil set was also used to check the alignment of the triplets. The main field was energized with  $\approx 400$  A of current. A 3rd-order polynomial is fit to the measurement during part of the rise time and its derivative is calculated, Figure F.5. With that time-derivative, the  $dB/dt$  for each triplet is calculated as a function of time and compared to that which is measured. The normalized vector components and the magnitude of the vector for each triplet, averaged from  $t = 0.345 \rightarrow 0.435$  s, are compared in F.6. The magnitude of the measured vectors agree with



the calculation to within 1-4% for all diagnostics. The uncertainty in the magnitude for triplet with poloidal index  $i$  is designated as  $\sigma_{i,Mag}$ .

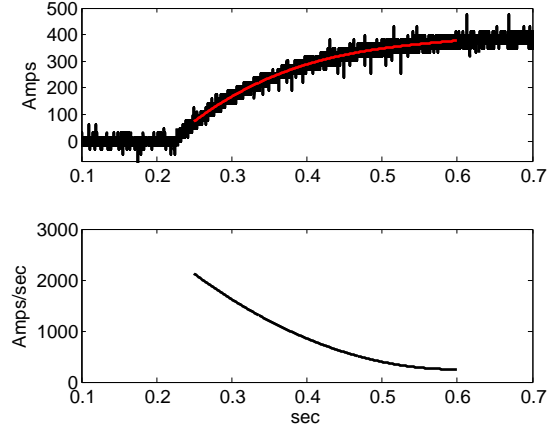


Figure F.5 The main field current, as measured by the main shunt resistor, a 3rd-order fit polynomial, and its derivative as a function of time.

The angle of the misalignment between the calculated vector,  $\mathbf{B}_{theory}$  and the measurement,  $\mathbf{B}_{measure}$  can be calculated by

$$\gamma_{Misalign} = \arccos \left( \frac{\mathbf{B}_{theory} \cdot \mathbf{B}_{measure}}{|\mathbf{B}_{theory}| |\mathbf{B}_{measure}|} \right) \quad (F.1)$$

The unit vector that  $\mathbf{B}_{measure}$  is rotated about by  $\theta_{Misalign}$  to align it with  $\mathbf{B}_{theory}$  is given by

$$\hat{n}_{Rotate} = \frac{\mathbf{B}_{measure} \times \mathbf{B}_{theory}}{|\mathbf{B}_{theory}| |\mathbf{B}_{measure}| \sin(\theta_{Misalign})} \quad (F.2)$$

The misalignment for each triplet is shown in the bottom panels of Figures F.4 and F.6. Typical misalignment is in the range of a few degrees.

The components of the rotation vector and misalignment angle for each triplet, during each auxiliary coil test and the main field coil test is shown in Figure F.8. The components of the rotation vector are in the laboratory-coordinate system. The rotation vector is not the same when different auxiliary coils or when the main coil set are used to produce the magnetic field. The reason for this has not been identified. The magnitude of the misalignment angles are similar for a particular triplet, regardless of the auxiliary coil. The mean value of the magnitude of the

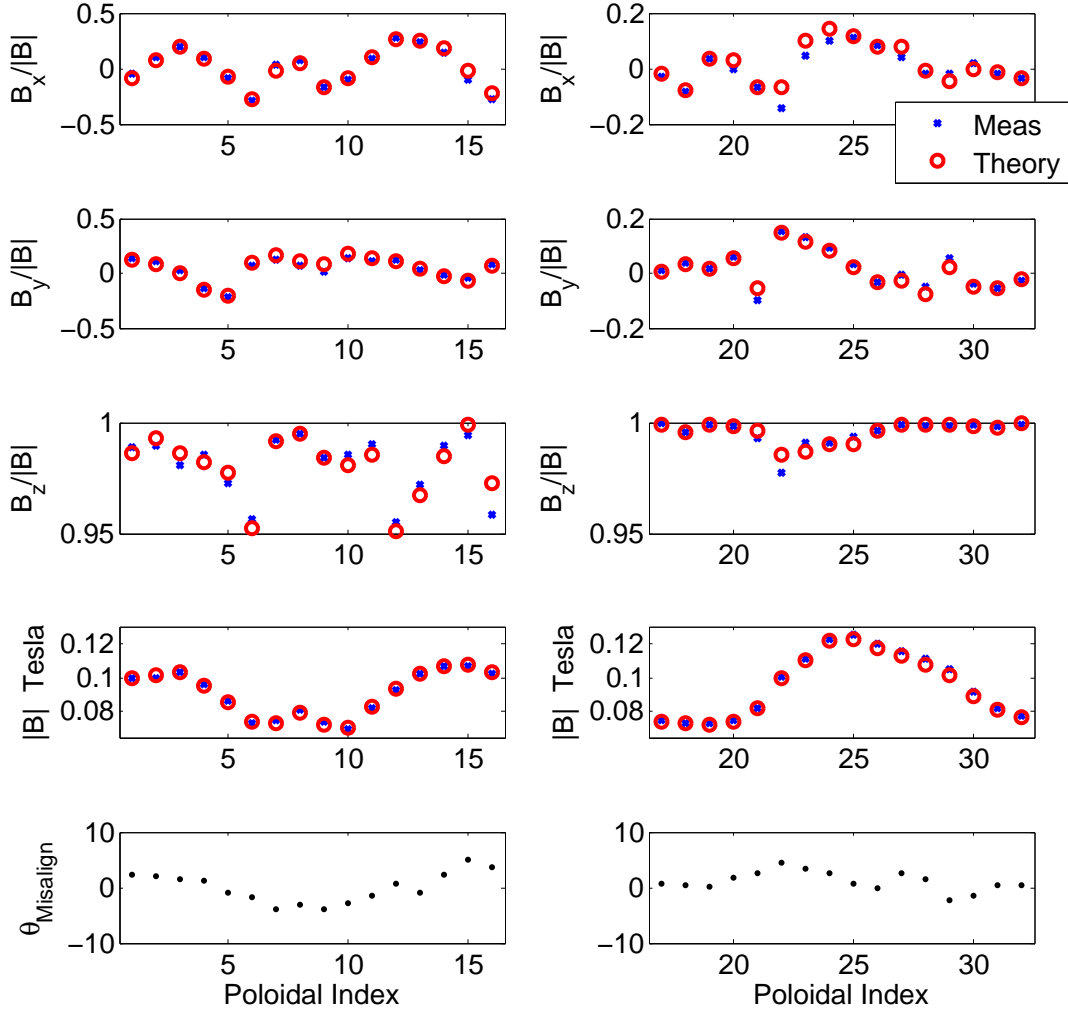


Figure F.6 Comparison between calculated and measured signals of the external magnetic diagnostic array.

misalignment angle for a particular triplet is used as the systematic error due to misalignment of that particular triplet. This random error is typically a  $1\text{-}3^\circ$  for the majority of the triplets, with the maximum misalignment angle being  $5^\circ$ . This misalignment angle for triplet with poloidal index  $i$  is designated as  $\gamma_i$ .

To account for the uncertainty in the location and orientation of the external magnetic vector diagnostics, the local magnetic vector needs to be calculated. The magnetic vector at the location

of triplet  $i$  is given by

$$\tilde{\mathbf{B}}_i(t) = \tilde{B}_{i,x}(t)\hat{x} + \tilde{B}_{i,y}(t)\hat{y} + \tilde{B}_{i,z}(t)\hat{z} \quad (\text{F.3})$$

$\tilde{B}_{i,x}(t)$ ,  $\tilde{B}_{i,y}(t)$ , and  $\tilde{B}_{i,z}(t)$  are the magnetic field signals due to the plasma, given by Eqn 4.22. Misalignment of the diagnostic will result in a portion of the signal from one channel of the triplet (x, y, or z) being projected onto the other channels. The level of angular misalignment has been estimated for each triplet as  $\gamma_i$ . For an estimated misalignment,  $\gamma_i$ , a misaligned vector  $\vec{P} = P_x\hat{x} + P_y\hat{y} + P_z\hat{z}$  is found with:

$$\tilde{B}_{i,xy} = |\tilde{B}_{i,x}\hat{x} + \tilde{B}_{i,y}\hat{y}| \quad (\text{F.4})$$

$$\lambda_i = \arctan \frac{|\tilde{\mathbf{B}}_i|}{\tilde{B}_{i,xy}} \quad (\text{F.5})$$

$$\kappa_i = \lambda_i + \gamma_i \quad (\text{F.6})$$

$$\tilde{B}'_{i,xy} = |\tilde{\mathbf{B}}_i| \cos \kappa_i \quad (\text{F.7})$$

$$P_x = \tilde{B}_{i,x} \cdot \frac{\tilde{B}'_{i,xy}}{\tilde{B}_{i,xy}} \quad (\text{F.8})$$

$$P_y = \tilde{B}_{i,y} \cdot \frac{\tilde{B}'_{i,xy}}{\tilde{B}_{i,xy}} \quad (\text{F.9})$$

$$P_z = |\tilde{\mathbf{B}}_i| \sin \kappa_i \quad (\text{F.10})$$

The misalignment vector,  $\mathbf{P}$  is then rotated about  $\tilde{\mathbf{B}}_i$  by Rodrigues' rotation formula [2] [3] and a circular locus of points,  $R$ , is generated. This set of points is projected on to the x-, y-, and z-axes and half the difference between the minimum and maximum projected points (on each axis) is the estimate of the uncertainty due to misalignment on the respective channel. With the x, y, and z components of  $R$  denoted as  $R_x$ ,  $R_y$ , and  $R_z$ , the uncertainty for a particular channel, which is calculated for each time sample, is

$$\sigma_{B_{i,k},MA}(t) = \frac{1}{2} |\max(R_k) - \min(R_k)| \quad (\text{F.11})$$

where  $k = (x, y, z)$ . In Figure F.7,  $\tilde{\mathbf{B}}_i$ , is shown in blue,  $\mathbf{P}$ , in red, the locus of points,  $R$ , in black and the projections to the axes,  $R_x$ ,  $R_y$ , and  $R_z$ , are shown in green.

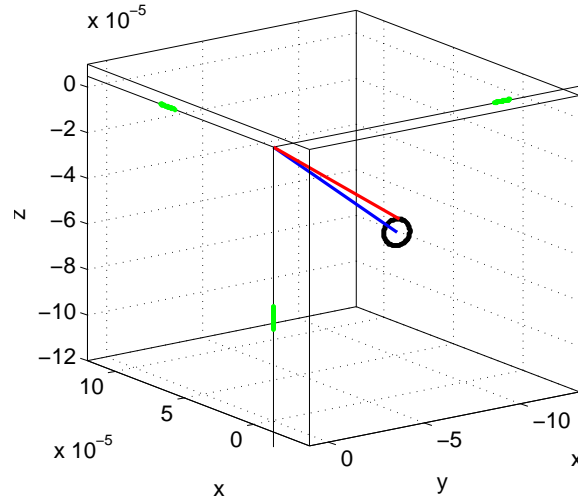


Figure F.7 The calculated magnetic vector,  $\tilde{\mathbf{B}}_i$  (blue), a misaligned vector,  $\mathbf{P}$  (red), the locus of points found by rotating this misaligned vector around the magnetic vector (black), and the projections to the x-, y- and z- axes (green). Units are in Tesla

## F.2 Internal Magnetic Diagnostics

To check the location of the internal poloidal array Section ??, their response to the magnetic field generated by the main coil set was compared to the calculated response. The time-rate-of-change of the main field current measured by a Rogowski coil around one of the main field coils and the location of each coil is used to calculate its expected response. This expected response and the measured response are both shown in Figure F.9 and are in good agreement. These diagnostics only have a single channel at each location and can not measure the total field vector, only the component along the axis of the diagnostic, so there is no estimate of the misalignment uncertainty. The uncertainty due to the gain of the coil+amplifier system is estimated, conservatively, at 5%.

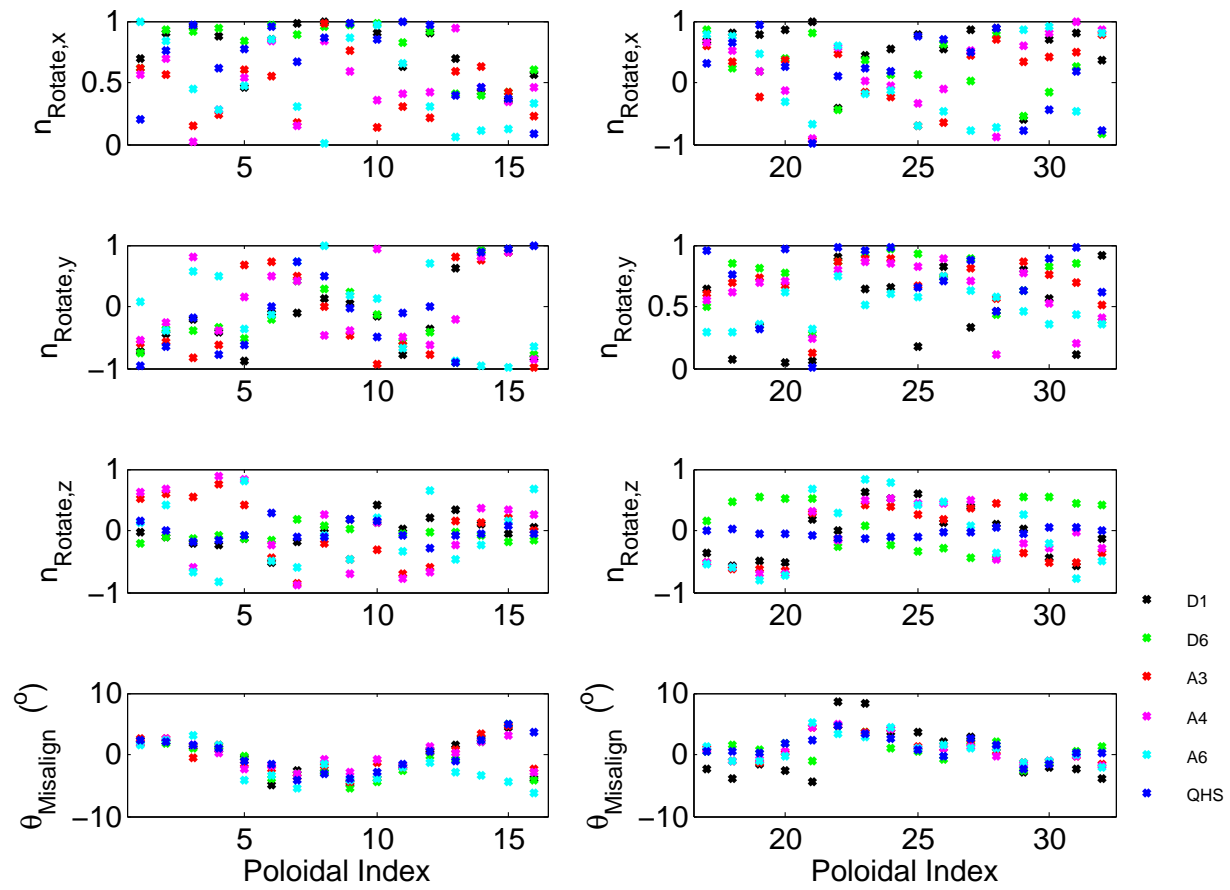


Figure F.8 Rotation vector components and misalignment angle.

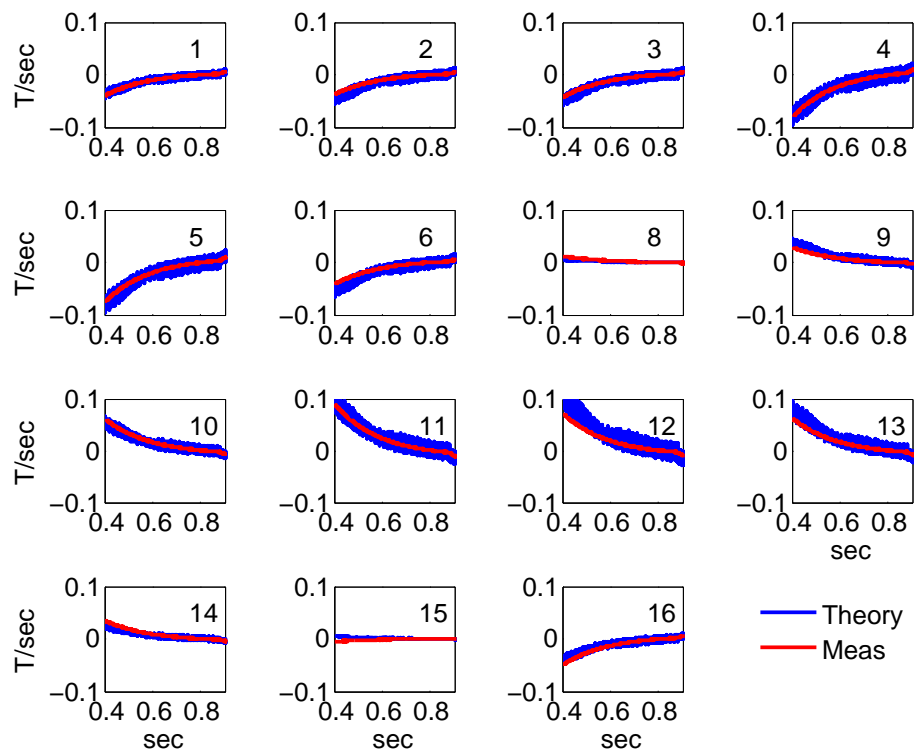


Figure F.9 Comparison of expected signals for internal poloidal array.

## Appendix F: References

- [1] Romer Cimcore Model 5028, <http://us.romer.com>
- [2] <http://mathworld.wolfram.com/RodriguesRotationFormula.html>
- [3] <http://mathworld.wolfram.com/RotationFormula.html>

## Appendix G: Singular Value Decomposition

The reconstruction of plasma profiles in 3-D configurations has been an open question for many years. In a 2-D axisymmetric system, the amount of information that can be extracted from the external magnetic diagnostics is limited to a few quantities. Typically, the net toroidal current and total diamagnetic current are easily resolved, but radial profile information of these two quantities is severely limited, based on magnetic signals. Trying to determine the plasma pressure and current profiles based on external magnetic diagnostic signals tends to lead to many ambiguous and indistinguishable possibilities [1]. Peaked pressure profiles and broad, flat pressure profiles produce similar magnetic signatures, as do peaked and flat current density profiles with similar net currents.

In a 3-D system, the magnetic fields generated by plasma currents reveal more information regarding their radial distribution [2]. The plasma pressure and current distribution can be determined to a higher degree of certainty if enough information, i.e. measurements, of the plasma boundary are possible. The plasma currents in a 3-D system produce magnetic fields that are more sensitive to profile features than in a 2-D axisymmetric system. The NCSX magnetic diagnostic system was designed by identifying which coils were optimal in reconstructing the plasma profile. A singular value decomposition (SVD) of the diagnostic and response matrix was used to iteratively improve the virtual diagnostic set, such that most efficient subset was found [3]. The number of eigenvalues found in the SVD that are above a certain threshold, and the amount of noise in the signal, determines the number of ‘effective signal patterns’. The magnetic signals for NCSX had 19 singular values above a noise threshold of 1 G. For the W7-AS stellarator, the magnetic diagnostics were simulated for experimentally relevant plasma pressure files and no net toroidal current and a Principle Component Analysis (PCA) was used to identify the most significant eigenvectors and that were present in the dataset [4]. The recovery of the pressure profile was strongly affected by the assumed noise level in the diagnostic signals. As the noise is increased, the precision of the profile was reduced. For W7-X, the modeling and analysis has shown that



the plasma energy and net current are well resolved, but profile information has uncertainties of  $\approx 25\%$  [5].

The result of an SVD study for the QHS configuration shows the the amount of profile information that can be extracted depends strongly on the level of noise in the diagnostics. More information is available when more diagnostics are included in the data set. A set of 1800 randomly generated plasma pressure profiles and current profiles were generated. The pressure profiles, which are characteristic of profiles achieved in the QHS configuration in HSX with carbonized was, were generated by randomly selecting  $P_0 - P_2$  and  $a_0$  in

$$P(s) = P_0(1 - s)^{a_0} + P_1 \cdot (1 - s)^2 + P_2 \cdot s \cdot (1 - s); \quad (\text{G.1})$$

The current profiles were generated by randomly selecting coefficients on 5 polynomials. Samples of the pressure profiles and current density profiles are in Figures G.1 and G.2. The magnetic

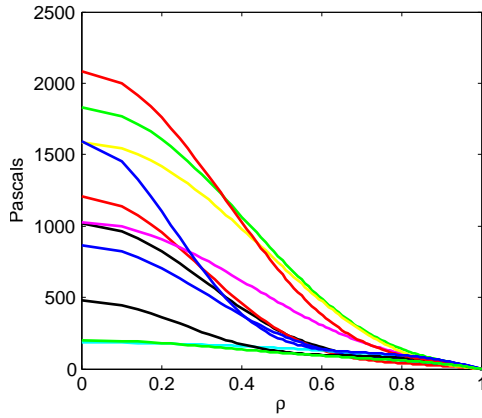


Figure G.1 Sample pressure profiles.

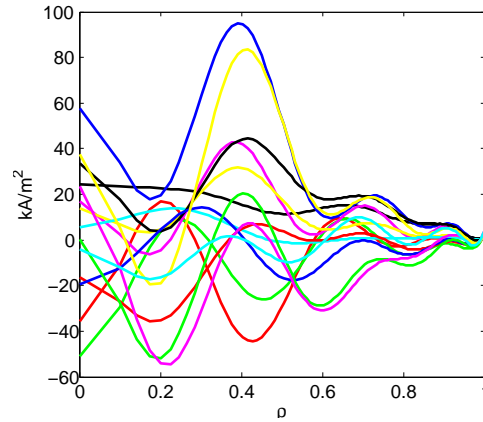


Figure G.2 Sample current density profiles.

diagnostic signals for the magnetic diagnostic mentioned in chapter 4 were calculated for each of the random profiles by V3FIT. In addition, the diagnostic signals for a set of 192 virtual 'triplets' that cover  $1/2$  of a field period, Figure G.3, were calculated and stored. Three signals for each virtual triplet were generated, one signal in the poloidal direction, one in the radial direction, and one in the toroidal direction. The data for each diagnostic was stored in a matrix,  $\mathbf{D}$ , one column for each random profile and one row for each diagnostic.

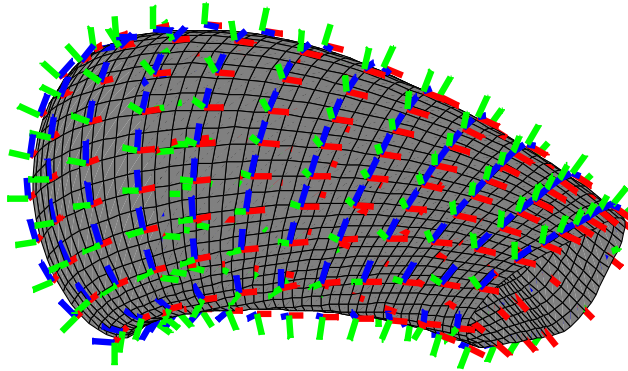


Figure G.3 The vacuum vessel and virtual triplets.

The SVD, Eqn 4.75, decomposes the matrix,  $\mathbf{D}$ , of size  $n \times m$  into three matrices:

$$\mathbf{D} = \mathbf{U} \cdot \mathbf{W} \cdot \mathbf{V}^T \quad (\text{G.2})$$

The matrix  $\mathbf{U}$  is orthonormal and has size  $n \times n$ .  $\mathbf{V}$  is also orthonormal and has size  $m \times m$ . The matrix  $\mathbf{W}$  is a diagonal matrix with the same size as  $\mathbf{D}$ , whose elements are sorted in decreasing order,  $W_{i,i} \geq W_{i+1,i+1}$ . The number of eigenvalues above some limit indicates the number of significant patterns that can be extracted from the data set. Noise is added to the signal set by adding uniformly distributed random signals to the matrix. The addition of noise reduces the number of patterns that can be identified in the data.

The normalized quantity,  $W_{i,i}/W_{1,1}$ , for the virtual triplet set is shown in Figure G.4. The 'No noise limit' is the ideal case with no noise added to the signal matrix. The results of the SVD with  $\pm 0.05$  G,  $\pm 0.25$  G, and  $\pm 0.5$  G are also shown. As the level of noise increases, the minimum value of the eigenvalues is increased. This probably indicates that the number of parameters that can be extracted from the data is also reduced. The number of eigenvalues above the 'noise floor' (the asymptote) gives an indication to the number of fit parameters that can be used to model the pressure and current profiles. It does not give an indication of which parameters those may be. More analysis is required to project the eigenvalues and eigenvectors back to the pressure and current profiles to determine what information they may represent. The results of the SVD study for the set of diagnostics that includes only the external magnetic diagnostic array, with and without

noise, are shown in Figure G.5, and the results of an SVD with only the internal poloidal array, which has 15 signals, is shown in Figure G.6. The differences in the SVD between the virtual set and the external diagnostic array are small, indicating that the external set may already be partially optimized to measure the plasma profiles. The SVD analysis of the internal array show that this set is more sensitive to the noise level.

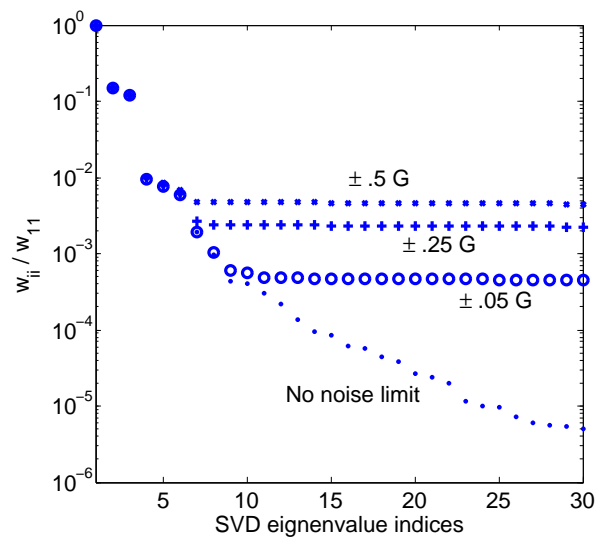


Figure G.4 Normalized eigenvalues for the SVD with the complete virtual diagnostic set.

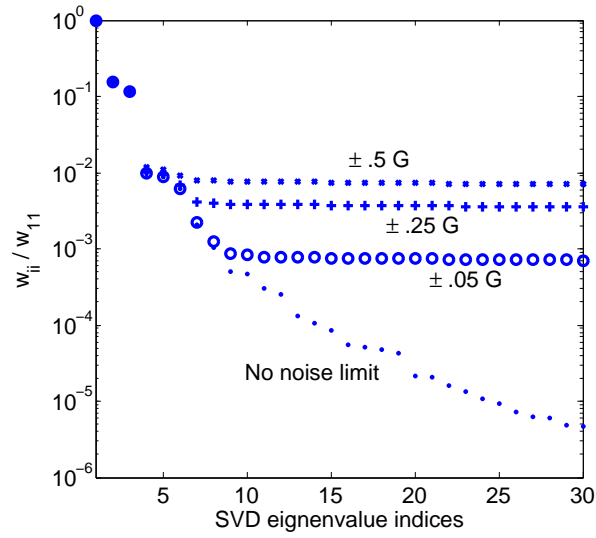


Figure G.5 Normalized eigenvalues for the SVD that includes the external magnetic diagnostic triplets and internal poloidal array.

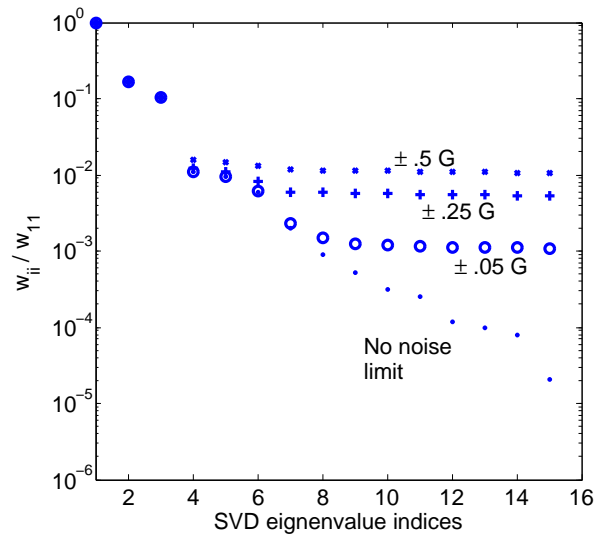


Figure G.6 Normalized eigenvalues for the SVD that includes only the internal poloidal array.

## Appendix G: References

- [1] V. D. Pustovitov, Nucl. Fusion **41**, 721 (2001).
- [2] H. E. Mynick and N. Pomphrey, Phys. Plasmas **9**, 1050 (2002).
- [3] N. Pomphrey, E. Lazarus, M. Zarnstorff, A. Boozer, A. Brooks, Phys. Plasmas **14**, 056103 (2007).
- [4] H. P. Callaghan, P. J. McCarthy, and J. Geiger, Plasma Physics and Cont. Fusion **42**, 1013 (2000).
- [5] J. Geiger, M. Endler, and A. Werner, CPP **42**, 736 (2010).

## Appendix H: Mirror Flip Field

Plasmas were made in the Mirror configuration, which adds the  $(n, m) = (4, 0)$  and  $(n, m) = (8, 0)$  symmetry-breaking terms to the magnetic spectrum, Figure 1.7. For these cases, 100 kW of ECRH (launched) was used and  $\rho_{ECRH} \lesssim 0.1$ . The intention of these shots was to attempt to match the temperature and density profiles achieved in QHS to study the effects that the differences in the magnetic spectrum have on the bootstrap current. Plasmas were made with the main magnetic field in both the CCW and CW directions. The electron temperature and density profiles are shown in Figures H.1 and H.2. One of the cases is for plasmas with the field in the CCW direction  $\bar{N}_e \sim 4.2$ , as measured by the microwave interferometer. The other two cases are for plasmas made with the field in the CW direction, and  $\bar{N}_e \sim 4.2$  and a case with a slightly higher line-averaged density. The measured net toroidal current during the three cases is shown in Figure H.3.

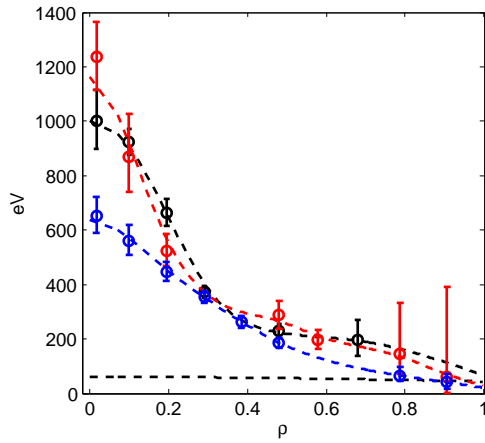


Figure H.1 Mirror, 100 kW,  $\rho_{ECRH} \lesssim 0.1$ :  $T_e$  for CCW (black), and CW  $\bar{N}_e \sim 4.2$  (red) and CW  $\bar{N}_e \sim 5$  (blue).  $T_i$  estimate from ChERS (black, dashed).

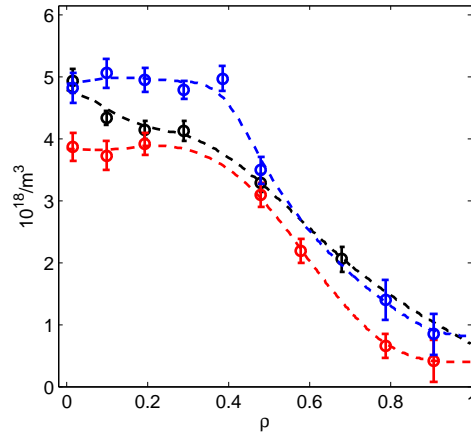


Figure H.2 Mirror, 100 kW,  $\rho_{ECRH} \lesssim 0.1$ :  $N_e$  for CCW (black), and CW  $\bar{N}_e \sim 4.2$  (red) and CW  $\bar{N}_e \sim 5$  (blue).

The temperature and density profiles for the two  $\bar{N}_e \sim 4.2$  cases (CCW and CW) are similar, while for the higher density case (CW), the temperature is reduced on-axis and the density is higher. The measured net toroidal current is different for all three cases. For the two  $\bar{N}_e \sim 4.2$  cases, the profiles are similar enough that PENTA calculations are very similar. The ambipolar  $E_r$

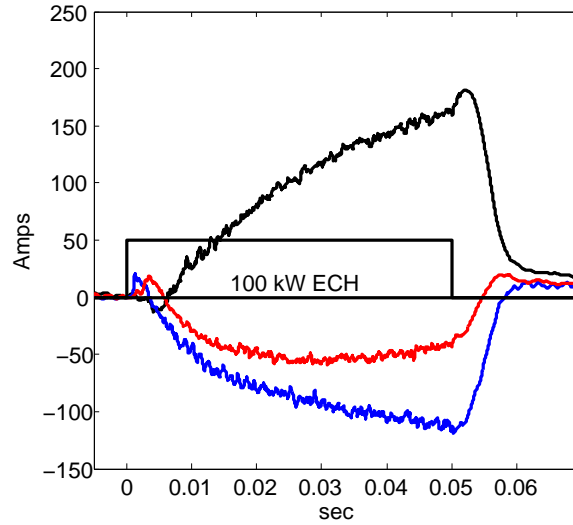


Figure H.3 Measured net toroidal current for an ensemble average of shots with Mirror, 100 kW,  $\rho_{ECRH} \lesssim 0.1$ : CCW  $\bar{N}_e \sim 4.2$  (9 shots, black), and CW  $\bar{N}_e \sim 4.2$  (8 shots, red) and CW  $\bar{N}_e \sim 5$  (5 shots, blue).

Field Configuration	$\rho_{ECRH}$	$P_{ECRH,launched}$	$\bar{N}_e \times 10^{18}/m^3$	$I_{tor}(t = \infty)$
Mirror CCW	$\rho \lesssim 0.1$	100 kW	4.2	$204. \pm 18. \text{ A}$
Mirror CW	$\rho \lesssim 0.1$	100 kW	4.2	$-51. \pm 9. \text{ A}$
Mirror CW	$\rho \lesssim 0.1$	100 kW	$\sim 5$	$-123. \pm 14. \text{ A}$

Table H.1 Configuration space explored with balanced fueling in the Mirror configuration.

and current density for the CCW case, including and neglecting momentum conservation (MC), net enclosed current profile, and conductivity are shown in Figures H.4 - H.8.

For the  $\bar{N}_e \sim 4.2$  cases (CCW and CW), with similar Thomson profiles, the PENTA calculation shows that the net toroidal current should be around are 156 A if MC is neglected, for both i-root and e-root dominated current density profiles. If MC is included, the net current should be about 118 A in the i-root dominated solution and reduced to 31 A in the e-root dominated solution. The extrapolated net toroidal current from the measurement, Figure H.3, with the main field in the CCW direction is 204. A, and agrees better with the i-root dominated solution, or even with the

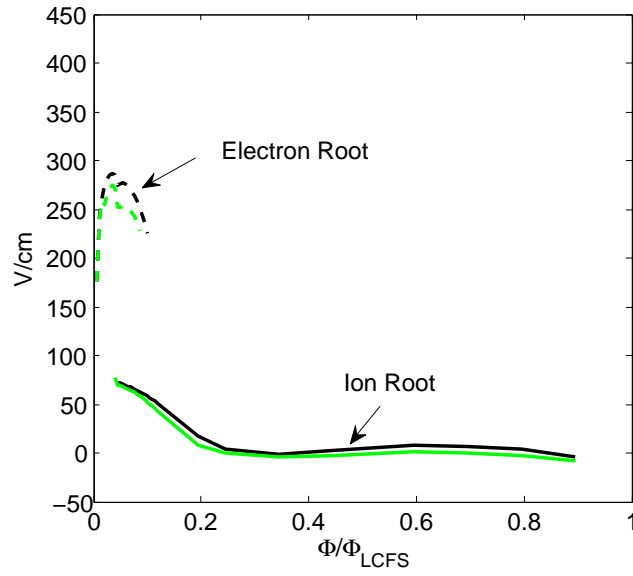


Figure H.4 Mirror,  $100\text{ kW}$ ,  $\rho_{ECRH} \lesssim 0.1$ : Stable ambipolar  $E_r$  solutions with MC (black) and without MC (green). Calculation by PENTA.

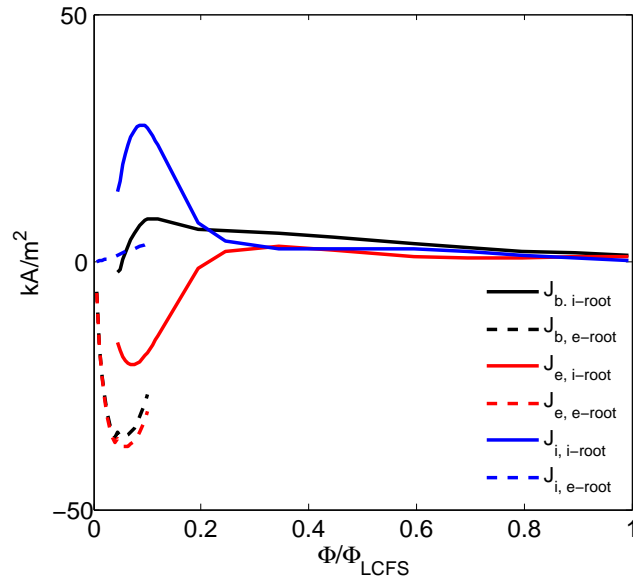


Figure H.5 Mirror,  $100\text{ kW}$ ,  $\rho_{ECRH} \lesssim 0.1$ , With MC: Ion (blue), electron (red) and total (black) parallel current. Solid lines coincide with the ion root solution and dashed lines coincide with the electron root solution. Calculation by PENTA.



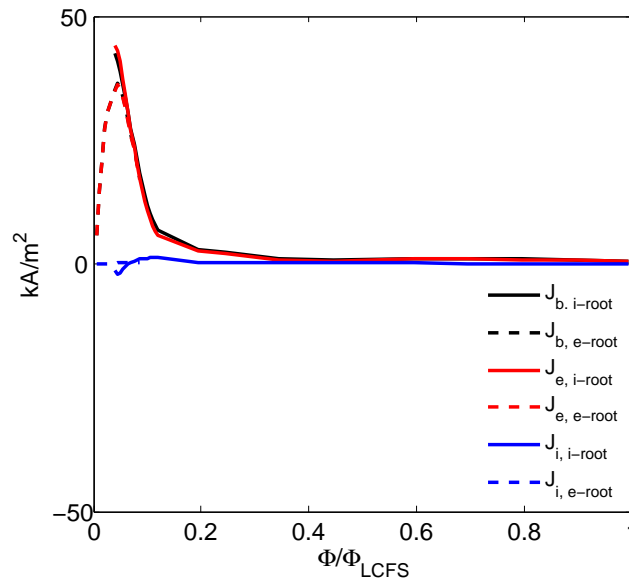


Figure H.6 Mirror, 100 kW,  $\rho_{ECRH} \lesssim 0.1$ , Without MC: Ion (blue), electron (red) and total (black) parallel current. Solid lines coincide with the ion root solution and dashed lines coincide with the electron root solution. The ion current is small for each case, so the total current is nearly identical to the electron current. Calculation by PENTA.

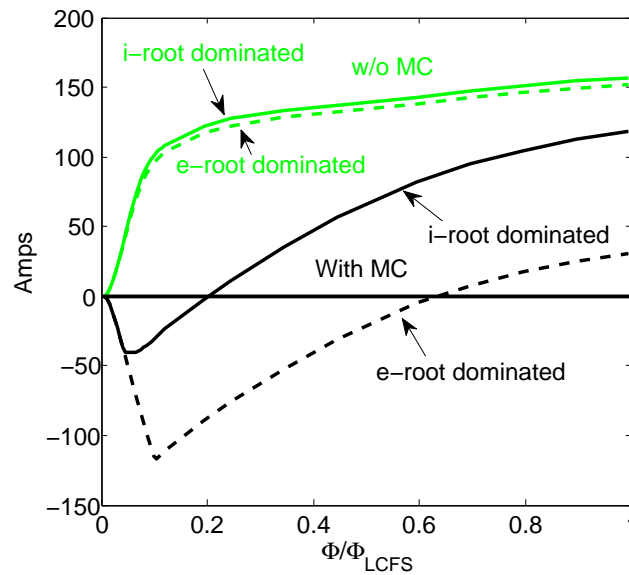


Figure H.7 Mirror, 100 kW,  $\rho_{ECRH} \lesssim 0.1$ , Without MC: Enclosed current profile for different scenarios of current density. With MC (black) and without MC (green)

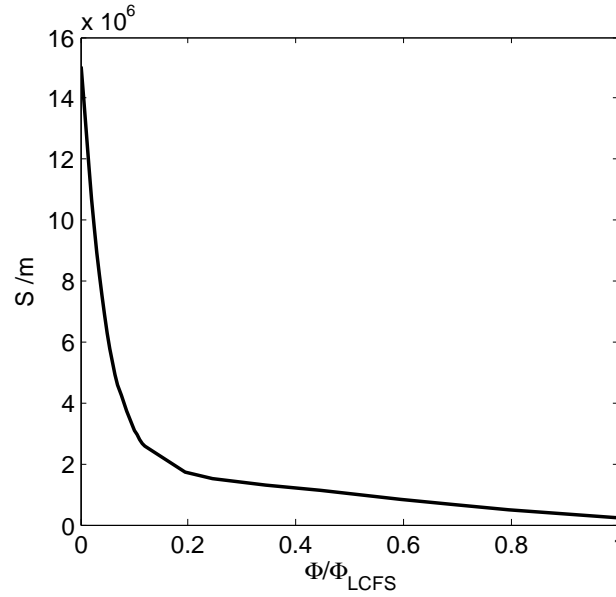


Figure H.8 Mirror, 100 kW,  $\rho_{ECRH} \lesssim 0.1$ : Parallel conductivity of the plasma, including trapped particle effect. Calculation by PENTA.

solution that ignores MC. With the main field in the CW direction, the net current has reached a nearly steady state value of  $-51$  A, and agrees better with the e-root dominated solution. (The enclosed current profiles are shown for the CCW direction, and need to include a factor of  $\times -1$  for the CW case.).

The current evolution calculation with IEG was completed for each of the cases. For the CCW case, the enclosed current profile associated with the i-root dominated solution in Figure H.7 was chosen as the steady-state current profile since its net current agreed better in magnitude with the extrapolated state-state net current. For the CW case, the e-root dominated solution was chosen. For both, the conductivity profile in the calculation is the one shown in Figure H.8.

For the CCW case, the simulated and measured loop voltage is shown in Figure H.9. The simulated loop voltage goes to zero and switches sign early in the shot, while the measured loop voltage is negative during the entire discharge. Like the case with QHS 50 kW,  $\rho_{ECRH} \lesssim 0.1$  in section 5.1, this indicates that the chosen enclosed current profile underestimates the total net toroidal current and an extra parallel electric field, in the same direction as the total current and opposite to the bootstrap-induced electric field, is required to drive this current.

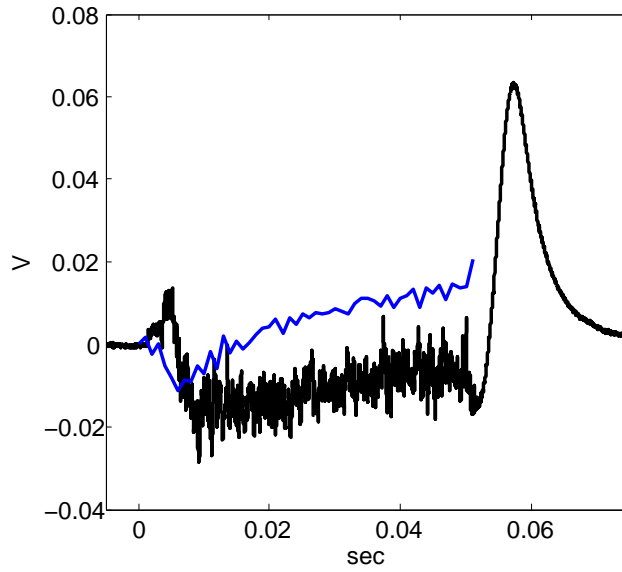


Figure H.9 Mirror CCW, 100 kW,  $\rho_{ECRH} \lesssim 0.1$ : Measured(black) and simulated(blue) loop voltage. Calculation by IEG.

For the CCW case, the measured pressure profile, a Lorentz-fit and the reconstructed pressure profile are shown in Figure H.10. The measured pressure profile, reconstructed profile and profiles that satisfy  $\chi^2_\nu \leq \chi^2_{\nu,\min} + 1$  are shown in Figure H.11. The evolved current profile at  $t = 50ms$ , an arctan-fit and the reconstructed profile are shown in Figure H.12. Profiles that satisfy  $\chi^2_\nu \leq \chi^2_{\nu,\min} + 1$  are shown in Figure H.13. The results of the reconstruction are summarized in Table H.2.

The reconstructed plasma pressure profile are similar to the measured ones. The pressure gradient near the axis is poorly resolved. The reconstructed current profile agrees well in total net current, but shows a low level of certainty regarding the current density, because a large number of different enclosed current profiles produce similar signals to that of the reconstruction.

For the CW case, the simulated and measured loop voltage is shown in Figure H.14. The simulated loop voltage falls to zero much faster than the measurement, indicating that the calculated current profile is probably incorrect. The measured pressure profile, a Lorentz-fit and the reconstructed pressure profile are shown in Figure H.15. The evolved current profile at  $t = 50ms$ , an

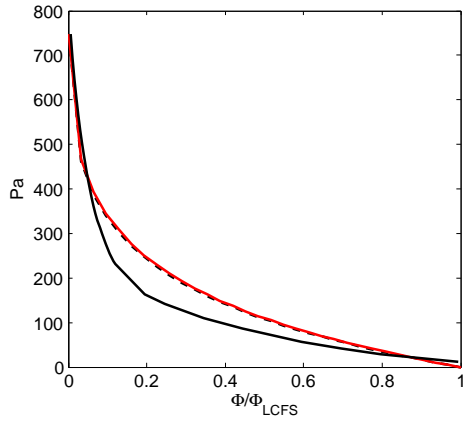


Figure H.10 Mirror CCW,  
100 kW,  $\rho_{ECRH} \lesssim 0.1$ : Measured plasma  
pressure profile (black), the Lorentz-fit initial  
guess (black, dashed), and **Reconstruction**.  
See Table H.2.

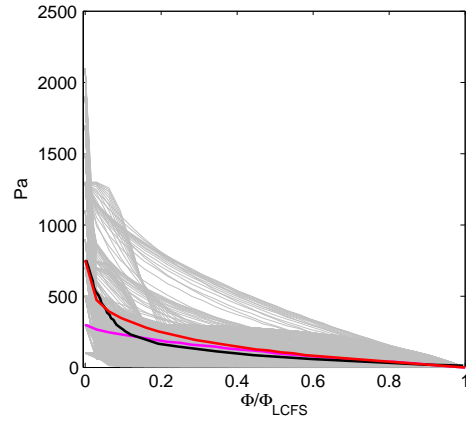


Figure H.11 Mirror CCW,  
100 kW,  $\rho_{ECRH} \lesssim 0.1$ : Measured plasma  
pressure (black), **Reconstruction**, and the  
minimum found during **Parameter scan #1**.  
The pressure profiles from the scan that  
satisfy  $\chi^2_{\nu} \leq \chi^2_{\nu, \min} + 1$  are indicated in gray.  
See Table H.2.

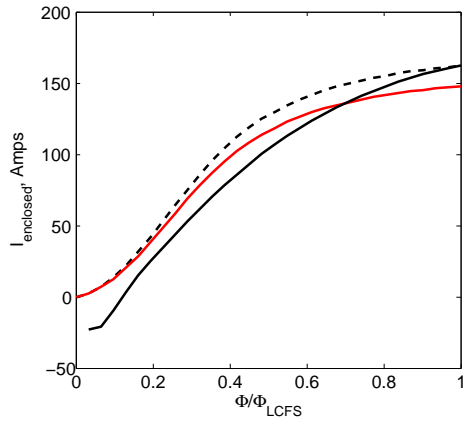


Figure H.12 Mirror CCW,  
100 kW,  $\rho_{ECRH} \lesssim 0.1$ : The calculated  
enclosed current profile (black), the arctan  
initial guess (black, dashed), and  
**Reconstruction**. See Table H.2.

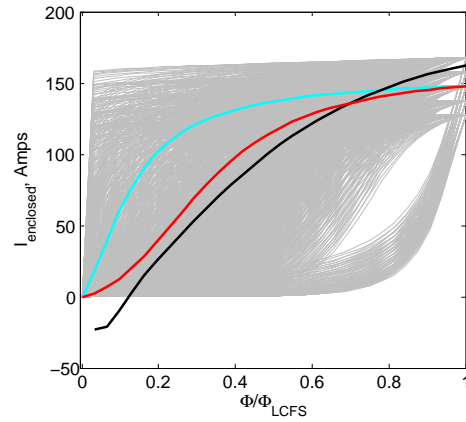


Figure H.13 Mirror CCW,  
100 kW,  $\rho_{ECRH} \lesssim 0.1$ : The calculated  
enclosed current profile (black),  
**Reconstruction**, and the minimum found  
during **Parameter scan #2**. The current  
profiles from the scan that satisfy  
 $\chi^2_{\nu} \leq \chi^2_{\nu, \min} + 1$  are indicated in gray. See  
Table H.2.

Parameter		PRES_SCALE		AM(2)		AM(3)		PHIEDGE	
		Value	$\sigma$	Value	$\sigma$	Value	$\sigma$	Value	$\sigma$
Initial Guess		748.	-	1	-	0.419	-	0.0400	-
Reconstruction		748.	8799.	1*	-	0.426	5.830	0.0397	0.0007
Parameter Scan #1 **		300.	-	4.	-	0.657	-	0.0396*	-
Parameter Scan #2 **		748.*	-	1*	-	0.426*	-	0.0397*	-

CURTOR		AC(2)		AC(3)		$\chi^2$	$\nu$	$\chi^2_\nu$	$F_\chi$
Value	$\sigma$	Value	$\sigma$	Value	$\sigma$				
162	-	4.06.	-	1.5	-	4.57	-	-	-
145.	1.	4.06	9.61	1.5*	-	2.10	11	0.19	-
145.*	-	4.06*	-	1.5*	-	1.96	10	0.20	-
148.	-	9.68	-	1.15	-	1.76	10	0.18	-

Table H.2 Mirror CCW, 100kW,  $\rho_{ECRH} \lesssim 0.1$ . V3FIT reconstruction results using internal poloidal array, Rogowski coil, and limiter signal. Black: Initial guess. **Reconstruction with 5 free parameters.** Scan of pressure profile parameters, holding the current profile constant. Scan of current profile parameters, holding the pressure profile constant. The  $\chi^2$  and  $\chi^2_\nu$  values are also shown. (\*) Quantity was not a fit parameter for this case. (\*\*) The limiter signal was disabled and PHIEDGE was not a fit parameter.

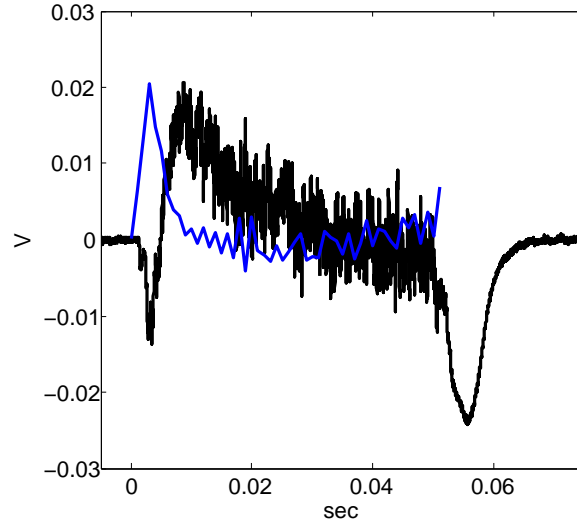


Figure H.14 Mirror CW, 100 kW,  $\rho_{ECRH} \lesssim 0.1$ : Measured (black) and simulated (blue) loop voltage. Calculation by IEG.

arctan-fit and the reconstructed profile are in Figure H.17. The results of the reconstruction are summarized in Table H.3.

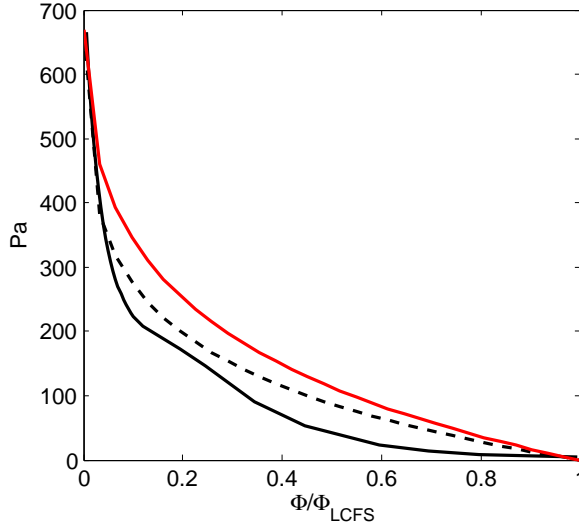


Figure H.15 Mirror CW,  
100 kW,  $\rho_{ECRH} \lesssim 0.1$ : Measured plasma  
pressure profile (black), the Lorentz-fit initial  
guess (black, dashed), and **Reconstruction**.  
See Table H.3.

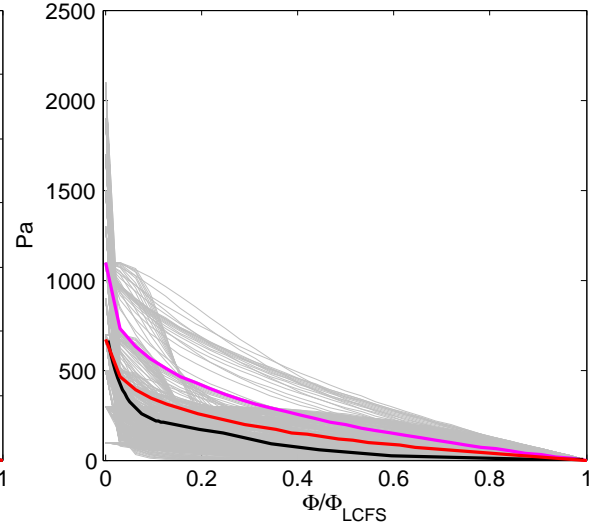


Figure H.16 Mirror CW,  
100 kW,  $\rho_{ECRH} \lesssim 0.1$ : Measured plasma  
pressure profile (black), **Reconstruction**, and  
the minimum found during **Parameter scan**  
**#1**. The pressure profiles from the scan that  
satisfy  $\chi^2_{\nu} \leq \chi^2_{\nu,\min} + 1$  are indicated in gray.  
See Table H.3.

The reconstructed pressure profile agrees well with the measured profiles, but current profile is not resolved very well. The net enclosed current is in agreement, but the enclosed current has a large uncertainty for the majority of the profile. For this case,  $AC(0)$  was one of the fit parameters. This parameter allows for a net current to exist on-axis. As can be seen in Figure H.18, the enclosed current profile can take on large number of possible solutions, and the current density profile can not be determined. The reversal of the current density, due to the electron root can not be detected in this case.

For the CW case with the slightly higher line-averaged density,  $\sim 5$ , the ambipolar  $E_r$  and current density, including and neglecting momentum conservation (MC), from the PENTA calculations are shown in Figures H.19 - H.23.

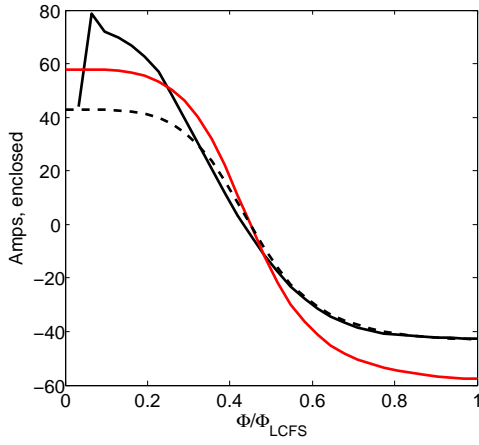


Figure H.17 Mirror CW,  $100\text{ kW}$ ,  $\rho_{ECRH} \lesssim 0.1$ : The calculated enclosed current profile (black), the arctan initial guess (black, dashed), and **Reconstruction**. See Table H.3.

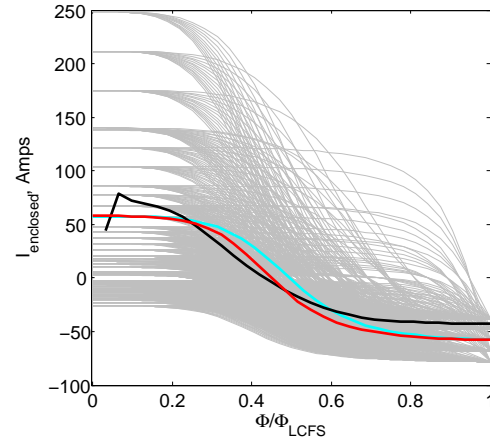


Figure H.18 Mirror CW,  $100\text{ kW}$ ,  $\rho_{ECRH} \lesssim 0.1$ : The calculated enclosed current profile (black), **Reconstruction**, and the minimum found during **Parameter scan #2**. The current profiles from the scan that satisfy  $\chi^2_v \leq \chi^2_{v,\min} + 1$  are indicated in gray. See Table H.3.

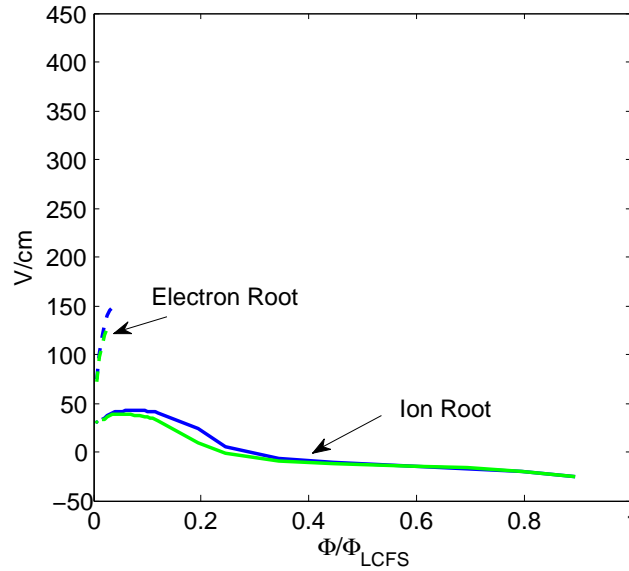


Figure H.19 Mirror CW,  $100\text{ kW}$ ,  $\rho_{ECRH} \lesssim 0.1$ : Stable ambipolar  $E_r$  solutions with MC (blue) and without MC (green). Calculation by PENTA.

Parameter		PRES_SCALE		AM(2)		AM(3)		PHIEDGE	
		Value	$\sigma$	Value	$\sigma$	Value	$\sigma$	Value	$\sigma$
Initial Guess		666.	-	1	-	0.379	-	-0.0400	-
Reconstruction		668.	6146.	1*	-	0.491	5.194	-0.0397	0.0009
Parameter Scan #1 **		1100.	-	3.44	-	0.379	-	-0.0397*	-
Parameter Scan #2 **		668.*	-	1*	-	0.491*	-	-0.0397*	-
CURTOR		AC(0)		AC(2)		$\chi^2$	$\nu$	$\chi_\nu^2$	$F_\chi$
Value	$\sigma$	Value	$\sigma$	Value	$\sigma$				
-43	-	1.	-	10.	-	4.62	-	-	-
-57.	9.	-1.001	1.185	10.0	62.9	1.28	10	0.13	-
-57.*	-	-1.001*	-	10.0*	-	1.13	9	0.14	-
-58.	-	-1.	-	6.49	-	1.26	9	0.14	-

Table H.3 Mirror CW,  $100kW$ ,  $\rho_{ECRH} \lesssim 0.1$ . V3FIT reconstruction results using internal poloidal array, Rogowski coil, and limiter signal. Black: Initial guess. **Reconstruction with 5 free parameters.** Scan of pressure profile parameters, holding the current profile constant. Scan of current profile parameters, holding the pressure profile constant. The  $\chi^2$  and  $\chi_\nu^2$  values are also shown, where relevant. (\*) Quantity was not a fit parameter for this case. (\*\*) The limiter signal was disabled and PHIEDGE was not a fit parameter.

For this case, the PENTA results without MC included predict a steady state current of only  $\sim 60$  A, while the calculations that include MC predict a net current of 140 A (e-root dominated) to 160 A (i-root dominated). Again, the PENTA calculation does not include a factor of  $\times -1$  to account for the field direction. The extrapolated steady-state current for the experiment is  $-123$  A, which agrees better with e-root dominated solution that included MC. The e-root dominated current density profile and the conductivity profile in are used in the IEG code to calculate the time evolution of the current profile. The simulated and measured loop voltage is shown in Figure H.24.

The simulated loop voltage is slightly smaller than the measured one. Indicating that the non-inductive current density is underestimated and requires an additional parallel electric field to drive the current. The calculated current profile reverses sign near the axis, but the arctan-fit was fixed at zero on axis since the difference is small.



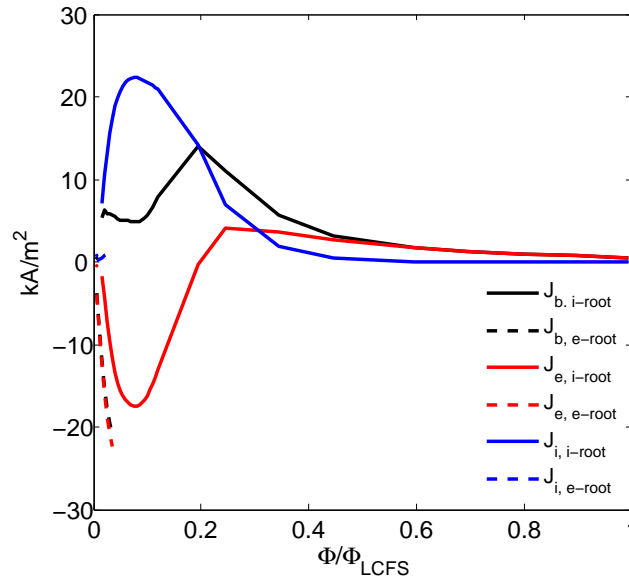


Figure H.20 Mirror CW, 100  $kW$ ,  $\rho_{ECRH} \lesssim 0.1$ , With MC: Ion (blue), electron (red) and total (black) parallel current. Solid lines coincide with the ion root solution and dashed lines coincide with the electron root solution. Calculation by PENTA.

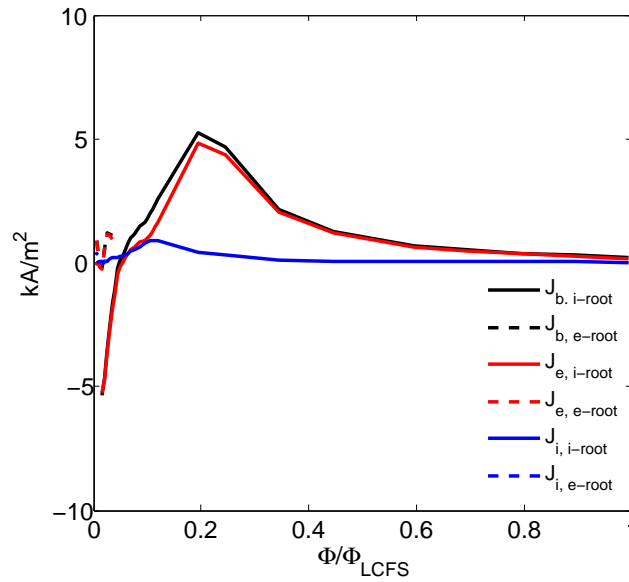


Figure H.21 Mirror, 100  $kW$ ,  $\rho_{ECRH} \lesssim 0.1$ , Without MC: Ion (blue), electron (red) and total (black) parallel current. Solid lines coincide with the ion root solution and dashed lines coincide with the electron root solution. Calculation by PENTA..

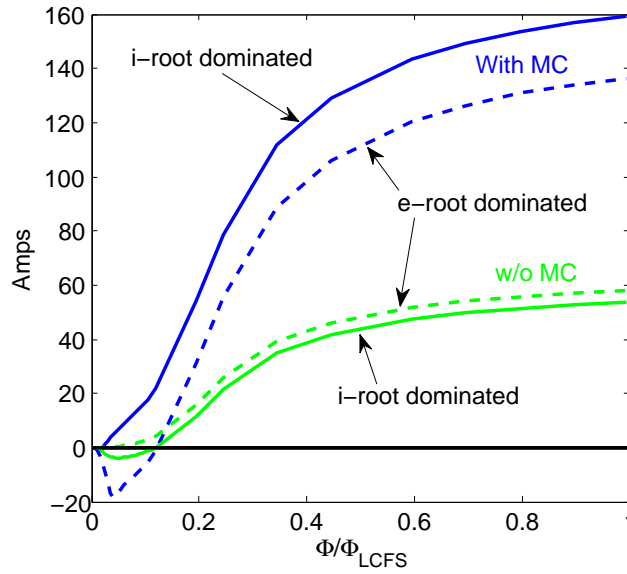


Figure H.22 Mirror,  $100\text{ kW}$ ,  $\rho_{ECRH} \lesssim 0.1$ ,: Enclosed current profile for different scenarios of current density. With MC (blue) and without MC (green)

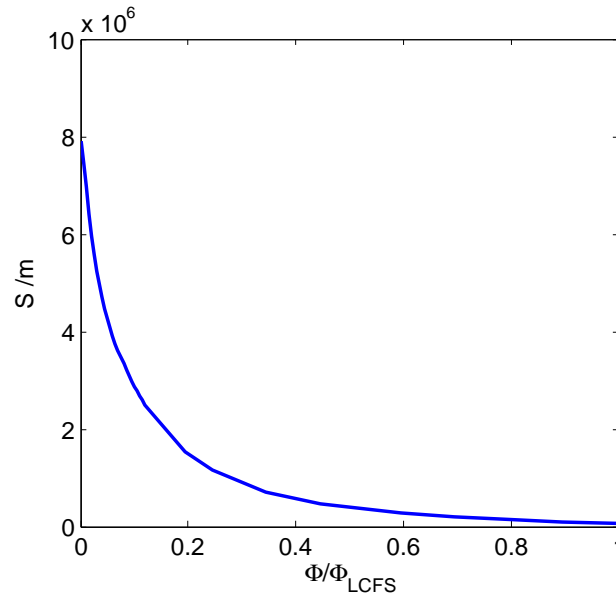


Figure H.23 Mirror,  $100\text{ kW}$ ,  $\rho_{ECRH} \lesssim 0.1$ , higher line-averaged density case: Parallel conductivity of the plasma, including trapped particle effect. Calculation by PENTA.

The measured pressure profile, a Lorentz-fit and the reconstructed pressure profile are shown in Figure H.25. The evolved current profile at  $t = 50\text{ms}$ , an arctan-fit and the reconstructed profile

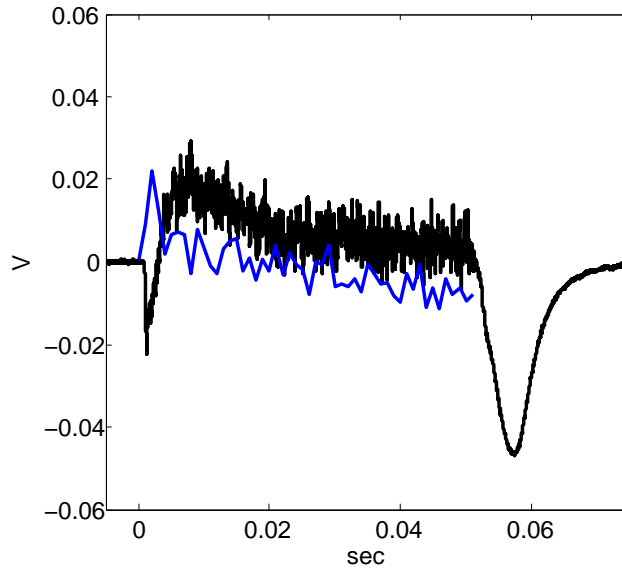


Figure H.24 Mirror CW, 100 kW,  $\rho_{ECRH} \lesssim 0.1$ : Measured (black) and simulated (blue) loop voltage. Calculation by IEG.

are shown in Figure H.27. Current profiles that satisfy  $\chi_\nu^2 \leq \chi_{\nu,\min}^2 + 1$  are shown in Figure H.28, along with the evolved current profile and reconstructed one. The results of the reconstruction are summarized in Table H.4.

As with the other reconstructions, the reconstructed pressure profile is similar to the measured pressure profile, and the pressure gradient is poorly resolved on-axis. The reconstructed current profile is close to the calculated one, even though it is fixed to be 0 on axis and the calculation predicts a sign switch in the enclosed current. The current density profile (not shown), which is the radial derivative of current profile, is poorly resolved and has a large uncertainty associated.

The results of the Mirror flip-field experiments indicate that the net toroidal current depends on direction of the main magnetic field. With similar  $T_e$ , and  $N_e$  profiles, the measured net toroidal current was larger in the CCW direction by more than 100 A. Raising the operating density while operating in the CW direction had the effect of lowering the  $T_e$  profile, but increasing the net toroidal current. The reason for this is not known. The HSX machine is usually operated with the main magnetic field in the CCW direction. It has been suggested that by reversing the magnetic

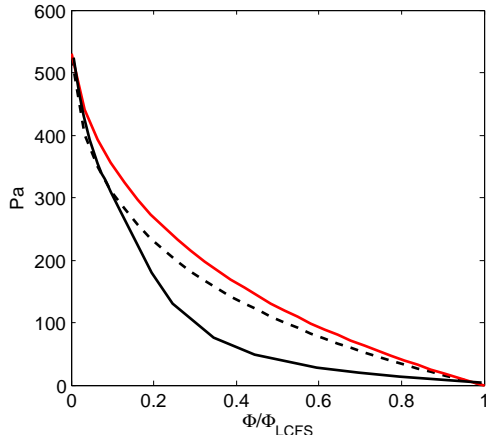


Figure H.25 Mirror CW,  
100 kW,  $\rho_{ECRH} \lesssim 0.1$ : Measured plasma  
pressure profile (black), the Lorentz-fit initial  
guess (black, dashed), and **Reconstruction**.  
See Table H.4.

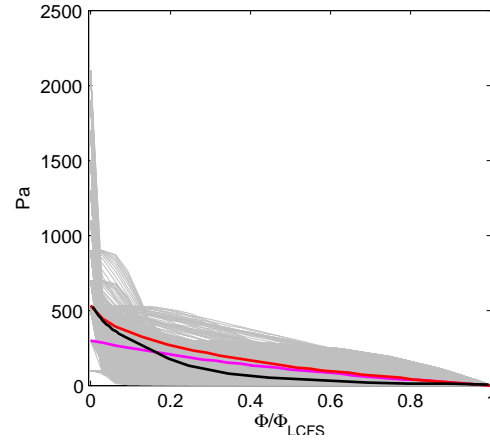


Figure H.26 Mirror CW,  
100 kW,  $\rho_{ECRH} \lesssim 0.1$ : Measured plasma  
pressure profile (black), **Reconstruction**, and  
the minimum found during **Parameter scan**  
**#1**. The pressure profiles from the scan that  
satisfy  $\chi^2_{\nu} \leq \chi^2_{\nu, \min} + 1$  are indicated in gray.  
See Table H.4.

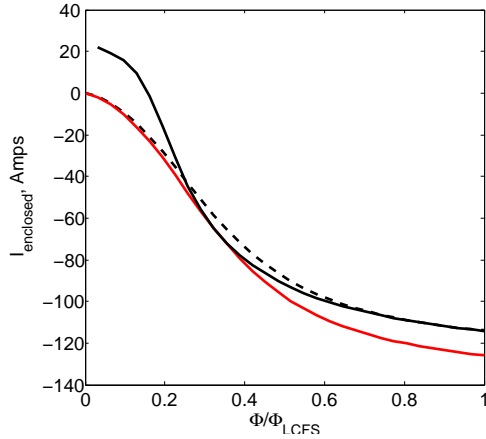


Figure H.27 Mirror CW,  
100 kW,  $\rho_{ECRH} \lesssim 0.1$ : The calculated  
enclosed current profile (black), the arctan  
initial guess (black, dashed), and  
**Reconstruction**. See Table H.4.

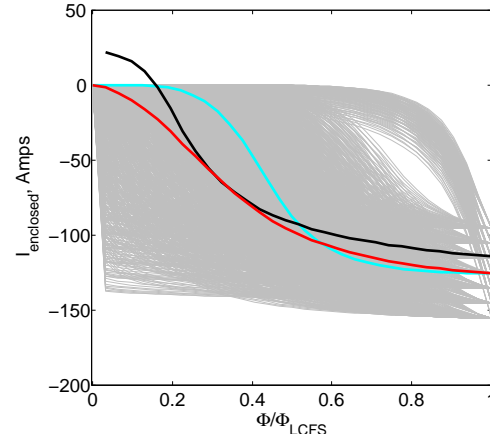


Figure H.28 Mirror CW,  
100 kW,  $\rho_{ECRH} \lesssim 0.1$ : The calculated  
enclosed current profile (black),  
**Reconstruction**, and the minimum found  
during **Parameter scan #2**. The current  
profiles from the scan that satisfy  
 $\chi^2_{\nu} \leq \chi^2_{\nu, \min} + 1$  are indicated in gray. See  
Table H.4.

Parameter		PRES_SCALE		AM(2)		AM(3)		PHIEDGE	
		Value	$\sigma$	Value	$\sigma$	Value	$\sigma$	Value	$\sigma$
Initial Guess		524.	-	1	-	0.587	-	-0.0400	-
Reconstruction		530.	2389.	1*	-	0.694	4.276	-0.0396	0.0008
Parameter Scan #1 **		300.	-	1.21	-	0.936	-	-0.0396*	-
Parameter Scan #2 **		530.*	-	1 *	-	0.694*	-	-0.0396*	-
CURTOR		AC(2)		AC(3)		$\chi^2$	$\nu$	$\chi^2_\nu$	$F_\chi$
Value	$\sigma$	Value	$\sigma$	Value	$\sigma$				
-114	-	3.86	-	1.5	-	2.91	-	-	-
-126.	11.	3.86	10.37	1.5*	-	1.25	11	0.11	-
-126.*	-	3.86*	-	1.5*	-	1.22	10	0.12	-
-126.	-	15.	-	3.95	-	1.10	10	0.11	-

Table H.4 Mirror CW,  $100kW$ ,  $\rho_{ECRH} \lesssim 0.1$ . V3FIT reconstruction results using internal poloidal array, Rogowski coil, and limiter signal. Black: Initial guess. **Reconstruction with 5 free parameters.** Scan of pressure profile parameters, holding the current profile constant. Scan of current profile parameters, holding the pressure profile constant. The  $\chi^2$  and  $\chi^2_\nu$  values are also shown. (\*) Quantity was not a fit parameter for this case. (\*\*) The limiter signal was disabled and PHIEDGE was not a fit parameter.

field, the plasma may make contact with the vacuum vessel at slightly different strike points (regions were open field lines outside the last closed flux surface strike the vacuum vessel), changing the impurity content. The plasma flows for different impurity species can be different from the bulk flow, even reversing direction [1]. To determine if this is the case, this set of experiments should be performed again, making careful measurements of the impurity content of the plasma. The radiated power measurement was not available for the plasmas made in the CCW direction for this experiment, but the Fast Spectroscopy System (FSS), indicated that an impurity radiation line associated with CV increases about 10% – 20% when operating in the CW direction compared to the CCW direction.

## **Appendix H: References**

- [1] L. R. Baylor, et al., Physics of Plasmas **11**, 3100 (2004).

## Appendix I: QHS Near-ECH Fueling

Up until now, the fueling source for the plasmas discussed in this dissertation was the puff valve located far away from the ECH launch mirror, at the opposite side of the machine near boxport A, Figure 5.2. Now, the results of flip field experiments with the fueling provided by the puff valve in field period C will be presented and discussed. This puff valve is located only a short distance away toroidally from the ECH antenna in the CCW direction.

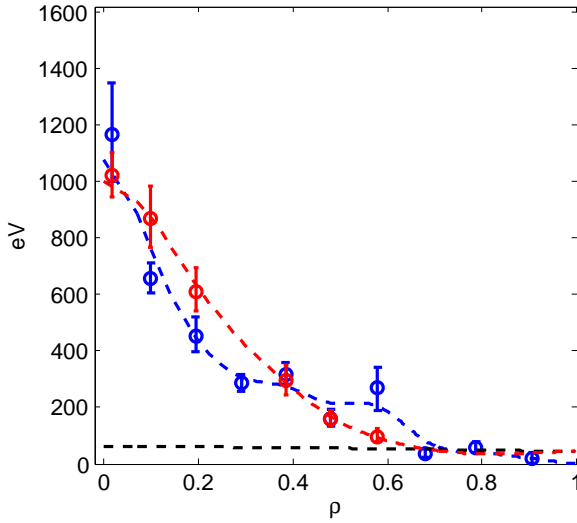


Figure I.1 QHS,  $\bar{N}_e = 2 \times 10^{18}/m^3$ , 50 kW,  $\rho_{ECRH} \lesssim 0.1$ :  $T_e$  for CCW (blue) and CW (red).  $T_i$  estimate from ChERS (black, dashed).

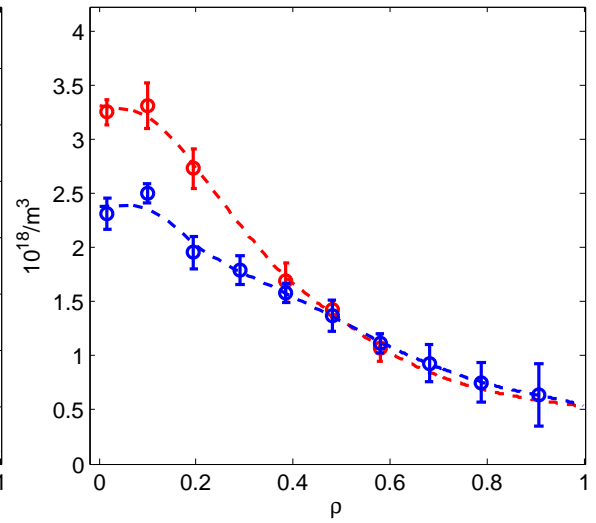


Figure I.2 QHS,  $\bar{N}_e = 2 \times 10^{18}/m^3$ , 50 kW,  $\rho_{ECRH} \lesssim 0.1$ :  $N_e$  for CCW (blue) and CW (red).

Plasmas in the QHS magnetic configuration were made for four different operating line-averaged operating densities,  $\bar{N}_e = (2, 3, 4, 5) \times 10^{18}/m^3$  (measured with interferometry), with the magnetic field in both the CCW and the CW direction. The ECRH power (launched) for these cases was 50 kW, and the resonance location was  $\rho_{ECRH} \lesssim 0.1$ . The measured electron temperature and density profiles for these cases are shown in Figures I.1-I.8. For each individual operating density the measured electron temperature profiles were similar, although not identical, with the magnetic field in CCW or CW. However, the measured density profiles show some differences,

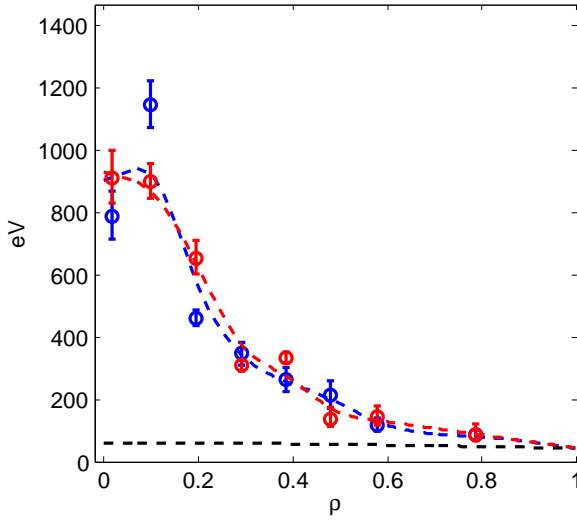


Figure I.3 QHS,  $\bar{N}_e = 3 \times 10^{18}/m^3$ ,  $50 \text{ kW}$ ,  $\rho_{ECRH} \lesssim 0.1$ :  $T_e$  for CCW (blue) and CW (red).  $T_i$  estimate from ChERS (black, dashed).

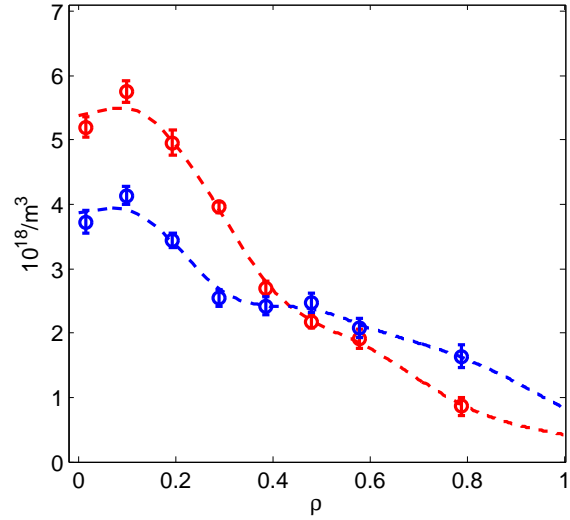


Figure I.4 QHS,  $\bar{N}_e = 3 \times 10^{18}/m^3$ ,  $50 \text{ kW}$ ,  $\rho_{ECRH} \lesssim 0.1$ :  $N_e$  for CCW (blue) and CW (red).

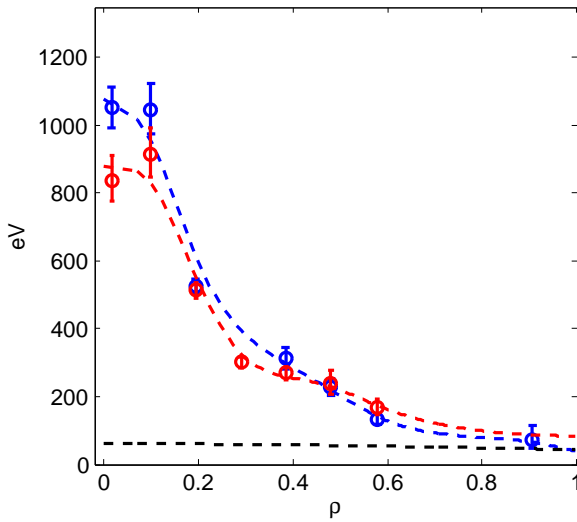


Figure I.5 QHS,  $\bar{N}_e = 4 \times 10^{18}/m^3$ ,  $50 \text{ kW}$ ,  $\rho_{ECRH} \lesssim 0.1$ :  $T_e$  for CCW (blue) and CW (red).  $T_i$  estimate from ChERS (black, dashed).

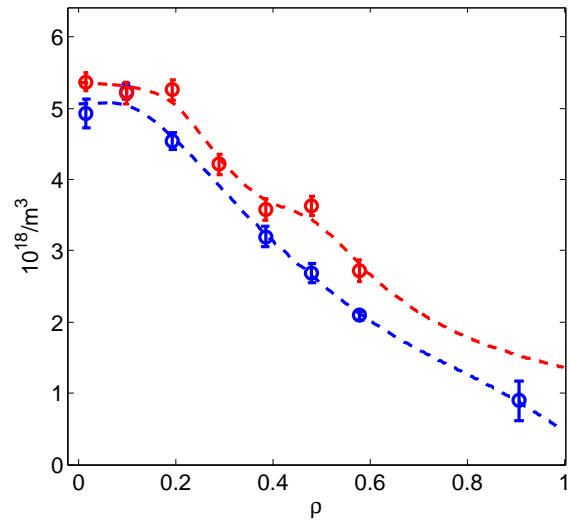


Figure I.6 QHS,  $\bar{N}_e = 4 \times 10^{18}/m^3$ ,  $50 \text{ kW}$ ,  $\rho_{ECRH} \lesssim 0.1$ :  $N_e$  for CCW (blue) and CW (red).



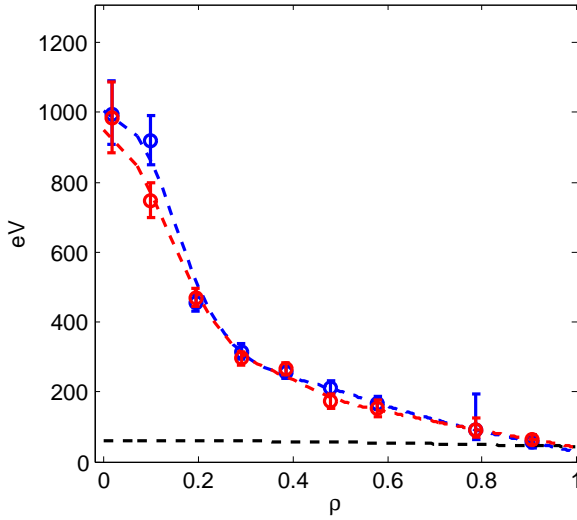


Figure I.7 QHS,  $\bar{N}_e = 5 \times 10^{18}/m^3$ ,  $50 \text{ kW}$ ,  $\rho_{ECRH} \lesssim 0.1$ :  $T_e$  for CCW (blue) and CW (red).  $T_i$  estimate from ChERS (black, dashed).

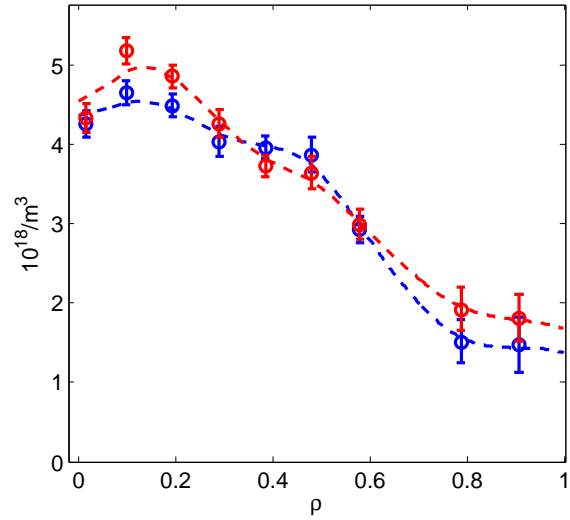


Figure I.8 QHS,  $\bar{N}_e = 5 \times 10^{18}/m^3$ ,  $50 \text{ kW}$ ,  $\rho_{ECRH} \lesssim 0.1$ :  $N_e$  for CCW (blue) and CW (red).

predominantly at the lower  $\bar{N}_e$ . At  $\bar{N}_e = 2, 3 \times 10^{18}/m^3$ , the plasmas made with the field in the CW direction was higher for  $\rho \lesssim 0.4$ . The differences at higher densities are smaller. At the highest density,  $\bar{N}_e = 5 \times 10^{18}/m^3$ , the profiles agreed well.

The measured net current for each case is shown in Figure I.9. The extrapolated steady-state current for each of these cases is shown in Figure I.10. The value for plasmas in the CW direction have been multiplied by  $-1$  to make comparisons of the magnitude easier. The net toroidal current increases with density when the magnetic field is in the CW direction. When the field is in the CW direction, the extrapolated current saturates at operating densities of  $N_e = 4 \times 10^{18}/m^3$  and higher. For each case, PENTA was used to calculate the total enclosed bootstrap current for the ion-root dominated case, and that is also plotted in the figure. The electron-root dominated solution (not shown) was between 0 A and 60 A for each case. In the CW direction, the PENTA calculation predicts the highest level of total bootstrap current at  $N_e = 2 \times 10^{18}/m^3$ , and in the CCW direction, PENTA predicts the current to increase with density, with a plateau for densities from  $N_e = 3 - 4 \times 10^{18}/m^3$ .

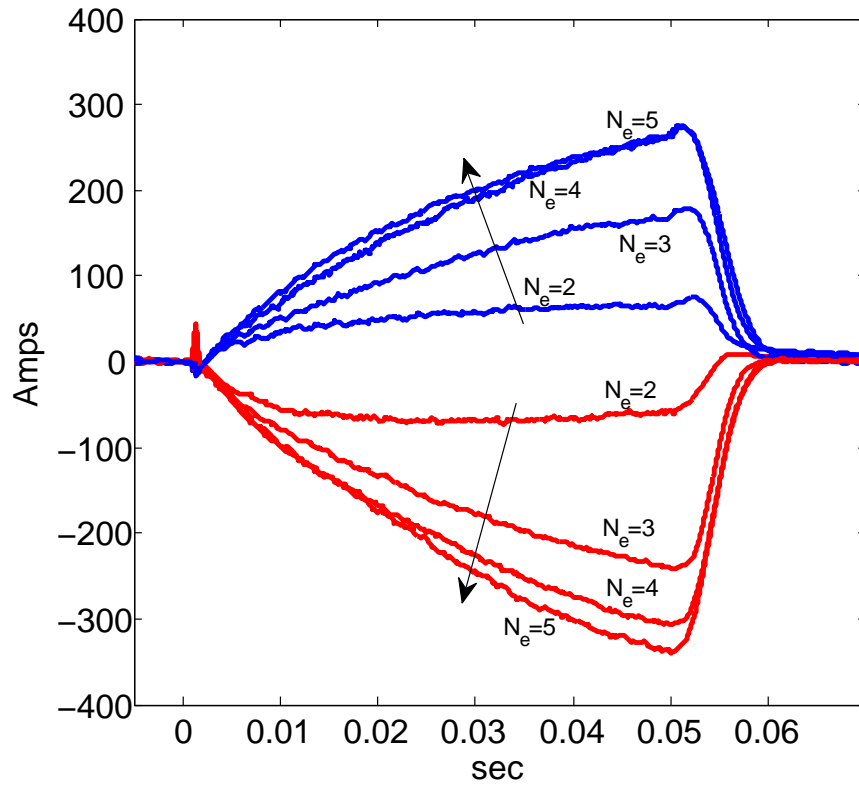


Figure I.9 Measured toroidal current for the 4 densities with the magnetic field in the CCW (blue) and CW (red) directions.

The level of agreement between the experiment and the PENTA calculations is poor. Currently, the reason behind this is not understood, but seems to be associated with the location of the puff valve used for fueling. It is speculated that the interaction of the neutral gas with the plasma likely results in region of local cooling. This may alter the electron distribution function in a few ways. The thermal temperature of the bulk electrons may be anisotropic along the field lines. Another possibility is that the minority electrons, those that have been heated by the ECH, may have their distribution function modified. It is unclear what other effects the location of the gas fueling may have on the plasma and the neoclassical transport analysis.

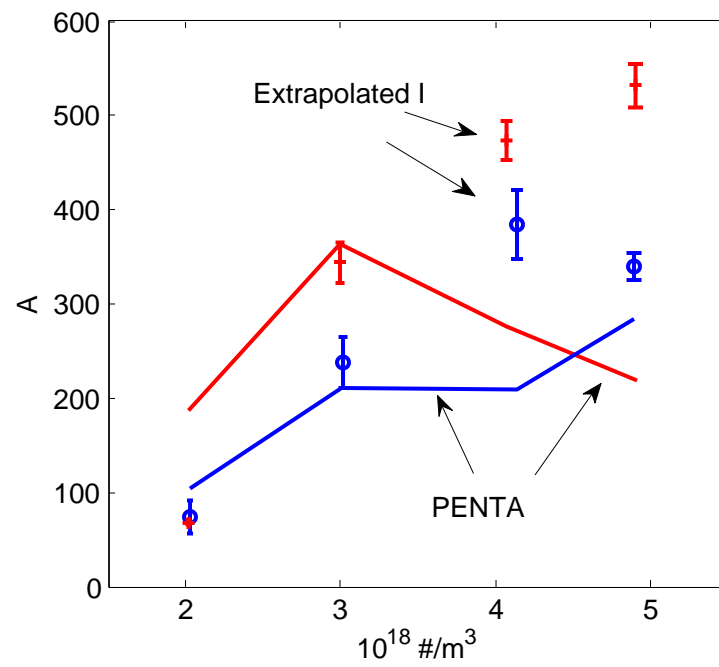


Figure I.10 Extrapolated steady state current (circles) and the net toroidal current predicted by PENTA for an ion-root dominated solution. Results for the main field in the CCW direction are in blue. Results for the main field in the CW direction have been multiplied by  $-1$  and are in red.